A Route to Optical Spectroscopy on the Nanoscale

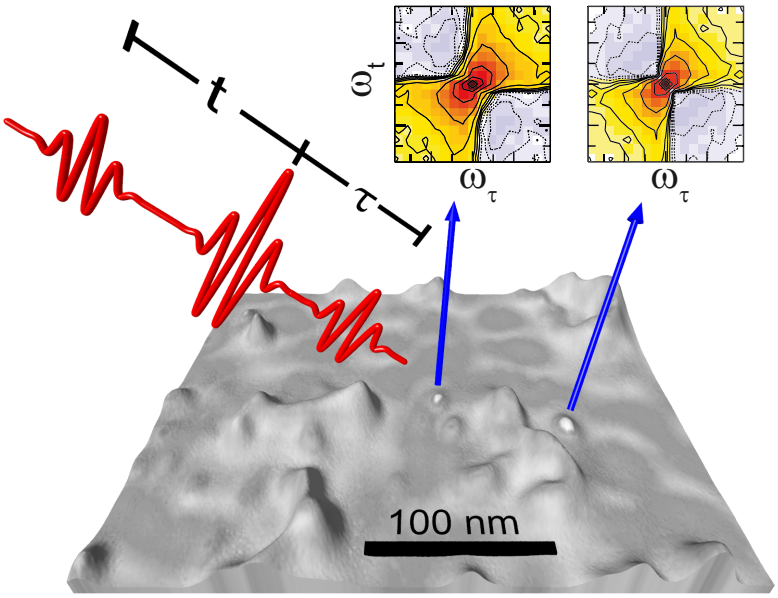

Dissertation zur Erlangung des naturwissenschaftlichen Doktorgrades der Julius-Maximilians-Universität Würzburg

vorgelegt von
Philip Tuchscherer
aus Pohlheim

Würzburg 2012

Eingereicht am 30. Januar 2012
bei der Fakultät für Physik und Astronomie

1. Gutachter: Prof. Dr. Tobias Brixner
2. Gutachter: Prof. Dr. Bert Hecht
der Dissertation

1. Prüfer: Prof. Dr. Tobias Brixner
2. Prüfer: Prof. Dr. Bert Hecht
3. Prüfer: Prof. Dr. Wolfgang Kinzel
im Promotionskolloquium

Tag des Promotionskolloquiums: 23. Juli 2012

Doktorurkunde ausgehändigt am: _____

List of Publications

Parts of the content of Chapters 3 to 7 have been published in the following references:

Chapter 3:

J.S. Huang, D.V. Voronine, P. Tuchscherer, T. Brixner, and B. Hecht,
Deterministic spatiotemporal control of optical fields in nanoantennas and plasmonic circuits,
Phys. Rev. B **79**, 195441 (2009).

Chapter 4:

P. Tuchscherer, C. Rewitz, D.V. Voronine, F.J. García de Abajo, W. Pfeiffer, and T. Brixner,
Analytic coherent control of plasmon propagation in nanostructures,
Opt. Express **17**, 14235 (2009).

Chapter 5:

M. Aeschlimann, M. Bauer, D. Bayer, T. Brixner, S. Cunovic, A. Fischer, P. Melchior, W. Pfeiffer, M. Rohmer, C. Schneider, C. Strüber, P. Tuchscherer, and D.V. Voronine,
Deterministic control of subwavelength field localization in plasmonic nanoantennas,
in *Ultrafast Phenomena XVII* (M. Chergui, D.M. Jonas, E. Riedle, R.W. Schoenlein, A.J. Taylor, Eds.), pp. 667–669, Oxford University Press, New York (2011).

M. Aeschlimann, M. Bauer, D. Bayer, T. Brixner, S. Cunovic, A. Fischer, P. Melchior, W. Pfeiffer, M. Rohmer, C. Schneider, C. Strüber, P. Tuchscherer, and D.V. Voronine,
Optimal open-loop near-field control of plasmonic nanostructures
New J. Phys. **14**, 033030 (2012).

Chapter 6:

M. Aeschlimann, T. Brixner, S. Cunovic, A. Fischer, P. Melchior, W. Pfeiffer, M. Rohmer, C. Schneider, C. Strüber, P. Tuchscherer, and D.V. Voronine,
Nano-optical Control of Hot-Spot Field Superenhancement on a Corrugated Silver Surface,
IEEE J. Sel. Top. Quant. **18**, 275 (2012).

Chapter 7:

M. Aeschlimann, T. Brixner, A. Fischer, C. Kramer, P. Melchior, W. Pfeiffer, C. Schneider, C. Strüber, P. Tuchscherer, and D.V. Voronine,
Coherent Two-Dimensional Nanoscopy,
Science **333**, 1723 (2011).

Additional publications that are not presented in this work are:

C. Rewitz, T. Keitzel, P. Tuchscherer, J.S. Huang, P. Geisler, G. Razinskas, B. Hecht, and T. Brixner,
Ultrafast Plasmon Propagation in Nanowires Characterized by Far-Field Spectral Interferometry,
Nano Lett. **12**, 45 (2012).

C. Rewitz, T. Keitzel, P. Tuchscherer, S. Goetz, P. Geisler, G. Razinskas, B. Hecht, and T. Brixner,
Spectral-interference microscopy for characterization of functional plasmonic elements,
Opt. Express **20**, 14632 (2012).

Contents

1 Introduction

One of the main interests in physics has always been to magnify and visualize spatial regions so small that they cannot be explored by the bare eye. Starting with single lenses in the early days of physics, the history of optical microscopy was initiated. Using a combination of different lenses, the magnification was increased and applications of these microscopes yielded, e.g., a first observation and description of single-celled organisms [1]. However, by further improvements of optical microscopes it was discovered by Abbe more than a hundred years ago that their resolution is limited by diffraction [2]. He found out that the maximum resolution is given by approximately half of the wavelength of the light that is used for investigation. Therefore, sophisticated methods have been introduced in the last decades to overcome this limit. A promising method that has been developed employs optical near fields. These near fields are solutions of Maxwell's equations for metal–dielectric interfaces and yield strong spatial confinement of optical waves. Near-field scanning optical microscopy enables resolution down to a few nanometers and has been used to, e.g., visualize nanostructured samples [3].

In other applications, light has been used to investigate the spectral properties of matter. In the beginning, optical spectroscopy has been used to investigate static properties but has nowadays been advanced to the investigation of dynamic processes. Using time-resolved optical spectroscopy, which is one of the main topics of our research group, time dependent interaction of light with matter is studied. In such experiments a quantum system is excited with a first "pump" pulse from thermal equilibrium and the dynamics of the excited system are then mapped using a variable time-delayed "probe" pulse. Pulses with durations on the order of femtoseconds have become commonly accessible in the last decades, and pump–probe measurements enabled mapping of chemical reactions and revealed information of molecular dynamics [4]. Femtosecond pulse shaping methods, which have been developed in the optical regime, even enabled control of such chemical reactions [5]. Depending on the investigated system and on the requested information, different spectroscopic techniques, such as transient absorption [4] or fluorescence spectroscopy [6], have been applied. To obtain further insight into coherences of quantum mechanical states, coherent two-dimensional (2D) spectroscopy [7] has turned out to be a powerful tool in recent years. Using this technique, overlapping contributions of congested linear spectra can be separated, since this information is spread out along a second spectral dimension. Vibrational as well as electronic couplings in quantum systems can be revealed by evaluating the off-diagonal peaks [8]. Additionally, homogeneous and inhomogeneous broadening can be distinguished by analysis of the 2D lineshapes [7].

However, in all these implementations of optical spectroscopy the spatial resolution that determines the interaction volume with the sample has the same lower bound that was found for optical microscopy. The diffraction limit of the optical waves is on the

order of several hundreds of nanometers and this causes averaging over an ensemble of quantum systems present in the interaction volume. Although single molecule experiments have been performed by using low emitter density in combination with tight focusing [9, 10], their spatial resolution is still diffraction limited, and investigation of single molecules in, e.g., molecular aggregates, has not been achieved. Thus, we are at a point, where quantum mechanical processes can be understood and mapped using sophisticated spectroscopical methods. However, spectroscopy that can reveal information about single quantum systems within their natural surrounding is still missing. Therefore, new spectroscopic methods have to be developed to overcome the optical diffraction limit and to directly disclose spatial coupling and transfer processes. In this thesis, a route to optical spectroscopy on the nanoscale is given by utilizing two different approaches. The first approach picks up the same idea that was already used to overcome the diffraction limit in microscopy and employs optical near fields. The second approach combines optical excitation with a non-optical detection that yields a high spatial resolution.

The utilization of optical near fields for spectroscopic applications is especially interesting since advanced methods have been developed in the last decades to produce appropriate nanostructured samples. Illumination of these nanostructures with femtosecond laser pulses enable strong spatial and temporal confinements of optical fields in their vicinity. Due to constructive and destructive interference of different near-field modes that are caused by two independent far-field polarizations, the technique of femtosecond polarization pulse shaping enables control of these confinements. Using this control, optimal far-field polarization-shaped pulses were presented that by illumination of a suitable nanostructure enable near-field excitation schemes for spectroscopic applications [11]. In these excitations schemes, pump–probe pulses are not only separated temporally on a femtosecond scale—as in conventional time-resolved spectroscopy—but they are also separated in space on the nanometer scale. A promising application is the excitation of a quantum system with a near-field pulse at one position at a certain time and probing of the quantum system at a different position at a later time. So far, the polarization-shaped laser pulses that provide these near-field excitation schemes were found in an adaptive fashion without using information about the involved near-field control mechanisms [11–14]. Thus, parameters that are scanned in optical spectroscopy, such as the temporal delay or the relative phase between two pulses, cannot be accessed easily. The optimal polarization-shaped laser pulses would have to be found for each near-field scanning step in a separate time-consuming adaptive optimization. Hence, for broad spectroscopic implementations, the near-field control mechanisms have to be used to find these optimal pulses in a deterministic fashion.

After describing the basic theoretical and experimental concepts in Chapter 2 as well as introducing the properties of near fields in Chapter 3, general analytic solutions are derived for that purpose in Chapter 4. These solutions enable deterministic near-field control in arbitrary nanostructures by calculating the optimal polarization-shaped laser pulses. The main idea of the analytic approach is to disentangle the mechanisms for spatial and temporal control by using two independent steps. The solutions are then employed in simulations to guide electromagnetic energy in a branching T-chain of nanospheres. Simple deterministic rules are found to switch the near-field intensity in

the vicinity of a nanostructure from one position to another. The benefit of the analytic rules to optical spectroscopy is presented by calculating polarization-shaped laser pulses that generate a near-field double pulse with a spatial distance between the two pulses that is determined by the nanostructure and a temporal separation that can be adjusted in an arbitrary manner. In Chapter 5, an experimental realization of the analytic rules is shown for gold nanoprisms. In this experiment, the near-field intensity is switched from one corner of the prisms to another corner in a deterministic fashion. Verification of the obtained results for theoretical and experimental deterministic control is achieved by comparison to adaptive optimizations.

Additionally, possible applications of near-field control to surface-enhanced Raman spectroscopy are investigated in Chapter 6. In these experiments, optimal polarization shaped laser pulses are found in an adaptive fashion to spatially control the near-field intensity on a corrugated silver surface. Interesting behavior of the optimal pulse shapes are observed indicating unexpected coherences on the silver surface.

In the second approach to overcome the optical diffraction limit in spectroscopic applications, a combination of optical excitation with photoemission electron microscopy (PEEM) is used. In this microscope, the sample is excited with weakly focussed optical waves and the photoelectrons that are emitted from the sample are detected. Hence, the area that is excited with the laser pulses is on the order of several micrometers. However, due to the smaller wavelength of the detected electrons, the diffraction limit of these electrons is about three orders of magnitude smaller than that of visible light. This avoids spatial averaging since a resolution down to a few nanometers is achieved. Although time-resolved PEEM experiments have been realized already in terms of two-pulse correlation measurements [15], they—in general—do not reveal coherences directly that are essential to determine couplings in quantum systems.

Therefore, a new technique, termed "coherent 2D nanoscopy", that enables direct observation of coherences is developed in Chapter 7. This technique combines "conventional" coherent 2D spectroscopy, as it was performed so far, with the spatial resolution of PEEM. The sample is excited with quadruple-pulse sequences and the electrons that are emitted from the sample carry information about the quantum mechanical processes. The technique enables mapping of these processes with a nanometer spatial and femtosecond temporal resolution. In a first implementation of 2D nanoscopy, the corrugated silver surface that showed indications for unexpected coherences is investigated, and the measured data is explained by a model of coupled near-field modes that vary on the nanoscale.

2 Basic Theoretical and Experimental Concepts

In this chapter, the basic theoretical and experimental concepts of polarization-shaped femtosecond laser pulses and photoelectron-emission microscopy are introduced. First femtosecond pulses are described in terms of their general linear (Section 2.1) and vectorial properties (Sections 2.2). Then femtosecond laser pulse shaping that is used for control of near-field control and to generate pulse sequences is introduced (Section 2.3). To identify near-field control mechanisms, the pulse shapes that will be found in a deterministic fashion have to be characterized carefully (Section 2.4) and are compared to pulse shapes found by an evolutionary algorithm (Section 2.5). The spatial resolution that is needed on the one hand to experimentally investigate the optical near fields and on the other hand for spectroscopic application is provided by a photoemission electron microscope (Section 2.6).

2.1 Mathematical Description of Femtosecond Laser Pulses

Before discussing the vectorial character of femtosecond laser pulses in terms of polarization this section gives an introduction to the general behavior of linearly polarized femtosecond laser pulses. The description is based on the literature of Diels and Rudolph [16], Brixner [17], and Wollenhaupt *et al.* [18].

2.1.1 Temporal and Spectral Description

A linearly polarized femtosecond laser pulse at a fixed point in space is described as a scalar real-valued function of time t

$$E(t) = 2A(t)\cos[\phi(t)], \tag{2.1}$$

where $A(t)$ is half of the temporal amplitude or envelope and $\phi(t)$ is the temporal varying phase. The phase term $\phi(t)$ includes a linear term which results in fast oscillations due to the carrier frequency ω_0 of visible light. Separation of this term yields

$$\phi(t) = \omega_0 t + \varphi(t), \tag{2.2}$$

where $\varphi(t)$ includes all higher order terms as well as a constant term. For a better understanding of the temporal phase $\phi(t)$ it is advantageous to expand it in a Taylor

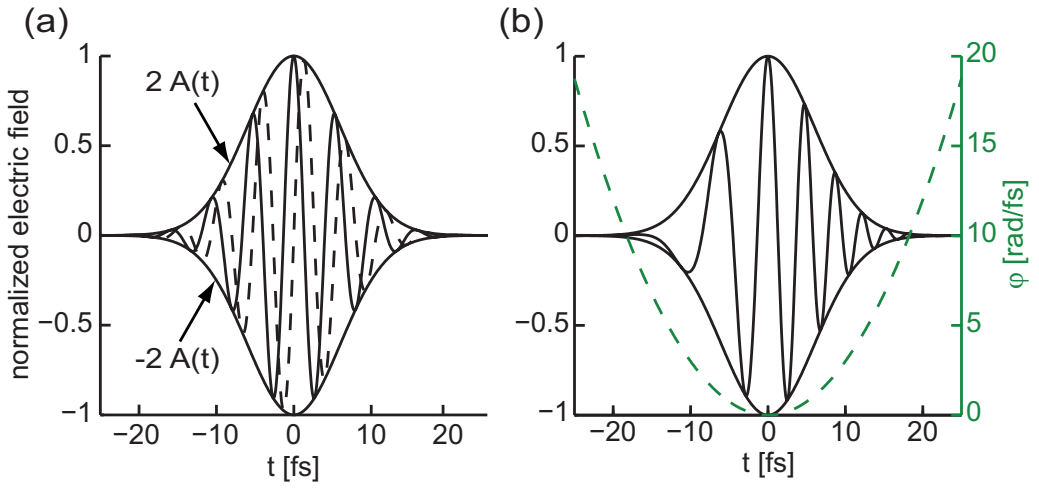

Figure 2.1: Laser pulse examples. Both laser pulses have the same amplitudes $A(t)$ and the same carrier frequency $\omega_0 = 1.17\,\mathrm{rad/fs}$. The envelope of the laser pulses $[2A(t)]$ is indicated by the solid lines. (a) The effect of the absolute phase a_0. The solid line describes the electric field of a laser pulse with $a_0 = 0\,\mathrm{rad}$, whereas the absolute phase is shifted by $a_0 = -\pi/2\,\mathrm{rad}$ for the electric field indicated with the dashed line. (b) The effect of a linear upchirp $a_2 = 0.06\,\mathrm{rad/fs^2}$. The oscillation period of the electric field changes from large to small values. The green curve shows the phase $\varphi(t) = 0.03\,\mathrm{rad/fs^2} \cdot t^2$.

series

$$\phi(t) = \sum_{j=0}^{\infty} \frac{a_j}{j!} (t - t_0)^j \qquad \text{with } a_j = \left. \frac{\mathrm{d}^j \phi(t)}{\mathrm{d}t^j} \right|_{t=t_0} . \tag{2.3}$$

Without loss of generality, the laser pulse can be assumed to be centered around $t_0 = 0$. The zeroth order coefficient a_0 is the absolute phase of the laser pulse. It describes the shift of the fast oscillations with respect to the envelope's center $A(t_0)$. For $a_0 = 0$ the electric field $E(t)$ reaches the maximum amplitude $2A(t_0)$ (solid line Fig. 2.1a), whereas for different values $a_0 \neq 0$ the oscillations are shifted and the electric field $E(t)$ does not reach the maximum amplitude $2A(t_0)$ (dashed line Fig. 2.1a). For pulse durations τ much longer than the oscillation period of light $T = 2\pi/\omega_0$, as will be used for all experiments in this thesis, the absolute phase is negligible for linear polarized light. However, for the vectorial description of laser pulses (Section 2.2) it is of high importance. As can be inferred from Eq. (2.2) the first order coefficient a_1 is equal to the carrier frequency ω_0.

The physical meaning of the higher order terms of the temporal phase $\phi(t)$ becomes clearer by considering the momentary frequency

$$\omega(t) = \frac{\mathrm{d}\phi(t)}{\mathrm{d}t} = \omega_0 + \frac{\mathrm{d}\varphi(t)}{\mathrm{d}t}. \tag{2.4}$$

It reflects that the higher order terms which are absorbed into $\varphi(t)$ result in a change of the momentary frequency. If $\mathrm{d}\varphi(t)/\mathrm{d}t = 0$, i.e. $a_j = 0$ for all $j \geq 2$, the momentary frequency $\omega(t)$ is ω_0 and does not change over the period of the pulse. In this case the pulse is called unchirped. One speaks of a chirped pulse if $\mathrm{d}^2\varphi(t)/\mathrm{d}t^2 \neq 0$, i.e.,

the momentary frequency changes with time. If the momentary frequency increases [decreases] with time because $\mathrm{d}^2\varphi(t)/\mathrm{d}t^2 > 0$ [$\mathrm{d}^2\varphi(t)/\mathrm{d}t^2 < 0$] the pulse is said to be upchirped [downchirped]. An example of an upchirped pulse is shown in Fig. 2.1b, where in this special case the momentary frequency changes linearly (i.e., $a_2 \neq 0$ and $a_j = 0$ for all $j \geq 3$) and therefore one speaks of a linear chirp.

In general, the electric field can either be described in time- or in frequency-domain, where both representations yield the same information. An equivalent spectral-domain representation of Eq. (2.1) is obtained by the complex-valued Fourier transform

$$E(\omega) = \frac{1}{\sqrt{2\pi}} \int_{-\infty}^{\infty} E(t)\, \mathrm{e}^{-\mathrm{i}\omega t}\, \mathrm{d}t. \tag{2.5}$$

The original temporal electric field can be recovered by the inverse Fourier transform

$$E(t) = \frac{1}{\sqrt{2\pi}} \int_{-\infty}^{\infty} E(\omega)\, \mathrm{e}^{\mathrm{i}\omega t}\, \mathrm{d}\omega, \tag{2.6}$$

which corresponds to the decomposition of $E(t)$ into monochromatic waves. Although the temporal electric field $E(t)$ is real-valued, a complex-valued representation is advantageous for mathematical reasons. To express the temporal field $E(t)$ as a complex function we first have to consider the spectral electric field which is Hermitian, and therefore follows the condition:

$$E(\omega) = E^*(-\omega), \tag{2.7}$$

where the star denotes complex conjugation. Hence, the electric field of the positive frequencies already gives an unambiguous description and we can define a complex-valued temporal electric field [16]:

$$E^+(t) = \frac{1}{\sqrt{2\pi}} \int_{0}^{\infty} E(\omega)\, \mathrm{e}^{\mathrm{i}\omega t}\, \mathrm{d}\omega. \tag{2.8}$$

Analogously, we can also define $E^-(t)$ which contains just the information of the negative frequencies. By virtue of Eq. (2.7) the temporal function $E^-(t)$ is the complex conjugate of $E^+(t)$ and the real-valued temporal electric field can be written as

$$E(t) = E^+(t) + E^-(t) = 2\,\mathrm{Re}\left\{E^+(t)\right\}. \tag{2.9}$$

The complex-valued function $E^+(t)$ can be separated into

$$E^+(t) = A(t)\, \mathrm{e}^{\mathrm{i}\phi(t)} = \hat{A}(t)\, \mathrm{e}^{\mathrm{i}\omega_0 t}, \tag{2.10}$$

where the amplitude $A(t)$ and the temporal phase term $\phi(t)$ are the same quantities as introduced in Eq. (2.1). The last identity is obtained by plugging in Eq. (2.2), where the phase $\varphi(t)$ is absorbed into the complex envelope function $\hat{A}(t)$.

According to Eq. (2.8) we can define a spectral electric field, which includes only positive frequencies

$$E^{+}(\omega) = \begin{cases} E(\omega) & \text{if} \quad \omega \geq 0, \\ 0 & \text{if} \quad \omega < 0. \end{cases} \tag{2.11}$$

Hence, the two quantities

$$E^{+}(\omega) = \frac{1}{\sqrt{2\pi}} \int_{-\infty}^{\infty} E^{+}(t)\, \mathrm{e}^{-\mathrm{i}\omega t}\, \mathrm{d}t \tag{2.12}$$

and

$$E^{+}(t) = \frac{1}{\sqrt{2\pi}} \int_{-\infty}^{\infty} E^{+}(\omega)\, \mathrm{e}^{\mathrm{i}\omega t}\, \mathrm{d}\omega \tag{2.13}$$

then constitute a complex-valued Fourier pair containing the full information of the electric field. The complete spectral electric field is maintained by

$$E(\omega) = E^{+}(\omega) + E^{-}(\omega), \tag{2.14}$$

where $E^{-}(\omega)$ and $E^{-}(t)$ again constitute a complex-valued Fourier pair. The mathematically constructed function $E^{+}(\omega)$ can explicitly be written as a product of a real-valued amplitude and a complex-valued phase

$$E^{+}(\omega) = A(\omega)\, \mathrm{e}^{-\mathrm{i}\varphi(\omega)}\,. \tag{2.15}$$

As will be described in Section 2.3, using a pulse shaper it is possible to manipulate the two quantities amplitude $A(\omega)$ and phase $\varphi(\omega)$ which enables tailoring of the temporal shape of the femtosecond laser pulse. The spectral phase is often expanded in a Taylor series

$$\varphi(\omega) = \sum_{j=0}^{\infty} \frac{b_j}{j!}\, (\omega - \omega_0)^j \qquad \text{with } b_j = \left. \frac{\mathrm{d}^j \varphi(\omega)}{\mathrm{d}\omega^j} \right|_{\omega=\omega_0} \tag{2.16}$$

around the carrier frequency ω_0, which is normally defined as the center of spectral amplitude and therefore is often called center frequency. It is not possible to directly relate the coefficients b_j to changes of the temporal profile of the laser pulse. However, it is easy to show that the zeroth order term b_0 is identical with the zeroth coefficient a_0 of the temporal phase. Due to the Fourier transform shift theorem, the first order term b_1 shifts the temporal profile which is centered around t_0 by its amount to $t_0 + b_1$. The temporal pulse envelope does not change as long as $b_j = 0$ for all $j \geq 2$. In all other cases the temporal pulse envelope changes.

The temporal intensity of a femtosecond laser pulse is defined proportional to the temporal average of the squared electric field $E^2(t)$

$$I(t) = \epsilon_0 c n \langle E^2(t) \rangle = \epsilon_0 c n \frac{1}{T} \int_{t-T/2}^{t+T/2} E^2(t')\mathrm{d}t' \tag{2.17}$$

with the vacuum dielectric constant ϵ_0, the vacuum velocity of light c, and the index of refraction n of the medium in which the intensity is measured. The averaging is performed over the oscillation period $T = 2\pi/\omega(t)$. Assuming that the pulse envelope varies slowly compared to the fast oscillating optical field ($|\mathrm{d}A(t)/\mathrm{d}t| \ll |\omega_0 A(t)|$), i.e., the slowly varying envelope approximation [16] applies, Eq. (2.17) simplifies to

$$I(t) = 2\epsilon_0 cnA^2(t). \tag{2.18}$$

In analogy the spectral intensity is defined as

$$I(\omega) = 2\epsilon_0 cnA^2(\omega). \tag{2.19}$$

Due to Parseval's theorem [19] the total linear flux

$$F = \int_{-\infty}^{\infty} I(t)\mathrm{d}t = \int_{-\infty}^{\infty} I(\omega)\mathrm{d}\omega \tag{2.20}$$

has to be the same in time and frequency domain. This identity will be used in Chapter 4 to find an analytic control rule for the linear flux in nanostructures.

Although the Fourier transform relates the time and frequency domain, in the laboratory laser spectra are usually measured as a function of wavelength λ. To transform the measured spectra we can also use the identity of the linear flux for both representations:

$$\int_{-\infty}^{\infty} I_\omega(\omega)\mathrm{d}\omega = \int_{-\infty}^{\infty} I_\lambda(\lambda)\mathrm{d}\lambda. \tag{2.21}$$

Using $\lambda = 2\pi c/\omega$ and $\mathrm{d}\lambda/\mathrm{d}\omega = -2\pi c/\omega^2$ we can rewrite $I_\omega(\omega)$ in terms of a Jacobi transformation [18]:

$$I_\omega(\omega) = (-)I_\lambda\left(\frac{2\pi c}{\omega}\right)\frac{2\pi c}{\omega^2} \tag{2.22}$$

where the minus sign indicates a change in the direction of the axis. Equation (2.22) reveals the proportionality of ω^{-2} which must be taken into account to relate the measured intensity I_λ and the intensity I_ω as a function of ω.

The pulse duration and the spectral width are associated with the temporal and spectral intensity, respectively. Different definitions can be chosen to assign the two quantities [16]. The most customary and the definitions used in this thesis are assigned using the full width at half maximum (FWHM) of the temporal intensity $I(t)$ and of the spectral intensity $I(\omega)$

$$\tau_p = \mathrm{FWHM}\{I(t)\} \tag{2.23}$$

and

$$\Delta\omega = \mathrm{FWHM}\{I(\omega)\}. \tag{2.24}$$

Note that these definitions only make sense for simple pulses. For more complex pulses a definition via the second order moment [17] should be considered. Due to the Fourier

relation of the temporal and spectral electric field the two quantities are not independent. The two quantities are related via a time-bandwidth product

$$\tau_p \Delta\omega \geq c_B. \tag{2.25}$$

Hence, the shorter the pulse duration the broader the spectrum and the narrower the spectrum the longer is the pulse duration. The time-bandwidth product constant c_B depends on the definition of the pulse duration, the spectral width and on the actual pulse shape. Using Eqs. (2.23) and (2.24) and assuming a gaussian laser pulse it results in $c_B = 4 \ln 2$.

2.1.2 Spatial Propagation

In general, the temporal and spatial properties of electric fields are described by Maxwell equations. Using these equations the inhomogeneous wave equation can be derived that describes the interaction of the electric field $\vec{E}(\vec{r},t)$ with non-magnetic matter

$$\nabla^2 \vec{E}(\vec{r},t) - \frac{1}{c^2}\frac{\partial^2}{\partial t^2}\vec{E}(\vec{r},t) = \mu_0 \frac{\partial^2}{\partial t^2}\vec{P}(\vec{r},t), \tag{2.26}$$

where c denotes the velocity of light in vacuum and μ_0 is the permeability of the vacuum. The polarization $\vec{P}(\vec{r},t)$ describes the response of a medium in the presence of an electric field and also includes any influence of the medium on the electric field. It can be expanded into orders of the electric field such that

$$\vec{P}(\vec{r},t) = \sum_n \vec{P}^{(n)}(\vec{r},t). \tag{2.27}$$

A detailed description and discussion of the polarization is given in Chapter 7. The polarization $\vec{P}(\vec{r},t)$ can be expanded in frequency domain analogously to the Fourier relation (2.6)

$$\vec{P}(\vec{r},t) = \frac{1}{\sqrt{2\pi}} \int_{-\infty}^{\infty} \vec{P}(\vec{r},\omega)\, \mathrm{e}^{\mathrm{i}\omega t}\, \mathrm{d}\omega. \tag{2.28}$$

Plugging in this description of the polarization and the corresponding description of the electric field [Eq. (2.6)] the wave equation (2.26) can be transformed to the frequency domain

$$\nabla^2 \vec{E}(\vec{r},\omega) + \frac{\omega^2}{c^2}\vec{E}(\vec{r},\omega) = \mu_0 \omega^2 \vec{P}(\vec{r},\omega). \tag{2.29}$$

A solution of this equation assuming only linear polarization (i.e., $\vec{P}^{(n)}(\vec{r},t) = 0$ for $n > 1$) yield optical near fields in the vicinity of nanostructures (Chapter 3). The solution for the wave equation in vacuum, i.e., $\vec{P}(\vec{r},\omega) = 0$, is straight forward and yields a propagating wave described by

$$\vec{E}(\vec{r},\omega) = \vec{E}(\vec{r}_0,\omega)\, \mathrm{e}^{\mathrm{i}\vec{k}\vec{r}} \tag{2.30}$$

Herein, the wavevector is given by

$$\vec{k} = \frac{\omega}{c}\vec{s}, \tag{2.31}$$

where $\vec{s}$ is a unit vector that describes the direction of propagation. Solutions of Eq. (2.29) including higher order polarization terms (i.e., $\vec{P}^{(n)}(\vec{r},t) \neq 0$ for $n > 1$) can be found elsewhere [16, 20].

2.2 Description and Representation of Polarization-Shaped Laser Pulses

Supported by the definitions for the scalar description of femtosecond laser pulses in the last section we will now discuss the vectorial behavior of electric fields based on the derivations of Brixner [17]. In this thesis laser pulses that have vectorial properties, i.e., they cannot be described by scalar fields, are called polarization-shaped laser pulses. However, the explicit mechanisms of pulse shaping will be introduced in the next section.

Considering light as a transverse wave, two linear independent vector components are sufficient to describe any state of polarization. In analogy to Eq. (2.1) the vectorial electric field is written as

$$\vec{E}(t) = \begin{pmatrix} E_1(t) \\ E_2(t) \end{pmatrix} = \begin{pmatrix} A_1(t)\cos\left[\omega_0 t + \varphi_1(t)\right] \\ A_2(t)\cos\left[\omega_0 t + \varphi_2(t)\right] \end{pmatrix} \tag{2.32}$$

where the subscripts 1 and 2 describe the two linearly independent polarization components and the factor 2 of Eq. (2.1) has been absorbed into the amplitudes for the sake of simplicity. Although Eq. (2.32) already gives a complete mathematical description of the electric field, it is advantageous to define more intuitive quantities which reveal the polarization state of the laser pulse. Due to the coherent superposition of the two polarization components, the polarization state can be expressed in the so called "elliptical representation" [17, 21].

2.2.1 Elliptical Representation

In the slowly varying envelope approximation, the temporal oscillation period around time t of the electric field vector $\vec{E}(t)$ is described as an ellipse with the two characteristic quantities $\varepsilon(t)$ and $\theta(t)$, being the angle of ellipticity and the orientation angle of the ellipse, respectively. The principal axes of the ellipse $\tilde{E}_1$ and $\tilde{E}_2$, shown in Fig. 2.2, which in general differ from the laboratory frame axes E_1 and E_2 can be obtained by principal axes transformation. Given that the principal axes can vary in time the time-dependent angle of ellipticity is determined by

$$\tan[\varepsilon(t)] = \frac{\tilde{A}_2(t)}{\tilde{A}_1(t)}, \tag{2.33}$$

where $\tilde{A}_1(t)$ and $\tilde{A}_2(t)$ are defined along the axis $\tilde{E}_1$ and $\tilde{E}_2$, respectively (Fig. 2.2). Furthermore, the orientation angle θ is defined as the angle between the principle axis $\tilde{E}_1$ and the laboratory axis E_1. In order to calculate ε and θ, the auxiliar angle χ is defined as

$$\chi(t) = \arctan\left[\frac{A_2(t)}{A_1(t)}\right] \qquad \in [0, \pi/2], \tag{2.34}$$

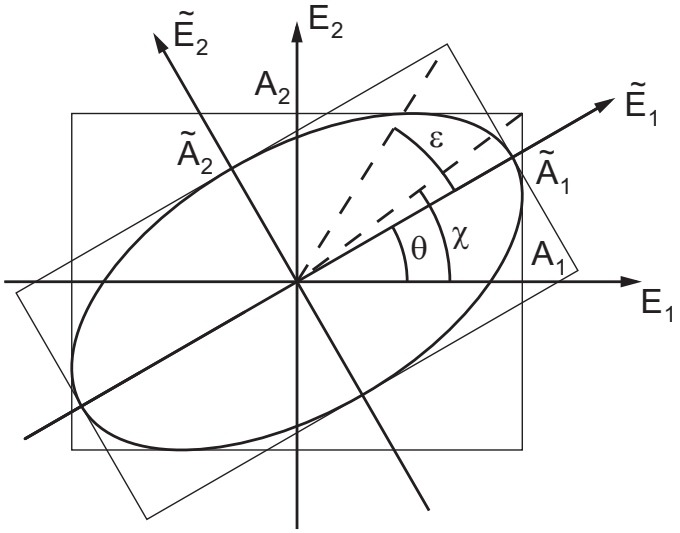

Figure 2.2: Definition of the elliptical pulse parameter. The time-dependent polarization ellipse is given by the amplitudes $\tilde{A}_1$, defined on the major principal axis $\tilde{E}_1$, and $\tilde{A}_2$, defined on the minor principal axis $\tilde{E}_2$. These two amplitudes specify the angle of ellipticity ε. The orientation angle θ defines the rotation of the ellipse-inherent coordinate system $\tilde{E}_1$-$\tilde{E}_2$ with respect to the laboratory frame coordinate system E_1-E_2. The time arguments are omitted here for the sake of simplicity. Taken from Brixner [17].

depending on the ratio of the laboratory-frame temporal amplitude components, and to simplify the following equations we also define the difference

$$\delta(t) = \varphi_2(t) - \varphi_1(t) \qquad \in [-\pi, \pi], \tag{2.35}$$

of the temporal phase modulations. In these and the following equations, the definition intervals are indicated as square brackets. Using the two previous definitions it can be shown [17] that

$$\theta(t) = \begin{cases} \tilde{\theta}(t) & \in [-\pi/4, \pi/4] \quad \text{if } \chi(t) \leq \pi/4, \\ \tilde{\theta}(t) + \pi/2 & \in [\pi/4, \pi/2] \quad \text{if } \chi(t) > \pi/4 \wedge \tilde{\theta}(t) < 0, \\ \tilde{\theta}(t) - \pi/2 & \in [-\pi/2, -\pi/4] \quad \text{if } \chi(t) > \pi/4 \wedge \tilde{\theta}(t) \geq 0, \end{cases} \tag{2.36}$$

with

$$\tilde{\theta}(t) = \frac{1}{2} \arctan\left\{\tan\left[2\chi(t)\right] \cos\delta(t)\right\} \qquad \in [-\pi/4, \pi/4], \tag{2.37}$$

where the orientation angle $\theta(t)$ is defined in the first or fourth quadrant.

In addition the angle of ellipticity can be expressed as [17]

$$\varepsilon(t) = \frac{1}{2} \arcsin\left\{\sin\left[2\chi(t)\right] \sin\delta(t)\right\} \qquad \in [-\pi/4, \pi/4], \tag{2.38}$$

where $\varepsilon(t)$ is always defined as the ratio of amplitude along the minor divided by the amplitude along major principle axis of the ellipse. Positive values of $\varepsilon(t)$ indicate

a momentary left, and negative values of $\varepsilon(t)$ a momentary right elliptical state of polarization. Here, the helicity, i.e., the sense of rotation of the electric field vector, is defined with respect to the axis given by the negative propagation direction.

With the angles $\varepsilon(t)$ and $\theta(t)$ it is possible to describe the momentary state of polarization of the electric field, i.e., the shape and orientation of the ellipse. Note that the state of polarization just depends on the relative amplitude and the relative phase of the two polarizations, which can also be expressed as the ratio of the complex-valued temporal field [Eq. (2.10)]

$$\frac{E_2^+(t)}{E_1^+(t)} = \frac{A_2(t)\,\mathrm{e}^{\mathrm{i}\phi_2(t)}}{A_1(t)\,\mathrm{e}^{\mathrm{i}\phi_1(t)}} = \tan\chi(t)\,\mathrm{e}^{\mathrm{i}\delta(t)}\,. \tag{2.39}$$

As will be shown in Section 3.2, it is exactly this ratio which has to be adjusted to control the spatial distribution of optical near-fields in nanostructures.

In addition to the relative values $\varepsilon(t)$ and $\theta(t)$, which define the shape and orientation of the electric field ellipse, we also need to define the ellipse's momentary size. This can be done by considering the total momentary intensity

$$I(t) = \tilde{I}_1(t) + \tilde{I}_2(t) = I_1(t) + I_2(t), \tag{2.40}$$

where the individual intensity components are proportional to the squares of the corresponding amplitudes. The rightmost identity of Eq. (2.40) is due to the fact that the total momentary intensity has to be independent of the choice of the coordinate system.

The last elliptical pulse characterization parameter is the total phase $\varphi(t)$. It is defined similar to the phase $\phi(t)$ of the scalar description of $E(t)$ [Eq. (2.1)], where the reference point of zero phase is always passed if the electric field has reached its amplitude, i.e., $E(t) = 2A(t)$. For polarization shaped pulses the total phase $\varphi(t)$ has its reference point, i.e., zero phase, at the point where the total electric field has reached its maximum amplitude, given by the major principle amplitude $\tilde{A}_1(t)$. Using this requirement it can be shown [17] that the total phase is defined as

$$\varphi(t) = \varphi_1(t) + \operatorname{sign}\{\theta(t)\varepsilon(t)\} \arccos\left[\sqrt{\frac{I(t)}{I_1(t)}}\cos\theta(t)\cos\varepsilon(t)\right], \tag{2.41}$$

where phase jumps of $\pm\pi$ have to be removed afterwards to assure a continuous function of time. Equation (2.41) includes the intuitive behavior of total phase of following the phase of the stronger component if the other component is small. Just as $\varepsilon(t)$ and $I(t)$, the total phase $\varphi(t)$ is defined independent of the choice of the coordinate system, whereas $\theta(t)$ defines the rotation angle of the inherent ellipse frame to the laboratory frame. The corresponding total momentary frequency of the elliptic laser pulse can be obtained in analogy to Eq. (2.4) by taking the derivative of the total phase with respect to time

$$\omega(t) = \omega_0 + \frac{\mathrm{d}\varphi(t)}{\mathrm{d}t}, \tag{2.42}$$

where ω_0 is the carrier frequency of the pulse [Eq. (2.2)].

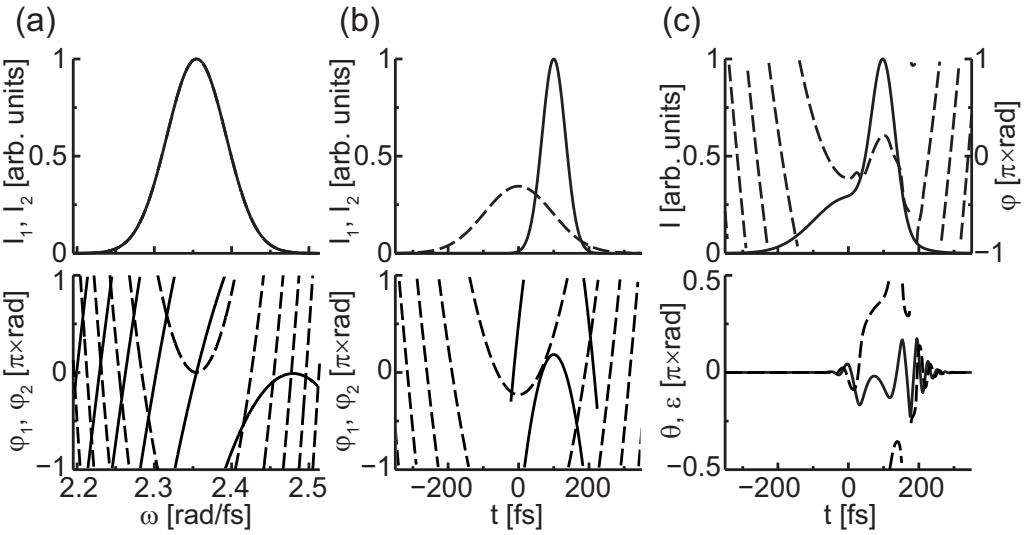

Figure 2.3: Three identical representations of a simulated polarization-shaped laser pulse. Both polarization components of the pulse are shown in the frequency- (a) and time-domain (b), with intensities in the upper part and phases in the lower part. The dashed (solid) line indicates polarization component E_1 (E_2) and the phase is only plotted for nonvanishing intensities. The time-domain elliptical parameters (c) contain the total intensity (solid line, upper panel) and total phase (dashed line, upper panel), as well as the temporal evolution of the angle of ellipticity ε (solid line, lower panel) and the orientation angle θ (dashed line, lower panel).

2.2.2 Representation of Polarization-Shaped Laser Pulses

Considering the definitions of the previous subsection, it is now helpful to discuss different kinds of representations by means of an example of a polarization-shaped laser pulse (Fig. 2.3). Three mathematically equivalent representations of this laser pulse are shown for this simulation, using frequency domain linear parameters $\{I_1(\omega), I_2(\omega), \varphi_1(\omega), \varphi_2(\omega)\}$ in Fig. 2.3a, time domain linear parameters $\{I_1(t), I_2(t), \varphi_1(t), \varphi_2(t)\}$ in Fig. 2.3b, and time domain elliptical parameters $\{I(t), \varphi(t), \theta(t), \varepsilon(t)\}$ in Fig. 2.3c.

The simulated polarization-shaped laser pulse has identical gaussian spectral intensities (Fig. 2.3a upper panel) for both polarization components $I_1(\omega)$ and $I_2(\omega)$, where the spectral width supports bandwidth-limited laser pulses of 30 fs. The spectral phases (Fig. 2.3a lower panel) are modulated in terms of their Taylor coefficients [Eq. (2.3)]. A quadratic phase $b_2 = 2500\,\mathrm{fs}^2/\mathrm{rad}$ is applied for $\varphi_1(\omega)$ (dashed line). A linear phase $b_1 = 100\,\mathrm{fs}$ and a negative quadratic phase $b_2 = -800\,\mathrm{fs}^2/\mathrm{rad}$ is applied for $\varphi_2(\omega)$ (solid line). According to these spectral phases the temporal intensities (Fig. 2.3b upper panel) as well as the temporal phases (Fig. 2.3b lower panel) change in contrast to constant spectral phases that would yield Gaussian shaped temporal intensities and constant temporal phases.

Figure 2.3b displays the temporal evolution of the two polarizations independently. However, to represent the evolution of the polarization state we have to consider the elliptical representation (Fig. 2.3c). The total intensity $I(t)$ (solid line, upper panel)

shows the double-pulse structure of the combined individual intensities $I_1(t)$ and $I_2(t)$. The total phase $\varphi(t)$ (dashed line, upper panel) follows the phase of the component with the dominating momentary intensity and therefore, contains information of both individual phases $\varphi_1(t)$ and $\varphi_2(t)$. In the beginning and in the end, i.e., in the temporal region where $I_2(t)$ is vanishing, the total phase follows the shape of $\varphi_1(t)$, i.e., a positive quadratic phase. In the temporal region around $t = 100\,\mathrm{fs}$, the intensity $I_2(t)$ is much higher than $I_1(t)$ and therefore the total phase is dominated by the negative quadratic phase of $\varphi_2(t)$. Additional information about the momentary polarization state is represented in the bottom part of Fig. 2.3c. Similar to the total phase $\varphi(t)$ the elliptical parameters depend on the ratio of the two individual intensities. In the region of small $I_2(t)$, the orientation angle $\theta(t)$ and the ellipticity $\varepsilon(t)$ are zero, indicating linearly polarized light oriented along the laboratory-frame coordinate axis E_1. This observation is not surprising considering the fact that only $I_1(t)$ is present in these regions. For regions where both intensities $I_1(t)$ and $I_2(t)$ are present, superposition results in a oscillation of the ellipticity $\varepsilon(t)$ around $\varepsilon = 0$ and the orientation angle $\theta(t)$ increases to values of about $\theta = \pi/2$.

To represent the general properties of these variations in more detail we will now consider two additional illustrations. First, an intuitive representation of the evolution of the polarization state is introduced by means of movement on the Poincaré surface. Second, a quasi three-dimensional representation of the polarization-shaped laser pulse is introduced, including the evolution of the polarization state and the total phase.

Any possible polarization state is defined as a set of angles $\{\theta, \varepsilon\}$ and can be represented on the so called Poincaré surface [22], which is shown in Fig. 2.4. This surface is spanned by the axis $-\pi/2 \leq \theta \leq \pi/2$ and $-\pi/4 \leq \varepsilon \leq \pi/4$ given by the definition intervals of $\theta(t)$ and $\varepsilon(t)$, respectively. The linear polarizations, i.e., $\varepsilon = 0$, are represented along the horizontal axis, where the orientation varies with θ. With increasing distance from this horizontal axis, the ellipticity rises and for $|\varepsilon| = \pi/4$ the electric field is circularly polarized for all θ. The upper half of the plane represents left elliptically polarized light and the lower part represents right elliptically polarized light.

The temporal evolution of the polarization state of a polarization shaped laser pulse is given by the Poincaré curve $\{\theta(t), \varepsilon(t)\}$, with the time parameter t. The Poincaré curve of the simulated laser pulse of Fig. 2.3 is shown in Fig. 2.4. Herein, the color saturation of the circles is weighted with the corresponding momentary total intensity. White and red indicate zero and maximum intensity, respectively. The Poincaré curve starts and ends at the origin of the Poincaré surface, i.e., $\{\theta = 0, \varepsilon = 0\}$, indicating the linear polarization along the laboratory-frame coordinate axis E_1, due to the vanishing I_2. During superposition of the two polarizations, the orientation of the ellipse first evolves to the left and then changes direction and evolves to the right, corresponding to a clockwise and counter-clockwise rotation of the ellipse, respectively. The degree of ellipticity ε changes simultaneously with the orientation angle and takes values close to $|\varepsilon| = \pi/4$, corresponding to circular polarization. Additionally, crossings at the axis at $\varepsilon = 0$ (only linear polarization) are observed indicating a change in helicity. For the boundary crossings of the planar Poincaré surface it is important to note that the Poincaré surface is conventionally treated as a surface of a sphere and is topologically closed. Therefore, the Poincaré curve, described on a planar projection of the Poincaré

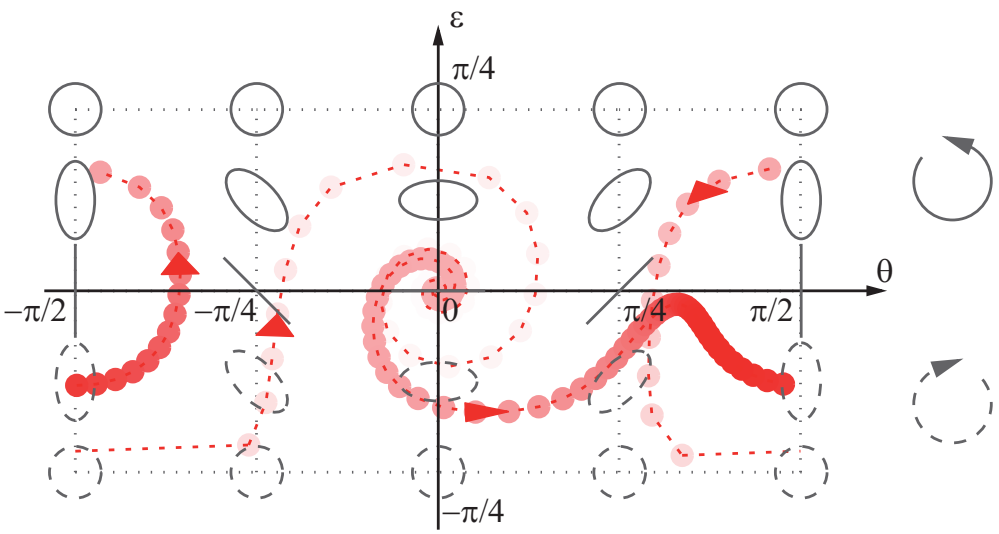

Figure 2.4: Polarization-shaped laser pulse of Fig. 2.3 represented on the Poincaré surface. The evolution of the polarization state is shown as a parametric function from −350 fs to 350 fs. Each circle displays the momentary polarization state of the pulse, where the time interval between two circle is $\Delta t = 2.40$ fs. The direction of evolution is indicated by the arrowheads. The color saturation of the circles is scaled with the momentary total intensity. White and red color indicates zero and maximum intensity, respectively.

surface, is discontinuous when it passes $\theta = \pm\pi/2$ or $\varepsilon = \pm\pi/4$. As can be observed in Fig. 2.4, crossing of the Poincaré curve at $\theta = \pm\pi/2$ results in continuation at $\theta = \mp\pi/2$ without change of the slope of the Poincaré curve $\mathrm{d}\varepsilon/\mathrm{d}\theta$. Although a crossing of the Poincaré curve at $\varepsilon = \pm\pi/4$ is not observed in the present example, it can be obtained by considering the origin of the Poincaré surface to be the surface of a sphere with the poles at $\varepsilon = \pm\pi/4$. Hence, it is obvious that a Poincaré curve that passes the upper boundary $\varepsilon = \pi/4$ (lower boundary $\varepsilon = -\pi/4$) evolves downwards (upwards) with the inverted slope at a orientation angle that is shifted by $\theta' = \theta - \pi/2$.

The increasing color saturation indicates an increase of the total intensity. As expected, the maximum intensity is reached near the boundary $\theta = \pi/2$, i.e., linear polarization along the laboratory-frame coordinate axis E_2. Here, the curve crosses the boundary and continues at $\theta = -\pi/2$. Although the representation on the Poincaré surface includes all parameters to define the momentary polarization state $\{I(t), \theta(t), \varepsilon(t)\}$, it lacks to indicate the total phase $\varphi(t)$.

To display the complete information, including the total phase $\varphi(t)$, in a single and intuitive graph, the quasi three-dimensional electric field representation is introduced. As a basis for this representation the polarization states are taken during movement through the Poincaré surface for each evaluated point in time. Here, the momentary light ellipse is given by the set of angles $\{\theta, \varepsilon\}$ and the size of the ellipse is proportional to the total amplitude [i.e. the square root of the total intensity (Eq. 2.40)]. Stacking of these temporal snapshots of the momentary polarization state results in a quasi-three-dimensional electric field representation. The time evolves from left to right and the

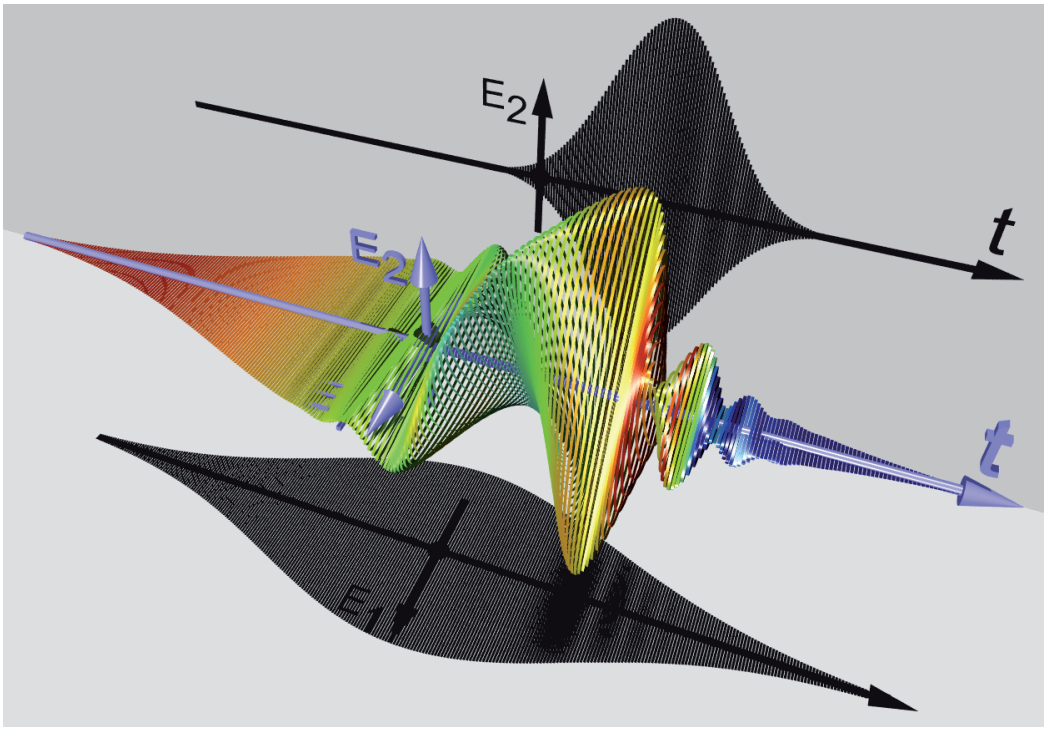

Figure 2.5: Quasi-three-dimensional electric field representation of the simulated pulse shown in Fig. 2.3. The time axis t is plotted from -350 to 350 fs and the time evolves from left to right. The lower and upper shadow represents the electric field amplitude of E_1 and E_2, respectively. The color of the ellipses indicates the total momentary frequency (Eq. 2.42), where green color indicates center frequency ω_0. Lower and higher total momentary frequencies are indicated with reddish and blueish colors, respectively.

lower (upper) shadow represents the electric fields amplitude A_1 (A_2) in the direction of E_1 (E_2). Note that the period of adjacent ellipses does not necessarily display the oscillation period of the electric field but depends only on the evaluation points in time. Figure 2.5 represents the simulated polarization-shaped laser pulse of Fig. 2.3. The pulse is again shown from -350 fs (left end of the time axis t) to 350 fs (right end of the time axis t). The momentary polarization state, as inferred from the shape of the individual ellipses, starts and ends with the same polarization along the laboratory-frame coordinate axis E_1. Caused by the superposition with the second polarization component A_2, which is centered around $t = 100$ fs, the momentary polarization state varies in this region. Additionally to the momentary polarization state, already represented by the Poincaré curve, here the momentary total phase [Eq. (2.41)] by means of the momentary frequency is encoded in the color of the ellipses. A momentary frequency close to the carrier frequency ω_0 is indicated in green color. Red (blue) color indicates momentary frequencies which are lower (higher) then the center frequency ω_0. Therefore, the ellipses are reddish at the beginning and bluish at the end of the pulse, indicating negative and positive slope of the total phase (dashed line, Fig. 2.3c upper panel), respectively. In regions of constant total phase, the ellipses are greenish, corresponding to momentary

frequencies close to the center frequency ω_0.

2.2.3 Jones-Matrix Formalism

After introducing the vectorial character of the electric field in Eq. (2.32), it is important to mathematically describe the influence of optical elements without nonlinear properties, e.g. mirrors, lenses, or polarizers. Since, the description here is linear and the response is instantaneous, the frequencies can be treated separately. The influence of a certain optical element to the incoming electric field $\vec{E}^+_{\mathrm{in}}(\omega)$ is described mathematically by multiplying it with a two-by-two complex-valued frequency-dependent matrix $J(\omega)$ [23] from the left side

$$\vec{E}^+_{\mathrm{out}}(\omega) = J(\omega)\vec{E}^+_{\mathrm{in}}(\omega). \tag{2.43}$$

The transfer matrix $J(\omega)$ is called Jones-matrix [24] of the optical element and contains the corresponding linear properties. In index notation, this equation is expressed as

$$\begin{pmatrix} E^+_{1,\mathrm{out}}(\omega) \\ E^+_{2,\mathrm{out}}(\omega) \end{pmatrix} = \begin{pmatrix} J_{11}(\omega) & J_{12}(\omega) \\ J_{21}(\omega) & J_{22}(\omega) \end{pmatrix} \begin{pmatrix} E^+_{1,\mathrm{in}}(\omega) \\ E^+_{2,\mathrm{in}}(\omega) \end{pmatrix}. \tag{2.44}$$

This description can be expressed in any coordinate system, whereas transformation between different coordinate systems has to be done by the corresponding transformation matrix. As an example, the influence of a quarter wave plate with fast axis at 45° with respect to component 1 is defined as

$$\begin{aligned} \begin{pmatrix} E^+_{1,\mathrm{out}}(\omega) \\ E^+_{2,\mathrm{out}}(\omega) \end{pmatrix} &= R(45°) \begin{pmatrix} 1 & 0 \\ 0 & \mathrm{i} \end{pmatrix} R^{-1}(45°) \begin{pmatrix} E^+_{1,\mathrm{in}}(\omega) \\ E^+_{2,\mathrm{in}}(\omega) \end{pmatrix} \\ &= \frac{1}{\sqrt{2}} \begin{pmatrix} \mathrm{e}^{\mathrm{i}\pi/4} & \mathrm{e}^{-\mathrm{i}\pi/4} \\ \mathrm{e}^{-\mathrm{i}\pi/4} & \mathrm{e}^{\mathrm{i}\pi/4} \end{pmatrix} \begin{pmatrix} E^+_{1,\mathrm{in}}(\omega) \\ E^+_{2,\mathrm{in}}(\omega) \end{pmatrix} \\ &= \frac{1}{\sqrt{2}} \begin{pmatrix} E^+_{1,\mathrm{in}}(\omega)\,\mathrm{e}^{\mathrm{i}\pi/4} + E^+_{2,\mathrm{in}}(\omega)\,\mathrm{e}^{-\mathrm{i}\pi/4} \\ E^+_{1,\mathrm{in}}(\omega)\,\mathrm{e}^{-\mathrm{i}\pi/4} + E^+_{2,\mathrm{in}}(\omega)\,\mathrm{e}^{\mathrm{i}\pi/4} \end{pmatrix}, \end{aligned} \tag{2.45}$$

where $R(45°)$ and $R^{-1}(45°)$ are the rotation matrix for an angle of 45° and its inverse matrix, respectively. Here, the Jones-matrix is complex valued which introduces a phase retardation to the incoming electric field. The mixing of the x and y component is due to the angle of the quarter wave plate's fast axis with respect to the ordinary coordinate system.

Considering n different optical components the total Jones matrix $J(\omega)$ is given by a multiplication of the individual Jones matrices $J^{(i)}(\omega)$:

$$J(\omega) = J^{(n)}(\omega)J^{(n-1)}(\omega)...J^{(1)}(\omega). \tag{2.46}$$

Due to the noncommutativity of matrix multiplication, the matrix of the first optical element $J^{(1)}(\omega)$ is located on the right side and the matrix of the last element $J^{(n)}(\omega)$ on the left. Consequently, every experimental setup can be described by a Jones matrix. Since the knowledge of the Jones matrix enables easy identification of the outcoming field, the Jones matrix formalism is of particular interest for the characterization of polarization shaped laser pulses, as will be introduced in Section 2.4.3.

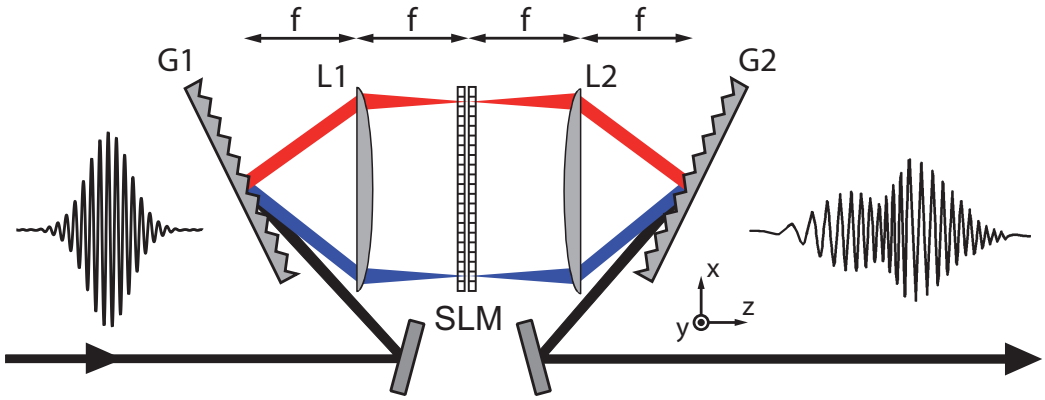

Figure 2.6: Schematic $4f$ zero-dispersion setup including a spatial light modulator (SLM) in the Fourier plane. The incoming beam is spatially dispersed (indicated by red and blue color) by a grating (G1) and focused by a plano-cylindrical lens (L1 with focal length f) to the Fourier plane, where a SLM is used to modulate the electric field. Another lens-grating-pair (L2 and G2) recollimates the beam, completing the $4f$ setup. Modified from Brixner [17].

2.3 Femtosecond Laser Pulse Shaping

The results presented in this thesis deal with the control and the investigation of optical excitations in nanostructures by modulation of the exciting electric field. Since there are no electric devices that would allow modulation of the electric field with a femtosecond resolution, the variation is done in the frequency domain. As introduced in the last section such a modulation in the frequency domain can be introduced by optical elements and can be described by a transfer matrix, called Jones matrix. The optical element which allows almost arbitrary modulation of the electric field, i.e., automated variation of the Jones matrix, is a pulse shaper. First experimental realizations using fixed shaping masks in the picosecond and the femtosecond regime were shown by Heritage *et al.* [25] and Weiner *et al.* [26], respectively. Further improvement was done by using electronic devices for automated adjustment of the phase masks [27]. The basic concept of these pulse shapers as well as complex polarization pulse shaping is described in this section.

2.3.1 Basic Concept

The basic concept of the used pulse shaper is a spatial light modulator (SLM) which is placed in the center of a $4f$ zero-dispersion compressor (Fig. 2.6).

The incoming beam is spatially dispersed in the x direction using a grating (G1). A plano-cylindrical lens (L1) is positioned at one focal length f with respect to the grating (a lens is used here for schematic reasons, whereas in the experiment a curved mirror is used). Since the lens is positioned at the distance of one focal length, the subsequent propagation of the separated spectral components is parallel to the z-axis and due to the finite size of the incoming beam the individual components are focused to a vertical line along the y axis at another focal length. Further, the x-y plane at this z position ($2f$ with respect to G1) is called Fourier plane yielding the highest frequency resolution and

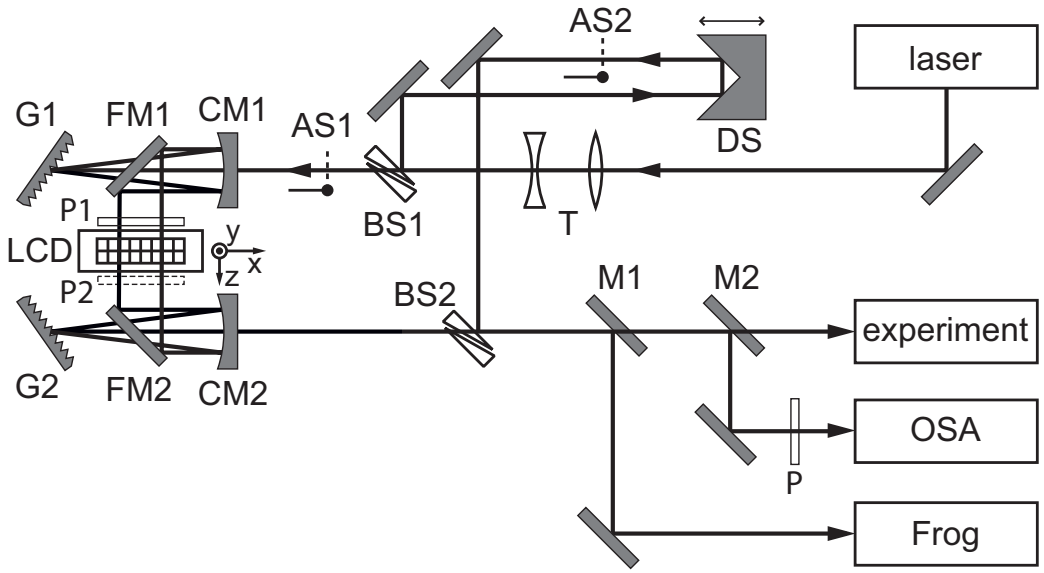

Figure 2.7: Polarization pulse shaper setup. The beam, which is coupled out of the laser, is adjusted in its beam diameter using a telescope (T). The glass wedges serving as beam splitters (BS1 and BS2) combined with the delay stage (DS) and the automatic shutters (AS1 and AS2) provide a reference pulse for spectral interferometry (Section 2.4.2), which is measured with a spectrometer (OSA) via mirror M2. The adjustable polarizer (P) in front of the spectrometer enables independent characterization of the two polarizations. Additionally, the shaped pulse can be characterized with a FROG (Section 2.4.1) via mirror M1. In the experiment both mirrors are removed. In the all-reflective $4f$ setup the beam is dispersed and recollimated with two identical gratings (G1 and G2) and curved mirrors (CM1 and CM2). The folding mirrors (FM1 and FM2) ensure on-axis reflection of the curved mirrors. In front of the two-layer liquid crystal display (LCD) a polarizer (P1) cleans up the polarization of the incoming beam. The polarizer (P2) is only used in amplitude and phase shaping mode, i.e., is removed for polarization pulse shaping.

each frequency component of the laser pulse spectrum is focused at a certain position x. For the modification of the spectral phase a SLM is positioned in this plane which changes the spectral phase by introducing individual optical pathways to the spectral components. After passing the SLM the beam is recollimated by another lens (L2) and grating (G2) resulting in the $4f$ setup.

2.3.2 Polarization Pulse Shaping

The experimental setup of the polarization pulse shaper which is used for adaptive and deterministic control of near-fields (Chapters 5 and 6) is shown in Fig. 2.7. As can be inferred the setup follows the introduced basic concept (Fig. 2.6). Before entering the $4f$ setup the beam diameter has to be adjusted to 2 mm (the pixel height) using a telescope (T). Then part of the pulse is sidelined using a pair of beam splitters (BS1 and BS2) for pulse characterization via spectral interferometry as is explained in section 2.4.2. Here, the beam splitters are a pair of glass wedges to avoid multiple reflections within

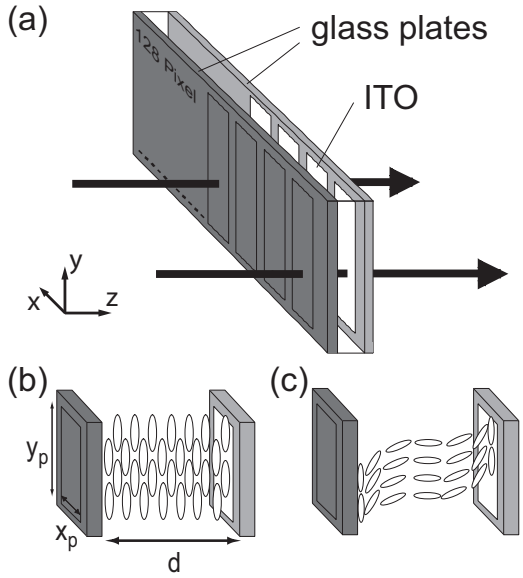

parameter	value
focal length	80 mm
grating line density	1800 mm^{-1}
minimum wavelength	770 nm
maximum wavelength	828 nm
focal spot width	60 μm
frequency range per pixel	0.00135 fs^{-1}
number of LCD pixels	2×128
LCD pixel width x_p	97 μm
LCD interpixel gap	3 μm
LCD pixel height y_p	2 mm
LCD response time	150 ms

Figure 2.8: LCD setup and table of properties of the polarization pulse shaper. The LCD consists of two glass plates (a), coated on the inside with a layer of transparent and electrically conducting indium-tin oxide (ITO). The layer contains 128 pixels along the x-direction and the incoming light propagates in z direction. The liquid crystal molecules inside the glass plates (b) are oriented along their preferential axis in y direction for zero voltage applied. If a voltage is applied the molecules are tilted in the y-z plane, yielding a voltage dependent change of the refractive index $n_y(\omega)$ (c). The characteristic properties of the used polarization pulse shaper are specified in the table. Taken from Fechner [28].

the beam splitter. In the all-reflective $4f$ setup, which is used to suppress chromatic aberrations and material dispersion, the beam is dispersed and recollimated by a pair of holographic gratings (G1 and G2) with 1800 lines/mm and a pair of curved mirrors (CM1 and CM2) with focal length of 80 mm. The folding mirrors (FM1 and FM2) ensure on-axis reflection of the curved mirrors, leading to a reduction of higher-order aberrations. After passing the pulse-shaper setup the beam can either be guided to diagnostic tools via mirror M1 and M2 (Section 2.4) or to the experiment.

To spatially modulate the light in the Fourier plane of the $4f$ setup a two layer liquid crystal display (LCD) (SLM-256-NIR from Cambridge Research & Instrumentation) is used. A single layer of the LCD and the operation mode of a single pixel is illustrated in Fig. 2.8. Each layer, composed of 128 pixels, is arranged along the x axis and consists of two parallel glass plates at a distance d (Fig. 2.8a). The inside of the glass plates is coated by a layer of transparent and electrically conducting indium-tin oxide (ITO) and the space between the glass plates is filled with liquid crystal molecules [29] in the nematic phase (Fig. 2.8b). The preferential orientation axis of the molecules, i.e., the orientation of the molecules with no voltage applied, is along the y axis (Fig. 2.8b), given by a special coating of the glass plates. If a voltage U (with $0\,\mathrm{V} \leq U < 10\,\mathrm{V}$) is applied to the electrodes in z-direction, the molecules are tilted in the y-z plane (Fig. 2.8c). The tilt of the molecules along the direction of the electric field lines depends on the magnitude

of the applied voltage. The resulting change of the projection of the dipole moment on the y axis induces a change of the refractive index component $n_y(\omega)$. Consequently, the optical path length for light with frequency ω, which is polarized along the y direction, can be controlled by the applied voltage U. The corresponding phase retardation is

$$\Delta\phi(U,\omega) = \frac{\omega d}{c}\left[n_y(U,\omega) - n_y(U=0,\omega)\right], \tag{2.47}$$

with $n_y(U=0,\omega)$ being the voltage-free refractive index. Since the LCD is positioned in the Fourier plane each pixel corresponds to a certain frequency component of the incoming laser pulse and can be controlled independently with a suitable controller (SLM-ELT-256 from Cambridge Research & Instrumentation). Since the relation of the applied voltage U and the introduced phase retardation $\Delta\phi$ is not linear, an appropriate calibration of the LCD has to be performed before the experiment, yielding a maximum phase range of 6π [30]. An additional calibration has to be performed to assign each pixel to the corresponding frequency of the laser pulse. The technical parameters of the used pulse shaper are summarized in the table of Fig. 2.8.

For polarization pulse shaping as introduced here a two-layer LCD is needed, since two parameters have to be adjusted. One parameter is the polarization state of the laser pulse, which is adjusted by the relative phase between both layers. The other parameter is the spectral phase, which is modulated by an offset that is added to both layers and enables adjustment of the relative phase between different frequencies. Therefore, the preferential orientation axes of the molecules, i.e., the modulation axes, of the two layers have to be perpendicular to each other. Figure 2.9 illustrates the effect of the SLM to a single frequency, where the incoming light is polarized along the x axis. Layer 1 (red) and layer 2 (green) are tilted by 45° and −45° with respect to the polarization of the incoming light, respectively. Hence, the incoming light has equal amplitude in both directions. The liquid-crystal molecules are tilted in the 1-z and in the 2-z plane, accordingly. In the example of Fig. 2.9 a voltage is applied only to layer 1 and the refractive index $n_y(U,\omega)$ decreases with respect to the voltage-free refractive index $n_y(U=0,\omega)$. Consequently, the optical path length of the component along layer 1 of the incoming light is reduced and therefore the output polarization is elliptically. According to the Jones matrix formalism (Section 2.2.3) this is described in the x-y coordinate system by

$$\begin{aligned}
\vec{E}^{+}_{\text{out}} &= R(-45°)\begin{pmatrix} \mathrm{e}^{-\mathrm{i}\Delta\phi_1} & 0 \\ 0 & 1 \end{pmatrix} R^{-1}(-45°)\begin{pmatrix} E^{+}_{x,\text{in}} \\ 0 \end{pmatrix} \\
&= \mathrm{e}^{-\mathrm{i}\frac{\Delta\phi_1}{2}}\begin{pmatrix} \cos\left(\frac{\Delta\phi_1}{2}\right) & -\mathrm{i}\sin\left(\frac{\Delta\phi_1}{2}\right) \\ -\mathrm{i}\sin\left(\frac{\Delta\phi_1}{2}\right) & \cos\left(\frac{\Delta\phi_1}{2}\right) \end{pmatrix}\begin{pmatrix} E^{+}_{x,\text{in}} \\ 0 \end{pmatrix} \\
&= \mathrm{e}^{-\mathrm{i}\frac{\Delta\phi_1}{2}}\begin{pmatrix} E^{+}_{x,\text{in}}\cos\left(\frac{\Delta\phi_1}{2}\right) \\ -\mathrm{i}E^{+}_{x,\text{in}}\sin\left(\frac{\Delta\phi_1}{2}\right) \end{pmatrix},
\end{aligned} \tag{2.48}$$

where the rotation matrix R is used to relate the coordinate system of the LCD layer to the x-y coordinate system. As can be inferred from Eq. (2.48) it is also possible to adjust the polarization state by a single layer LCD. However, to additionally adjust the spectral phase, a second layer is needed. To describe the effect of both layers Eq. (2.48)

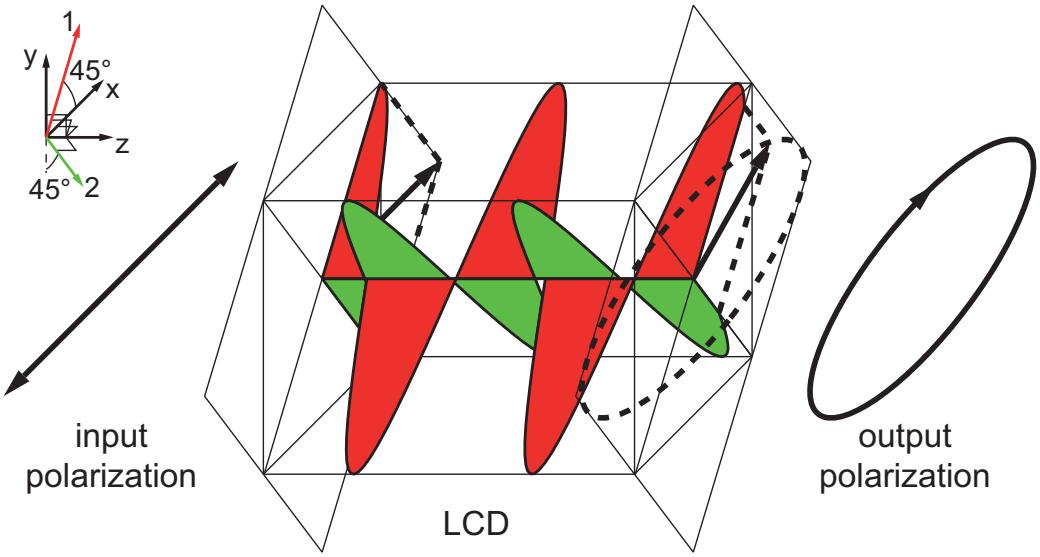

Figure 2.9: Polarization pulse shaping. The incoming light is x-polarized and can be decomposed in the two components 1 and 2, which are the modulations axes of the LCD. If one of the components is modulated with respect to the other one, the two components propagate with different optical path lengths and the resulting polarization state after passing the LCD is changed to an elliptical state. Modified from Brixner [17].

has to be modified to

$$\begin{aligned}
\vec{E}^{+}_{\text{out}} &= R(-45°)\begin{pmatrix} \mathrm{e}^{-\mathrm{i}\Delta\phi_1} & 0 \\ 0 & \mathrm{e}^{-\mathrm{i}\Delta\phi_2} \end{pmatrix} R^{-1}(-45°)\begin{pmatrix} E^{+}_{x,\text{in}} \\ 0 \end{pmatrix} \\
&= \mathrm{e}^{-\mathrm{i}\frac{\Delta\phi_1+\Delta\phi_2}{2}}\begin{pmatrix} \cos\left(\frac{\Delta\phi_1-\Delta\phi_2}{2}\right) & -\mathrm{i}\sin\left(\frac{\Delta\phi_1-\Delta\phi_2}{2}\right) \\ -\mathrm{i}\sin\left(\frac{\Delta\phi_1-\Delta\phi_2}{2}\right) & \cos\left(\frac{\Delta\phi_1-\Delta\phi_2}{2}\right) \end{pmatrix}\begin{pmatrix} E^{+}_{x,\text{in}} \\ 0 \end{pmatrix} \\
&= \mathrm{e}^{-\mathrm{i}\frac{\Delta\phi_1+\Delta\phi_2}{2}}\begin{pmatrix} E^{+}_{x,\text{in}}\cos\left(\frac{\Delta\phi_1-\Delta\phi_2}{2}\right) \\ -\mathrm{i}E^{+}_{x,\text{in}}\sin\left(\frac{\Delta\phi_1-\Delta\phi_2}{2}\right) \end{pmatrix}
\end{aligned} \tag{2.49}$$

Thus, the modification of the spectral phase is given by the sum of the phase retardations $\Delta\phi_1 + \Delta\phi_2$, whereas the modification of the polarization state is given by the difference of the phase retardations $\Delta\phi_1 - \Delta\phi_2$.

2.3.3 Amplitude and Phase Shaping

In Chapter 7 a new spectroscopic technique is introduced which requires adjustable pulse sequences in a collinear configuration with a high phase stability. A perfect tool to produce these pulse sequences is a pulse shaper since inherent phase stability is guaranteed. However, to produce pulse sequences with a pulse shaper, the spectral amplitude and phase has to be manipulated. Therefore, the setup used for polarization shaping has to be modified with an additional polarizer behind the second layer of the LCD (P2 in Fig. 2.7). The polarizer is oriented to filter out components along the y direction, i.e., only light that is polarized along the input polarization is transmitted. Thus unwanted

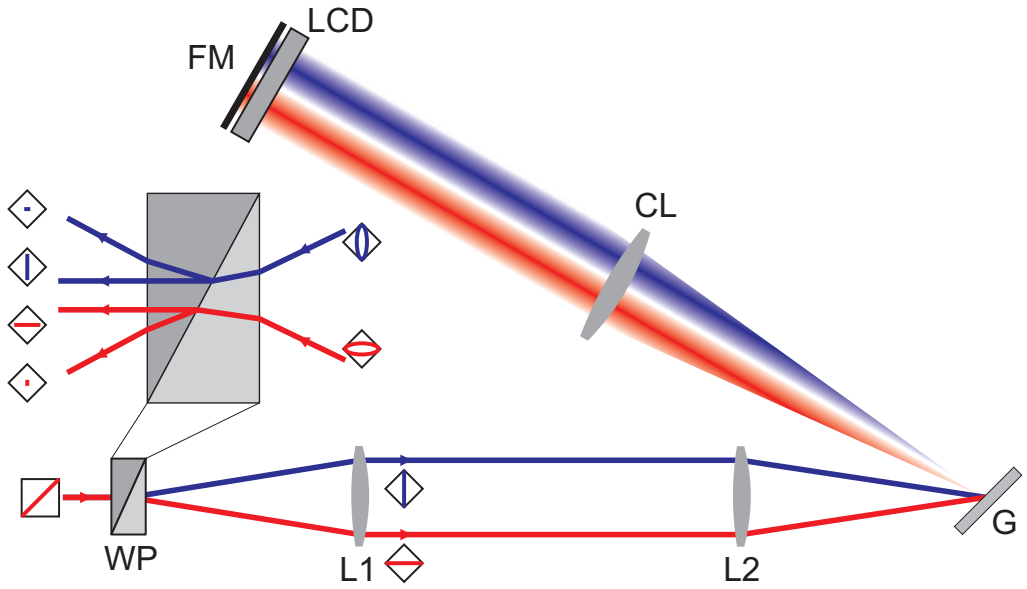

Figure 2.10: Vector field synthesizer setup as implemented by Ninck *et al.* [31]. A Wollaston prism (WP) acts as a polarization beam splitter and a telescope (L1 and L2) adjusts the angles of incidence of the two polarizations to the grating. The folded (FM) $4f$ setup consists of a grating (G) and a cylindrical lens (CL), and the light is modulated by a two-layer LCD.

spectral components are modulated with the two layer LCD to be polarized along the y direction and then are filtered out. Accordingly Eq. (2.49) has to be modified to

$$E^{+}_{\mathrm{out}} = \mathrm{e}^{-\mathrm{i}\frac{\Delta\phi_1+\Delta\phi_2}{2}} \cos\left(\frac{\Delta\phi_1-\Delta\phi_2}{2}\right) E^{+}_{\mathrm{in}}, \tag{2.50}$$

where the scalar function indicates that linearly polarized light is modulated. The spectral phase of the output field is again modulated by the sum of the phase retardations $\Delta\phi_1+\Delta\phi_2$, whereas the amplitude is modulated by the difference of the phase retardations $\Delta\phi_1-\Delta\phi_2$.

2.3.4 Full Vector Field Synthesizer

Polarization pulse shaping as described above gives the ability to design pulse shapes by independently manipulating the spectral phase of the two components 1 and 2. However, this means that the possible pulse shapes of the polarization pulse shaper used here are constrained since it is not possible to manipulate the spectral amplitude of any component. To fully synthesize the electrical field vector, as is desired for the theoretic near-field control described in Chapter 4, a different setup (Fig. 2.10) was implemented by Ninck *et al.* [31]. The concept is very similar to the setup described in Fig. 2.6. The beam is dispersed and recollimated in a $4f$ setup by a grating (G) and a cylindrical lens (CL). For stability reasons, the symmetric $4f$ setup is folded by a folding mirror (FM). A Wollaston prism is used to split incoming light into two perpendicular polarization components and a telescope (L1 and L2) is then used to adjust the angle of incidence

on the grating such that the two polarizations are shaped in separated regions of the display. Spectral amplitude and phase is shaped independently for each component by first adjusting the phase and polarization state with the two-layer LCD, as described above, and then the Wollaston prism is used to filter out the undesired component. This is very similar to the amplitude and phase-shaping setup where the undesired components are filtered out by a polarizer.

The main importance of the setup of the full vector field synthesizer introduced by Ninck *et al.* is the common path of the two components which assures inherent phase stability. In this configuration it is possible to adjust four independent parameters, i.e., the spectral phase and amplitude for each polarization component. Hence, full vector field synthesizing of the electrical field of a femtosecond laser pulse can be realized.

2.4 Laser Pulse Characterization

The goal of the experiments presented in Chapter 5 is to get a deeper understanding of the involved mechanisms for near-field control. To assign certain pulse shape properties to the control mechanisms a careful analysis of the complex shaped femtosecond laser pulses which excite the nanostructure is required. To characterize the pulses, i.e., extract the amplitude and phase of the laser pulses, two experimental techniques are described in this section. First, frequency-resolved optical gating (FROG) is introduced, which enables the characterization by using a pulse replica and second-harmonic signal generation. Second, dual-channel spectral interferometry (SI) is explained, which is a linear technique and enables characterization of polarization shaped laser pulses via a known reference pulse. The Jones-Matrix formalism serves as an additional characterization tool. Although it is not a pulse characterization measurement itself it uses the Jones-Matrix of all optical elements including the pulse shaper to assign a transfer function depending on the applied phases and enabling the calculation of the shaped pulse.

2.4.1 Second-Harmonic-Generation Frequency-Resolved Optical Gating

A commonly used tool for complex laser pulse characterization is frequency-resolved optical gating (FROG). This technique was first introduced by Kane and Trebino [32–34] and is realizable in different geometries [35]. The type of FROG introduced here and also used throughout the thesis is a second-harmonic generation (SHG) FROG [36, 37]. A schematic of the setup is displayed in Fig. 2.11. It consists of an interferometer, where a beam splitter (BS) splits the incoming pulse into two replicas. One of the two arms of the interferometer can be varied with a delay stage (DS), introducing a delay τ between the two replicas. The unchanged arm contains a compensation plate (CP) to compensate for the different pathways through glass. The two replicas are focused and spatially overlapped on a SHG-crystal (Beta-Bariumborat crystal, BBO) with a lens (L). The lens is used here to symbolize the focussing. However, in the experiment a focussing mirror is used to avoid additional dispersion which would be introduced by the lens. Due to the conservation of momentum the SHG signal, which is generated in

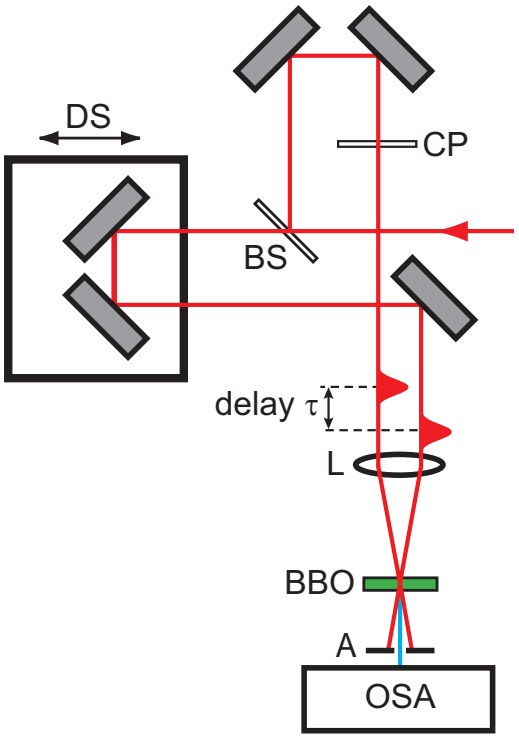

Figure 2.11: Setup for second-harmonic frequency resolved optical gating (SHG-FROG). The beam is sent through an Michelson interferometer where one arm can be adjusted by a delay stage (DS). The other arm contains a compensation plate (CP) to compensate for the dispersion of the beam splitter. The two beams are adjusted parallel to each other and are focused to a SHG-crystal (Beta-Bariumborat crystal, BBO) with a lens (L). The SHG-signal, generated by the combined electric field, is detected with a spectrometer (OSA). Adapted from Fechner [28].

the crystal and has the double carrier frequency, is directed along

$$\vec{k}_{\mathrm{SHG}} = \vec{k}_1 + \vec{k}_2, \tag{2.51}$$

where $\vec{k}_1$ and $\vec{k}_2$ describe the momentum of the two replica pulses and $\vec{k}_{\mathrm{SHG}}$ is the momentum of the SHG signal. Consequently, the SHG signal is emitted along the bisecting line of the angle which is defined by the directions of the two replicas. This geometry and an additional aperture (A) ensures the blocking of the fundamental signal as well as SHG signal which is generated from just one of the two pulse replicas.

The spectrum of the SHG signal is recorded with an optical signal analyzer (OSA) and by continuous variation of the delay τ a so-called FROG trace is recorded. The measured signal can be written as

$$I_{\mathrm{FROG}}(\tau,\omega) \propto \left| \int_{-\infty}^{\infty} E^{+}(t)E^{+}(t-\tau)\,\mathrm{e}^{-\mathrm{i}\omega t}\,\mathrm{d}t \right|^2 . \tag{2.52}$$

Although it is not possible to derive the electric field directly from this trace, iterative algorithms can reconstruct the amplitude and phase. This is done by calculating FROG traces from guessed electric fields. The calculated FROG traces are then iteratively fitted to the measured FROG trace by minimizing the deviation, i.e., the FROG error [38, 39]. The used algorithm (FROG 3.2 from Femtosoft) is very robust and reliably finds very similar electric fields for consecutive evaluations of the same FROG trace.

The limitation of the phase retrieval is due to the inherent time symmetry of the measured signal

$$I_{\mathrm{FROG}}(\tau,\omega) = I_{\mathrm{FROG}}(-\tau,\omega). \tag{2.53}$$

Therefore, the sign of the phase cannot be retrieved with the algorithm directly, but has to be determined by inserting an additional dispersive element of known thickness and dispersion.

However, characterization of polarization shaped laser pulses using FROG is a time-consuming task. Although two polarizations can be characterized independently by measuring each polarization in a separate step, the determination of the relative phase and the relative time delay between both polarizations demands a third FROG measurement [40]. Hence, three FROG measurements have to be performed for the evaluation of a single polarization shaped laser pulses. An additional problem, which has to be considered for the characterization of pulse sequences as needed in Chapter 7, is the π-phase ambiguity which arises for the determination of the relative phase between temporally isolated subpulses [41]. Nevertheless, since SHG-FROG is a self-referencing method, it is used to characterize the reference pulses for spectral interferometry, which is introduced in the next section.

2.4.2 Dual-Channel Spectral Interferometry

A technique that overcomes the disadvantages of FROG, i.e., the complex procedure to measure polarization shaped laser pulses as well as the relative phase between temporally isolated subpulses, is dual-channel spectral interferometry. Dual-channel spectral interferometry is based on spectral interferometry [42], but enables characterization of polarization shaped laser pulses by measuring two independent polarizations. It is a linear technique, offering high sensitivity and allowing for non-iterative evaluation of the characterized pulse shape. However, it is a cross-referencing technique, which has the disadvantage that information about the reference pulse has to be obtained in advance. In the experiments described in this thesis, this is done by a SHG-FROG (Section 2.4.1) and the combination of the two techniques is called POLLIWOG (POLarized Light Interference versus Wavelength of Only a Glint) [43]. Although the dual-channel spectral interferometry setup as used in the experiments was already introduced in Fig. 2.3 a schematic setup is depicted in Fig. 2.12a that omits all optics which are not relevant for the characterization discussed here. The schematic is very similar to the SHG-FROG setup. However, in contrast to the SHG-FROG setup, the pulse shaper (PS) is placed in one of the arms, whereas it is in front of the first beam splitter (BS1) in the SHG-FROG setup (not shown in Fig. 2.11). After passing the interferometric setup, i.e., after the second beam splitter (BS2), the two beams are recombined and the resulting electric field is a superposition of the reference pulse $\vec{E}_0(t)$ and the shaped pulse $\vec{E}(t)$. For the characterization measurement, the projection on the polarizations 1 and 2 of the superposition of both electric fields is spectrally resolved. Therefore, the time delay τ is set to a fixed value and the spectrometer has to be calibrated carefully [44].

To realize the dual-channel measurement a polarizer (P) is placed in front of the spectrometer and two perpendicular polarization components which are rotated by 45° and −45° with respect to the reference pulse are measured independently. An illustration of the measured polarization components [1 (dashed arrow) and 2 (solid arrow)] together with the momentary reference pulse $E_0(t)$ (red dotted line) and the momentary shaped pulse $E(t)$ (red solid line) is displayed in Fig. 2.12b.

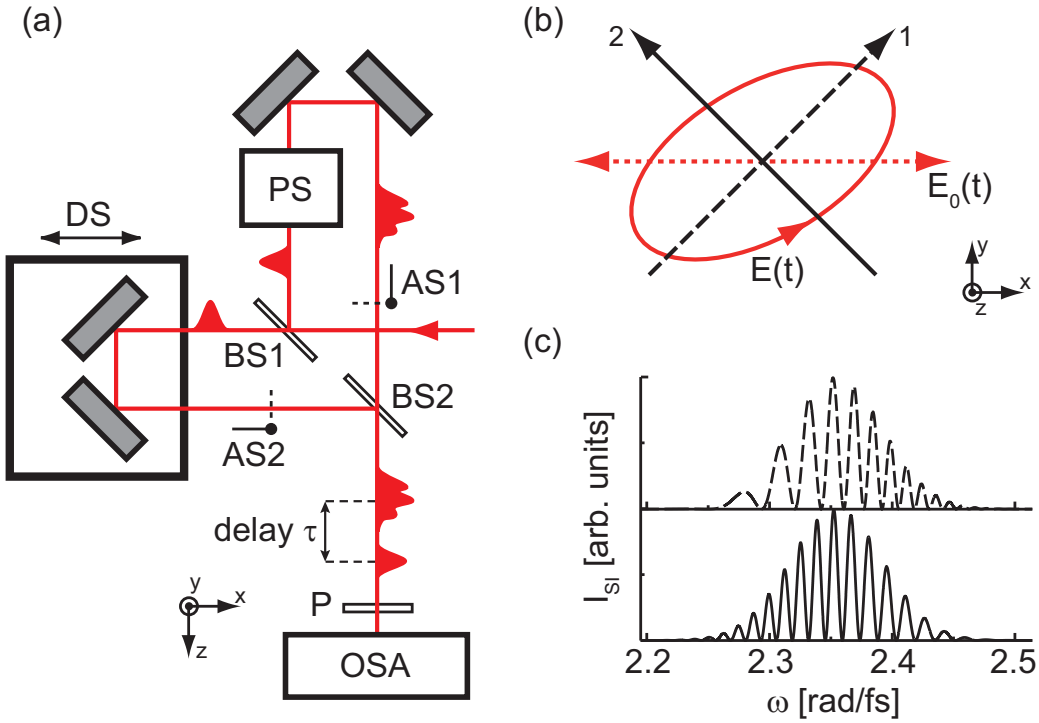

Figure 2.12: Spectral interferometry for polarization shaped laser pulses. (a) The schematic setup of spectral interferometry which corresponds to the experimental setup depicted in Fig. 2.7. Adapted from Fechner [28]. (b) The polarization-shaped laser pulse $E(t)$ (red solid line) displayed as an ellipse together with the reference pulse $E_0(t)$ (red dotted line), which is oriented along the x axis. The orientation of the measured polarizations, which are chosen by a polarizer (P) in front of the spectrometer. (c) The interferometric signal $I_{1,\mathrm{SI}}$ (dashed line) and $I_{2,\mathrm{SI}}$ (solid line) of the polarizations 1 and 2 of the polarization shaped laser pulse of Fig. 2.3.

The interference patterns $I_{1,\mathrm{SI}}(\omega)$ (dashed line) and $I_{2,\mathrm{SI}}(\omega)$ (solid line) for the polarization components 1 and 2 of the polarization shaped laser pulse of Fig. 2.3 are plotted in Fig. 2.12c for a time delay $\tau = 350\,\mathrm{fs}$. The fringes appear at an approximate period of $2\pi/\tau$, where deviations are due to an introduced phase by the pulse shaper. An decreasing fringe spacing with respect to ω is observed for the upchirped ($b_2 = 2500\,\mathrm{fs}^2$) component 1 (dashed line). The fringe spacing for component 2 (solid line) is increasing due to the introduced downchirp ($b_2 = -800\,\mathrm{fs}^2$). Additionally, a decreased fringe spacing is observed at $2\pi/(\tau + b_1)$ due to the introduced linear phase $b_1 = 100\,\mathrm{fs}$. In the following description of the analysis procedure only one component is considered. The complete polarization shaped laser pulse can be retrieved by a coherent superposition of the two polarizations.

The interferometric signal detected by a spectrometer (OSA) is proportional to

$$I_{SI}(\omega) = \left| E_0^+(\omega) + E^+(\omega)\,\mathrm{e}^{-\mathrm{i}\omega\tau} \right|^2 , \tag{2.54}$$

where the additional phase $\omega\tau$ is due to the temporal delay τ of the shaped pulse $E^+(\omega) = A(\omega)\,\mathrm{e}^{-\mathrm{i}\varphi(\omega)}$ with respect to the reference pulse $E_0^+(\omega) = A_0(\omega)\,\mathrm{e}^{-\mathrm{i}\varphi_0(\omega)}$. The

proportionality factors of Eq. (2.19) are omitted for the sake of simplicity. Additionally the spectral intensity of the two arms, i.e., the spectral intensity of the reference and the shaped pulse, can be measured independently by automatic shutters (AS1 and AS2).

To quantitatively analyze the spectral interferometry data described in Eq. (2.54) a Fourier-transform method [42] is carried out. In the first step the spectral intensities of the two arms, i.e., $I(\omega) = A^2(\omega)$ and $I_0(\omega) = A_0^2(\omega)$, are measured independently and are subtracted from $I_{SI}(\omega)$. The resulting interference term

$$\begin{aligned} S(\omega) &= I_{SI}(\omega) - I(\omega) - I_0(\omega) \\ &= \left[E_0^+(\omega)\right]^* E^+(\omega)\,\mathrm{e}^{-\mathrm{i}\omega\tau} + E_0^+(\omega)\left[E^+(\omega)\right]^*\mathrm{e}^{\mathrm{i}\omega\tau} \qquad (2.55) \\ &= 2\sqrt{I_0(\omega)I(\omega)}\cos\left[\varphi_0(\omega) - \varphi(\omega) - \omega\tau\right] \qquad (2.56) \end{aligned}$$

contains the desired phase $\varphi(\omega)$. Since, the direct evaluation via the arccosine function can lead to large phase errors in spectral regions where the cosine approaches unity [42], a Fourier transform filtering method is used. Therefore, the interference term [Eq. (2.55)] is inversely Fourier transformed

$$\begin{aligned} S(t) &= \frac{1}{\sqrt{2\pi}}\int_{-\infty}^{\infty} S(\omega)\,\mathrm{e}^{\mathrm{i}\omega t}\,\mathrm{d}\omega \\ &= \frac{1}{\sqrt{2\pi}}\int_{-\infty}^{\infty}\left[E_0^+(\omega)\right]^* E^+(\omega)\,\mathrm{e}^{\mathrm{i}\omega(t-\tau)}\,\mathrm{d}\omega \\ &\quad + \left\{\frac{1}{\sqrt{2\pi}}\int_{-\infty}^{\infty}\left[E_0^+(\omega)\right]^* E^+(\omega)\,\mathrm{e}^{\mathrm{i}\omega(-t-\tau)}\,\mathrm{d}\omega\right\}^* \\ &= \tilde{S}(t-\tau) + \tilde{S}^*(-t-\tau), \qquad (2.57) \end{aligned}$$

with

$$\tilde{S}(t) = \frac{1}{\sqrt{2\pi}}\int_{-\infty}^{\infty}\left[E_0^+(\omega)\right]^* E^+(\omega)\,\mathrm{e}^{\mathrm{i}\omega t}\,\mathrm{d}\omega. \qquad (2.58)$$

Since the spectral interference term $S(\omega)$ is a real-valued physical observable, the temporal counterpart is Hermitian [$S(t) = S(-t)^*$], and therefore, the full information is contained in the positive temporal part of S(t), which can be extracted by filtering. Similar to the spectral electric field definition of Eq. (2.11) we can define

$$S^+(t) = \tilde{S}(t-\tau). \qquad (2.59)$$

Hence, the spectral analogue $S^+(\omega)$ can be calculated by a Fourier-transform

$$\begin{aligned} S^+(\omega) &= \frac{1}{\sqrt{2\pi}}\int_{-\infty}^{\infty}\tilde{S}(t-\tau)\,\mathrm{e}^{-\mathrm{i}\omega t}\,\mathrm{d}t \\ &= \left[E_0^+(\omega)\right]^* E^+(\omega)\,\mathrm{e}^{-\mathrm{i}\omega\tau} \\ &= \sqrt{I_0(\omega)I(\omega)}\,\mathrm{e}^{\mathrm{i}[\varphi_0(\omega)-\varphi(\omega)-\omega\tau]}, \qquad (2.60) \end{aligned}$$

and the undesirable cosine function of Eq. (2.56) has been transformed into a complex-valued relation, which is much less sensitive to noise. Consequently, the desired phase $\varphi(\omega)$ of the shaped laser pulse is given by

$$\varphi(\omega) + \omega\tau = \varphi_0(\omega) - \arg\left\{S^+(\omega)\right\}. \tag{2.61}$$

As already mentioned at the beginning of this section, the phase of the reference pulse $\varphi_0(\omega)$ has to be measured additionally with a self-referencing technique, which was chosen to be SHG-FROG in the presented experiments.

In a last step the remaining phase term $\omega\tau$ has to be removed. It can be removed by a linear fit if the absolute point in time of the laser pulse is not important for the experiment (Sections 6.3 and 6.4 and Chapter 7). For experiments where the absolute point in time is relevant, the delay time τ has to be measured for an unshaped pulse, i.e., zero phase applied to both layers. The phase term $\omega\tau$ can then be subtracted for adaptively optimized pulses with the predetermined time delay τ (Section 5.4).

The total electric field $E^+(\omega) = \sqrt{I(\omega)}\,\mathrm{e}^{-\mathrm{i}\varphi(\omega)}$ is calculated by using the measured spectral intensity $I(\omega)$.

Coming back to polarization shaped laser pulses, one receives the two polarizations independently, where the same time delay τ has to be chosen for the evaluation of both electric fields $E_1^+(\omega)$ and $E_2^+(\omega)$. In addition it is very important that the measurements of the two interferometric signals $I_{1,\mathrm{SI}}$ and $I_{2,\mathrm{SI}}$ are measured under interferometric stable conditions. A small deviation of the time delay τ can lead to a wrong relative phase $\varphi_2(\omega) - \varphi_1(\omega)$ and hence to a wrong polarization state. To assure interferometric stable conditions the setup is covered with a box and the two interferometric signals $I_{SI\,1}$ and $I_{SI\,2}$ are measured within a few seconds. The electric field of the polarization shaped laser pulse is then obtained as a coherent superposition

$$\vec{E}^+(\omega) = \begin{pmatrix} E_1^+(\omega) \\ E_2^+(\omega) \end{pmatrix} = \begin{pmatrix} \sqrt{I_1(\omega)}\,\mathrm{e}^{-\mathrm{i}\varphi_1(\omega)} \\ \sqrt{I_2(\omega)}\,\mathrm{e}^{-\mathrm{i}\varphi_2(\omega)} \end{pmatrix}, \tag{2.62}$$

where $I_i(\omega)$ is the measured spectral intensity of the polarization component i. An experimental setup to circumvent the need of interferometric stable measurement is to use a polarizing beam-splitter cube and measure both polarization components simultaneously using a two-dimensional detector in the spectrometer. Nevertheless, here the two polarization components had to be measured consecutively since the used spectrometer has a single-line detector.

For the experiments it is very crucial to choose an appropriate value for the fixed time delay τ. On the one hand, since the signal is Fourier-filtered in time domain [Eq. (2.59)] it is very important to choose τ large enough, such that the signal $\tilde{S}(t-\tau)$ is clearly separated from time zero. This is of special interest for adaptive optimizations where pulse durations of several picoseconds can be obtained. On the other hand larger values of τ result in a smaller fringe spacing and hence in a reduced fringe contrast that is due to the finite spectral resolution of the used spectrometer (approximately 0.06 nm) [45]. As a compromise a time delay of $\tau \approx 2.5\,\mathrm{ps}$ was chosen for the experiments.

Although the analysis of spectral interferometry is derived in ω-space, the measured signal is obtained with a spectrometer which yields approximate equally spaced values

with respect to wavelength λ for the characterized wavelengths region, i.e., from 750 to 850 nm. However, to perform the Fourier-filtering equally spaced values with respect to frequency ω are required. To avoid errors introduced by an interpolation of the interference pattern the interference term [Eq. (2.55)] can also be filtered in the reciprocal λ-domain [46]. The phase is then first extracted in λ-space and interpolated afterward to equally spaced frequencies, whereas the intensity with equally spaced frequencies has to be calculated using the Jacobian relation of Eq. (2.22).

2.4.3 Experimental Jones-Matrix Determination

As already mentioned Section 2.2.3, the Jones-matrix formalism can also be used to characterize polarization shaped laser pulses. Therefore the transfer function of the experimental setup was measured with respect to the phase retardations φ_1 and φ_2 applied by the corresponding pulse shaper layers 1 and 2. For the following argumentation the coordinate system of the layers is chosen (indicated by 1 and 2 for the corresponding axes of Fig. 2.9) and the frequency dependence is omitted for the sake of simplicity.

The Jones-matrices of the experimental setup displayed in Fig. 2.7 was measured with spectral interferometry. Consequently, the Jones-matrix can be written as

$$\begin{pmatrix} E^+_{1,\mathrm{out}} \\ E^+_{2,\mathrm{out}} \end{pmatrix} = \begin{pmatrix} J^{(2)}_{11} & J^{(2)}_{12} \\ J^{(2)}_{21} & J^{(2)}_{22} \end{pmatrix} \begin{pmatrix} \mathrm{e}^{-\mathrm{i}\varphi_1} & 0 \\ 0 & \mathrm{e}^{-\mathrm{i}\varphi_2} \end{pmatrix} \begin{pmatrix} J^{(1)}_{11} & J^{(1)}_{12} \\ J^{(1)}_{21} & J^{(1)}_{22} \end{pmatrix} \begin{pmatrix} E^+_{1,\mathrm{in}} \\ E^+_{2,\mathrm{in}} \end{pmatrix}, \tag{2.63}$$

where $J^{(1)}$ describes the influence of all optical elements from the first beam splitter (BS1) to the LCD, the diagonal matrix with the phase retardations φ_1 and φ_2 describes effect of the corresponding LCD layers, and $J^{(2)}$ describes the effect of all optical components between the LCD and the experiment. Since misalignment, i.e., a relative angle between optical elements in the experimental setup, can be expressed as additional matrices, the measured Jones-matrix includes such experimental inaccuracies.

In order to get an expression for the Jones-matrix of the setup that just depends on the phase retardations of the LCD layers it is advantageous to rewrite Eq. (2.63) by carrying out the matrix multiplication such that

$$\begin{aligned} \begin{pmatrix} E^+_{1,\mathrm{out}} \\ E^+_{2,\mathrm{out}} \end{pmatrix} &= \begin{pmatrix} J^{(2)}_{11}(J^{(1)}_{11}E^+_{1,\mathrm{in}} + J^{(1)}_{12}E^+_{2,\mathrm{in}}) & J^{(2)}_{12}(J^{(1)}_{21}E^+_{1,\mathrm{in}} + J^{(1)}_{22}E^+_{2,\mathrm{in}}) \\ J^{(2)}_{21}(J^{(1)}_{11}E^+_{1,\mathrm{in}} + J^{(1)}_{12}E^+_{2,\mathrm{in}}) & J^{(2)}_{22}(J^{(1)}_{21}E^+_{1,\mathrm{in}} + J^{(1)}_{22}E^+_{2,\mathrm{in}}) \end{pmatrix} \begin{pmatrix} \mathrm{e}^{-\mathrm{i}\varphi_1} \\ \mathrm{e}^{-\mathrm{i}\varphi_2} \end{pmatrix} \\ &= \begin{pmatrix} A_{11} & A_{12} \\ A_{21} & A_{22} \end{pmatrix} \begin{pmatrix} \mathrm{e}^{-\mathrm{i}\varphi_1} \\ \mathrm{e}^{-\mathrm{i}\varphi_2} \end{pmatrix}. \end{aligned} \tag{2.64}$$

This simplification separates the influence of "passive" optical elements including the incoming electric field, combined in the two-by-two matrix A, from the influence of the "active" LCD, written as a two-dimensional vector.

Assuming that the "passive" optical elements as well as the incoming electric field, i.e., the laser light, are stable during the experiment, the matrix A of Eq. (2.64) is constant for all pulse shapes produced by the polarization pulse shaper. Consequently, the knowledge of this matrix leads to the characterization of the polarization shaped laser pulse E^+_{out} that impinges at the experiment.

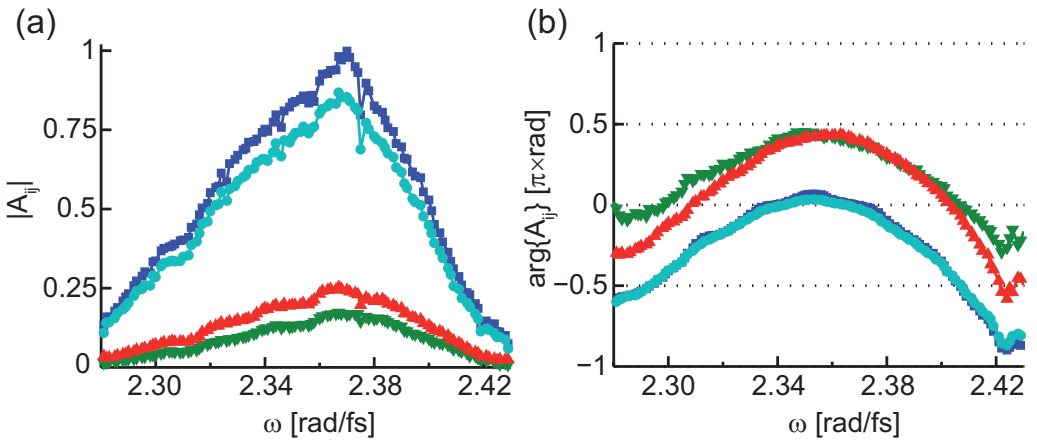

Figure 2.13: The measured matrix A of Eq. (2.64). The matrix elements A_{11} (blue squares), A_{12} (green downward-pointing triangles), A_{21} (red upward-pointing triangles), and A_{22} (cyan dots) are shown for each frequency, separated in the absolute magnitudes (a) and the phases (b).

To extract the matrix A of Eq. (2.64), a certain number of pulse shapes was measured with POLLIWOG, i.e. dual-channel spectral interferometry in combination with FROG, for a set of known phases. For the characterization of the different pulses it is important that the pulses were measured under interferometric stable conditions as described in Section 2.4.2. The matrix for each frequency can then be retrieved independently in a least-square sense [17]. In principle, this is already possible using two pulse shapes. However, to reduce the experimental uncertainties eight pulse were measured with a constant phase for layer one $\varphi_1 = 0\,\text{rad}$ and eight different phases for layer two $\varphi_2 = \{-\frac{3}{2}\pi, -\pi, -\frac{1}{2}\pi, 0, \frac{1}{2}\pi, \pi, \frac{3}{2}\pi, 2\pi\}\,\text{rad}$.

The absolute values and the argument values of the measured matrix A are displayed in Fig. 2.13a and Fig. 2.13b, respectively. The absolute magnitude of the diagonal elements A_{11} (blue squares) and A_{22} (cyan dots) are about five times larger than the off-diagonal elements A_{12} (green downward-pointing triangles) and A_{21} (red upward-pointing triangles). The gaussian shape of the absolute magnitude of all elements indicate the included incoming electric field E^{+}_{in}. The phases for the diagonal elements are almost constant at 0 rad whereas the off-diagonal elements have values around 0.4π rad. The marginal downchirp indicates a small misalignment of the zero dispersion compressor of the polarization pulse shaper. Since the deviations from a perfectly aligned pulse shaper, which would have equal real-valued diagonal elements and off-diagonal elements with magnitude zero, are small, the alignment of the pulse shaper can assumed to be sufficiently good.

2.5 Evolutionary Algorithm

Femtosecond pulse shaping was successfully used for optimal control of optical excitations in nanostructures [11, 13, 47, 48]. To find the optimal laser pulse shapes two differ-

ent approaches are applied. Open loop optimizations are used if the response function of the nanostructure is known and an appropriate approach can be found to determine the optimal pulse shape [48–50]. While one kind of such an optimization scheme will be developed and described in Chapter 4, a second approach has to be considered if the response function is unknown. In this case an extremely large parameter space has to be explored and learning algorithms have to be used in terms of closed loop optimizations [11, 13]. For closed loop optimizations, described in this thesis, an evolutionary algorithm [51, 52] is used. Such an algorithm finds the optimal pulse shape in an adaptive fashion based on biological evolution.

The fundamental principles of biological evolution are replication, selection, and mutation [53]. Evolution requires populations of reproducing individuals, where the genomic material is replicated and passed on to the offspring. Selection results via a fitness that rates certain individuals better than others and hence prefer reproduction of these individuals. Mutation is the result of imperfect reproduction and generates different types of individuals. Due to the fitness of the different individuals, selection will choose some innovations and dismiss others.

A diagram of the evolutionary algorithm for polarization pulse shaping that is used in this work is depicted in Fig. 2.14. Each pulse shape is encoded into genes, represented as the voltages of the LCD and a corresponding fitness is defined by a feedback from the experiment or simulation, respectively. In the pool of individuals all individuals of one generation are rated and selected by means of the assigned fitness. Selection chooses the fittest individuals to produce the next generation. Mutation randomly changes the genes of the fittest individuals. Cloning choses the fittest individuals to survive and passes them to the next generation. Crossover produces new individuals possessing genes from two of the fittest individuals. The unused individuals, i.e., the individuals that are neither used for mutation, cloning, nor crossover, are dumped. After the assembling of the individuals for the next generation, the next iteration is started and the algorithm is run until convergence.

For the experiments and simulations the number of individuals was 40. Each optimization was started with individuals which are sampled randomly in the parameter space. The encoding of the pulse shape into genes was done in two different bases depending on the type of experiment. For the simulations in Chapter 4 a basis was used, where the amplitudes and phases for each polarization ($2 \times 2 \times 128$ parameter) can be chosen independently for each frequency. To reduce the number of genes the genes were chosen as nodes, where the interjacent values were spline interpolated. In the experiments described in Chapters 5 and 6, only the phase of each polarization was shaped and the number of genes was further decreased by defining a dispersion basis. In the dispersion basis the phases applied on each layer are expanded into Taylor coefficients around the center frequency [Eq. (2.16)] and the genes define the coefficients.

In Chapters 4 and 5 the results of closed looped optimizations with an evolutionary algorithm are used to confirm the results that are gained with an open loop approach. Since the agreement in both cases is very good and due to the reproducibility of optimizations, as will be shown in Chapter 6, the evolutionary algorithm seems to be an appropriate tool for optimal control of optical excitations in nanostructures.

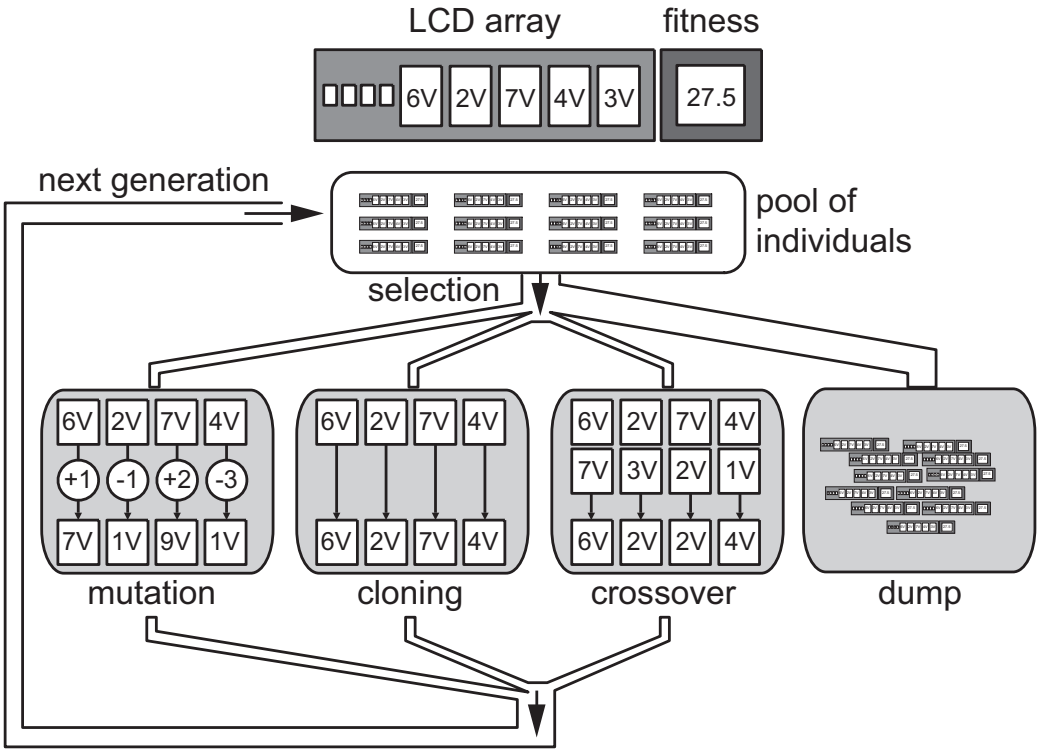

Figure 2.14: Evolutionary algorithm used for adaptive optimizations with the pulseshaper. The individuals of one generation are presented by a pool and are sorted according to their assigned fitness. Each individual represents one pulse shape that is encoded into genes, defining the applied voltages. The fittest individuals are reproduced in terms of mutation, cloning and crossover and are pooled together to form the next generation. Taken from Brixner [17].

2.6 Photoemission Electron Microscope

Optical excitations in metallic nanostructures are confined to the nanometer scale on the surface of the nanostructure. The measurement of these electric fields is challenging [54, 55] and the optical diffraction limit avoids direct measurement with conventional confocal microscopes [56, 57]. The device, chosen for the presented experiments, is a photoemission electron microscope (PEEM). Due to the fact that the emission of electrons depends on the photon flux, the measurement of the photoemission enables a measurement of the electric field strength. This is of special interest for the mapping of local electric fields confined on the nanometer scale since the emitted electrons can be spatially resolved below the diffraction limit of the exciting optical fields.

2.6.1 Photoemission

The underlying physics of the PEEM technique is the photoemission of electrons [58]. Photoemission is a light-matter interaction where the absorption of photons leads to emission of electrons from matter. Although matter in general also includes non-metals, liquids and gases, here matter equates with solid metals. The process of photoemission

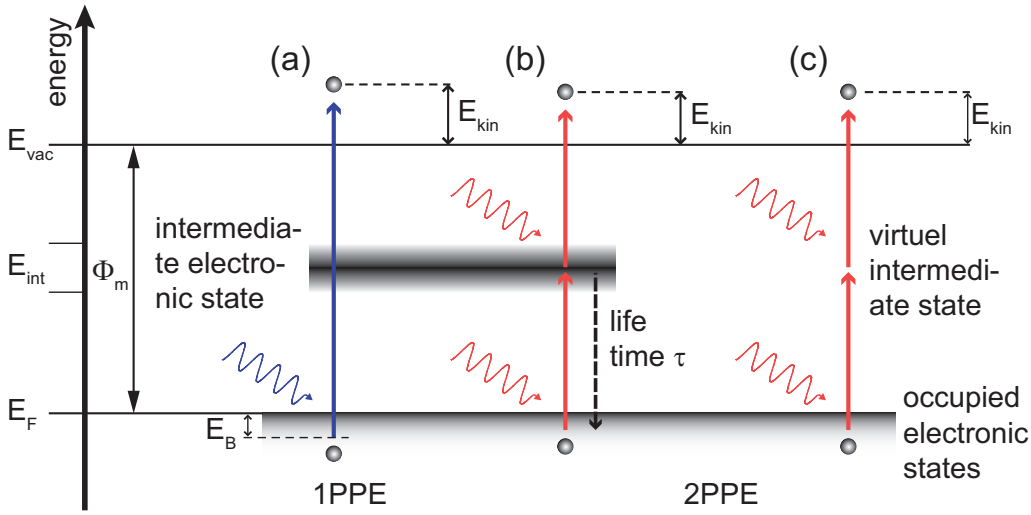

Figure 2.15: Schematic of photoelectron emission. The electrons in the solid are bounded with an energy E_B below the the Fermi energy E_F and are excited with light. The vacuum energy E_{vac} is defined via the material dependent work function Φ_m. (a) One photon photoemission (1PPE) occurs if the energy of a single photon is sufficient to excite the electron above the vacuum energy E_{vac}. Hence, the electron is emitted with the remaining energy E_{kin}. (b,c) Two photon photoemission (2PPE) occurs if two photons are necessary to excite the electron above the vacuum energy E_{vac}. In this case one photon excites the electron to an intermediate state. This state can be either a real electronic state with a lifetime τ (b) or a virtual intermediate state (c), i.e., the lifetime is zero. Taken from Kramer [62].

is a quantum electrical effect, which was first observed by Hertz [59] and Hallwachs [60]. A first quantitative analysis of the effect was done by Einstein [61], who found the energy of an emitted electron as

$$E_{\mathrm{max,kin}} = \sum_{n=1}^{N} h\nu_n - P, \tag{2.65}$$

where the sum describes the quantized energy of N absorbed photons with their individual energies ν_n and h being Planck's constant. Hence, the energy of the emitted electron is reduced by P with respect to the energy of the absorbed photons. For electrons populated at the Fermi energy the reduction P is identical with the work function Φ_m, which is a material dependent quantity. If the emitted electron is bounded within the solid the corresponding energy is below the Fermi level and an additional bounding energy E_{B} has to be taken into account. Hence, Eq. (2.65) can be rewritten as

$$E_{\mathrm{kin}} = \sum_{n=1}^{N} h\nu_n - \Phi_m - E_{\mathrm{B}}. \tag{2.66}$$

Figure 2.15 shows a schematic of one [$N = 1$, 1PPE, (a)] and two photon photoemission [$N = 2$, 2PPE, (b) and (c)]. The work function Φ_m is the energy between the Fermi level

E_F and the vacuum level E_{vac}, whereas the bounding energy E_B reflects the reduction of energy for electrons that are emitted from below the Fermi level.

In case of 1PPE the energy of the absorbed photon has to exceed the reduction P to excite the electron above the vacuum energy. However, as can be inferred from Figs. 2.15b and c, if the energy of a single photon is smaller than P, high photon flux can lead to multiphoton photoemission. In case of multiphoton photoemission at least one intermediate state has to be present. In the example of Fig. 2.15 2PPE is considered to be initiated by two photons with the same energy. The emission of the electron occurs in two steps. First, one photon is absorbed and the electron is excited to an intermediate state. This intermediate state is above the Fermi energy but below the vacuum energy and has to be in the energy range that is accessible with the absorbed photon. Second, another photon is absorbed and the electron is lifted from the intermediate state above the vacuum energy. Consequently, the electron is emitted from the metal and the kinetic energy can be calculated via Eq. (2.66). The intermediate state can have two different origins. The 2PPE can occur via virtual states that have a vanishing lifetime $\tau = 0$ (Fig. 2.15c). The other possibility is a real intermediate state which has a finite lifetime τ (Fig. 2.15b). The lifetime of such a real state is in the range of a few femtoseconds due to electron-electron scattering processes in the solid [63] and can be measured in terms of time-resolved 2PPE measurements [64, 65].

2.6.2 Experimental Setup

The photoemission electron microscope (PEEM) provides a tool to detect the electrons which are emitted from a sample with a high spatial resolution. Therefore, an electrostatic lens system maps the emitted electrons onto an amplifying imaging system. The theoretical spatial resolution of the emitted electrons' location is limited by diffraction and hence, is given by the de Broglie wavelength λ_0 of the emitted electron with mass m_e and a kinetic energy E_{kin}

$$\lambda_0 = \frac{h}{\sqrt{2 m_e E_{kin}}}. \tag{2.67}$$

Assuming a realistic kinetic energy of $E_{kin} = 1\,\text{eV}$ the highest theoretic resolution is in the order of the corresponding de Broglie wavelength $\lambda_0 = 1.2\,\text{nm}$ [66]. Recent improvement of PEEM instrumentations report a resolution in this range with 2 nm [67]. However, to realize such a resolution an aberration-corrected device is necessary, which is not present for the experiments described in this thesis. Here, a commercial *Focus* IS-PEEM[1] is used and spherical as well as chromatic aberration of the electrostatic lenses and of the acceleration field have to be taken into account [68]. The highest resolution reached with this type of PEEM is reduced to about 25 nm [69]. However, the maximum resolution of the PEEM used for the presented experiments is 40 nm and depends on the used sample as will be discussed in more detail in Chapter 7.

The principle setup of the *Focus* IS-PEEM [66, 68] is depicted in Fig. 2.16. It consists of three lenses: The tetrode objective lens, the intermediate lens and the projection

[1]Integrated Sample (IS) describes that the sample holder is installed at the column, which reduces vibrations of the sample with respect to the detector and therefore increases the resolution.

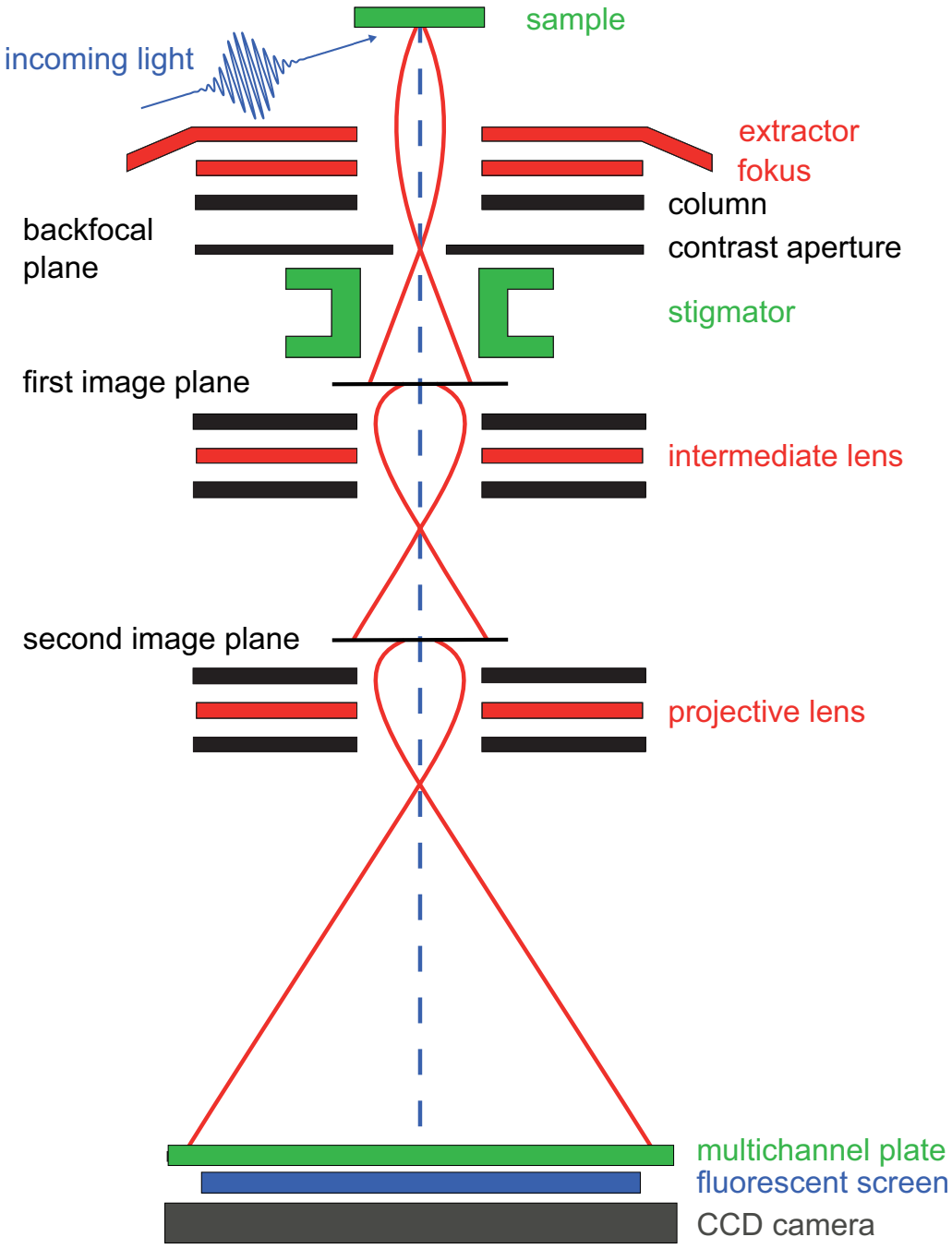

Figure 2.16: Schematic PEEM setup. A electrostatic lens system magnifies the spatially resolved photoemitted electrons and maps them on a CCD camera using a fluorescent screen. The first lens, a tetrode objective lens, also includes the sample. A high voltage between the sample and the extractor detracts the emitted electrons and sends them through the lens system. The first image is magnified with the intermediate and the projective lens to increase the resolution and to compensate for distortions. The contrast aperture and the stigmator reduce aberration. Modified from Schneider [70].

lens. The tetrode objective lens contains the sample, which serves as the cathode, and the extractor, the focus, and the column electrode. A high voltage is applied between the sample and the extractor to extract the emitted electrons from the sample and map them on the first image plane. In the Fourier plane (backfocal plane) a contrast aperture blocks electrons with higher spatial frequencies. The spatial frequencies contain the angle information of the emitted electrons. Small spatial frequencies correspond to electrons which are emitted close to the optical axis (blue dashed line), whereas high spatial frequencies correspond to electrons emitted far away from the optical axis. Hence, the contrast aperture in the backfocal plane can be adjusted to decreases angle dependent aberrations. The aberrations caused by the electro static lenses are minimized by an octopole stigmator. The first image is magnified by the intermediate lens and the projective lens. Here, a two lens system is used to reduce distortions of the image.

The imaging unit consists of a multichannel plate, a fluorescent screen and a CCD camera. The multichannel plate amplifies the electrons and the optical image produced by the fluorescent screen is recorded by a Peltier-cooled CCD camera (LaVision Imager 3LS).

The image contrast of PEEM is defined as

$$K = \frac{I_{\max} - I_{\min}}{I_{\max} + I_{\min}}, \tag{2.68}$$

where $I_{\max}$ and $I_{\min}$ are the maximum and minimum intensities of the emitted electrons. To analyze the PEEM images three main contrast mechanisms have to be considered [68]. First, the contrast strongly depends on the material. Different work functions Φ_m lead to different probabilities for photoemission. The best material contrast is reached if the photon energy $h\nu$ is between the work functions of two different materials, i.e., $\phi_{m,1} < h\nu < \phi_{m,2}$. In this case, only 1PPE will be present for the material with $\phi_{m,1}$, whereas electrons can only be emitted in a 2PPE process from the material with $\phi_{m,2}$ and for low light intensity these electrons can be neglected. Second, the probability of photoemission depends on the topography of the investigated sample. The electronic flux is perpendicular to conductive surfaces and therefore inhomogeneous for bended surfaces. In such regions the emitted electrons are diffracted in different directions depending on the inhomogeneous electronic flux and the image contrast can vary although the photoemission is homogeneous with respect to the surface [68]. Third and most important for this thesis, the photoemission depends on the electric field strength on the surface of the investigated sample. This leads to enhanced photoemission for regions with resonant near-field enhancement (Chapter 3) [71].

As can be inferred from Fig. 2.16, the sample cannot be excited under normal incidence due to the tetrode objective lens. The illumination condition of the sample is depicted in Fig. 2.17. The incident beam is irradiated under an angle of 65° with respect to the normal vector $\vec{z}$ of the sample. Consequently, the polarization components (red) are tilted with respect to the sample-inherent coordinate system (green). The vertically oriented polarization component (s) is parallel to the surface of the sample, i.e, parallel to the y direction. The component that is oriented in the plane spanned by the incoming laser beam and the normal vector $\vec{z}$ is called p component and has a projection onto that normal vector $\vec{z}$. The strong electric field component perpendicular to the surface

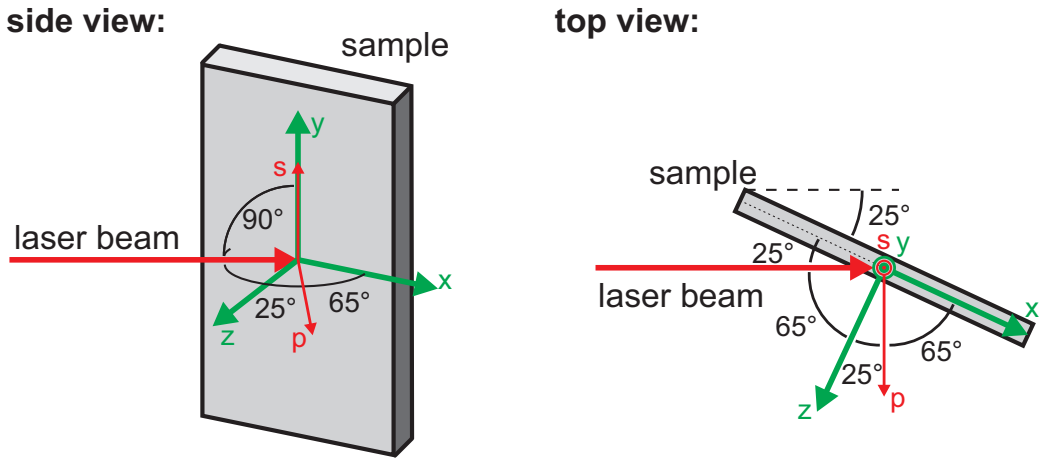

Figure 2.17: Angle of incidence of the incoming laser beam with respect to the sample. Due to the incident angle of 25° with respect to the sample plane the p component of the incoming laser beam has a component in the direction of the normal vector $\vec{z}$. Taken from Strüber [72].

leads to an enhanced multiphoton photoemission probability of this component [72].

2.6.3 Drift Correction

The experiments described in this thesis need a huge number of PEEM images. Especially, for the 2D nanoscopy measurements (Chapter 7) more than 20000 images had to be taken and hence a measurement sequence took about twelve hours. A problem that comes with these long measurement times is the thermal drift of the sample holder with respect to the contrast aperture and the imaging system. For the data analysis it is important that the evaluated regions are defined with respect to the sample and not with respect to the image. Since the drift is in the order of 50 nm/h, it can be neglected for single images which are exposed for not more than 10 s. However, for experiments in the order of several hours the evaluation has to be adjusted to correct for drift effects. These effects would result in systematic errors and the resolution would be reduced drastically. The drift correction is of special importance if the PEEM is used with maximum magnification, i.e., with maximum resolution of about 40 nm. Hence, to account for the thermal drift and to avoid systematic errors, the drift has to be detected and corrected for each image of the experiment.

Therefore, an image processing routine [72] is used (Fig. 2.18). To detect the drift of the sample holder reference images R_i are taken sequently during the measurement images M_i (a). Each M_i does not necessarily indicate a single image, but can also indicate several measurement images which would than be corrected using the same reference image R_i. The reference images have to be taken under identical conditions, i.e., with identical pulse shaper settings, to directly attribute the drift to the sample holder. Using the reference images the drift is then detected with respect to the first reference image in terms of a two dimensional cross-correlation (b). The cross-correlation simply shifts each reference image R_i over the first reference image R_1 in both directions and calculates the

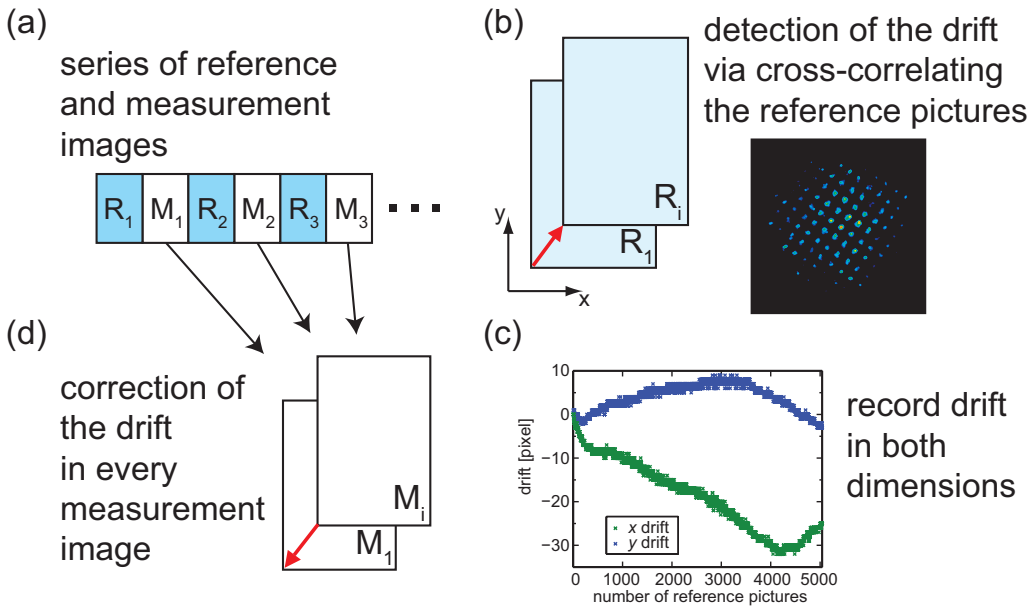

Figure 2.18: Image processing of PEEM data. (a) Reference images R_i are taken sequently during the measurement images M_i. (b) The reference images R_i are used to detect the drift via a cross-correlation. (c) The drift in both dimensions is recorded for each reference image and then (d) used to correct the corresponding measurement images M_i. Modified from Strüber [72].

correlation by a scalar product of the two images for each shift position. The highest scalar product then reveals the best overlap and the corresponding drift. To exclude regions of the image which are due to imaging defects of the imaging system and hence do not drift, a drift mask is defined in advance. Therefore, only a certain part of the image is used for the cross-correlation. The remaining part of the image is filled with noise. The drift is recorded for each reference image in both dimensions (c) with a resolution of 1 pixel of the CCD camera. In the last step the measured data images are corrected with the assigned drift (d).

Two different types of drift correction have to be considered. First, for measurements which are done in scanning mode the drift detection and correction can be done as a part of the data analysis, i.e., the detection and correction is done after finishing the experiment. Second, for adaptive optimizations of the photoemission yield (Chapters 5 and 6) the drift has to be detected and corrected on-the-fly. This is important since the optimizations require pre-defined regions to calculate the feedback for the optimization.

3 Optical Near Fields

One of the main subjects that is treated in this thesis is the control of optical near fields. The properties of near fields (Section 3.1) enable to circumvent the optical diffraction limit and provide a high number of possible applications as will be discussed throughout the thesis. Especially interesting is the control of near fields that is gained by excitation of nanostructures with polarization shaped laser pulses (Section 3.2). Since optical near fields can be calculated by self consistently solving Maxwells equations, computer based simulations provide an easy and reliable access to these fields (Section 3.3).

3.1 Principles of Nanooptic

Before describing the properties of optical fields localized below the diffraction limit, we first have to understand how it is possible to beat the diffraction limit. This is done using the basic concept of focusing [54].

Considering an unfocused beam propagating in z direction, the wavevector $\vec{k}$ of this propagating wave is given by $k_z = |\vec{k}|$ and $k_x = k_y = 0$. However, in case of focusing, the components k_x and k_y have nonvanishing contributions. As can be inferred from Fig. 3.1 the focusing is an interference effect caused by the superposition of planar waves. These waves propagate under different angles θ with respect to the beam direction and hence possess different wavevectors, where only a two-dimensional space is considered here. The more propagating waves with different angles θ, i.e., k_x components, are present the more waves can interfere to increase the localization on the x axis. This effect can easily be explained in terms of Fourier transform theory: A high localization in position space Δx, requires a broad spectrum of spatial frequencies Δk_x. Analogously to the time-bandwidth product of Eq. (2.25) the product of spatial localization and spatial frequency spread has a lower limit given by

$$\Delta x \Delta k_x \geq c_k, \tag{3.1}$$

where c_k is a constant on the order of one, which depends on the focusing conditions. In general, the absolute value of the wavevector is given by

$$|\vec{k}| = \sqrt{k_x^2 + k_y^2 + k_z^2} = \frac{2\pi}{\lambda} \tag{3.2}$$

and is inversely proportional to the wavelength λ. Hence, the broadest theoretical spectrum of spatial frequencies of the component k_x is the total length of the free-space wavevector $|\vec{k}|$, i.e., $\theta = \pi/2$ and $k_z = 0$. Using the definition of the total length of the free-space wavevector $|\vec{k}|$ [Eq. (3.2)] as the spread in spatial frequencies, Eq. (3.1) can

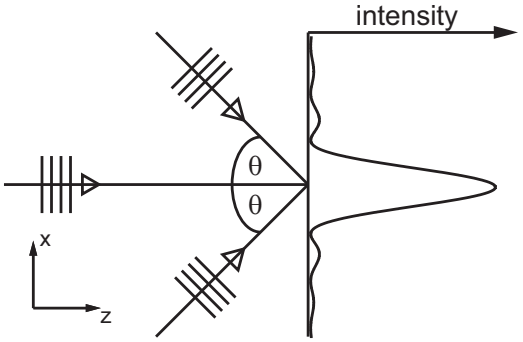

Figure 3.1: Schematic of focusing. The superposition of multiple plane waves, arriving from different directions defined by the angle θ with respect to the z axis, result in constructive and destructive interference in the focal plane. The observed intensity distribution yields high intensity in the focus with concentric bright rings around it and is known as Airy pattern. Taken from Rewitz [73].

be rewritten as

$$\Delta x \geq \frac{\lambda}{c_k 2\pi}. \tag{3.3}$$

Consequently, the spatial confinement is limited by the spread of wavevector components in the respective direction. This limit also leads to the expression of the Abbe diffraction limit and restricts the spatial resolution of optical microscopy. However, it is only restricted by the spread of the wavevector components in a given direction. One way to mathematically overcome this restriction for the two-dimensional space chosen here is to assign a purely imaginary k_z. As can be inferred from Eq. (3.2), this can lead to increased values of the wavevector component k_x, such that

$$k_x > |\vec{k}| \tag{3.4}$$

and Δx can be smaller than the diffraction limit. Plugging in the purely imaginary wavevector component k_z into the definition of a spatially propagating field [Eq. (2.30)] reveals the physical meaning of the mathematical trick. The electric field in z direction is then exponentially decaying

$$E_z(z,\omega) = E_z(0,\omega)\,\mathrm{e}^{\mathrm{i}k_z z} = E_z(0,\omega)\,\mathrm{e}^{-|k_z|z}\,. \tag{3.5}$$

On the one hand this would lead to decaying electric fields for $z > 0$, on the other hand the electric field increases exponentially for values $z < 0$, which does not make physical sense. Therefore, Eq. (3.3) is always valid in free space, but as will be explained in Section 3.1.1, for two half-spaces with different refractive indices, exponentially decreasing electric fields can exist and a localization of the electric field below the diffraction limit [Eq. (3.3)] is possible. Since the resulting electric fields are bound to the surface because of their exponential decay, they are also called near fields. Apart from near fields that are bound to planar interfaces, in Section 3.1.2 near-field properties of particles with dimensions much smaller than the wavelength are discussed. The interparticle coupling of such near fields is explained in Section 3.1.3.

3.1.1 Propagating Surface Plasmon Polaritons

Picking up the reasoning above, we will now take a look at surface plasmon polaritons (SPPs) excited at an interface, i.e., two half-spaces with different dielectric functions.

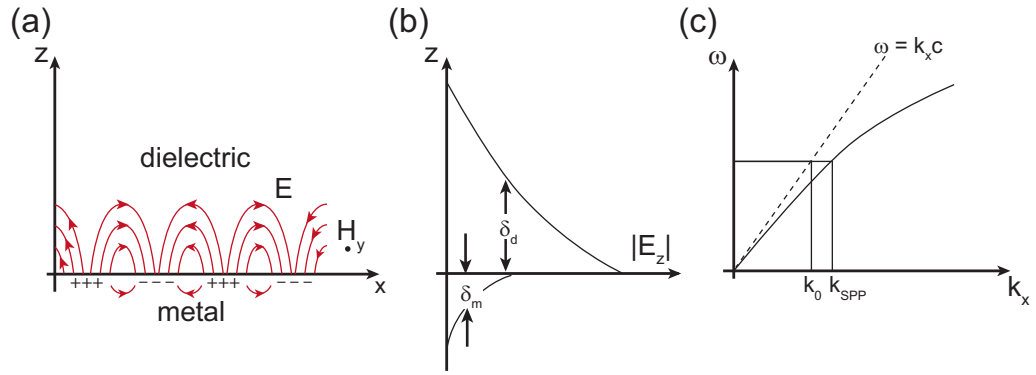

Figure 3.2: Surface plasmon polaritons (SPPs) propagating along the x axis. (a) The electric field (red arrows) of an propagating SPP bounded to a metal-dielectric interface resulting from collective oscillations of the free electron gas density in the metal (indicated with + and −). The magnetic field is indicated with H_y and is polarized parallel to the surface. The bounding of the fields is indicated in (b). The penetration depths of the z component of the electric field are indicated with δ_d and δ_m for $z > 0$ (dielectric) and $z < 0$ (metal), respectively. (c) The dispersion relation of SPPs and that of light in vacuum, i.e., $\omega = k_x c$, are indicated with solid and dashed lines, respectively. Since the dispersion relation of SPPs is below the light line, the condition $k_{\mathrm{SPP}} > k_0$ holds for all frequencies. Taken from Barnes *et al.* [74]. Copyright (2003) by Macmillan Publishers Ltd.

Surface plasmon polaritons are collective excitations of electrons in the conduction band of a metal. They describe the interaction of electromagnetic waves with the electron plasma and are solutions to Maxwell's equations on a metal-insulator interface. Figure 3.2 shows the main properties of propagating plasmon polaritons. As can be inferred from Fig. 3.2a, the electric field (red arrows) is bounded to the surface and is coupled to the collective oscillations of the free electron gas in the metal (+ and − signs). The magnetic field, indicated with H_y, just has a component in y direction, i.e., is parallel to the interface. This is a main property of SPPs and it can be shown by solving Maxwells equations that SPPs only exist for transverse magnetic (TM) polarization [55]. The z component of the electric field is exponentially decreasing and the penetration depth δ_d in the dielectric is longer than the depth δ_m in the metal (Fig. 3.2b). Consequently, the electric field, bound to the interface is called near field. Using appropriate boundary conditions, the dispersion relation of a propagating plasmon at an interface located in the x-y plane at $z = 0$ is

$$k_x(\omega) = \frac{\omega}{c}\sqrt{\frac{\varepsilon_m(\omega)\varepsilon_d(\omega)}{\varepsilon_m(\omega) + \varepsilon_d(\omega)}}, \tag{3.6}$$

where $\varepsilon_m(\omega)$ and $\varepsilon_d(\omega)$ are the dielectric functions of the metal and the dielectric material, respectively. The real part of $k_x(\omega)$ defines the SPP wavelength, whereas the imaginary part defines the propagation length along the interface. The propagation distances are typically on the order of several tens of micrometers. As can be inferred from Fig. 3.2c the dispersion relation of SPPs [Eq. (3.6)] does not cross the dispersion relation

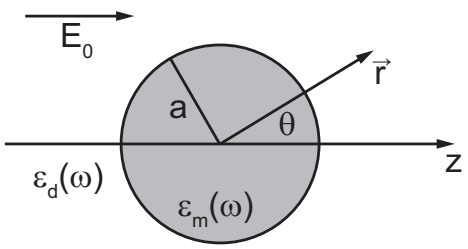

Figure 3.3: Metal sphere in an isotropic surrounding. The metal sphere with a dielectric function $\varepsilon_m(\omega)$ surrounded by an isotropic and non-absorbing material $[\varepsilon_d(\omega)]$ is illuminated with a static electric field $\vec{E}_0$ pointing in z direction. The induced local field is calculated at position $\vec{r}$. The angle between the vector $\vec{r}$ and the z axis is given by θ. Adapted from Maier [55].

of light in vacuum ($\omega = ck_x$). For any frequency ω the momentum, i.e., the absolute value of the k vector, of the SPP is larger than that of a photon, i.e., $k_{\mathrm{SPP}} > k_0$. This is a very critical property that, on the one hand, avoids a direct excitation of SPPs on a dielectric-metal interface with far-field illumination. On the other hand, scattering of SPPs to the far-field is suppressed, which results in the long propagation length.

However, to match the momenta of SPPs and photons different concepts are applied. It is possible to excite SPPs using evanescent waves that arise from total internal reflection, e.g., at a glass air interface. This can be understood by a decrease of the slope of the light line $\omega = ck_x/n$ by using a dielectric with a diffraction index $n > 1$ [54]. This leads to an intersection of the two dispersion relations and excitation of SPPs is achieved. For the first time this was realized by Otto [75] and Kretschmann [76] by means of evanescent waves created by a glass prism. A different approach to excite SPPs is to adjust the dispersion relation of the SPPs to match the light line. This can be done by writing a grating into the metal surface [77]. The lack of momentum of the light is then provided by the grating.

3.1.2 Resonant Plasmonic Modes

For a particle that is much smaller than the wavelength of the exciting field, e.g., a sphere with diameter $d = 2a \ll \lambda$, the phase of the field can be considered constant over the complete volume of the particle. Therefore, the local field can be calculated in a quasi static approximation. After gaining the solutions for the static electric field the time dependent oscillations of the local field can be multiplied.

As an example the local field is calculated for a homogeneous isotropic sphere with radius a and dielectric function $\varepsilon_m(\omega)$ in the static electric field $\vec{E}_0 = E_0\vec{e}_z$ (Fig. 3.3) [55]. The surrounding material is isotropic and non-absorbing, with real-valued dielectric constant $\varepsilon_d(\omega)$. Since we consider an electrostatic approach, we have to solve the Laplace equation for the potential $\nabla^2\Phi(\omega) = 0$. Note that $\Phi(\omega)$ does not describe a phase here, but the electric potential. The electric field can then be calculated by $\vec{E}(\omega) = -\nabla\Phi(\omega)$. Using the azimuthal symmetry of the problem, the solution is expressed in terms of

Legendre Polynomials $P_l(\cos\theta)$ [20]

$$\Phi(r,\theta) = \sum_{l=0}^{\infty} \left[B_l r^l + C_l r^{-(l+1)}\right] P_l(\cos\theta), \tag{3.7}$$

where l is the polynomial order. The dependence on the position vector $\vec{r}$ is taken into account with the angle θ which is defined between the vector itself and the z axis and the distance from the origin of the sphere $r = |\vec{r}|$. Two different solutions are found: Φ_{in} inside and Φ_{out} outside the sphere. The requirement of a finite field in the origin of the sphere leads to [55]

$$\Phi_{\text{in}}(\vec{r}) = \sum_{l=0}^{\infty} B_l r^l P_l(\cos\theta) \tag{3.8}$$

$$\Phi_{\text{out}}(\vec{r}) = \sum_{l=0}^{\infty} \left[C_l r^l + D_l r^{-(l+1)}\right] P_l(\cos\theta). \tag{3.9}$$

Using the boundary conditions $\Phi_{\text{out}}(\vec{r}) \to -E_0 r\cos\theta$ at $r \to \infty$ and the continuity of the tangential components of the electric field as well as the continuity of the normal component of the displacement field at $r = a$, the coefficients B_l, C_l and D_l can be determined. The potentials can then be written as [20]

$$\Phi_{\text{in}}(\vec{r},\omega) = -\frac{3\varepsilon_d(\omega)}{\varepsilon_m(\omega) + 2\varepsilon_d(\omega)} E_0 r\cos\theta \tag{3.10}$$

$$\Phi_{\text{out}}(\vec{r},\omega) = -E_0 r\cos\theta + \frac{\varepsilon_m(\omega) - \varepsilon_d(\omega)}{\varepsilon_m(\omega) + 2\varepsilon_d(\omega)} E_0 a^3 \frac{\cos\theta}{r^2}. \tag{3.11}$$

Here, the frequency dependent dielectric functions are included and hence, the potential also depends on the frequency. Furthermore, Eq. (3.11) can be rewritten by defining a dipole moment $\vec{p}(\omega)$ such that

$$\Phi_{\text{out}}(\vec{r},\omega) = -E_0 r\cos\theta + \frac{\vec{p}(\omega)\cdot\vec{r}}{4\pi\varepsilon_0\varepsilon_d r^3}, \tag{3.12}$$

with

$$\vec{p}(\omega) = 4\pi\varepsilon_0\varepsilon_d(\omega) a^3 \frac{\varepsilon_m(\omega) - \varepsilon_d(\omega)}{\varepsilon_m(\omega) + 2\varepsilon_d(\omega)} \vec{E}_0. \tag{3.13}$$

As can be inferred from Eq. (3.13) the applied electric field induces a dipole moment, which is proportional to $\vec{E}_0$. Using the dipole moment defined in Eq. (3.13) and the identity $\vec{p}(\omega) = \varepsilon_0\varepsilon_d(\omega)\alpha(\omega)\vec{E}_0$, the polarizability $\alpha(\omega)$ can be introduced:

$$\alpha(\omega) = 4\pi a^3 \frac{\varepsilon_m(\omega) - \varepsilon_d(\omega)}{\varepsilon_m(\omega) + 2\varepsilon_d(\omega)}. \tag{3.14}$$

The polarizability of a silver sphere is shown in Fig. 3.4, where the dielectric function of silver is taken from Palik [78]. The surrounding material is vacuum, i.e., $\varepsilon_d(\omega) = 1$. A resonant enhancement of the polarizability is observed around the frequency $\omega =$

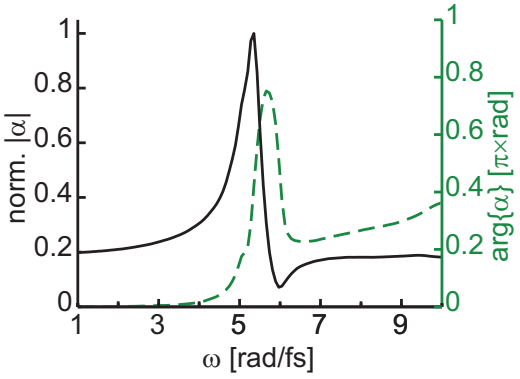

Figure 3.4: Absolute value $|\alpha|$ (solid black line) and phase $\arg\{\alpha\}$ (dashed green line) of the polarizability of a silver nanosphere as a function of the frequency ω. The polarizability was calculated via Eq. (3.14) using the measured dielectric function of silver [78].

5.4 rad/fs, corresponding to the minimum of $|\varepsilon_m(\omega) + 2\varepsilon_d(\omega)|$, i.e., the absolute value of the denominator of Eq. (3.14). Mathematically, the magnitude of the polarizability could be infinity, if $\varepsilon_m(\omega) = -2\varepsilon_d(\omega)$. However, due to the real-valued dielectric function of the surrounding material it is limited by the imaginary part of $\varepsilon_m(\omega)$. If the imaginary part of $\varepsilon_m(\omega)$ is almost constant around the resonance, the resonance condition for the maximum simplifies to the so-called Fröhlich relation condition

$$\mathrm{Re}\,\{\varepsilon_m(\omega)\} = -2\varepsilon_d(\omega). \tag{3.15}$$

The mode of the local field that is observed for an electric field at the resonance frequency is called the dipole surface plasmon. As can be concluded from Eq. (3.14) the surrounding material strongly affects the resonance frequency. A red-shift is observed for an increase of $\epsilon_d(\omega)$.

Using the calculated potentials $\Phi_{\mathrm{in}}(\vec{r},\omega)$ and $\Phi_{\mathrm{out}}(\vec{r},\omega)$, the position dependent electric field is gained via $\vec{E}(\vec{r},\omega) = -\nabla\Phi(\vec{r},\omega)$

$$\vec{E}_{\mathrm{in}}(\vec{r},\omega) = \frac{3\varepsilon_d(\omega)}{\varepsilon_m(\omega)+2\varepsilon_d(\omega)}\vec{E}_0 \tag{3.16}$$

$$\vec{E}_{\mathrm{out}}(\vec{r},\omega) = \vec{E}_0 + \frac{3\vec{n}(\vec{n}\cdot\vec{p}(\omega)) - \vec{p}(\omega)}{4\pi\varepsilon_0\varepsilon_d(\omega)}\frac{1}{r^3}. \tag{3.17}$$

Here, $\vec{n}$ describes the unit vector in the direction of $\vec{r}$. Two dimensional cuts of the spatial distribution of the electric field are depicted in Fig. 3.5 for two different characteristic excitation frequencies. Due to the azimuthal symmetry only one half space is plotted, containing all the information. As can be inferred from Eqs. (3.16) and (3.17) the resonance condition of the polarizability $\alpha(\omega)$ also holds for the local electric field inside and outside the sphere. Hence, a field enhancement of about five is observed by comparing the amplitude of the electric field for the resonance frequency ($\omega = 5.4$ rad/fs) and for an off-resonant frequency ($\omega = 1.5$ rad/fs) in Figs. 3.5a and 3.5b, respectively. Additionally to spherical objects, similar solutions can be derived for ellipsoids [55].

Many applications of plasmonic excitations, such as optical devices [79], optical nonlinearities [80] and sensors [81, 82], rely on this field enhancement. Additional applications are found in spectroscopy such as surface enhanced Raman scattering (SERS) [83] and coherent control on single molecules [9]. The highest field enhancements can be reached

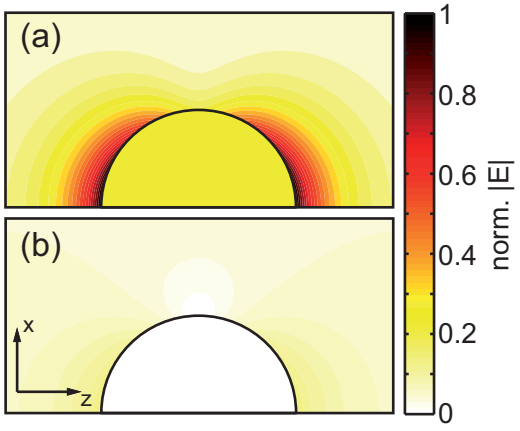

Figure 3.5: Half spaces of the local electric field distribution of a silver nanosphere. The amplitude of the local electric field [Eqs. (3.16) and (3.17)] for (a) the resonance frequency at $\omega = 5.4\,\mathrm{rad/fs}$ and (b) for $\omega = 1.5\,\mathrm{rad/fs}$ normalized to the maximum amplitude for the resonance frequency is plotted as a function of spatial coordinates.

with so-called optical nanoantennas [84, 85], leading to a resonant enhancement factor of more than 1000 [85].

As already mentioned above the solution for the local electric field was found in a quasi static approximation, i.e., a constant electric field $\vec{E}_0$. To recover the time dependent dipole moment as well as the local field, the solutions of Eqs. (3.13), (3.16) and (3.17) have to be extended with the oscillating term $\mathrm{e}^{-\mathrm{i}\omega t}$ such that $\vec{E}_0(t) = \vec{E}_0\,\mathrm{e}^{-\mathrm{i}\omega t}$. The local field is then determined for a monochromatic incident field with frequency ω and plane-wave illumination.

In Eq. (3.12) the dipole character of the induced local field is introduced. Using the general description of the quasi-static total electric field induced by an oscillating dipole with frequency ω [20]

$$\vec{E}(\vec{r},\omega) = \frac{1}{4\pi\varepsilon_0\varepsilon_d(\omega)}\left\{k^2\left[\vec{n}\times\vec{p}(\omega)\right]\times\vec{n}\frac{\mathrm{e}^{\mathrm{i}kr}}{r} + \left\{3\vec{n}\left[\vec{n}\cdot\vec{p}(\omega)\right]-\vec{p}(\omega)\right\}\left(\frac{1}{r^3}-\frac{\mathrm{i}k}{r^2}\right)\mathrm{e}^{\mathrm{i}kr}\right\}, \tag{3.18}$$

the far ($kr \gg 1$, $1/r$ dependence), intermediate ($kr \approx 1$, $1/r^2$ dependence) and near zone ($kr \ll 1$, $1/r^3$ dependence) can be defined, where the electric field in the near zone is also called near-field and equates with the local field outside of the sphere derived above [Eq. (3.17)]. Again, the time dependence of the total electric field is obtained by multiplication of the quasi-static total electric field [Eq. (3.18)] with the oscillating term $\mathrm{e}^{-\mathrm{i}\omega t}$.

Factoring out the scalar description of the exciting electric field in Eq. (3.17) and introducing a frequency dependent $E_0(\omega)$ yields

$$\vec{E}_{\mathrm{out}}(\omega,\vec{r}) = \underbrace{\left[\vec{e}_z + \alpha(\omega)\frac{3\vec{n}(\vec{n}\cdot\vec{e}_z)-\vec{e}_z}{4\pi}\frac{1}{r^3}\right]}_{\vec{A}(\vec{r},\omega)} E_0(\omega), \tag{3.19}$$

where $\vec{A}(\vec{r},\omega)$ is defined as the optical response function of the sphere to a certain polarization component, here the z component. Although, this is the solution for a certain structure found by a simplified approach, due to the linearity of Maxwell's equations it is always possible to write the local field in frequency space at a certain point $\vec{r}$ as

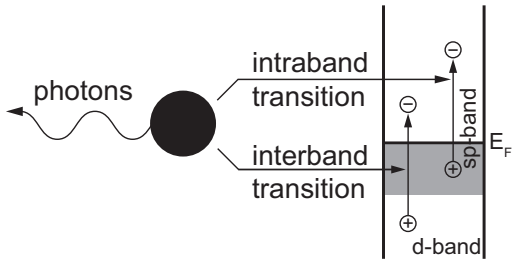

Figure 3.6: Schematic of decay of particle plasmons [55]. Radiative decay is observed via emission of photons (left). Non-radiative decay is observed due to the creation of electron hole pairs (right). In noble metals two different transitions can occur: Intraband excitations within the sp conduction band and interband excitations from lower-lying d-bands to the sp conduction band.

a product of the response function $\vec{A}(\vec{r},\omega)$ and the exciting electric field $E_0(\omega)$ with a certain polarization component. Note that two important physical properties come with this notation: First, it is possible to shape the local field, i.e., the optical near-field, of nanostructures via shaping the far-field excitation, i.e., introducing a complex-valued $E_0(\omega)$. Second, due to the vector character of the response $\vec{A}(\vec{r},\omega)$ the local electric field vector $\vec{E}_{\mathrm{out}}(\omega,\vec{r})$ does not have to have the same direction as the excitation field $\vec{E}_0$. These two properties will be used in Section 3.2 to explain the control of near fields in nanostructures.

Although the quasi-static approximation gives good agreement for particles much smaller than the wavelength it does not predict a size dependent resonance condition as it is observed for particles on the order of the wavelength [86]. To explain the scattering colors of colloidal gold particles and to derive equations that can be used independent of the size of the particle, Mie developed a complete theory. This theory expands the internal and the scattered field into normal modes described by vector harmonics [87]. Since the detailed expression for the higher terms is not of interest for the scope of this thesis and is discussed elsewhere, it is just important to point out that the denominator of the polarizability [Eq. (3.14)] includes a size dependent parameter $x = \pi a/\lambda_0$ which relates the radius a of a sphere to the excitation free-space wavelength λ_0. This parameter shifts the resonance to smaller frequencies as the radius a increases.

So far, only single frequency excitation was considered. However, since in this thesis excitation of nanostructures with femtosecond laser pulses are described—corresponding to a finite width of the exciting spectrum—we have to take dynamic damping processes caused by the nanostructure into account. The dominating damping processes of resonant modes in noble metal nanoparticles are shown in Fig. 3.6. Since electromagnetic fields, i.e., photons, couple strongly to the resonant plasmonic modes, inversion of this coupling results in radiation damping of the plasmonic modes caused by transfer of the coherent electron oscillation, i.e., plasmons, into photons (left) [88]. This damping process increases for increasing particle size [89]. Apart from radiative there is also non-radiative damping, which is due to the excitation of electron–hole pairs in the metal (right). The electron-hole pairs can either be excited via intraband excitations within the sp conduction band or via interband excitations from d-bands to the sp conduction band. The electron–hole pairs excited by the strong field enhancement due to resonant

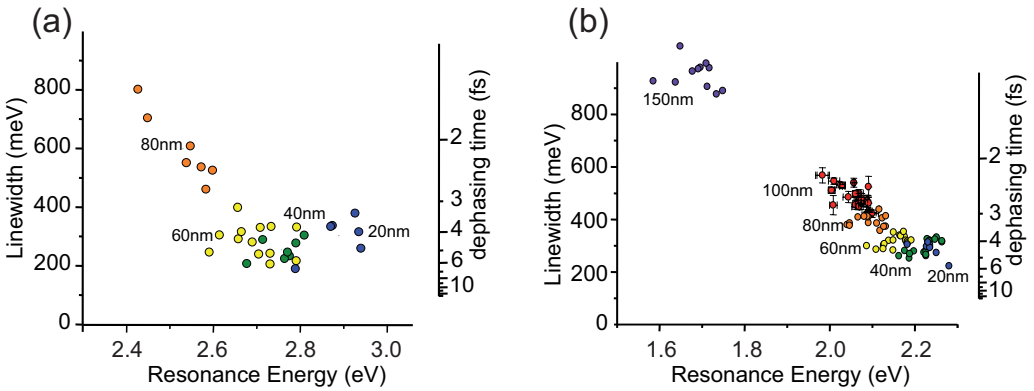

Figure 3.7: Dephasing times of particle plasmons measured by Sönnichsen *et al.* [92]. The resonance linewidth and corresponding dephasing time versus the resonance energy of silver (a) and gold (b) nanospheres with different diameters are measured using dark-field microscopy.

modes can lead to broadband photoluminescence [90, 91].

Both of these damping processes, i.e., radiative and non-radiative decay, result in a population relaxation and are expressed in terms of the decay time T_1. An additional process not considered above and in the decay time T_1 is the so called pure dephasing time T_2^* resulting from elastic collisions of the electrons leading to a dephasing of the collective motion of the electrons within the metal. Combination of these two processes yield the dephasing time

$$\frac{1}{T_2} = \frac{1}{2T_1} + \frac{1}{T_2^*}. \tag{3.20}$$

Even though both times T_1 and T_2^* contribute to the dephasing time T_2, it was shown that in general $T_2^* \gg T_1$ [89]. Hence, the dephasing time is mainly governed by the decay time, such that $T_2 = 2T_1$. Sönnichsen *et al.* [92] showed that for gold and silver particles that are smaller than 100 nm, the dephasing time T_2 is smaller than 10 fs (Fig. 3.7). They measured the homogeneous linewidth, which is inversely proportional to the dephasing time, of (a) silver and (b) gold nanospheres with different sizes using dark field microscopy. They observed a strong size dependence on the dephasing time that results from increasing radiative decay with increasing particle size. Additionally, the redshift for increasing particles size as mentioned above is observed and a material dependent shift is observed by comparing, e.g., particles of size 20 nm, yielding a resonance at around 2.9 eV for silver and around 2.25 eV for gold.

It is important to point out that the optical response function $\vec{A}(\omega)$, which will be used in the following to describe optical near-fields, includes these damping processes via the measured dielectric functions.

3.1.3 Coupling of Localized Plasmons

Above, single particles are discussed in terms of their response to optical excitations and a single optical resonance frequency ω_R is found. However, in Chapter 4 a one

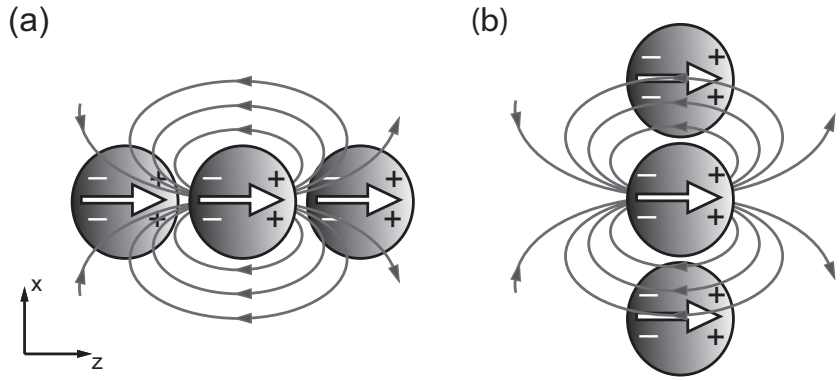

Figure 3.8: Schematic of the near-field coupling in chains of nanoparticles excited with light polarized along the z direction. The field lines of the near-field are indicated with grey arrows for (a) the longitudinal mode and (b) the transversal mode. White arrows in the spheres indicate the direction of the induced dipoles. Adapted from Maier [55].

dimensional chain of silver spheres is excited. Therefore, we want to discuss the change of optical properties that come with multiple coupled particles in the following.

If the interparticle distance d is much smaller than the wavelength λ the coupling is dominated by near-field interactions. In this case the particle array can be assumed to consist of an array of point dipoles interacting via their near fields and the electric field is strongly localized in the nano-sized gap. The field localization reflects the excitation of plasmon modes that suppresses scattering to the far field [93].

As an example Fig. 3.8 shows a chain of three coupled spheres. The dipolar character of the spheres is indicated with white arrows in the spheres pointing in the corresponding direction. If the interparticle distance is small, the electric field induced by the dipole, indicated with the gray arrows, couples to neighboring spheres. As can be inferred by the charge distribution, indicated with plus and minus signs, the coupling leads to Coulomb forces between the particles. Two different modes have to be distinguished for in-phase excitation, i.e., all dipoles in the chain point in the same direction [55]. The longitudinal mode (Fig. 3.8a) is excited if the dipoles point in the direction of the chain's main axis, i.e., the polarization of the exciting light and the chain's main axis point in z direction. In this case the restoring force acting on the oscillating electrons is decreased, with respect to a single sphere, by the charge distribution of the neighboring particles, i.e., plus signs are adjacent to minus signs. Hence, the resonance is shifted to frequencies $\omega < \omega_R$, where ω_R is the resonance of a single sphere. The transverse mode (Fig. 3.8b) is excited if the dipoles point in the direction perpendicular to the chain's main axis, i.e., the polarization of the exciting light points in z direction whereas the chain's main axis points in x direction. Consequently, the resonance is shifted to higher frequencies ($\omega > \omega_R$) due to the increased restoring force, i.e., plus signs are adjacent to plus signs. As already mentioned above, the dipolar coupling is a near-field property that strongly depends on the interparticle distance. Hence, the resonance shifts of the two modes scale with d^{-3} and converge to the resonance of a single sphere ω_R for $d \to \infty$ [94]. An additional dependence on the chain length, i.e., the number of spheres in the

chain, is observed [95].

As a very intuitive consequence of the strong coupling, particle chains are suitable to guide electromagnetic energy. The investigation of this property needs a localized excitation scheme. Theoretically, it is possible to place a dipole source next to a chain. Using this approach two different speeds can be assigned to the two different travelling modes (transverse and longitudinal mode) [96]. In an experiment, the local excitation has been realized by a near-field microscope tip [97].

3.2 Control Mechanisms

One of the main topics of this thesis is the control of optical near fields to provide ultrafast optical excitations localized below the optical diffraction limit. In this section the mechanisms are introduced that allow for the control of near fields in terms of constructive and destructive interference as well as temporal compression [12]. The latter is explicitly needed to provide femtosecond resolution in, e.g., spectroscopic applications.

As already introduced in Section 3.1.2 the optical response function to the excitation polarization component i can be expressed in frequency domain by

$$\vec{A}^{(i)}(\vec{r},\omega) = \begin{pmatrix} A_x^{(i)}(\vec{r},\omega) \\ A_y^{(i)}(\vec{r},\omega) \\ A_z^{(i)}(\vec{r},\omega) \end{pmatrix}. \tag{3.21}$$

Physically, this can be understood as different optical modes $\vec{A}^{(i)}(\vec{r},\omega)$ that are excited with polarization component i in nanostructures, e.g., as described in Fig. 3.8. The amplitudes $|A_\alpha^{(i)}(\vec{r},\omega)|$ with $\alpha = x, y, z$ describe the extent to which the far-field polarization component i couples to the optical near-field components, whereas the phases $\theta_\alpha^{(i)}(\vec{r},\omega) = \arg\{A_\alpha^{(i)}(\vec{r},\omega)\}$ determine their vectorial superposition and dispersion properties. These quantities are characteristics of the nanostructure and depend on the focusing conditions. However, the response is independent of the applied pulse shape that will be considered below.

As already introduced in Chapter 2 the incident polarization-shaped laser pulse, propagating in z direction, can be expressed in frequency domain by two orthogonal polarization components: $E_1^{\mathrm{in}}(\omega)$, oriented along the x axis, and $E_2^{\mathrm{in}}(\omega)$, oriented along the y axis, consisting of spectral amplitudes $\sqrt{I_i(\omega)}$ and phases $\varphi_i(\omega)$ which can all be varied independently using a full vector-field synthesizer (Section 2.3.4):

$$E_i^{\mathrm{in}}(\omega) = \sqrt{I_i(\omega)}\, \mathrm{e}^{-\mathrm{i}\varphi_i(\omega)}. \tag{3.22}$$

Note, that this description equates with the expression of $E^+(\omega)$ introduced in Chapter 2 [i.e., Eq. (2.15)]. However, the spectral amplitude is expressed here as the square root of the intensity.

Due to the linearity of Maxwell's equations, the total local near-field $\vec{E}(\vec{r},\omega)$ is obtained by calculating the near field for each far-field polarization separately and taking

the linear superposition [11]:

$$\vec{E}(\vec{r},\omega) = \begin{pmatrix} A_x^{(1)}(\vec{r},\omega) \\ A_y^{(1)}(\vec{r},\omega) \\ A_z^{(1)}(\vec{r},\omega) \end{pmatrix} \sqrt{I_1(\omega)}\, \mathrm{e}^{-\mathrm{i}\varphi_1(\omega)} + \begin{pmatrix} A_x^{(2)}(\vec{r},\omega) \\ A_y^{(2)}(\vec{r},\omega) \\ A_z^{(2)}(\vec{r},\omega) \end{pmatrix} \sqrt{I_2(\omega)}\, \mathrm{e}^{-\mathrm{i}\varphi_2(\omega)}\,. \quad (3.23)$$

Since Eq. (3.23) gives a complete picture, i.e., the amplitude and phase of the local electric field in the frequency domain, the local electric field in the time domain $\vec{E}(\vec{r},t)$ can be obtained by inverse Fourier transforming $\vec{E}(\vec{r},\omega)$ for each vector component separately.

In the following subsections it is shown that the independent external far-field parameters that determine the local fields are better expressed in the following equation:

$$\vec{E}(\vec{r},\omega) = \left\{ \begin{pmatrix} A_x^{(1)}(\vec{r},\omega) \\ A_y^{(1)}(\vec{r},\omega) \\ A_z^{(1)}(\vec{r},\omega) \end{pmatrix} \sqrt{I_1(\omega)} + \begin{pmatrix} A_x^{(2)}(\vec{r},\omega) \\ A_y^{(2)}(\vec{r},\omega) \\ A_z^{(2)}(\vec{r},\omega) \end{pmatrix} \sqrt{I_2(\omega)}\, \mathrm{e}^{-\mathrm{i}\Phi(\omega)} \right\} \mathrm{e}^{-\mathrm{i}\varphi_1(\omega)}, \quad (3.24)$$

where the phase difference of the two external polarization components is defined analogously to Eq. (2.35), such that

$$\Phi(\omega) = \varphi_2(\omega) - \varphi_1(\omega). \quad (3.25)$$

Below, it will be shown that the phase difference $\Phi(\omega)$ and the spectral amplitudes $\sqrt{I_1(\omega)}$ and $\sqrt{I_2(\omega)}$ of the incident polarization components determine the local linear flux (Section 3.2.1) whereas the phase offset $\varphi_1(\omega)$ provides a handle to manipulate the temporal evolution of the local fields (Section 3.2.2).

3.2.1 Spatial Control

For the control of the spatial distribution of the optical near field $\vec{E}(\vec{r},\omega)$ the interference of two near-field modes excited with two different far-field polarizations are utilized. Figure 3.9 illustrates the main concept of the interference in two dimensions for a single frequency in a quasi-static approximation. Without loss of generality, the electric far-field, i.e., electric field that propagates in space, can be described by two orthogonal polarizations (left panel). No interference is observed for the two components in the far-field. However, the superposition of these two polarizations can describe any state of polarization as will be needed for polarization-shaped laser pulses. Each far-field polarization component E_i^{in} induces an optical near-field described by the optical response function $\vec{A}^{(i)}$ (right panel). Since $\vec{A}^{(1)}$ and $\vec{A}^{(2)}$ do not have to be perpendicular, they can interfere with each other. Hence, by adjusting the relative phase $\Phi(\omega)$ and the amplitudes $\sqrt{I_1(\omega)}$ and $\sqrt{I_2(\omega)}$ of the far-field polarizations the two modes can be chosen to interfere constructively or destructively at a certain position. As an example the optical near field is depicted for two different excitation pulse shapes. The solid red arrow indicates the optical near field $\vec{E}^{\mathrm{un}}$ of an unshaped pulse, i.e., $\Phi = 0$, resulting from the superposition of the response functions $\vec{A}^{(1)}$ and $\vec{A}^{(2)}$. The dashed red arrow

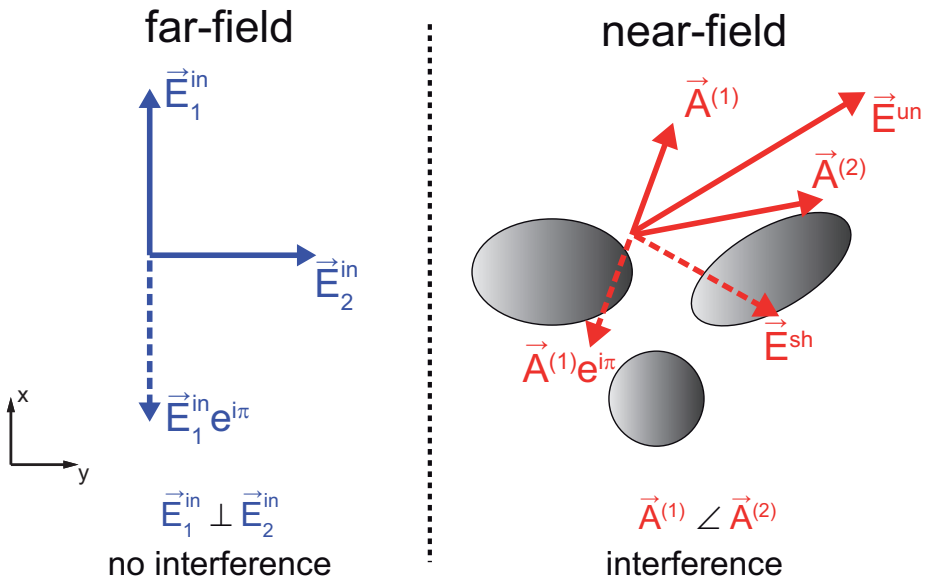

Figure 3.9: Schematic for spatial optical near-field control. Left panel: The electric far-field can in general be described by two perpendicular polarizations $\vec{E}_1^{in}$ and $\vec{E}_2^{in}$, which do not interfere. An applied phase of π to polarization component 1 results in $\vec{E}_1^{in}\, e^{i\pi}$ (dashed blue arrow). Right panel: Each of these far-field polarizations excite position dependent optical near-field modes expressed via their optical response functions $\vec{A}_1(\vec{r})$ and $\vec{A}_2(\vec{r})$. Since these modes have optical near-field properties they do not have to be perpendicular and can interfere constructively or destructively. By manipulation of the far-field polarization components the optical near-field $\vec{E}$ can be controlled. Two different examples are depicted: The solid red arrows show the optical near field $\vec{E}^{un}$ for an unshaped pulse. The dashed red arrows show the optical near-field $\vec{E}^{sh}$ for an applied phase of π to the far-field polarization component $\vec{E}_1^{in}$. Adapted from Brixner *et al.* [12].

indicates the near field $\vec{E}^{sh}$ of a shaped pulse that is obtained for applying a phase of π to the far-field polarization component $\vec{E}_1^{in}$, i.e., $\Phi = -\pi$. Accordingly, the near field is the superposition of $\vec{A}^{(1)}\, e^{i\pi}$ and $\vec{A}^{(2)}$. As can be inferred the two different far-field pulse shapes do not only change the direction of the resulting near field but also change the amplitude, i.e., the length, of the near-field vector. Hence, constructive and destructive interference is observed for unshaped and shaped pulse, respectively, i.e., $|\vec{E}^{un}| > |\vec{E}^{sh}|$ in this example.

Since the optical response functions can differ for positions that are separated less than the diffraction limit, the optical near field distribution can be adjusted with a resolution below the optical diffraction limit by far-field polarization pulse shaping. First theoretical and experimental applications of this mechanisms where shown by Brixner *et al.* [11–13]. However, in these applications the optimal excitation pulse shapes were found adaptively using an evolutionary algorithm. In Chapter 4 the understanding of the spatial near-field control mechanism is used to define deterministic rules that enable analytic calculation of the optimal parameters $\Phi(\omega)$, $\sqrt{I_1(\omega)}$ and $\sqrt{I_2(\omega)}$.

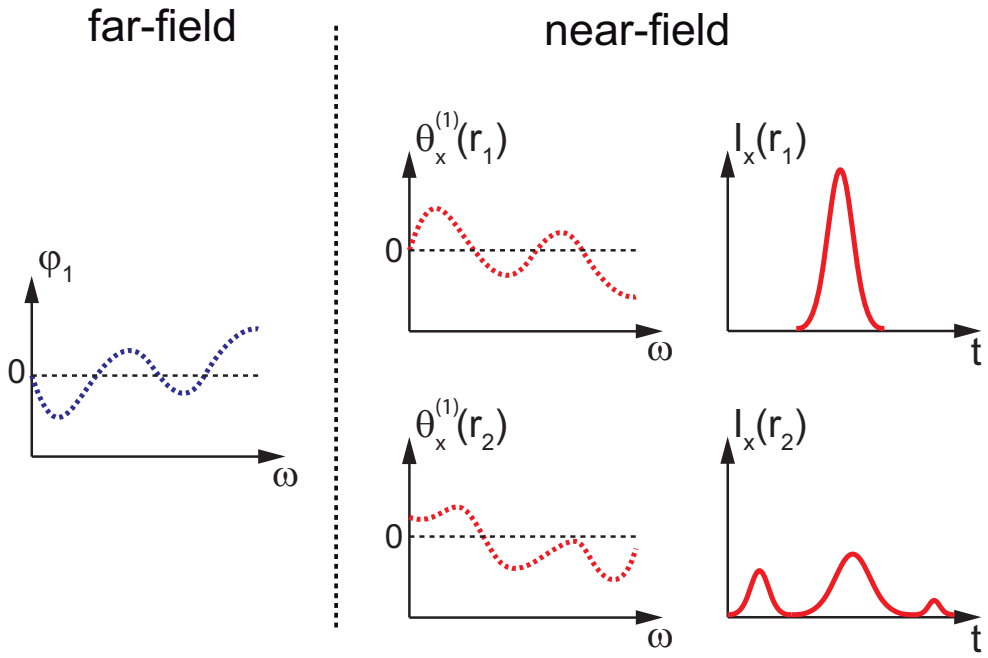

Figure 3.10: Schematic of optical near-field pulse compression. Middle panel: the phase $\theta_x^{(1)}(\vec{r}_1)$ of the x component of the optical response function $A_x^{(1)}(\vec{r})$ is shown for two different locations $\vec{r}_1$ and $\vec{r}_2$. Left panel: The negative optical near-field phase of position $\vec{r}_1$ is applied to far-field excitation, i.e., $\varphi_1 = -\theta_x^{(1)}(\vec{r}_1)$. Right panel: The applied phase results in a temporally compressed optical near-field intensity at position $\vec{r}_1$ whereas no compression is achieved for position $\vec{r}_2$. Adapted from Brixner *et al.* [12].

3.2.2 Temporal Control

Equation (3.24) yields four independent parameter that determine the local electric field, i.e., the amplitudes $\sqrt{I_1(\omega)}$ and $\sqrt{I_2(\omega)}$, the phase difference $\Phi(\omega)$ and the phase $\varphi_1(\omega)$. Three of them are already used to control the spatial distribution of the optical near field. In this section, the remaining parameter $\varphi_1(\omega)$ is used to compress the optical near field in time. The basic principle of near-field compression works analogously to automated laser pulse compression in the case of conventional far-field optics that has been addressed more than 10 years ago [98, 99]. The basic idea is that in order to achieve the shortest possible laser pulse, a linear spectral phase is required according to the Fourier relation between frequency and time domain. In the experimental implementation, learning algorithms were used to modify the spectral phase such that a nonlinear signal (second-harmonic generation in a nonlinear crystal) was maximized. Thus, the material dispersion in optical components can be compensated in order to reach highest peak intensities at the position of the experiments.

Figure 3.10 illustrates the pulse compression scheme transferred to the optical near field. Assuming only one component (e.g., the x component) of the near field, the spectral near-field phase $\theta_x^{(1)}(\vec{r}_1)$ for excitation with an unshaped pulse polarized along polarization component 1 is displayed in the upper middle panel. By applying exactly

the negative spectral phase to the exciting laser pulse $\varphi_1 = -\theta_x^{(1)}(\vec{r}_1)$ (left panel) the resulting near field phase is zero over the complete spectrum and the local intensity is optimally compressed in time (upper right panel). However, at a different position $\vec{r}_2$ the phase $\theta_x^{(1)}(\vec{r}_2)$ can differ (lower middle panel) and no compression is achieved for this position (lower right panel). Hence, a nonlinear signal, e.g., SHG, excited with the local electric field at position $\vec{r}_1$ would have large values whereas the nonlinear signal would be small at position $\vec{r}_2$. Of course, by varying the far-field phase φ_1 to be the inverse of the near-field phase $\theta_x^{(1)}(\vec{r}_2)$ it is possible to compress the near-field intensity at position $\vec{r}_2$ and to switch the maximum nonlinear signal.

However, this approach is limited because only one excitation polarization is considered (component 1) and only one local electric field component (x component) can be compressed. A detailed discussion of the near-field compression including all three components of the near field is found in Section 4.4.2. The near-field compression in combination with the spatial control mechanism introduced in the last section will be used to guide and compress the optical near field in a T-chain nanostructure (Chapter 4).

As an example of optical near-field compression in nanostructures, a simple waveguide structure composed of a nanoantenna and a two-wire transmission line (left panel Fig. 3.11) was investigated in a collaboration with the group of Bert Hecht[1]. The optical near fields were calculated using the commercial Finite Difference Time Domain (FDTD) Method of *Lumerical Solutions*. The structure was excited with a 10 fs pulse (FWHM) at 800 nm center wavelength focused down to the diffraction limit on Point A (red dashed circle). Upon illumination of the dipole antenna with polarization along the antenna arms (red dashed line), the optical near field is first spatially confined and enhanced in the feed gap of the antenna and then travels as a strongly confined mode between the two wires of the transmission line. As shown in Fig. 3.11a, the temporal responses obtained at different positions along the transmission line show broadening, which is increasing with the distance traveled (point A–D) due to dispersion. By applying a phase-shaped pulse (Fig. 3.11b, black dashed lines: unshaped pulse; red dashed line: shaped pulse) to the incoupling antenna using the method outlined above, the optical near-field intensity was recompressed at point D and the maximum optical near-field intensity was improved by a factor of 1.5 as shown in Fig. 3.11b (red solid line as compared to black solid line). Hence, the dispersion was pre-compensated by applying a longer pulse at the input (Fig. 3.11b left) that resulted in a compressed pulse at the target position (Fig. 3.11b right).

3.3 Multiple Elastic Scattering of Multipole Expansions

In Section 3.1.2 a simplified approach was used to calculate the local field in the vicinity of a small sphere. This approach is very limited since it only works in the quasi-static regime and the response of more complex structures would have to be calculated using Mie theory. Here, a different but very general approach to calculate the complex-valued linear optical response of the nanostructure in the frequency domain is introduced. The

[1]Nano-Optics and Biophotonics Group, Experimentelle Physik 5, Universität Würzburg, Am Hubland, 97074 Würzburg, Germany

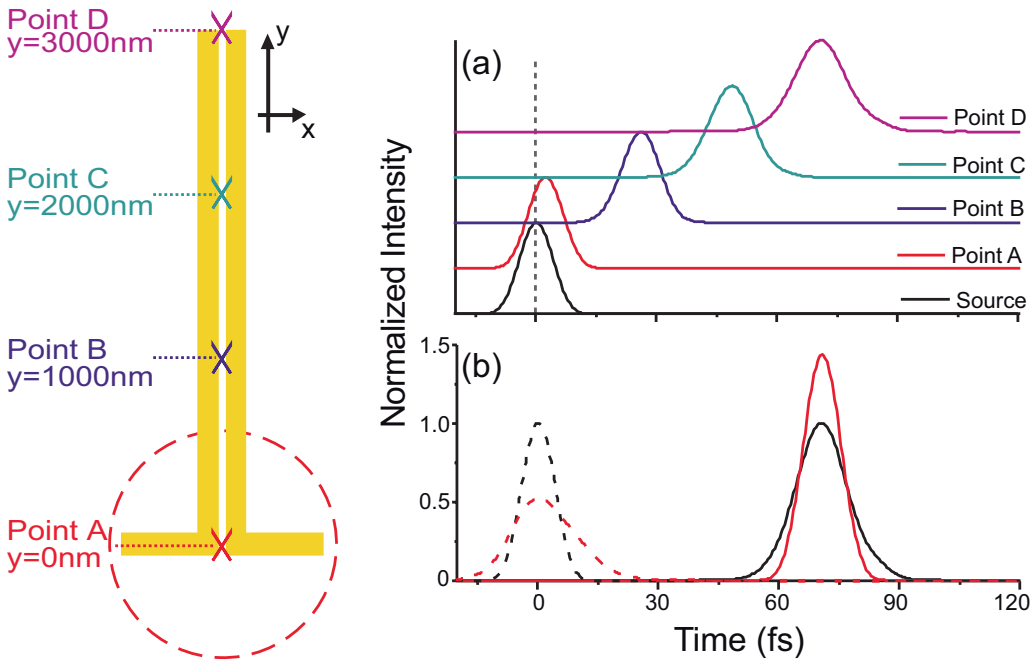

Figure 3.11: Near-field pulse compression in a wave guide. Left panel: sketch of the transmission line and the observation points. Two long gold nanowires with $20 \times 20\,\mathrm{nm}^2$ cross section and 10 nm separation are attached to two arms of a $20 \times 20 \times 190\,\mathrm{nm}^3$ antenna. The red dashed circle denotes the excitation focus. Observation: point A is located at the feed gap center, while points B–D are shifted in the positive y direction from point A by 1000 nm, 2000 nm, and 3000 nm, respectively. Right panel: (a) normalized temporal intensity profiles recorded at points A (red), B (blue), C (green), and D (pink) obtained with the default source (black); (b) normalized original (black line) and shaped (red line) temporal intensity profiles of the source (dashed) and the response at point D (solid). Taken from Huang *et al.* [100]. Copyright (2009) by The American Physical Society.

method relys on a multiple scattering approach realized in the multiple elastic scattering of multipole expansions (MESME) code [101, 102]. The code was introduced by García de Abajo and is based on the formalism of cluster models for the simulation of electron diffraction in solids [103, 104]. It is a fast, accurate, and general technique, which can be used to obtain the linear optical response of clusters of distributed scatterers of arbitrary shapes and dimensions in the frequency domain. Additional features of MESME are the calculation of radiation cross sections and electron energy losses. However, in the scope of this thesis it is used to calculate the optical response of a T-chain nanostructure excited with tight focused optical far-field illumination (Chapter 4).

The following discussion is based on the description of García de Abajo [101, 102] and Tutsch [105]. Here, the frequency dependence is omitted for the sake of simplicity and the description is reduced to the electric field whereas the magnetic field can be calculated in analogy. First, scalar functions are introduced to describe the electric field (Section 3.3.1). These scalar functions are then used to calculate the direct scattered field of a single object (Section 3.3.2). The remaining contribution to the scattered

field is calculated via the self-consistent induced field coming from different objects in the cluster (Section 3.3.3). Finally, the implementation as incorporated in the code is presented (Section 3.3.4).

3.3.1 Expansion of External Field into Multipoles

The electromagnetic field in a homogeneous region of space, which is free of charges and currents, can be expressed in terms of multipole expansions with respect to a given origin r_α. Since the electric field is transversal in that region it can be written as

$$\vec{E} = \vec{L}_\alpha \psi_\alpha^M - \frac{\mathrm{i}}{k} \nabla \times \vec{L}_\alpha \psi_\alpha^E, \tag{3.26}$$

where k is the amplitude of the wavevector and ψ_α^M and ψ_α^E are magnetic and electric scalar functions depending on the three spatial coordinates, respectively. $\vec{L}_\alpha = -\mathrm{i}(\vec{r} - \vec{r}_\alpha) \times \nabla$ is the orbital angular momentum and is defined with respect to the position $\vec{r}_\alpha$. Assuming that the frequency dependent dielectric function ε_j and magnetic permeability μ_j describe the region under consideration the scalar functions are obtained from $\vec{E}$ by

$$\psi_\alpha^M = \frac{1}{L_\alpha^2} \vec{L}_\alpha \cdot \vec{E}, \tag{3.27}$$

and

$$\psi_\alpha^E = \frac{\mathrm{i}}{k\varepsilon_j \mu_j} \frac{1}{L_\alpha^2} \left(\vec{L}_\alpha \times \nabla \right) \cdot \vec{E}. \tag{3.28}$$

The scalar functions can be expanded in terms of spherical harmonics Y_L such that

$$\psi_\alpha^{\mathrm{ext}}(\vec{r}) = \sum_L j_L \left[k \left(\vec{r} - \vec{r}_\alpha \right) \right] \psi_{\alpha,L}^{\mathrm{ext}}, \tag{3.29}$$

where $L = (l, m)$ defines the momentum orders. The spherical harmonics Y_L are contained in $j_L(\vec{u}) = \mathrm{i}^l j_l(|\vec{u}|) Y_L(\vec{u})$ and j_l are spherical Bessel functions. Equation (3.29) reflects the advantage of using scalar functions for the calculation since they can be expanded into multipoles. Hence, MESME evaluates all calculations with these scalar functions and recovers the electric field in the end by using Eq. (3.26).

3.3.2 Single Object Scattering

After defining the electric field in terms of a multipole expansion, we now consider a single object α serving as a scatterer. The external field $\vec{E}^{\mathrm{ext}}$ induces charges and currents in the object depending on the material and the shape of the object. Consequently, an electric field $\vec{E}^{\mathrm{ind}}$ is induced and as already mentioned in Section 3.1.2, the total electric field is a superposition of the external and the induced electric field given by

$$\vec{E} = \vec{E}^{\mathrm{ext}} + \vec{E}^{\mathrm{ind}}. \tag{3.30}$$

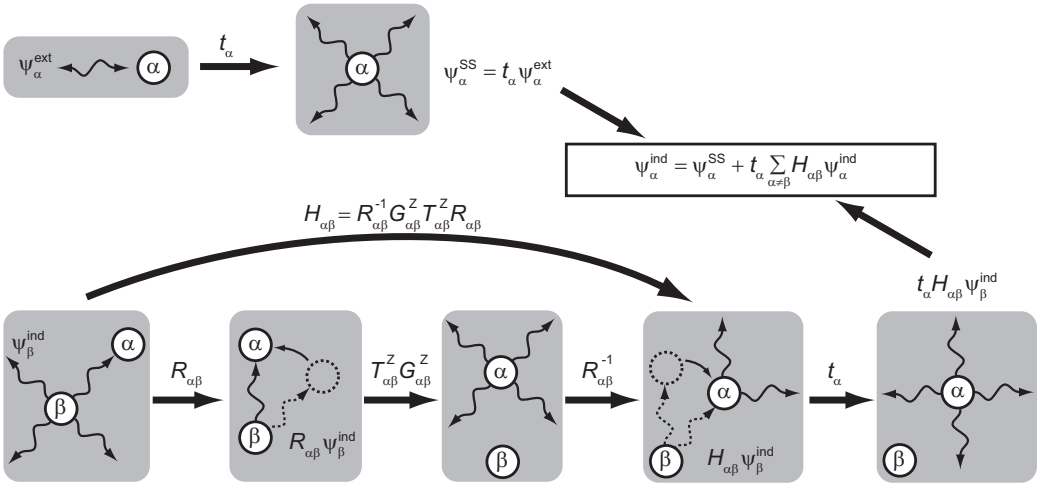

Figure 3.12: Schematic representation of MESME. The electromagnetic field is expressed as scalar functions ψ_α, made up of multipoles relative to the position $\vec{r}_\alpha$ of scatterer α [Eq. (3.29)]. Upper panel: The external field acting on scatterer α is a superposition of spherical plane waves [Eq. (3.31)]. The scattering process is expressed in terms of a scattering matrix t_α. Additional scattered fields coming from each other scatterer $\beta \neq \alpha$ are calculated in four steps (lower panel): First, the system is rotated with the rotation matrix $R_{\alpha\beta}$ to match the bond vector $\vec{r}_\alpha - \vec{r}_\beta$ with the positive x axis. Second, the outgoing waves centered at $\vec{r}_\beta$ are translated along the z axis to center them at $\vec{r}_\alpha$ using the operator $G^z_{\alpha\beta}$. Third, to overcome the invariance of multipoles under translations an additional operator $T^z_{\alpha\beta}$ is needed. Fourth, the result is then rotated back using inverse rotation matrix $R^{-1}_{\alpha\beta}$. The combination of these four operations is expressed as $H_{\alpha\beta}$ [Eq. (3.32)]. Finally, all scattered fields are added up to define the self-consistent field induced by object α as ψ^{ind}_α [Eq. (3.34)]. Modified from García de Abajo [102].

Assuming a field amplitude that is sufficiently small, nonlinear effects can be omitted and the linear-response approximation holds. Hence, the induced electric field is proportional to the external field and the corresponding scalar functions can be written as

$$\psi^{\text{ss}}_{\alpha,L} = \sum_{L'} t_{\alpha,L,L'} \psi^{\text{ext}}_{\alpha,L'}, \tag{3.31}$$

where $t_{\alpha,L,L'}$ is the so-called scattering matrix and the superscript ss indicates that this is the result of scattering on a single object. A schematic of the mathematical description is shown in the upper part of Fig. 3.12. Here, the external electric field acting on the scatterer α is represented by a double-arrow line and the induced electric field, which is calculated using the scattering matrix $t_\alpha \equiv t_{\alpha,L,L'}$, is represented as outgoing arrows.

The scattering matrix t_α is composed of Hankel functions that describe outgoing spherical waves. It depends on the size, shape and material properties of the scattering object α and can be obtained for every position in space by solving Maxwell's equations under certain boundary conditions [102]. Due to the high symmetry, analytic terms of t_α can be found for spheres, recovering expressions that are similar to Mie's scattering theory. In this case the scalar functions can be calculated at any point in space, explicitly

within the sphere. However, for arbitrary shaped scattering objects the calculation of the scattering matrix can be time consuming and scalar functions can only be calculated outside a sphere that contains the scattering object completely.

3.3.3 Multiple Scattering

So far, only scattering of a single scatterer α was discussed. Here, we want to consider scattering from another object, e.g., β. The scalar function $\psi_\beta^{\mathrm{ind}}$ then describes the electric field that was scattered by β. Since the scatterer α is still in the vicinity, the scattered electric field described by $\psi_\beta^{\mathrm{ind}}$ will induce charges and currents in α that cause another scattering process (first schematic, lower part of Fig. 3.12). This scattering process is calculated in four steps:

1. The difference vector $\vec{d}_{\alpha\beta} = \vec{r}_\alpha - \vec{r}_\beta$ is rotated using the rotation matrix $R_{\alpha\beta}$ to match the quantization axis, here the z axis.

2. The rotated scalar functions $R_{\alpha\beta}\psi_\beta^{\mathrm{ind}}$ that describe the spherical planar waves have to be translated from $\vec{r}_\beta$ to $\vec{r}_\alpha$. This is done by means of the propagation operator $G_{\alpha\beta}^z$ that propagates the spherical plane waves along the distance $|\vec{d}_{\alpha\beta}|$.

3. Due to the fact that the scalar functions are not invariant under translations of the origin coordinates, an additional transformation matrix $T_{\alpha\beta}^z$ has to be used to translate the origin of the multipoles accordingly.

4. The z axis has to be rotated back onto $\vec{d}_{\alpha\beta}$ using the inverse rotation matrix $R_{\alpha\beta}^{-1}$.

The lower part of Fig. 3.12 shows a schematic of the four steps and the combination of all steps yields the mathematical description:

$$H_{\alpha\beta} = R_{\alpha\beta}^{-1} T_{\alpha\beta}^z G_{\alpha\beta}^z R_{\alpha\beta}. \tag{3.32}$$

Going one step further, we introduce a cluster of different objects α at positions $\vec{r}_\alpha$. The resulting scalar function is then found by the superposition of each individual scattered electric field:

$$\psi^{\mathrm{ind}}(\vec{r}) = \sum_\alpha \psi_\alpha^{\mathrm{ind}}(\vec{r}). \tag{3.33}$$

Here, the individual scalar functions $\psi_\alpha^{\mathrm{ind}}(\vec{r})$ are calculated by

$$\tilde{\psi}_\alpha^{\mathrm{ind}} = \tilde{\psi}_\alpha^{\mathrm{ss}} + t_\alpha \sum_{\beta\neq\alpha} H_{\alpha\beta}\tilde{\psi}_\beta^{\mathrm{ind}}, \tag{3.34}$$

where $\tilde{\psi}_\alpha^{\mathrm{ind}}$ is the vector formed by the coefficients $\psi_{\alpha,L}^{\mathrm{ind}}$ of the multipole expansion of $\psi_\alpha^{\mathrm{ind}}$. $\tilde{\psi}_\alpha^{\mathrm{ss}}$ describes the scattered field of the single-scattering approach [Eq. (3.31)], i.e., the scattered field directly coming from α. The second term denotes the self-consistently scattered field coming from every other object $\beta \neq \alpha$ to α and the subsequent scattering of this field.

3.3.4 Iterative Implementation

To obtain the electric field at a certain point $\vec{r}$, the set of equations of Eq. (3.34) have to be solved for each object α first. Herein, the operators involved in $H_{\alpha\beta}$ [Eq. (3.32)] are represented by square matrices of dimension $[(l_{\max}+1)]^2$, where $l_{\max}$ is the maximum order of angular momentum that is considered in the calculation (convergence is achieved for $l_{\max}=12$ in most cases).

Since direct inversion of Eq. (3.34) needs enormous calculation effort for large clusters, an iterative method is advantageous. This is done by starting the calculation with a single scattered wave $\tilde{\psi}_\alpha^{\mathrm{ind},1}=\tilde{\psi}_\alpha^{\mathrm{ss}}$ and solving Eq. (3.34) iteratively:

$$\tilde{\psi}_\alpha^{\mathrm{ind},n}=\tilde{\psi}_\alpha^{\mathrm{ss}}+t_\alpha\sum_{\beta\neq\alpha}H_{\alpha\beta}\tilde{\psi}_\beta^{\mathrm{ind},n-1}. \tag{3.35}$$

If the scalar function converges such that $\tilde{\psi}_\alpha^{\mathrm{ind}}=\tilde{\psi}_\alpha^{\mathrm{ind},n}$ it is a convenient and fast procedure. However, for a cluster of strong scattering objects positioned in close vicinity the iterative method can lead to divergence and convergence is reinforced using the highly-convergent Lanczos method. After solving the set of equations of Eq. (3.34) for each object the total scalar function is calculated using Eq. (3.33), where $\psi_\alpha^{\mathrm{ind}}(\vec{r})$ is found using the multipole expansion of Eq. (3.29).

The complete calculation is done using the stand-alone code MESME and for the iterative method the computation time is proportional to

$$T_{\mathrm{iter}}\propto N^2\left(l_{\max}+1\right)^3, \tag{3.36}$$

where N is the number of particles in the cluster.

Before starting MESME the cluster has to be defined via the location, the shape and the material properties, i.e., the dielectric function and the magnetic permeability, of each scatterer as well as the dielectric function and the magnetic permeability of the cluster's host material. Additionally, the calculation parameter $l_{\max}$, i.e., the maximum order of angular momentum and the maximum order n of iterations have to be given.

As a result, the complex optical response function [Eq. (3.19)] is obtained as a function of spatial coordinates:

$$\vec{A}(\vec{r},\omega)=\begin{pmatrix}A_x(\vec{r},\omega)\\A_y(\vec{r},\omega)\\A_z(\vec{r},\omega)\end{pmatrix}. \tag{3.37}$$

4 Analytic Control of Near Fields

In this chapter, general mathematical formulas are derived for the analytic control of near fields in nanostructures using polarization pulse shaping. Exemplarily, the derived rules are used for the control of propagating fields in a branching chain of nanospheres. The main idea of the presented approach (Section 4.2) is to disentangle the two mechanisms for near-field control of spatial (Section 4.3) and temporal (Section 4.4) control that were introduced in the last chapter. The analytically obtained pulse shapes are compared to pulse shapes that are found in an adaptive fashion. The derived formulas also allow for analytic space–time control (Section 4.6) enabling a new type of near-field supported spectroscopy, in which pump and probe interactions are separated both spatially and temporally.

The work that is presented in this chapter resulted from a collaboration of our work group with Javier García de Abajo[1] and Walter Pfeiffer[2]. Javier García de Abajo provided his expertise of the calculation of near fields in terms of the used Maxwell equation solver. Walter Pfeiffer was involved in the discussion and interpretation of the obtained results.

4.1 Introduction

The emerging field of ultrafast nanooptics is a combination of femtosecond laser technology and nano-optical methods [106]. This offers unique perspectives for the confinement of light on a subwavelength spatial scale [54, 55] as well as an ultrafast time scale [11, 14].

On the one hand application of these confinements yields miniaturized photonic circuits [107, 108], in which one would need an efficient coupling of the far field to the near field [54], which would then propagate and be processed by logical elements. In this context, especially propagating optical near fields [74, 97, 109–112] are interesting. A route to logical processing elements are nanostructures excited with ultrashort shaped laser pulses. Plasmonic nanoantennas can be used for the efficient coupling of the laser pulses to the nanoplasmonic circuits [84, 108, 113]. Waveguides of nanoparticles [109, 114], single stripes [74, 107, 112, 115], and nano transmission lines [100, 108] can be used for plasmon propagation.

On the other hand, the spatial–temporal confinement exactly meets the demands of spectroscopic applications—as it is the scope of this thesis. First spectroscopic applications using these two confinements have been demonstrated very recently by Brinks *et al.* [9]. In this experiment a nanoantenna was used to enhance a single molecule signal. Since single molecule investigation was achieved there by low emitter density, it was not

[1]Instituto de Óptica, CSIC, Serrano 121, 28006 Madrid, Spain
[2]Fakultät für Physik, Universität Bielefeld, Universitätsstr. 25, 33615 Bielefeld, Germany

the strong spatial confinement that was used but the field enhancement induced by the nanoantenna (Section 3.1.2). In a different—more general—scheme, nanoscopic ultrafast space–time-resolved spectroscopy could be performed by providing optical excitations in which pump and probe interactions are separated both spatially and temporally [11]. To realize such excitation schemes, pulse shaping in combination with proper nanostructures turned out to be the perfect tool. The excitation scheme is then provided via the time-dependent near-field distribution in the vicinity of the nanostructure. In a pioneering work Stockman *et al.* demonstrated theoretically that coherent control of nanosystems is possible with chirped laser pulses [47]. In the following, many-parameter adaptive control of optical near-fields using polarization-shaped laser pulses was reported [11]. Thus, it is possible to manipulate electric fields spatially and temporally on a nanometer and femtosecond scale [11, 12, 47, 48, 116, 117]. Experimental results to tailor the optical near-field using polarization-shaped laser pulses have been demonstrated by Aeschliman *et al.* [13], and coherent pulse sequences for excitation control were employed by several groups [118, 119]. Recently, simultaneous control over spatial and temporal field properties was achieved experimentally [14]. In all these examples the optimal pulse shapes that have to be determined in a multiparameter space were found in a non-deterministic fashion. However, in a pump–probe experiment each polarization shaped pulse that would provide a certain temporal separation of pump and probe pulse would have to be found in a extra step. Therefore, it is essential for broad application of ultrafast space–time-resolved spectroscopy to develop a basic understanding of the control mechanisms and devise predefined rules to control local excitations. Hence, the optimal pulse shapes that provide the required near-field distribution have to be found in an analytic fashion, which enables a straightforward experimental procedure and simplifies the design of appropriate nanostructures.

In the following, exactly these aspects are addressed and general analytic solutions to near-field control on the example of plasmon propagation in a branching waveguide nanostructure are presented. Using the gained insight into control mechanisms, a pump–probe scheme enabling spectroscopy on the nanoscale with a femtosecond resolution is presented. In the future, these advances will enable sophisticated nonlinear spectroscopy involving multipulse sequences confined on the nanoscale provided by near fields.

4.2 Methods

4.2.1 Basic Idea

As explained in Section 3.2 two mechanisms are responsible for optical near-field control. The first mechanism is a local interference of near-field modes excited by two externally applied laser pulse polarization components (Section 3.2.1). Each far-field polarization component induces a local near-field mode that will interfere with the second local near-field mode excited by the other far-field component. Controlling constructive and destructive interference can then be employed to enhance or suppress the near field, respectively, at certain positions in the vicinity of the nanostructure. The second control mechanism is a temporal manipulation of the local near-fields to compress the electromagnetic energy in time at a desired spatial location, thereby enhancing nonlinear

signals (Section 3.2.2).

In general, ultrashort laser pulses provide a large space of control parameters for guiding the plasmonic energy and focusing it on the nano–femto scale. In this chapter, the full shaping capabilities are used, where amplitude, phase, ellipticity, and orientation angle may arbitrarily be manipulated at each frequency of the laser pulses [31]. The idea is to use an analytic approach that is based on the separation of the two control mechanisms described above. Derived spectral phases and amplitudes of each laser pulse polarization component will then be compared to adaptive optimizations. Thus, the control objective is reached in a deterministic and reproducible approach that can be understood easily.

As an example, a nanostructure consisting of a branching chain of nanospheres excited with shaped laser pulses under the conditions of tight focusing is considered (Fig. 4.1). The choice of this nanostructure is motivated by the experimentally observed propagation of plasmonic excitations along such chains [97] and the recent demonstration of coherent propagation control in a T-shaped nanoparticle arrangement [114, 120]. It consists of a long chain of 17 Ag spheres along the x axis, and a short arm of seven Ag spheres along the y axis. The y arm is coupled to the long chain in the middle between the tenth and the eleventh sphere. The spheres have a diameter of 50 nm and are separated by a 10 nm gap, which corresponds to a 60 nm unit cell. The nanostructure is excited at the beginning of the long chain with a tightly-focused shaped laser pulse (focal Gaussian beam diameter of about 200 nm intensity FWHM) propagating along the z axis perpendicular to the chain with the beam center located at the center of the first sphere. Two excitation polarizations are chosen: polarization 1 along the x axis and polarization 2 along the y axis. After coupling to the nanostructure, the pulse energy is guided by plasmons away from the focus to remote spatial positions on the two branches, e.g., $\vec{r}_1$ and $\vec{r}_2$. The inset of Fig. 4.1 shows the total scattering cross sections of this nanostructure excited by plane waves with polarization components 1 and 2 (black solid and red dashed curves, respectively). Clearly, two resonances are observed: the resonance of the long chain along the x direction at $\omega \sim 4.3\,\mathrm{rad/fs}$ and the resonance of the short chain along the y direction at $\omega \sim 5.4\,\mathrm{rad/fs}$ which are mostly excited by polarizations 1 and 2, respectively.

In a similar structure, however, with a different symmetry of the overall arrangement of the nanoparticles, Sukharev *et al.* theoretically showed the control of propagation direction after a junction by scanning the ellipticity of the excitation light using a two-dimensional parameter space [114, 120]. Here, their work is taken as a motivation extending it in several respects: first, a multidimensional parameter space is introduced using complete vector-shaped laser pulses [31]; second, the excitation field focusing conditions are taken into account; and third and most importantly, analytic control both of the linear and the nonlinear flux in nanosystems is obtained. Using this systematic approach, the interplay between the two control mechanisms described above is decoupled by first guiding the linear flux to the desired target position with shaping of the amplitudes of both polarization components as well as the phase difference between the two components. For linear flux the relative spectral phase is irrelevant within the pulse, since different frequency components do not interfere. For nonlinear flux, however, the different frequency components do interfere and the remaining relative spectral phase

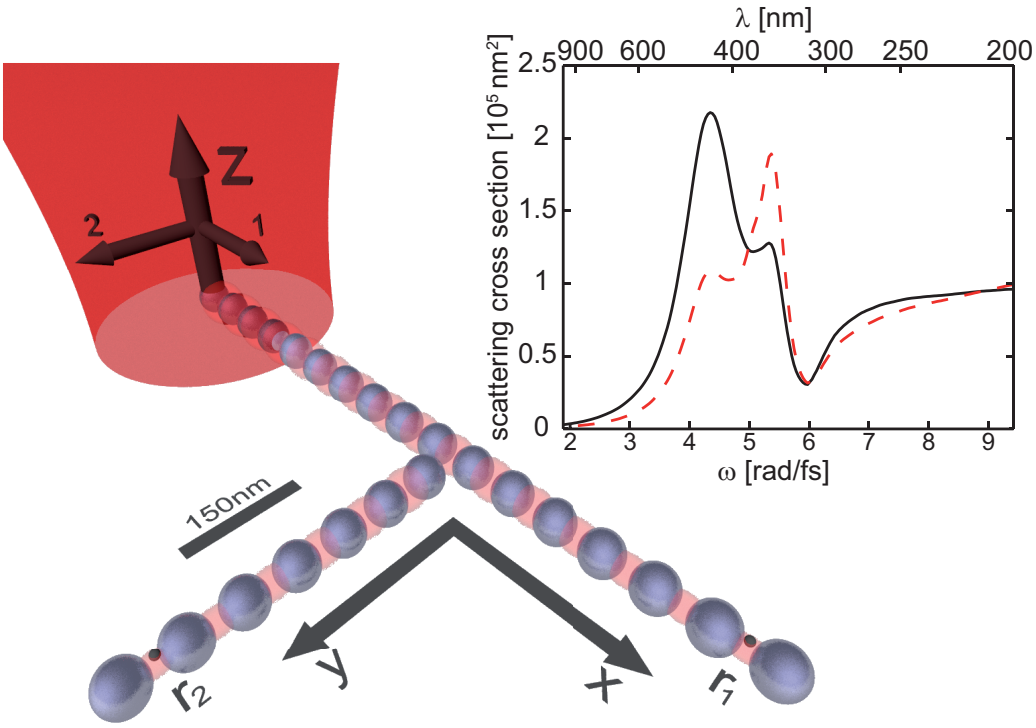

Figure 4.1: Nanoplasmonic branching waveguide consisting of 50 nm diameter spheres. The target points for coherent control [$\vec{r}_1 = (930, 0, 10)$ nm and $\vec{r}_2 = (570, 380, 10)$ nm] are chosen between the last two spheres of each arm and 10 nm above the $z = 0$ symmetry plane. The structure is excited with a tightly-focused Gaussian beam (indicated in red) at the beginning of the chain using the two polarizations 1 and 2 along the x and y direction, respectively (indicated with 1 and 2 in the focus). Inset: total scattering cross sections obtained for plane wave illumination with polarization 1 (black solid) and 2 (red dashed). Taken from Tuchscherer *et al.* [49]. Copyright (2009) by The Optical Society.

is used to enhance the nonlinear flux by compressing the local near-field at the desired target position.

4.2.2 Field Calculation

The complex-valued linear optical response function $\vec{A}^{(i)}(\vec{r}, \omega)$ for polarization $i = 1, 2$ of the nanostructure in the frequency domain was calculated as a function of the spatial coordinate $\vec{r}$ by self-consistently solving Maxwell's equations. The MESME code introduced in Section 3.3 was used here. Since the nanostructure is composed of silver spheres and the scattering matrix of spheres can be calculated analytically, accurate results were obtained and opposed to Finite-Different Time Domain methods [121] no staircasing of round nanostructures was needed.

The measured bulk dielectric function of silver [78], including dispersion and damping effects, was incorporated in the calculations of the response. Simulations were performed for 128 equally-spaced frequencies, corresponding to 128 pixels of a common laser pulse shaper. The spectral range was chosen such that it included the plasmonic resonance

of the long chain of the structure [i.e., 3.9–5.3 rad/fs (corresponding to 483–355 nm)]. The Gaussian laser pulse spectrum was centered in the middle of the calculated spectral range at $\omega_0 = 4.6\,\mathrm{rad/fs}$ (409 nm) with a FWHM of 0.35 rad/fs corresponding to ∼10 fs pulse duration. The field distribution in a tight focus was represented as a superposition of plane waves. For realistic simulations a Gaussian focus was used that is achieved by a high numerical aperture. The focal spot size (∼200 nm) was close to the diffraction limit, obtained by a coherent superposition of 1245 partial waves.

It is important to point out that plasmon excitation and propagation along the nanostructure chain is already implicitly included in $\vec{A}^{(i)}(\vec{r},\omega)$, as can be verified by inverse Fourier transformation to the time domain. As introduced in Section 3.1.3 the two excited modes propagating through the nanostructure can be understood as excitation of a longitudinal and a transverse mode.

In order to exemplify coherent propagation control, two spatial positions, $\vec{r}_1$ and $\vec{r}_2$, were considered as marked in Fig. 4.1, which were reached after plasmon propagation along the x arm or y arm, of the structure, respectively. The goal would then be to control linear and nonlinear signals at these two positions, especially contrast and pulse compression, even though the illumination region is spatially separated. In fact, this corresponds to control over direction ("spatial focusing", Section 4.3) and time ("temporal focusing", Section 4.4).

As already introduced in the discussion of near-field control mechanisms (Section 3.2), the incident laser pulse is expressed in frequency domain by two orthogonal polarization components: $E_1^{\mathrm{in}}(\omega)$, oriented along the x axis, and $E_2^{\mathrm{in}}(\omega)$, oriented along the y axis, consisting of spectral amplitudes $\sqrt{I_i(\omega)}$ and phases $\varphi_i(\omega)$, which could all be varied independently. Hence, the total optical near-field $\vec{E}(\vec{r},\omega)$ was obtained by calculating the near field for each far-field polarization separately and taking the linear superposition [same as Eq. (3.24)]

$$\vec{E}(\vec{r},\omega) = \left\{ \begin{pmatrix} A_x^{(1)}(\vec{r},\omega) \\ A_y^{(1)}(\vec{r},\omega) \\ A_z^{(1)}(\vec{r},\omega) \end{pmatrix} \sqrt{I_1(\omega)} + \begin{pmatrix} A_x^{(2)}(\vec{r},\omega) \\ A_y^{(2)}(\vec{r},\omega) \\ A_z^{(2)}(\vec{r},\omega) \end{pmatrix} \sqrt{I_2(\omega)}\, \mathrm{e}^{-\mathrm{i}\Phi(\omega)} \right\} \mathrm{e}^{-\mathrm{i}\varphi_1(\omega)} . \quad (4.1)$$

Here, the phases of the two far-field polarizations are adjusted to control the phases of the near-field modes. The constructive or destructive interference of the optical near-fields are controlled by adjusting the phase difference $\Phi(\omega)$ [Eq. (3.25)] and the spectral amplitudes of the incident laser, whereas the remaining offset phase $\varphi_1(\omega)$ [Eq. (4.1)] is used to adjust the temporal evolution of the optical near-fields.

4.2.3 Definition of Signals

Using MESME and Eq. (4.1), the local optical near-field $\vec{E}(\vec{r},\omega)$ is calculated at any position $\vec{r}$ induced by a vector-field-shaped laser pulse (Section 2.3.4). This quantity is then used to define different signals in analogy with far-field optics: local spectral intensity is defined as

$$S(\vec{r},\omega) = \sum_{\alpha=x,y,z} b_\alpha \left|E_\alpha(\vec{r},\omega)\right|^2 = \sum_{\alpha=x,y,z} b_\alpha \left|\mathcal{F}\left\{E_\alpha(\vec{r},t)\right\}\right|^2 , \quad (4.2)$$

where $\mathcal{F}$ indicates Fourier transformation and the parameters b_α describe which local polarization components are included in the signals. Setting $b_x = 1$ and $b_y = b_z = 0$, for example, describes field-matter interactions with transition dipoles oriented along the x axis. In the following calculations, $b_x = b_y = b_z = 1$ is used, corresponding to an isotropic distribution of dipole moments, unless mentioned otherwise. Local linear flux is defined using Parseval's theorem:

$$F_{\mathrm{lin}}(\vec{r}) = \int_{-\infty}^{\infty} \sum_{\alpha=x,y,z} b_\alpha E_\alpha^2(\vec{r},t)\mathrm{d}t = \frac{1}{2\pi} \int_{\omega_{\mathrm{min}}}^{\omega_{\mathrm{max}}} S(\vec{r},\omega)\mathrm{d}\omega. \tag{4.3}$$

Assuming a Gaussian laser spectrum with a center frequency ω_0 frequencies where the intensity is sufficiently small are neglected. Hence, integration is carried out over an appropriate interval $\omega_{min} = \omega_0 - \Delta\omega$ to $\omega_{max} = \omega_0 + \Delta\omega$, where $\Delta\omega$ is a suitable width, e.g., $\Delta\omega = 0.7\,\mathrm{rad/fs}$.

Since a finite and discrete grid of frequencies (i.e. pulse-shaper pixels) separated by $\delta\omega$ is considered, the frequency integral in Eq. (4.3) can be replaced by a sum over all frequencies of the local spectrum defined in Eq. (4.2):

$$F_{\mathrm{lin}}(\vec{r}) = \frac{\delta\omega}{2\pi} \sum_{\omega=\omega_{\mathrm{min}}}^{\omega_{\mathrm{max}}} \sum_{\alpha=x,y,z} b_\alpha E_\alpha(\vec{r},\omega) E_\alpha^*(\vec{r},\omega), \tag{4.4}$$

where the star denotes complex conjugation. In the following derivations $\delta\omega/2\pi$ is omitted for simplicity as the same grid is employed for all comparisons. By inserting the definition of the optical near-field of Eq. (4.1) into Eq. (4.2), the local spectrum as a function of external laser intensities $I_i(\omega)$ and phases $\varphi_i(\omega)$ is obtained:

$$\begin{aligned} S(\vec{r},\omega) = I_1(\omega) \sum_{\alpha=x,y,z} b_\alpha |A_\alpha^{(1)}(\vec{r},\omega)|^2 + I_2(\omega) \sum_{\alpha=x,y,z} b_\alpha |A_\alpha^{(2)}(\vec{r},\omega)|^2 \\ + 2\sqrt{I_1(\omega) I_2(\omega)}\, \mathrm{Re}\left\{ A_{\mathrm{mix}}(\vec{r},\omega)\, \mathrm{e}^{\mathrm{i}\Phi(\omega)} \right\}, \end{aligned} \tag{4.5}$$

with

$$A_{\mathrm{mix}}(\vec{r},\omega) = \sum_{\alpha=x,y,z} b_\alpha A_\alpha^{(1)}(\vec{r},\omega) A_\alpha^{(2)*}(\vec{r},\omega) = |A_{\mathrm{mix}}(\vec{r},\omega)|\, \mathrm{e}^{\mathrm{i}\theta_{\mathrm{mix}}(\vec{r},\omega)}, \tag{4.6}$$

where the phase difference $\Phi(\omega)$ is defined in Eq. (3.25) and Re denotes the real part. $A_{\mathrm{mix}}(\vec{r},\omega)$ is the complex scalar product with amplitude $|A_{\mathrm{mix}}(\vec{r},\omega)|$ and phase $\theta_{\mathrm{mix}}(\vec{r},\omega)$ describing the mixing of the two near-field modes $\vec{A}^{(1)}(\vec{r},\omega)$ and $\vec{A}^{(2)}(\vec{r},\omega)$, which can be calculated independently of the external field once the MESME calculation is done.

Analogously, local nonlinear (second-order) flux is defined as

$$F_{\mathrm{nl}}(\vec{r}) = \int_{-\infty}^{\infty} \left[\sum_{\alpha=x,y,z} b_\alpha E_\alpha^2(\vec{r},t) \right]^2 dt. \tag{4.7}$$

4.2.4 Adaptive Optimizations

While the analytic control approach is the main topic of this chapter as developed in the following sections, adaptive control with an evolutionary algorithm (Section 2.5) was carried out for comparison. For each shaping degree of freedom, i.e., $\varphi_1(\omega)$, $\varphi_2(\omega)$, $\sqrt{I_1(\omega)}$, and $\sqrt{I_2(\omega)}$, 32 genes encoded the information to interpolate (spline interpolation) 128 parameters (pulse shaper pixels). The algorithm ran until convergence, which was usually achieved within 50 to 500 generations depending on the size of the search space. The population was chosen to contain 40 individuals, where 50% of the best individuals of the last generation were used to produce the new 40 individuals for the next generation. 70% of these best individuals were gained from crossover, 20% from mutation and 10% from cloning. For the optimization of linear and nonlinear flux, $F_{\mathrm{lin}}(\vec{r})$ and $F_{\mathrm{nl}}(\vec{r})$ were chosen as input for the fitness function, respectively. Contrast control was achieved by the flux differences between different spatial positions as explained below. For a better identification of the lines in the figures, where the results of adaptive optimizations are compared to the analytic solutions, only every second data point of the adaptively optimized phases or amplitudes is plotted in the following amplitude and phase plots.

4.3 Spatial Focusing of Propagating Near Fields

4.3.1 Optimization of Linear Flux at One Position

The first control objective considered here is the maximization or minimization of local linear flux $F_{\mathrm{lin}}(\vec{r})$ at one specified location. In the examples below, this location will be chosen at either $\vec{r}_1$ or $\vec{r}_2$ as marked in Fig. 4.1. Equation (4.5) provides insight into the near-field control mechanisms. To optimize linear flux, the two laser phases $\varphi_1(\omega)$ and $\varphi_2(\omega)$ can be adjusted independently from the amplitudes $\sqrt{I_1(\omega)}$ and $\sqrt{I_2(\omega)}$ either to maximize or to minimize the last term in Eq. (4.5).

The amplitude of the mixed scalar product, $|A_{\mathrm{mix}}(\vec{r},\omega)|$, is a measure of how much the near-field modes project onto each other and determines the controllability at this point. For example, if the two near-field modes do not project onto each other, i.e., if the modes are perpendicular, they do not interfere and it is not possible to control the local linear flux with the laser pulse phases because $A_{\mathrm{mix}}(\vec{r},\omega) = 0$. Maximum controllability is obtained for parallel near-field modes, i.e., having a maximum projection.

The phase of the scalar product, $\theta_{\mathrm{mix}}(\vec{r},\omega)$, determines how the phase difference between the two external laser polarization components, $\Phi(\omega)$, should be chosen in order to make the interference term of Eq. (4.5) positive or negative. Constraints for the constructive $[\Phi_{\mathrm{max}}(\omega)]$ and destructive $[\Phi_{\mathrm{min}}(\omega)]$ interference are

$$\Phi_{\mathrm{max}}(\omega) = -\theta_{\mathrm{mix}}(\vec{r},\omega) \quad \text{and} \tag{4.8}$$

$$\Phi_{\mathrm{min}}(\omega) = -\theta_{\mathrm{mix}}(\vec{r},\omega) - \pi, \tag{4.9}$$

respectively. The dependence of linear flux on the phase difference $\Phi(\omega)$ only is due to the interference of the two near-field modes as the single control mechanism responsible

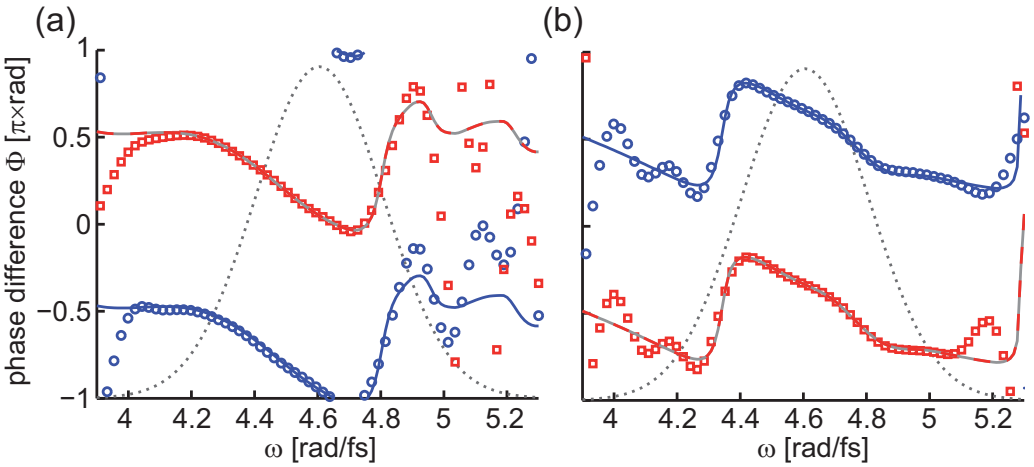

Figure 4.2: The phase differences for analytic maximization (solid blue line) and minimization (dashed red line) of the linear flux $F_{\mathrm{lin}}(\vec{r})$ at positions $\vec{r}_1$ (a) and $\vec{r}_2$ (b) compared to the results obtained by an adaptive optimization for maximization (blue circles) and minimization (red squares). The laser spectrum is indicated by a gray dotted line. Taken from Tuchscherer *et al.* [49]. Copyright (2009) by The Optical Society.

for the linear signal. In other words, the local field is determined by the polarization state of the incident light and $A_{\mathrm{mix}}(\vec{r},\omega)$ is a measure of the controllability that can be achieved by polarization shaping (i.e., adjusting the phases of the two far-field polarization components). Setting, for example, $b_x = 1$ and $b_y = b_z = 0$ one can get a good understanding of this effect, since the phase difference $\theta_{\mathrm{mix}}(\vec{r},\omega) = \theta_x^{(1)}(\vec{r},\omega) - \theta_x^{(2)}(\vec{r},\omega)$ of the two near-field modes induced by the nanostructure is then just compensated exactly, leading to optimal constructive or destructive interference for given amplitudes. Including more than one component, e.g. $b_x = b_y = b_z = 1$, the sum in Eq. (4.6) performs a weighting of the phases of each component by their amplitudes. If the near-field modes are not parallel, some part of the field will still remain even for destructive interference.

The required phase difference for linear flux control is thus available directly from either Eq. (4.8) or Eq. (4.9) and is plotted in Fig. 4.2 for two different examples, namely the location $\vec{r}_1$ [Fig. 4.2a] and $\vec{r}_2$ [Fig. 4.2b] as solid blue lines (maximum flux) and dashed red lines (minimum flux). The plots can be understood as follows: for example, as shown in Fig. 4.2a, linearly polarized light at $\omega \sim 4.65\,\mathrm{rad/fs}$ oriented along the (1,1,0) direction ($\Phi = 0$) minimizes the local flux at $\vec{r}_1$, whereas linearly polarized light oriented along the (-1,1,0) direction ($\Phi = \pi$) maximizes the local flux at $\vec{r}_1$. In contrast right ($\Phi = -\pi/2$) and left ($\Phi = \pi/2$) circularly polarized light at $\omega \sim 4.25\,\mathrm{rad/fs}$ generates the maximum and minimum local flux at $\vec{r}_1$, respectively. The control at other frequencies is achieved similarly using elliptically polarized light.

In order to confirm the analytic solutions, adaptive optimizations of $F_{\mathrm{lin}}(\vec{r})$ were performed using an evolutionary algorithm, and the resulting optimal spectral phases are plotted as blue circles (maximization) and red squares (minimization) in Fig. 4.2. Analytic and adaptive results are in excellent agreement in the region of relevant laser spectral intensity (gray dotted line). The predicted difference of π between the phase differences [see Eqs. (4.8) and (4.9)] can be seen as an offset between the red and blue

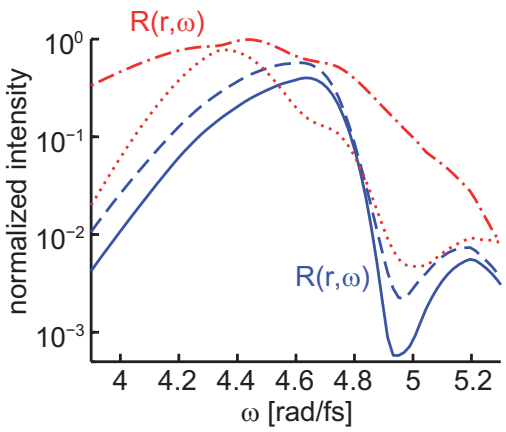

Figure 4.3: The local response intensities $R(\vec{r},\omega)$ plotted logarithmically for the position $\vec{r}_1$ for the maximum (blue dashed) and minimum (blue solid) local linear flux, and for the position $\vec{r}_2$ (red dash-dotted and red dotted lines for the maximum and the minimum local linear flux, respectively). The optimal phase differences for the linear flux as obtained from Eq. (4.8) and (4.9) are shown in Fig. 4.2. Taken from Tuchscherer *et al.* [49]. Copyright (2009) by The Optical Society.

curves, and the shape of the curves reflects the spectral response properties of the nanostructure as contained in the scalar product of Eq. (4.6). Parseval's theorem guarantees that the control can be done separately for each frequency component, as shown above using analytical methods. The adaptive optimization is however performed here for the entire pulse simultaneously, and therefore the agreement with the analytic model is a non-trivial cross validation of the results.

For a better interpretation of the actual near-field responses over a broad spectral range, the local response intensities are defined, i.e., the local spectrum [Eq. (4.5)] divided by the incident Gaussian laser spectrum $I_G(\omega)$:

$$R(\vec{r},\omega) = \frac{S(\vec{r},\omega)}{I_G(\omega)}. \tag{4.10}$$

The local response intensities at the positions $\vec{r}_1$ (blue lines) and $\vec{r}_2$ (red lines) are shown on a logarithmic scale in Fig. 4.3 for the optimal incident laser phase differences from Fig. 4.2. The maximum and minimum local linear flux phase differences were used to generate the maximum and minimum local response intensities, respectively. As can be seen in Fig. 4.3, the control of the near-fields is achieved over the whole spectral range, i.e., the blue dashed line is higher than the blue solid line, and the red dash-dotted line is higher than the red dotted line. In addition, it can be seen that the local response intensity at $\vec{r}_2$ (red) exceeds the local response intensity at $\vec{r}_1$ (blue) over a large part of the spectral range, which is due to better coupling of the two excited modes to the y arm. However, the minimized response at position $\vec{r}_2$ is smaller than the responses at position $\vec{r}_1$ in the region of $\omega \sim 4.7\,\mathrm{rad/fs}$, which will be relevant for the discussion of amplitude shaping.

The linear flux values [Eq. (4.4)] obtained with the excitation pulse phases from Fig. 4.2 are summarized in Table 4.1 in Section 4.3.2 and will be discussed there in comparison with other control objectives.

Now, polarization shaping with additional modulation of the external intensities $I_1(\omega)$ and $I_2(\omega)$ is considered, first without choosing the optimal laser pulse phases $\varphi_1(\omega)$ and $\varphi_2(\omega)$. In that case, the solutions for linear flux control at one spatial position are trivial

as can be inferred from Eq. (4.5). Given that amplitude shaping can only decrease the intensity of light at a particular frequency, the optimal solution for maximum linear flux is full pulse-shaper transmission, i.e., making use of the full available intensity over the complete laser pulse spectrum. Likewise, the solution for minimum local flux is given for zero transmission, i.e., for both $I_i(\omega) = 0$.

However, if complete vector shaping (all phases and amplitudes) is considered, there is also a nontrivial solution for total cancellation of flux at point $\vec{r}$. According to Eqs. (4.5) and (4.6), the destructive interference described above can be made perfect if $\vec{A}^{(1)}(\vec{r},\omega) = \beta(\omega)\vec{A}^{(2)}(\mathbf{r},\omega)$, i.e., if the local responses excited by the two laser pulse polarizations are parallel to each other, with any ratio $\beta(\omega) \in \mathbb{C}$. For such a case, the external laser intensities should be chosen such that their ratio fulfills $I_1(\omega)/I_2(\omega) = |\beta(\omega)|^2$. In that case, selection of the phase difference $\Phi(\omega)$ according to Eq. (4.9) resulting in $\Phi(\omega) = -\arg\{\beta(\omega)\} - \pi$ leads to the desired zero flux due to perfect destructive interference. If $\vec{A}^{(1)}(\vec{r},\omega)$ and $\vec{A}^{(2)}(\vec{r},\omega)$ are not parallel, the same procedure can be used to cancel out just one component $E_\alpha(\vec{r},\omega)$. This will be used in Section 4.6 to create a double pulse sequence, where the first pulse excites only position $\vec{r}_1$ and the second pulse only position $\vec{r}_2$, i.e., space–time control.

4.3.2 Controlling the Direction of Propagation

Using the results from Section 4.3.1, the procedure is now extended to consider the more interesting case of propagation-direction control. The objective will be to steer the plasmon along either the x arm or the y arm of the nanostructure (Fig. 4.1). In contrast to Section 4.3.1 the optimization goal is now determined simultaneously by the local response at two different locations, whereas in Section 4.3.1 both locations were treated independently. A suitable observable that characterizes this goal is the difference of linear local flux at the two spatial points $\vec{r}_1$ and $\vec{r}_2$,

$$f_{\mathrm{lin}}\left[\varphi_1(\omega),\varphi_2(\omega),I_1(\omega),I_2(\omega)\right] = F_{\mathrm{lin}}(\vec{r}_1) - F_{\mathrm{lin}}(\vec{r}_2), \tag{4.11}$$

which can be expressed using Eqs. (4.4) and (4.5) as

$$\begin{aligned} f_{\mathrm{lin}} &= \sum_{\omega=\omega_{\min}}^{\omega_{\max}} \sum_{\alpha=x,y,z} b_\alpha \left|E_\alpha(\vec{r}_1,\omega)\right|^2 - \sum_{\omega=\omega_{\min}}^{\omega_{\max}} \sum_{\alpha=x,y,z} b_\alpha \left|E_\alpha(\vec{r}_2,\omega)\right|^2 \\ &= \sum_{\omega=\omega_{\min}}^{\omega_{\max}} \Big(I_1(\omega)C_1(\omega) + I_2(\omega)C_2(\omega) + \\ &\qquad 2\sqrt{I_1(\omega)I_2(\omega)}\big\{ |A_{\mathrm{mix}}(\vec{r}_1,\omega)| \cos[\theta_{\mathrm{mix}}(\vec{r}_1,\omega) + \Phi(\omega)] - \\ &\qquad |A_{\mathrm{mix}}(\vec{r}_2,\omega)| \cos[\theta_{\mathrm{mix}}(\vec{r}_2,\omega) + \Phi(\omega)]\big\}\Big), \end{aligned} \tag{4.12}$$

where

$$C_i(\omega) = \sum_{\alpha=x,y,z} b_\alpha \left[\left|A_\alpha^{(i)}(\vec{r}_1,\omega)\right|^2 - \left|A_\alpha^{(i)}(\vec{r}_2,\omega)\right|^2 \right], \quad i = 1,2, \tag{4.13}$$

are again functions that are determined completely by the response of the nanostructure and do not depend on the phases and amplitudes of the incident laser pulse. By finding

the extrema of Eq. (4.12), the flux can be guided in the best possible way to either position $\vec{r}_1$ (f_{lin} maximum) or $\vec{r}_2$ (f_{lin} minimum). These extrema will be found by calculating first the correct phases and then the optimal amplitudes.

The optimal phases can be calculated by considering the functional derivative of Eq. (4.12) with respect to the external phase difference,

$$\frac{\delta}{\delta\Phi(\omega)} f_{\mathrm{lin}} = \sum_{\omega=\omega_{\mathrm{min}}}^{\omega_{\mathrm{max}}} g_{\mathrm{lin}}(\omega), \tag{4.14}$$

with

$$g_{\mathrm{lin}}(\omega) = 2\sqrt{I_1(\omega)I_2(\omega)}\Big\{ - |A_{\mathrm{mix}}(\vec{r}_1,\omega)| \sin\left[\theta_{\mathrm{mix}}(\vec{r}_1,\omega) + \Phi(\omega)\right] + |A_{\mathrm{mix}}(\vec{r}_2,\omega)| \sin\left[\theta_{\mathrm{mix}}(\vec{r}_2,\omega) + \Phi(\omega)\right] \Big\}. \tag{4.15}$$

Since we are interested in the global extremum and f_{lin} is a linear sum over the individual frequency components, each frequency can be considered separately. Thus, the extrema of f_{lin} are found for $g_{\mathrm{lin}}(\omega) = 0$. Assuming $I_1(\omega) \neq 0$ and $I_2(\omega) \neq 0$ [if one or both of the intensities are zero in any frequency interval, the phases $\varphi_1(\omega)$ and $\varphi_2(\omega)$ are irrelevant for linear control targets and can be chosen arbitrarily], the optimal spectral phase difference is then

$$\Phi(\omega) = \arctan\left\{ \frac{|A_{\mathrm{mix}}(\vec{r}_2,\omega)| \sin[\theta_{\mathrm{mix}}(\vec{r}_2,\omega)] - |A_{\mathrm{mix}}(\vec{r}_1,\omega)| \sin[\theta_{\mathrm{mix}}(\vec{r}_1,\omega)]}{|A_{\mathrm{mix}}(\vec{r}_1,\omega)| \cos[\theta_{\mathrm{mix}}(\vec{r}_1,\omega)] - |A_{\mathrm{mix}}(\vec{r}_2,\omega)| \cos[\theta_{\mathrm{mix}}(\vec{r}_2,\omega)]} \right\} + k\pi, \tag{4.16}$$

where $k = 0, 1, 2$ is chosen such that $\Phi(\omega) \in [-\pi, \pi]$. This results in two solutions that can be assigned to the global maximum or minimum by evaluation of Eq. (4.12) or by investigating the second derivative. For the special case of a vanishing denominator in Eq. (4.16), the solutions are $\Phi(\omega) = \pi/2$ and $\Phi(\omega) = -\pi/2$, which correspond to left and right circular polarization, respectively.

Just as for the optimization of linear flux at one location (Section 4.3.1), the flux difference of Eq. (4.11) depends only on the phase difference $\Phi(\omega)$ of the external polarization components and the maximum and minimum solutions differ by π. The analytically determined optimal phase difference does not depend on the pulse intensities $I_1(\omega)$ and $I_2(\omega)$. However, as is shown below, shaping the amplitudes additionally results in improved contrast.

The optimal analytic phases for maximization and minimization of the linear flux difference $F_{\mathrm{lin}}(\vec{r}_1) - F_{\mathrm{lin}}(\vec{r}_2)$ for the points $\vec{r}_1$ and $\vec{r}_2$ of the chosen nanostructure are shown in Fig. 4.4 (lines) and are again compared to the results of an adaptive optimization (symbols). For directional control along the x arm toward $\vec{r}_1$ (red) as well as along the y arm toward $\vec{r}_2$ (blue), both approaches agree well, and the phase difference of π between maximization and minimization of the difference signal is also confirmed.

It is noticeable that the general shape depicted in Fig. 4.4 is similar to the shape from the optimization at point $\vec{r}_2$ only [Fig. 4.2b]. In this particular example, the point $\vec{r}_2$ has more influence on the optimal phase because the absolute value of the optimal

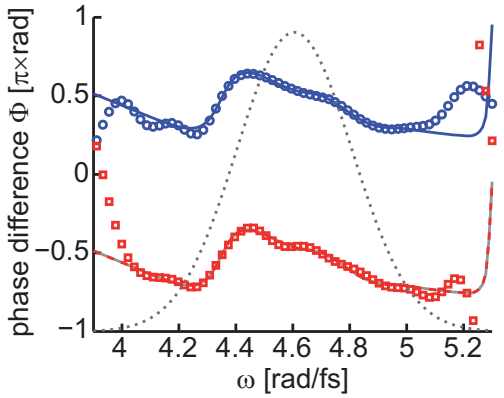

Figure 4.4: Phase difference for analytic maximization (red dashed line) and minimization (blue solid line) of the linear flux difference $F_{\mathrm{lin}}(\vec{r}_1) - F_{\mathrm{lin}}(\vec{r}_2)$ and its comparison to the adaptively optimized phases (red squares and blue circles, respectively). The laser spectrum is indicated by a gray dotted line. Taken from Tuchscherer *et al.* [49]. Copyright (2009) by The Optical Society.

Table 4.1: Analytic and adaptive linear flux control with phase-only shaping of the two polarization components. Flux values are given in the different columns for unshaped pulses corresponding to linear polarization at 45° orientation with respect to the x-y coordinates and for analytic as well as adaptive flux optimization. The different rows indicate maximization and minimization of flux at the locations $\vec{r}_1$, $\vec{r}_2$, and of the flux difference. The first and the second row correspond to control at one position from Section 4.3.1 and the third row describes the contrast control from Section 4.3.2. In all cases, the Gaussian spectrum was employed without amplitude shaping. All values are normalized to the sum of the linear flux $F_{\mathrm{lin}}(\vec{r}_1) + F_{\mathrm{lin}}(\vec{r}_2)$ excited with an unshaped pulse, i.e., the first two values in the first column sum up to unity.

	$\varphi_1 = \varphi_2 = 0$	$\varphi_2 - \varphi_1 = \Phi_{max}$		$\varphi_2 - \varphi_1 = \Phi_{min}$	
		analytic	adaptive	analytic	adaptive
$F_{\mathrm{lin}}(\vec{r}_1)$	0.415	0.599	0.599	0.401	0.401
$F_{\mathrm{lin}}(\vec{r}_2)$	0.585	0.984	0.984	0.410	0.410
$F_{\mathrm{lin}}(\vec{r}_1) - F_{\mathrm{lin}}(\vec{r}_2)$	-0.170	0.088	0.088	-0.483	-0.483

local response intensity $R(\vec{r}, \omega)$ is larger at $\vec{r}_2$ than at $\vec{r}_1$ over most of the spectral region (cf. Fig. 4.3).

Therefore, the maximization (minimization) of the linear flux difference [Eq. (4.11)] results to a large extent from the minimization (maximization) of $F_{\mathrm{lin}}(\vec{r}_2)$ for the chosen nanostructure. If one chose to control flux contrast between such positions where the individual fluxes were of more similar magnitude then the optimal phase would deviate more strongly from the optimizations of both of the separate fluxes. However, with the analytic approach one has the guarantee to nevertheless find the global optimum.

The normalized actual flux values reached in the analytic and adaptive control strategies are summarized in Table 4.1. It is seen that for all cases the flux values reached in adaptive control agree extremely well with the analytic results. This points at the good convergence of the evolutionary algorithm and is another measure for the excellent agreement of the phases, already seen in Figs. 4.2 and 4.4. The difference of the linear fluxes obtained by maximizing at $\vec{r}_1$ and minimizing at $\vec{r}_2$ separately is $(0.599 - 0.410 = 0.189)$, while maximizing the difference directly leads to 0.088. The difference between mini-

mization at $\vec{r}_1$ and maximization at $\vec{r}_2$ is $(0.401 - 0.984 = -0.583)$, and direct contrast control yields -0.483. The optimal solution for the difference signal provides a good compromise between control at the individual points $\vec{r}_1$ and $\vec{r}_2$ for this nanostructure.

It can also be seen in Table 4.1 that for all control objectives the obtained maxima of the observables are higher than for unshaped pulses and the minima are lower, which is of course expected. The positive versus negative values in the bottom row indicate that "switching" of the propagation direction is achieved such that the plasmon propagates predominantly either along the x arm or the y arm of the structure. In the following, additional amplitude shaping will even improve the control performance. It is important to point out that the results—described so far—for the optimal phases are valid without dependence on the particular intensities $I_1(\omega)$ and $I_2(\omega)$ of the two external polarization components. Thus the optimal amplitudes can be found in a separate step.

Amplitude shaping is described by multiplying the Gaussian input pulse amplitude $\sqrt{I_G(\omega)}$, which is the same for both polarizations i, by weighting amplitude coefficients $\gamma_i(\omega)$ varying from 0 to 1:

$$\sqrt{I_i(\omega)} = \gamma_i(\omega)\sqrt{I_G(\omega)}. \tag{4.17}$$

Inserting this definition into Eq. (4.12), we obtain a two-variable quadratic function for each frequency ω:

$$f_{\text{lin}}\left[\gamma_1(\omega), \gamma_2(\omega)\right] = I_G(\omega)\left[C_1(\omega)\gamma_1^2(\omega) + C_2(\omega)\gamma_2^2(\omega) + 2C_{\text{mix}}(\omega)\gamma_1(\omega)\gamma_2(\omega)\right], \tag{4.18}$$

where

$$C_{\text{mix}}(\omega) = |A_{\text{mix}}(\vec{r}_1, \omega)| \cos\left[\theta_{\text{mix}}(\vec{r}_1, \omega) + \Phi(\omega)\right] - |A_{\text{mix}}(\vec{r}_2, \omega)| \cos\left[\theta_{\text{mix}}(\vec{r}_2, \omega) + \Phi(\omega)\right]. \tag{4.19}$$

Here, the parameters $|A_{\text{mix}}(\vec{r}, \omega)|$, $\theta_{\text{mix}}(\vec{r}, \omega)$, $C_i(\omega)$, and $\Phi(\omega)$ are known from Eqs. (4.6), (4.13), and (4.16), respectively, and the weighting amplitude coefficients for both polarization components $\gamma_1(\omega)$ and $\gamma_2(\omega)$ are unknown.

The two-variable extremum analysis of the function in Eq. (4.18) under the constraints $0 \leq \gamma_1(\omega) \leq 1$ and $0 \leq \gamma_2(\omega) \leq 1$ yields the solutions

$$\left[\gamma_1(\omega), \gamma_2(\omega)\right] \in \left\{[0,0], [1, -C_{\text{mix}}(\omega)/C_2(\omega)], [-C_{\text{mix}}(\omega)/C_1(\omega), 1], [1,1]\right\}. \tag{4.20}$$

The assignment of which of these constitute minima or maxima depends on the values of $C_1(\omega)$, $C_2(\omega)$, and $C_{\text{mix}}(\omega)$, and is found by substitution into Eq. (4.18). By locating the desired minimum or maximum in this fashion separately for each frequency, the optimal amplitude shape for each laser polarization component can be obtained. These solutions provide the optimal amplitudes, which in turn depend on the chosen phases $\varphi_1(\omega)$ and $\varphi_2(\omega)$ through the parameter $C_{\text{mix}}(\omega)$.

For illustration, this procedure was carried out for maximization (Fig. 4.5a) as well as minimization (Fig. 4.5b) of the linear flux difference $F_{\text{lin}}(\mathbf{r}_1) - F_{\text{lin}}(\mathbf{r}_2)$ while using the optimal phases obtained above using Eq. 4.16. Again, an evolutionary algorithm was employed for comparison, in which the phase difference as well as the amplitude weighting coefficients were optimized. In Fig. 4.5, analytic (lines) and adaptive results (symbols) for both polarizations are compared. Similar to the adaptive optimizations for the case of phase-only shaping (Figs. 4.2 and 4.4), the analytic and adaptive results

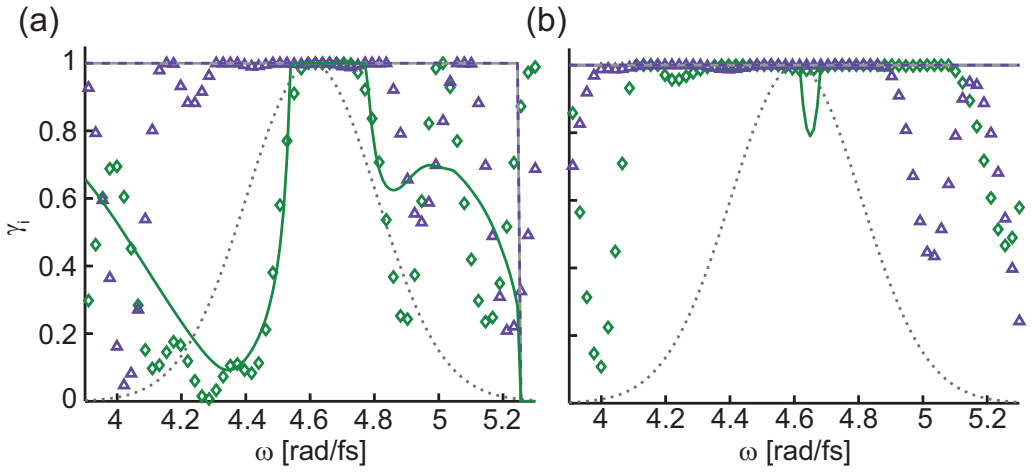

Figure 4.5: Amplitude weighting coefficients for polarization components 1 (green) and 2 (purple) for controlling the linear flux difference $F_{\mathrm{lin}}(\vec{r}_1) - F_{\mathrm{lin}}(\vec{r}_2)$. The analytic results (solid and dashed lines) are compared with those from adaptive optimization (diamond and triangle symbols, respectively). The maximization or minimization of the flux difference correspond to energy guidance to positions $\vec{r}_1$ (a) or $\vec{r}_2$ (b), respectively. Pulse amplitudes are obtained by multiplying these weighting coefficients with Gaussian profiles using Eq. (4.17). The laser spectral intensity is indicated by a gray dotted line. Taken from Tuchscherer *et al.* [49]. Copyright (2009) by The Optical Society.

for amplitude shaping agree well. The deviation of the amplitude coefficients from the adaptive optimizations appearing in the regions of low laser pulse intensities do not have any physical significance.

In the case of maximization (Fig. 4.5a), significant spectral shaping is required for polarization component 1 (green) and the linear flux difference is enhanced to $F_{\mathrm{lin}}(\vec{r}_1) - F_{\mathrm{lin}}(\vec{r}_2) = 0.201$. This value should be compared to the phase-only shaping result of 0.088 (cf. Table 4.1). Thus, the maximum of the linear flux difference is increased significantly. However, in the case of minimization (Fig. 4.5b), the optimal amplitudes are at their maxima over most of the spectrum (both weighting coefficients equal 1). This is because amplitude shaping cannot further decrease the linear flux difference of -0.483 (cf. Table 4.1). For interpretation of these results, the local response intensity $R(\vec{r}, \omega)$ shown in Fig. 4.3 for the two points $\vec{r}_1$ and $\vec{r}_2$ is used.

The small spectral region around $\omega \sim 4.7\,\mathrm{rad/fs}$ where the two responses at position $\vec{r}_1$ exceed the minimized response at position $\vec{r}_2$ is also imprinted in the weighting coefficient $\gamma_1(\omega)$ in Fig. 4.5a (green). The incident polarization component 1 is reduced in that spectral part where the local response intensity $R(\vec{r}_2, \omega)$ (Fig. 4.3) exceeds $R(\vec{r}_1, \omega)$. In the small part around $\omega = 4.7\,\mathrm{rad/fs}$, where $R(\vec{r}_1, \omega)$ dominates, both weighting coefficients equal 1 to ensure maximum contribution from the desired components.

The evolutionary algorithm confirms our predictions and successfully finds the steep slopes of amplitude coefficient $\gamma_1(\omega)$ predicted by the analytic theory.

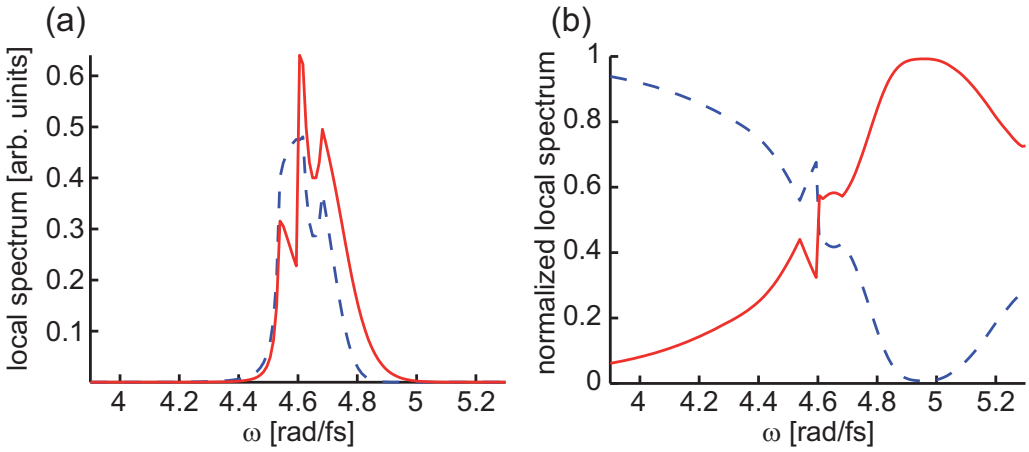

Figure 4.6: (a) The local spectrum [Eq. (4.2)] for the optimization where the "red" and "blue" halves of the spectrum are guided to positions $\vec{r}_1$ (dashed blue) and $\vec{r}_2$ (solid red), respectively. (b) The local spectrum normalized to the sum of the local spectra at positions $\vec{r}_1$ and $\vec{r}_2$. Taken from Tuchscherer *et al.* [49]. Copyright (2009) by The Optical Society.

4.3.3 Controlling the Local Spectral Intensity

In addition to maximizing or minimizing the local linear flux as an integral over the complete spectrum, it is also possible to control the local spectral intensity [Eq. (4.2)] in a more general way, for example to maximize one part of the spectrum and simultaneously to minimize the other part. Thus, one can guide the propagation of one part of the spectrum to position $\vec{r}_1$ and of the other part to $\vec{r}_2$. For illustration, the "red" half of the spectrum (3.9–4.6 rad/fs) was chosen to be guided to position $\vec{r}_1$, whereas the "blue" half (4.6–5.3 rad/fs) was guided to $\vec{r}_2$. The analytic results for the required optimal phases and amplitudes of the external control field were hence obtained in complete analogy to Section 4.3.2, with the difference that the results from maximization [Fig. 4.4 (red) and Fig. 4.5a] were applied in the "red" half of the spectrum and the results from minimization [Fig. 4.4 (blue) and Fig. 4.5b] in the "blue" half. The resulting local spectrum for this control target is plotted in Fig. 4.6a. The sharp peaks observed in the center of the spectrum are due to the steep slope of the amplitude coefficient $\gamma_1(\omega)$ (Fig. 4.5a) in the applied laser pulse shape, which resulted from the spectral part in the local response where $R(\vec{r}_1, \omega)$ exceeds the minimized local response $R(\vec{r}_2, \omega)$ shown in Fig. 4.3. In addition, the local spectrum normalized to the sum of the local spectra at positions $\vec{r}_1$ and $\vec{r}_2$ is shown in Fig. 4.6b. Note that the switching efficiency varies significantly with frequency. For some spectral components the switching efficiency is negligible (e.g., 4.5 rad/fs) whereas it is almost 100% in other regions (e.g., 4.8 rad/fs). This reflects the fact that each frequency component interferes with itself and thus the local switching efficiency is controlled by the local spectral response for each wavelength independently [12].

Hence, the desired optimization goal was achieved successfully: the spectrum was split into two parts and independent switching was obtained, i.e., for the lower frequencies the spectral intensity is higher at $\vec{r}_1$ (dashed blue) than at $\vec{r}_2$ (solid red), and for the

higher frequencies it is higher at $\vec{r}_2$ than at $\vec{r}_1$.

4.4 Temporal Near-Field Compression

In Section 4.3 it was discussed how plasmon propagation can be guided to steer local linear flux spatially. In the present section, additional control of nonlinear signals is considered. The analytic solution to temporal "focusing", i.e., the optimization of nonlinear flux, is not as straightforward as the control of linear flux. This is because the nonlinear flux defined in Eq. (4.7) cannot be expressed as a linear combination of single-frequency terms in the frequency domain, as is the case for the linear quantity.

The crucial point of the presented approach is that in Section 4.3 the optimal values are obtained for only three out of the four available degrees of freedom of the excitation laser pulse shape, and one phase can still be assigned independently, because it does not affect the linear intensity. In particular, Eqs. (4.8), (4.9) or (4.16) were used to assign the phase difference $\Phi(\omega) = \varphi_2(\omega) - \varphi_1(\omega)$ between the two excitation laser polarization components, and the prescription of Section 4.3.1 or Eq. (4.20) to find both intensities $I_1(\omega)$ and $I_2(\omega)$. Since the linear signals depend only on the phase difference $\Phi(\omega)$, Eq. (4.1), which was already introduced in the last Chapter (Section 3.2), can be used to vary the offset phase $\varphi_1(\omega)$ under the constraint for linear flux control, i.e., given all quantities in the curly brackets. The remaining control parameter $\varphi_1(\omega)$ can then be used to control the time evolution at a certain position, in particular to compress the near-field temporally (Section 3.2.2). Thus, for example, the nonlinear flux defined in Eq. (4.7) at that position where the linear flux was guided to can be optimized.

4.4.1 One Field Component

First, the simplest case is considered, in which just one polarization component of the local field contributes to the nonlinear flux by setting $b_\alpha = 1$ and $b_\beta = b_\gamma = 0$ with $\{\alpha, \beta, \gamma\} \in \{x, y, z\}$ in Eq. (4.7). The control target is set to optimize the x component of the near-field, i.e., $b_x = 1$ and $b_y = b_z = 0$. As already explained in Section 3.2.2 the temporal near-field compression is carried out in analogy to the laser pulse compression in the case of conventional far-field optics, i.e., a linear spectral phase is required to achieve the shortest possible laser pulse due to the Fourier relation of frequency and time domain. As can be inferred from Fig. 3.10 the same principle can be used in the context of nano-optics to compensate for the phase response that is introduced by the presence of nanostructures or electromagnetic propagation through them.

Hence, also in the work presented here, a phase is introduced by the pulse shaper such that the spectral phase of the local electric field at the target position of the nanostructure is flat. In the case of only one contributing local polarization component ($b_\alpha = 1$) the required phase $\varphi_1^\alpha(\omega)$ is obtained in a straightforward manner via Eq. (4.1) by requiring the phase of the local field to be uniformly zero, i.e., $\arg\{E_\alpha(\vec{r}, \omega)\} \equiv 0$. Using Eq. 4.1 the offset phase is obtained as

$$\varphi_1^\alpha(\omega) = -\arg\left\{ A_\alpha^{(1)}(\vec{r}, \omega)\sqrt{I_1(\omega)} + A_\alpha^{(2)}(\vec{r}, \omega)\sqrt{I_2(\omega)}\, \exp\left[-i\Phi(\omega)\right] \right\} \tag{4.21}$$

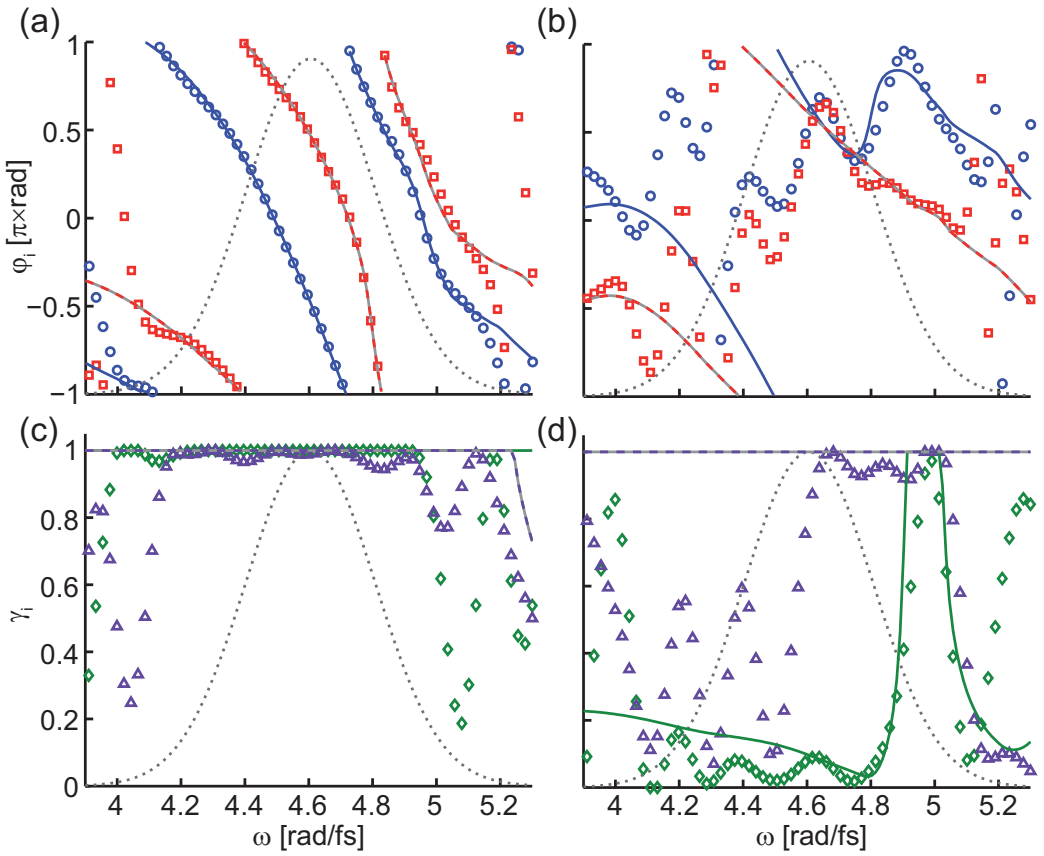

Figure 4.7: Analytic (lines) phases (a,b) φ_1 (blue) and φ_2 (red) and amplitudes (c,d) $\gamma_1(\omega)$ (green) and $\gamma_2(\omega)$ (purple) for the nonlinear guidance of the x component of the near-field by the decoupled process of first maximizing or minimizing the linear flux difference $F_{\mathrm{lin}}(\vec{r}_1) - F_{\mathrm{lin}}(\vec{r}_2)$ and then compressing the signal at the positions $\vec{r}_1$ (a,c) and $\vec{r}_2$ (b,d), compared to the adaptively optimized (symbols) phases and amplitudes using the difference of the nonlinear signal $F_{\mathrm{nl}}(\vec{r}_1) - F_{\mathrm{nl}}(\vec{r}_2)$ [Eq. (4.22)] as the fitness function. The laser spectrum is indicated by a gray dotted line. The adaptively optimized phases were adjusted with a linear phase and a phase offset to fit to the analytically calculated data since the evolutionary algorithm is not sensitive to these parameters. Taken from Tuchscherer *et al.* [49]. Copyright (2009) by The Optical Society.

for a given location $\mathbf{r}$ and component α.

For illustration, the example of directional control from Section 4.3.2 (with $b_x = 1$ and $b_y = b_z = 0$) was chosen as a basis and the parameters for maximum $f_{\mathrm{lin}} = F_{\mathrm{lin}}(\vec{r}_1) - F_{\mathrm{lin}}(\vec{r}_2)$ were used as constraints in Eq. (4.21). In addition to switching the plasmon propagation along the x arm, temporal compression at the target point $\vec{r}_1$ was requested. The resulting analytic phases and amplitudes are shown in Figs. 4.7a and 4.7c (lines), respectively, and are again compared to those found by the evolutionary algorithm (symbols). In this example, however, the fitness function for the adaptive optimization was chosen directly as the difference of the nonlinear flux [Eq. (4.7)] at the

two points $\vec{r}_1$ and $\vec{r}_2$:

$$f_{\mathrm{nl}}\left[\varphi_1(\omega), \varphi_2(\omega), \sqrt{I_1(\omega)}, \sqrt{I_2(\omega)}\right] = F_{\mathrm{nl}}(\vec{r}_1) - F_{\mathrm{nl}}(\vec{r}_2). \tag{4.22}$$

The agreement of the analytic phases [Fig. 4.7a] and amplitudes [Fig. 4.7c] with the ones found by the evolutionary algorithm is impressive, since two different observables are compared: for the analytic result, the process of first guiding the linear flux to a desired point and then temporally compressing the field at that position using the remaining degree of freedom was used, whereas with the evolutionary algorithm, the nonlinear flux was guided directly by optimizing the difference given in Eq. (4.22). The reason for this different choice of signals was that the direct nonlinear control is the procedure usually employed in experiments with suitable feedback signals and adaptive optimization. On the other hand, the several-step analytic procedure allows deterministic derivation of the optimal pulse shape. The agreement between lines and symbols in Figs. 4.7a and 4.7c is very good and is also reflected in the magnitude of the non-linear flux difference [Eq. (4.22)] yielding 0.0127 for the analytic and 0.0126 for the adaptive approach. This shows that our analytic approach is valid even if it does not directly model the fitness function of Eq. (4.22).

The same procedure can also be applied for switching the propagation along the y arm using the minimum $F_{\mathrm{lin}}(\vec{r}_1) - F_{\mathrm{lin}}(\vec{r}_2)$ from Section 4.3.2 (with $b_x = 1$ and $b_y = b_z = 0$) as a basis and compressing the pulse temporally at position $\vec{r}_2$. The optimal phases and amplitudes are compared with adaptive optimizations in Figs. 4.7b and 4.7d, respectively. Here, some variations between the two approaches can be seen. However, the amplitude coefficients [Fig. 4.7d] agree reasonably well and some of the relevant features in the phases [Fig. 4.7b] are also reproduced, such as the separation between the red and the blue curves in the region above $\omega \sim 4.8\,\mathrm{rad/fs}$. Below $\omega \sim 4.6\,\mathrm{rad/fs}$, the intensities in the incident fields is reduced [Fig. 4.7d], which partly explains the deviation of the phases between the two approaches. Comparing the non-linear flux difference obtained with the analytic optimization ($-1.208 \cdot 10^{-9}$) to the results obtained with an adaptive optimization ($-0.377 \cdot 10^{-9}$) shows again the validity of the presented analytic approach, i.e., in this case the analytic approach performs better.

All spectral phases in Fig. 4.7a and 4.7b show a predominant negative slope with additional curvatures. This is because the spectral near-field phase was chosen to be equal to zero for reaching pulse compression at the target location. Since the target points $\vec{r}_1$ and $\vec{r}_2$ are spatially separated from the excitation spot in the chosen nanostructure, plasmon propagation as a function of time is relevant. The propagation time corresponds to a linear spectral phase with a positive slope such that the dominant negative slopes of Fig. 4.7 lead to an arrival time of $t = 0$. By adding any linear phase this timing can be modified. Only the nonlinear part of the phase is responsible for compression.

4.4.2 Three Field Components

The solutions for nonlinear flux control become more complicated if more than one local field component is considered. The problem is then to assign a unique spectral phase that should in turn be compensated for pulse compression. From Eq. (4.1) it is clear

Table 4.2: $F^{\mathrm{opt}}_{\mathrm{lin},\alpha}(\vec{r})$. For comparison, all values are normalized to the sum of the linear flux $F_{\mathrm{lin}}(\vec{r}_1) + F_{\mathrm{lin}}(\vec{r}_2)$ excited with an unshaped pulse (cf. Table 4.1).

	$\alpha = x$	$\alpha = y$	$\alpha = z$
$F^{\mathrm{opt}}_{\mathrm{lin},\alpha}(\vec{r}_1)$	0.377	0.000	0.000
$F^{\mathrm{opt}}_{\mathrm{lin},\alpha}(\vec{r}_2)$	0.001	0.910	0.025

that—in general—the local spectral electric field is a three-component complex-valued vector, and each polarization component has a separate spectral phase. Thus, with $\varphi_1(\omega)$ as one (scalar) degree of freedom it is not possible to compensate for all three phases simultaneously. Therefore, different approximate solutions are considered here that find a suitable compromise between compensation of the different components. However, due to the geometry of the chosen nanostructure, the longitudinal components, i.e., the x component in the x arm and the y component in the y arm, are dominant and are compressed in roughly the same way using both approaches.

First, the phase of only the component that makes the biggest contribution to the linear flux [Eq. (4.4)] is compensated, which is found by evaluating

$$F^{\mathrm{opt}}_{\mathrm{lin},\alpha}(\vec{r}) \geq F^{\mathrm{opt}}_{\mathrm{lin},\beta,\gamma}(\vec{r}) \tag{4.23}$$

with $\{\alpha, \beta, \gamma\} \in \{x, y, z\}$ and

$$F^{\mathrm{opt}}_{\mathrm{lin},\chi}(\vec{r}) = b_\chi \sum_{\omega=\omega_{min}}^{\omega_{max}} \left| E^{\mathrm{opt}}_{\chi}(\vec{r},\omega) \right|^2 . \tag{4.24}$$

The optimized near-field $E^{\mathrm{opt}}(\vec{r},\omega)$ is calculated using the optimal phase difference (Fig. 4.4) and amplitudes (Fig. 4.5) of Section 4.3.2 that guide the linear flux to position $\vec{r}$. The offset phase $\varphi_1^{\max\,\alpha}(\omega)$ for component α, i.e., the component with the biggest contribution to the linear flux, is then obtained as in Eq. (4.21).

In the second approach, the phase of the sum of all components is compensated weighted by their amplitude contributions to the linear signal:

$$\varphi_1^{\Sigma}(\omega) = -\arg\left\{ \sum_{\alpha=x,y,z} A^{(1)}_{\alpha}(\vec{r}_1,\omega)\sqrt{I_1(\omega)} + \sum_{\alpha=x,y,z} A^{(2)}_{\alpha}(\vec{r}_1,\omega)\sqrt{I_2(\omega)}\, \exp\left[-i\phi(\omega)\right] \right\}. \tag{4.25}$$

The idea of Eq. (4.25) is that for maximum nonlinear flux the dominating electric-field polarization component should be compressed best.

To analyze both approaches the contribution of each component to the linear flux [Eq. (4.24)] at positions $\vec{r}_1$ and $\vec{r}_2$ are summarized in Table 4.2. As can be inferred, for the particular structure and target positions of the example chosen here, the x component has the strongest contribution to the linear flux at position $\vec{r}_1$, whereas the y component has the strongest contribution at position $\vec{r}_2$. This can easily be understood by recalling the electric field distributions of the two modes that can be excited in particle chain nanostructures, i.e., the longitudinal and the transversal mode (Section

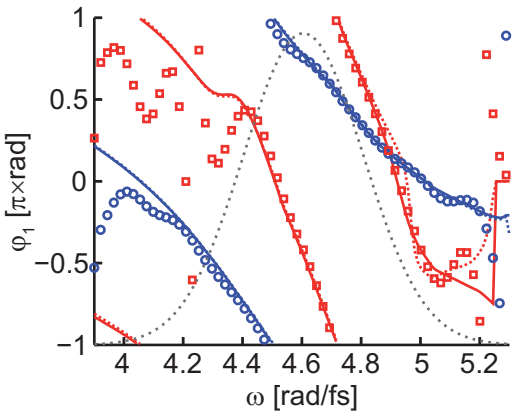

Figure 4.8: The phases $\varphi_1^{\max\alpha}(\omega)$ (solid lines) and $\varphi_1^{\Sigma}(\omega)$ (dotted lines) for analytic near-field compression at positions $\vec{r}_1$ (red) and $\vec{r}_2$ (blue) including all three near-field components calculated using either Eq. (4.21) for the strongest component, i.e., x at position $\vec{r}_1$ and y at position $\vec{r}_2$, or Eq. (4.25) are compared to adaptive optimizations using the fitness function of Eq. (4.22) (symbols). The laser spectrum is indicated by a gray dotted line. The adaptively optimized phases were adjusted as described in the caption of Fig 4.7.

3.1.3). Since the chosen control positions $\vec{r}_1$ and $\vec{r}_2$ are located in regions between the spheres (cf. Fig. 4.1), the longitudinal mode has the strongest amplitude and contributes strongest to the linear flux. Hence, the electric field is mostly directed along the main axis of the chain of particles (Fig. 3.8), i.e., in x and y direction at points $\vec{r}_1$ and $\vec{r}_2$, respectively.

Both approaches were carried out using the optimal phase differences (Fig. 4.4) and amplitudes (Fig. 4.5) of Section 4.3.2. The resulting phases $\varphi_1^{\max\alpha}(\omega)$ and $\varphi_1^{\Sigma}(\omega)$ are plotted in Fig. 4.8 for positions $\vec{r}_1$ and $\vec{r}_2$ as red and blue lines, respectively. Due to dominating components x at $\vec{r}_1$ and y at $\vec{r}_2$ (cf. Table 4.2), there is not a big difference between the combined usage of Eqs. (4.23) and (4.21) (solid lines) or the usage of Eq. (4.25) (dotted lines). The analytic results (lines, Fig. 4.8) were confirmed with adaptive optimizations using the fitness function of Eq. (4.22) (symbols, Fig. 4.8). Again, a striking agreement is observed supporting the validity of our approach of first guiding the linear flux to a position and then temporally compress the signal at that position.

In general, nanostructures can exhibit an optical response with comparable amplitudes for the three polarization components. In these cases, both approaches of defining the optimal local phase that has to be compensated will differ more strongly. Therefore, depending on the specific nanostructure–target combination the approaches presented in this section or similar ones have to be tested using the fitness function of Eq. (4.22) to find a suitable compromise.

The optimal shaped laser pulses for guiding to position $\vec{r}_1$ and $\vec{r}_2$ represented on the Poincaré surface (Section 2.2.2) are shown in Fig. 4.9 as red and blue curves, respectively. The pulse shape parameters, i.e., the amplitudes and phases of both polarization components, were obtained using the optimal phase differences (Fig. 4.4) and amplitudes (Fig. 4.5) of Section 4.3.2 combined with the phase $\varphi_1(\omega)$ for compression of the largest local near-field component (solid lines Fig. 4.8). It can be noticed that both optimal pulses are mostly circularly polarized in regions of high intensity, i.e., dots with saturated color. However, they differ in helicity such that guiding to position $\vec{r}_1$ is ob-

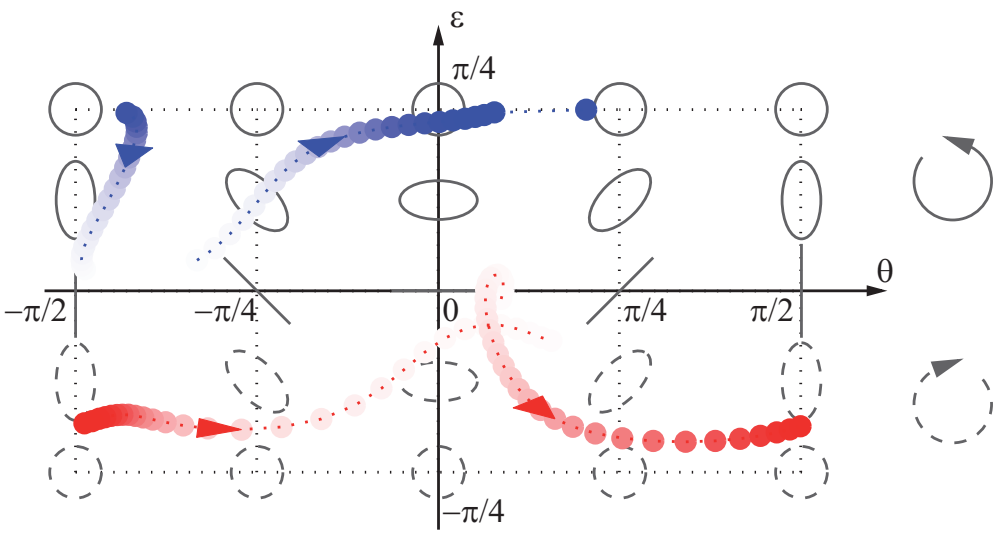

Figure 4.9: Poincaré curves of the optimally shaped excitation pulses. The optimal pulses are calculated using the optimal phase differences and amplitudes of Section 4.3.2 combined with the phase $\varphi_1^{\max\alpha}(\omega)$ for compression of the largest local near-field component α (solid lines Fig. 4.8). The curves are shown from −30.64 fs to 2.79 fs for guiding to $\vec{r}_1$ (red) and from −18.39 fs to 6.69 fs for guiding to $\vec{r}_2$ (blue) including intensities down to 1 % of the maximum intensity. The time interval between two circles is $\Delta t = 0.56$ fs.

tained for right circular polarized light whereas left circular polarized light guides the local near-field to position $\vec{r}_2$. This can be explained by considering the optimal phase differences (Fig. 4.4) described in Section 4.3: the optimal phase differences for guiding to $\vec{r}_1$ and $\vec{r}_2$ are approximately $-\pi/2$ and $\pi/2$, respectively.

4.5 Interpretation of Optimized Fields in the Time Domain

The formulation of the control problem in frequency space facilitates an analytic solution as discussed in Sections 4.3 and 4.4. By virtue of Fourier transformation, this picture already contains all information on the temporal evolution of the different quantities. Nevertheless, it is instructive to monitor the plasmon propagation directly as a function of time, which will be done here for the analytically derived optimal excitation pulses.

Figure 4.10a shows the temporal near-field intensities obtained with the excitation pulses of Section 4.3.2, i.e., the phase difference from Fig. 4.4 and amplitude coefficients from Fig. 4.5, combined with the phase $\varphi_1(\omega)$ for compression of the largest local near-field component (solid lines Fig. 4.8), and the temporal near-fields intensities obtained with an unshaped pulse. The switching of the local near-field intensity is visible by comparing the optimization of nonlinear flux guiding to $\vec{r}_1$ (red lines) with guiding to $\vec{r}_2$ (blue lines). The temporal near-fields at $\vec{r}_1$ and $\vec{r}_2$ are shown with solid and dashed-dotted lines, respectively. Clearly, the red solid line is higher than the red dashed line and the dashed blue line is higher than the solid blue line, thus confirming the successful

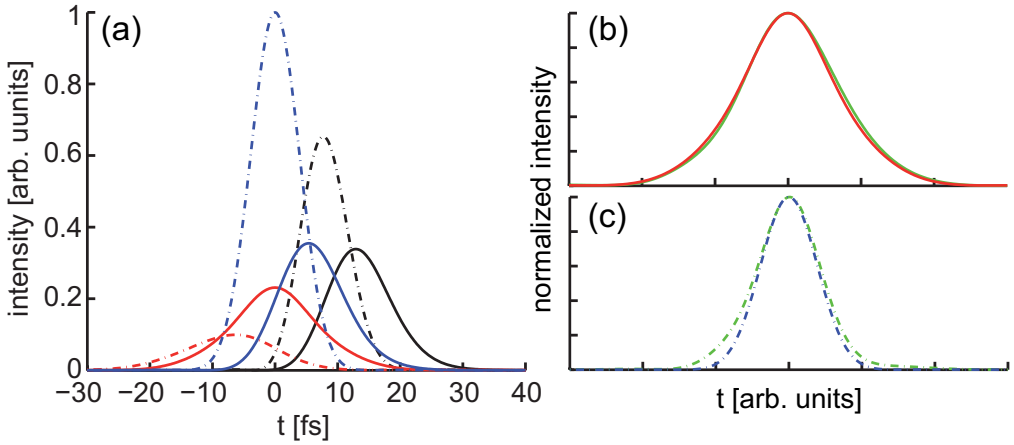

Figure 4.10: (a) Temporal near-field intensity $|\vec{E}(\vec{r},t)|^2$ at two locations $\vec{r}_1$ (solid) and $\vec{r}_2$ (dashed dotted). The near-field intensity for the unshaped pulse (black) is compared to the near-field intensities excited by optimal pulses, to guide the nonlinear flux to $\vec{r}_1$ (red) or $\vec{r}_2$ (blue). (b,c) To show near-field compression the near-field intensities are plotted for the case of guiding the linear flux and choosing $\varphi_1(\omega) \equiv 0$ (green) and are compared with the near-field intensities for optimal $\varphi_1(\omega)$ for $\vec{r}_1$ [(b), red] and $\vec{r}_2$ [(c), blue]. The curves in (a) have been shifted in time and normalized for $\vec{r}_1$ (b) and $\vec{r}_2$ (c). Taken from Tuchscherer *et al.* [49]. Copyright (2009) by The Optical Society.

linear flux control.

Using the nonlinear flux control, both guiding of linear flux and field compression under the constraint of an amplitude-shaped spectrum was achieved. Since the effective spectral width was reduced for the linear flux control [cf. Fig. 4.5a, green curve], the bandwidth-limited pulse duration increased correspondingly. Hence, the red solid line in Fig. 4.10a has a broader width than the black solid line. The effect of dispersion compensation at $\vec{r}_1$ and $\vec{r}_2$ can better be seen in Figs. 4.10b and 4.10c, respectively. Here, the normalized and time-shifted temporal intensity under the constraint of guiding the linear flux, but choosing $\varphi_1(\omega) \equiv 0$ (green lines) are compared to the normalized temporal intensity when additionally choosing the optimal $\varphi_1(\omega)$ for pulse compression (red and blue lines in Fig. 4.10b and 4.10c, respectively). The compression is small in Fig. 4.10b. However, for guiding to $\vec{r}_2$ [Fig. 4.10c] the dispersion is larger and the compression is more pronounced, i.e., the optimally compressed temporal near-field (dash-dotted blue) is shorter than the near-field for pulses with $\varphi_1(\omega) \equiv 0$ (dash-dotted green).

To illustrate the spatial and temporal evolution of the propagating plasmons, movies that show the amplitude of the x component of the propagating near-fields excited by optimally shaped ultrashort laser pulses were created. Two snapshots from these movies are shown in Fig. 4.11, where in addition to the projections of the two laser polarization components also the full quasi-3D profile (Section 2.2.2) of the vector-field shaped optimal pulses are shown.

Figure 4.11a[3] shows guiding of the linear and nonlinear flux to $\vec{r}_1$ with the excitation

[3]The corresponding movie is provided by Optics Express:
`http://www.opticsexpress.org/viewmedia.cfm?URI=oe-17-16-14235-1`

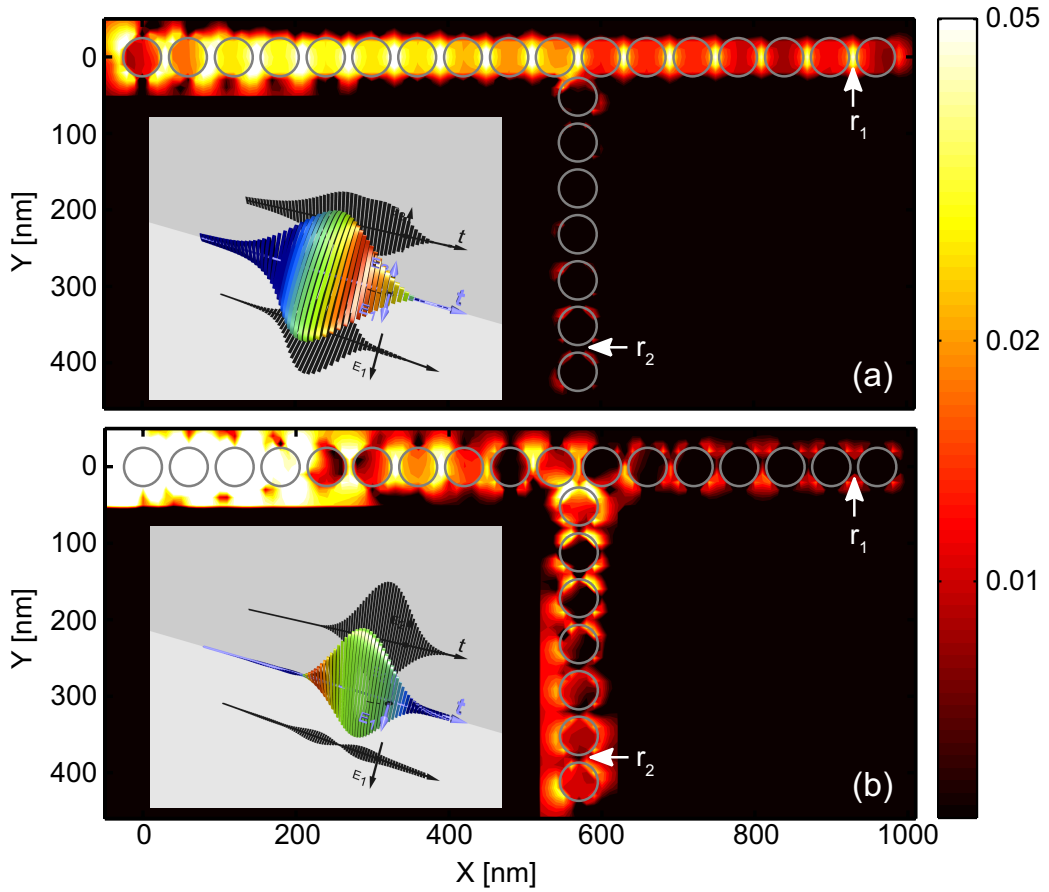

Figure 4.11: Snapshots of the movies of plasmon propagation at $t = 0$ for the nonlinear flux guidance of the x component to $\vec{r}_1$ (a) and $\vec{r}_2$ (b) (links to the media files are given in the footnote of the running text) . The amplitude of the x component of the near-field in the $z = 10\,\mathrm{nm}$ plane is plotted logarithmically, where the excitation pulses are obtained by setting $b_x = 1$ and $b_y = b_z = 0$, and using the analytic approach of Sections 4.3.2 and 4.4. The insets show quasi-three-dimensional representations of the optimal laser pulses. The white arrows indicate the optimized locations. Taken from Tuchscherer *et al.* [49]. Copyright (2009) by The Optical Society.

phases and amplitudes of Figs. 4.7a and 4.7c, respectively, and Fig. 4.11b[4] shows guidance to $\vec{r}_2$ with the optimal field shapes from Figs. 4.7b and 4.7d. Both of the snapshots are taken at $t = 0$, since the phase $\varphi_1(\omega)$ was chosen as in Eq. (4.21), which includes the linear spectral phase of the propagated near-field. Therefore, the excitation pulse appears at times $t < 0$ and the propagating mode arrives at the target location at $t = 0$. It can be clearly seen that after propagation from the excitation position, the field mode "switches " into the desired arm after the junction and is guided to and compressed at either $\vec{r}_1$ (Fig. 4.11a) or $\vec{r}_2$ (Fig. 4.11b).

[4]The corresponding movie is provided by Optics Express:
`http://www.opticsexpress.org/viewmedia.cfm?URI=oe-17-16-14235-2`

4.6 Space–Time Control

In a previous work Brixner *et al.* [11] suggested to use ultrafast coherent control over nano-optical fields for a new type of space–time-resolved spectroscopy below the diffraction limit. The idea was to create pump–probe-like fields in the vicinity of a nanostructure with such properties that the pump and probe interactions are not only separated in time—as usual—but also occur at different spatial positions. Thus, it should be possible to develop a direct spectroscopy for transport phenomena, in which the propagation of some excitation created by the pump pulse can be probed spatially and temporally separated. In the earlier work [11, 12], an evolutionary algorithm was used to find the optimal polarization-shaped excitation pulse. While that works for the suggested purpose, the question remained if a direct "inversion" of the problem could lead to the optimal excitation field analytically. Such a analytic derivation of the optimal excitation fields enables easy access to the pump–probe delay that would have to be scanned in experiment. This is of great importance, since using adaptive optimizations the finding of each pump–probe pulse configuration itself is a complex task and might not be possible. This is even more important by considering more complex nonlinear spectroscopy, e.g., two dimensional spectroscopy [7], on the nanoscale, where more than one parameter have to be scanned.

In this section, the concepts from Sections 4.3, 4.4, and 4.5 are extended to provide such a prescription, and illustrate results again for the example of the nanostructure array of Fig. 4.1 and propagating plasmons. However, it should be emphasized that the method itself can be applied to arbitrary structures and does not require propagating modes.

In Section 4.3.1 the optimal phase difference and amplitude coefficients were determined to cancel out one component of the near field at one spatial location $\vec{r}$. However, the near-field response at other locations is different, and therefore does not have to vanish. This can be used to achieve space–time control by splitting the spectrum into two parts and determining optimal pulse shapes for each of the parts independently. The temporal shape of the near-field can be optimized using the remaining free laser pulse shaping parameter $\varphi_1(\omega)$:

$$E_\alpha(\vec{r},\omega) = \left\{ A_\alpha^{(1)}(\vec{r},\omega)\sqrt{I_1(\omega)} + A_\alpha^{(2)}(\vec{r},\omega)\sqrt{I_2(\omega)}\,\mathrm{e}^{-\mathrm{i}\Phi(\omega)} \right\} \mathrm{e}^{-\mathrm{i}\varphi_1(\omega)}, \tag{4.26}$$

with $\alpha = x, y, z$.

This is illustrated with an example, where the "red" half of the spectrum is used to cancel out the x component of the near-field at $\vec{r}_1$, while the "blue" half is used to cancel out the y component at $\vec{r}_2$. This gives the possibility to shape the largest local component of the signal appearing in one arm of the nanostructure independently from the signal in the other arm.

Using Eq. (4.21), the signal is compressed at $t = 0$, but here a time delay of $\tau = 90$ fs was introduced by requesting additional linear spectral phases with different slopes in the two spectral regions. The spectral amplitudes for the largest near-field components, i.e., the x component at $\vec{r}_1$ and the y component at $\vec{r}_2$, are plotted in Fig. 4.12a. However, in Fig. 4.12b the temporal intensities, which include all three components, are shown

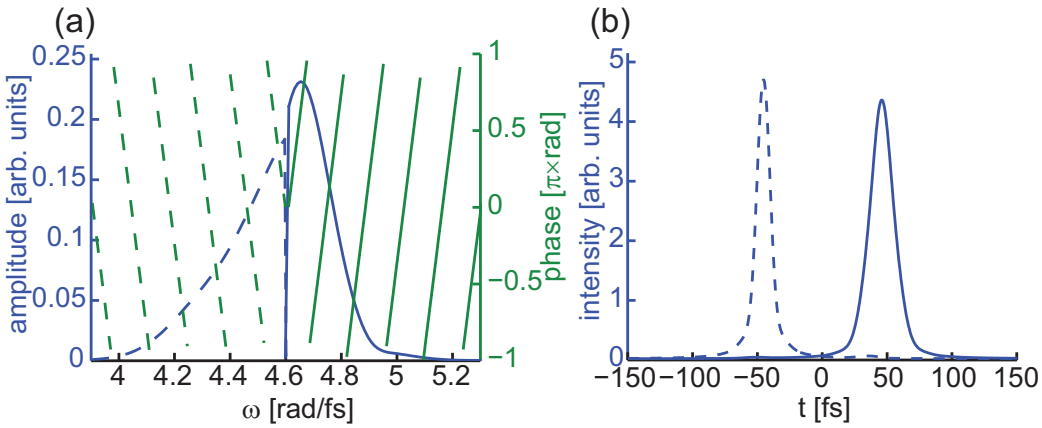

Figure 4.12: (a) Spectral amplitudes (blue) and phases (green) of the largest local component of the shaped near-fields at two positions $\vec{r}_1$ (solid, x component) and $\vec{r}_2$ (dashed, y component) with the linear spectral phase corresponding to a 90 fs delay between the corresponding temporal intensities, which include all three near-field components, shown in (b). Taken from Tuchscherer *et al.* [49]. Copyright (2009) by The Optical Society.

for the same polarization-shaped excitation pulse, and it can be seen that the desired spatial–temporal sequence can be reached with extremely good contrast. The pump and probe pulses peaking at $\tau = -45\,\mathrm{fs}$ and $\tau = +45\,\mathrm{fs}$ are limited exclusively to positions $\vec{r}_2$ (dashed) and $\vec{r}_1$ (solid), respectively.

While a particular example is discussed here, this method is not restricted to any specific time delay or temporal shape because the two parts of the spectrum can be shaped with complete independence. Therefore, this provides an approach to perform simultaneous spatial and temporal control analytically in a very general manner.

4.7 Conclusion and Outlook

In this chapter, general analytic solutions were derived for the control of nanoplasmonic energy propagation on a femtosecond time scale. In a first step, the direction of propagation at a branching point of a complex plasmonic nanostructure was controlled. Local linear flux could be switched between different target points by adjusting the interference of different near-field modes induced by the two perpendicular components of a polarization-shaped ultrashort laser pulse. In the second step, the remaining pulse shape parameter yielded a handle independent from the results obtained in the first part, to additionally manipulate the temporal evolution of the near fields. Specifically, the variation of all four degrees of freedom (amplitude and phase for each polarization component) that are available with recent pulse-shaping technology were considered. The analytic results were confirmed by an evolutionary algorithm. This proves the effectiveness of the analytic approach for controlling (propagating) optical near fields.

As already expected from the discussion of the near-field control mechanisms (Section 3.2.1) the results for controlling linear flux do not depend on the individual phases of both laser pulse polarization components but only on their difference, i.e., the polarization

state. This has implications for the experimental implementation, as only the phase difference is a relevant parameter. Also, this enables usage of the remaining phase parameter for temporal control, e.g., temporal compression in order to achieve high nonlinear signals. Another interesting point is that the phases of the maximum and the minimum signals are related to each other and differ by π. Consequently, once one optimal phase is found analytically or adaptively, the other phase can be calculated immediately. It is precisely this relation that will be used for the experiment described in Chapter 5 to simplify the experiment on the one hand and to identify interference as the main control mechanism on the other hand.

The best contrast for linear flux switching between point $\vec{r}_1$ and point $\vec{r}_2$ can be obtained if the mixed scalar products $A_{\mathrm{mix}}(\vec{r}_1,\omega)$ and $A_{\mathrm{mix}}(\vec{r}_2,\omega)$ as defined in Eq. (4.6) have a phase difference of $\theta_{\mathrm{mix}}(\vec{r}_1,\omega)-\theta_{\mathrm{mix}}(\vec{r}_2,\omega)=\pi$, such that the signal at $\vec{r}_1$ is maximized and at $\vec{r}_2$ minimized for the same phase difference $\Phi(\omega)=\varphi_2(\omega)-\varphi_1(\omega)$ between the two external polarization components. Considering this relation, the responses of the symmetric T-structure investigated by Sukharev and Seideman [120] can be analyzed observing exactly this behavior. This is the reason why the switching control in their structure works with good contrast. In general, this insight can also be used to design other nanostructures with the desired switching properties.

Apart from using the phases of the excitation laser pulse as control parameters, modifying the amplitudes as well can improve the control performance. With the analytic approach, this process can be performed separately from the phase determination. As a consequence, this insight also simplifies experiments using adaptive control because the phases and amplitudes can be determined in separate runs of the evolutionary algorithm. Thus, the size of the search space is reduced dramatically, and convergence rates could improve.

Although only single spatial points were considered in the nanostructure investigated here, as shown in Appendix A.1, solutions for the control of linear flux defined via regions can be found completely analogously. This might have applications in optimization of near-field confinement. In such an application a small region would have to be defined that is surrounded by a larger region. The confinement is then reached by maximizing the contrast such that strong linear flux is obtained in the small region and at the same time suppression of the linear flux in the surrounding region is achieved. However, different nanostructures would have to be chosen because in the quasi-one-dimensional nanostructure chosen here the field is already confined along the chains of particles.

Once the linear flux was guided to the desired location, the remaining phase parameter was used in an analytic approach to optimize the nonlinear flux difference. This is in principle different from the direct guiding of the nonlinear signal to the desired location. However, the results from the analytic two-step method were in good agreement with direct nonlinear guiding using the evolutionary algorithm. A complication arises if all local polarization components contribute to the nonlinear signal. In that case, it is not obvious how a function of the spectral phase should be defined, and two different possibilities have been discussed. For practical applications, the best choice depends on the precise nature of the nonlinear signal that is investigated. The definition can be adjusted to the particular system, while the general analytic approach remains the same.

In addition to spatial and temporal "focusing", it is also possible to manipulate different parts of the laser spectrum individually and independently. Thus, a degree of analytic spectral control can be added to the control over spatial–temporal characteristics. As one particular example, the previously suggested [11] pump–probe pulse can now be prepared analytically such that pump and probe interactions occur not only at different times but also at different positions (with different spectral content). This also enables an easy handle to the parameters that would be scanned in a pump–probe experiment, such as the separation time.

The analytic scheme discussed here can be used to guide the propagation of electromagnetic energy in a variety of complex nanostructures for nanoscale optical characterization, manipulation, information processing, and other applications. It is important to point out that the method is valid quite generally. Only one particular realization of a T-junction array have been chosen for illustration purposes, but the analytic approach is not limited to a certain nanostructure, number of frequencies, illumination conditions, or spectral range. The only requirement is a Maxwell's equations solver which calculates the responses $\vec{A}^{(i)}(\vec{r},\omega)$ as a function of spatial position and frequency for two perpendicular incident light polarizations. It is not even necessary to calculate the response in the frequency domain, but it can also be calculated using time-domain methods, such as Finite-Difference Time Domain (FDTD), and then Fourier-transformed [100]. Additionally to theoretically obtained optical response functions, they can also be determined experimentally [122–124], e.g., as described in Chapter 7. Then these results can be used for the analytic calculations of the control fields.

The analytic results are not only of interest for understanding the mechanisms of optical coherent control in nanostructures, but they also provide insights for simplifications and improvements of experiments. Applications can be found in logical processing elements in nanoplasmonic circuits as well as in nonlinear spatially and temporally resolved "nano–femto" spectroscopy. This is of special interest in the scope of this thesis. In Chapter 7 a new method will be introduced that allows detection of spectroscopic features below the diffraction limit. However, the method as described there relies on far-field illumination to excite the sample. Using appropriate nanostructures the method could be further improved by introducing a near-field pump–probe excitation scheme that allows excitation at different points separated below the optical diffraction limit. Further, an appropriate nanostructure can be designed by using the criteria for perfect constructive and destructive interference, i.e., $\theta_{\mathrm{mix}}(\vec{r}_1,\omega) - \theta_{\mathrm{mix}}(\vec{r}_2,\omega) = \pi$.

Adaptive learning loops have become a very successful technique for achieving coherent control in many different systems such as molecules or, more recently, nanostructures. However, very often the interpretation of control mechanisms is quite difficult. While here a particular nanostructure has been explicitly considered and the optimal control of plasmon propagation has been determined analytically, the approach may also be useful for even more general control scenarios, namely in molecular systems, as it can also be described in terms of optical response functions [7].

The results of this chapter provide a direct link between the Brumer–Shapiro frequency-space interference scheme for coherent control on the one hand [125], and many-parameter Tannor-Rice/Rabitz time-domain optimal control with shaped laser pulses on the other hand [126, 127]. The two schemes do not constitute competing approaches; it is rather

a combination of the "best of both worlds". While it turns out that the optimal control solution found by a learning algorithm indeed requires a complex laser pulse shape and not just a single "control knob", that precise pulse shape can be constructed analytically by exploiting the fundamental principles of coherent two-pathway interference.

5 Experimental Deterministic Control of Near Fields

In the last chapter, it was shown theoretically that it is possible to analytically control the spatial and temporal profile of plasmonic excitation in nanostructures. It turned out that if the response function of the nanostructure is known, the optimal pulse shapes can be calculated in an analytic fashion. If however, the response function of the nanostructure is unknown it was found that it is still possible to simplify the experiment. In case of adaptive optimization of a certain optimization goal, e.g., maximization of the linear flux at position $\vec{r}_1$ and minimization at another position $\vec{r}_2$, the opposite optimization goal, e.g., maximization of the linear flux is at position $\vec{r}_2$ and minimization at position $\vec{r}_1$, is obtained by applying a π phase to the optimal phase difference $\Phi = \varphi_2 - \varphi_1$ between both layers of the polarization pulse shaper. In this chapter, this deterministic rule is realized experimentally by switching the optical near field from one corner of a bow-tie antenna to another corner. Therefore, optimal puls shapes are found adaptively (Section 5.3) first and then these pulse shapes are used to find the optimal pulse shapes of the opposite optimization goal in a deterministic fashion (Section 5.4). The results display experimental deterministic switching and are discussed in terms of the optimal pulse shapes of adaptive and deterministic control (Section 5.5).

The work that is presented in this chapter resulted from a collaboration of our work group with the work groups of Martin Aeschlimann[1] and Walter Pfeiffer[2]. The measurements were performed at the Technische Universität Kaiserslautern in the group of Martin Aeschlimann. His group was responsible for the sample fabrication and provided their profound know-how of operating the photoemission electron microscope. The group of Walter Pfeiffer contributed in the measurement process as well as in the analysis and interpretation of the measured data.

5.1 Introduction

Ultrafast control of plasmonic excitations in nanostructures offers routes towards spectroscopic applications below the optical diffraction limit. As already used in surface enhanced Raman spectroscopy (SERS) [83], plasmonic excitations enable strong enhancement of the local electric fields on nanostructured metallic surfaces and single-molecule Raman spectra can be detected. However, random nanostructures are used for SERS and design of complex shaped electric fields to apply nonlinear spectroscopy is

[1]Fachbereich Physik and Research CenterOPTIMAS, Technische Universität Kaiserslautern, Erwin-Schrödinger-Str. 46, 67663 Kaiserslautern, Germany

[2]Fakultät für Physik, Universität Bielefeld, Universitätsstr. 25, 33615 Bielefeld, Germany

not possible in a deterministic fashion since the response function of the nanostuctures excited on the surface can have a huge influence on the local electric fields. Therefore, simple structures such as nanoantennas have recently been used to observe and manipulate wave-packets of single molecules [9]. As already discussed in the last chapter, more sophisticated spectroscopy on nanometer spatial and femtosecond temporal scale can be achieved by manipulation of the near field via polarization pulse shaping. Since all degrees of freedom of the incident light affect the local excitations, they offer possibilities to control plasmonic excitations both in space and time [11, 14]. With increasing complexity of the nanostructure it becomes, however, less obvious how a particular spatiotemporal excitation can be achieved using suitably shaped incident light. Although two-pulse correlation measurements [118], parameter scans [114], time-reversal concepts [48, 117], and adaptive optimization methods [11, 13] provided successful demonstrations of nanoplasmonic control, it is essential to develop a basic understanding of the control mechanisms and devise predefined rules to control local excitations. A particularly important issue is the question how optimal control can be achieved, i.e., how the global optimum can be found. In the last chapter analytic formulas were derived which enable calculation of the optimal far field pulses for a structure with a known response function. Optimal switching between the local linear flux in a nanostructure is achieved if the difference of the spectral phases of the two incident laser pulse polarization components is changed by π. Irrespective of the nanostructure shape, interference of different excited modes is the underlying control mechanism.

In this chapter this concept of an analytically derived predefined control rule is realized in an experiment by optimal switching of the excitation between two corners of a bow-tie antenna. Therefore, adaptive optimizations are performed first and deterministic control is then achieved by changing the relative phase of the two incident polarizations. Although the utilized nanostructure is a bow-tie antenna, the underlying physics are described by nanotriangles, since the interparticle distance is large such that coupling between both triangles can be neglected. Nevertheless, these nanotriangles are highly attractive for control experiments because they have a complex response with several modes [128–130].

Additionally to spectroscopic applications as discussed above, plasmonic excitations are also interesting for future applications in chip technology [131]. For these plasmonic devices the coupling between the far field and the nanoscale excitations is essential and optical resonant nanoantennas are developed to efficiently couple light to plasmonic nanostructures [54, 84, 85]. Nanoantennas are promising candidates for single-molecule applications [132, 133], high-harmonic generation radiation sources in the extreme ultraviolet [80], and nanophotonic circuitry [84, 108, 134].

5.2 Experimental Setup and Sample Characteristics

A schematic of the setup that was used for the presented experiment is depicted in Fig. 5.1. Light pulses (p polarized) were generated by a Ti:Sapphire oscillator (*Newport Spectra-Physics Tsunami*, 80 MHz, 795 nm, 30 fs FWHM, 9 nJ) and were actively stabilized with respect to beam pointing (*TEM Messtechnik Beamlok 4D*). One part

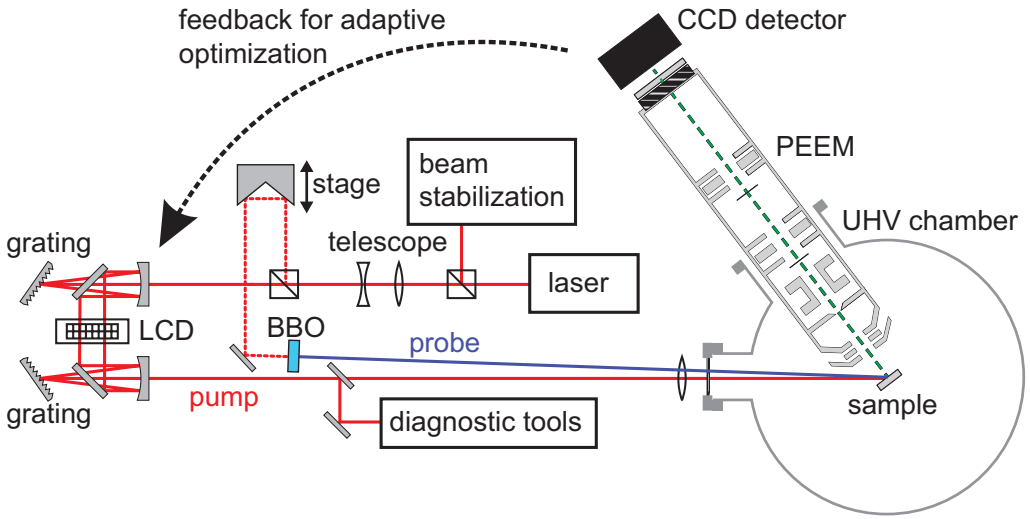

Figure 5.1: Schematic of the experimental setup for deterministic control. The laser pulses (Ti:Sapphire oscillator, 80 MHz, 795 nm, 30 fs FWHM) are beam stabilized and then split. One part of the pulses is sent through a polarization pulse shaper to act as the pump beam and either excite the sample that is placed in UHV chamber of the PEEM or are sent to diagnostic tools for pulse characterization. The second part is frequency-doubled in a BBO crystal and then overlapped with the probe beam under an angle of about 1° to serve as the probe beam. The photoemission pattern emitted from the sample is recorded with a CCD detector and provides the feedback for adaptive optimizations. By courtesy of C. Strüber.

(probe) was frequency-doubled by second-harmonic generation in a 300 µm BBO crystal yielding *s*-polarized laser pulses. The laser pulses with 398 nm center wavelength (corresponding to a photon energy of 3.1 eV) were compressed to 30 fs (FWHM) using a prism compressor (not shown) and were then directed onto the sample. The other part (pump) was polarization-shaped (Section 2.3.2) and was spatially overlapped under a small angle (∼1°) with the probe beam on the sample at 65° angle of incidence (see also Fig. 2.17). Both beams were focused very weakly on the sample using the same lens with a focal length of 30 cm resulting in about 70 µm diameter spot size on the sample. The temporal position of the probe pulse was set to coincide with the unshaped pump pulse using the delay stage. The polarization-shaped pulses (center wavelength 795 nm) were characterized using dual-channel spectral interferometry with reference pulses measured via FROG (Section 2.4). Since the sample was positioned in the PEEM (i.e., in a UHV chamber), it was not possible to characterize the laser pulses at the position of the sample. However, as can be observed from the schematic of the setup, only two additional mirrors were used to direct the shaped laser pulses to the characterization tools. Hence, the deviations of the pulses at the position of characterization with respect to the pulses at the position of the sample can assumed to be small. Characterization of unshaped pulses (i.e., transform-limited) revealed elongated pulses of 50 fs (FWHM) due to reduction of the spectral width induced by optical elements, i.e., the Jones matrix, of the polarization pulse shaper. The photoemission pattern of the sample was recorded with a PEEM (Section 2.6) and was used to define the feedback for adaptive optimizations.

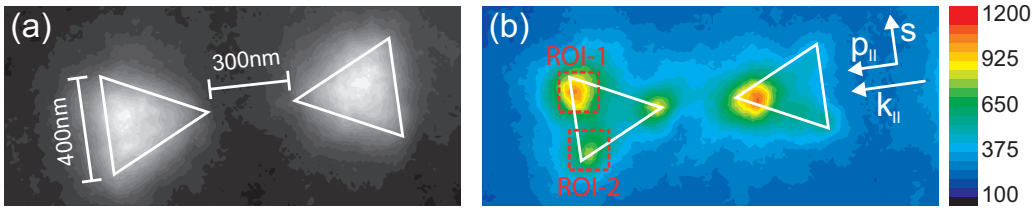

Figure 5.2: Bow-Tie antenna PEEM images with outlines. (a) One-photon UV PEEM image shows uniformly distributed photoemission. (b) Two-photon image for excitation with an unshaped p-polarized pump pulse and an s-polarized probe pulse. The projections of the polarization directions and the k vector are indicated with white arrows. The regions of interest (ROI) used for adaptive optimizations are indicated with red dashed squares. By courtesy of C. Strüber.

For the adaptive optimizations an evolutionary algorithm was used (Section 2.5). The optimizations were performed using independent spectral phase shaping of each polarization component. The spectral phases $\varphi_i(\omega)$ were parameterized independently in the dispersion basis using a sixth-order Taylor expansion with the absolute phase of one polarization component set constant. Thus, eleven independent parameter genes were varied and optimized in the adaptive learning loop. Forty individuals were used per generation, and convergence was usually reached after 20–40 generations. Even though only spectral phases were modulated with the LCD of the pulse shaper, the amplitudes of both polarizations were also modulated due to the Jones matrix of the setup (Section 2.4.3). A discussion of the influence of the Jones matrix is given in Section 5.5.

The investigated sample was an array of twelve bow-tie antennas (BTA) made of gold on an ITO/glass substrate. Note that due to the large spot size of 70 µm, the complete array is illuminated with pump and probe beam. The sample was covered with a thin layer of Cs to adjust the work function of photoelectrons for two-photon pump–probe excitation. The BTAs were compound of two equilateral nanoprisms with a side length of 400 nm, a height of 40 nm and a varying gap size of 100, 200 and 300 nm. Exemplary PEEM images of a BTA with 300 nm gap size are shown in Fig. 5.2. The high energy Hg lamp excitation provided a one-photon UV PEEM image (Fig. 5.2a), which shows the nanoantenna outlines with the photoelectron yield uniformly distributed over the nanostructure surface. Upon excitation with a femtosecond unshaped p-polarized pump pulse and the frequency-doubled s-polarized probe pulse the photoemission signals localized at various subwavelength distributed spatial positions (Fig. 5.2b). The polarization directions and the projection of the k-vector of incident laser pulses onto the sample are indicated with white arrows. Note, that the small tilt of the BTA was due to a tilt of the PEEM camera and not due to a tilt of the sample with respect to incident light, i.e., the projection of the k-vector onto the plane of the sample was directed along the main axis of the antenna. As can be observed, p-polarization of the incident light has a projection along the main axis of the antenna. Due to the 65° incident angle, the p-polarization has an additional component pointing into the plane of the antenna. This unsymmetrical

illumination condition is also reflected in the PEEM pattern, i.e., the photoemission pattern of the left nanoprism differs from the pattern of the right nanoprism.

Since the gap size of the BTA is on the order of the wavelength, the coupling of the two nanoprisms can be neglected here and the PEEM pattern corresponds to excitation of two isolated nanoprisms. No strong field enhancement is observed in the center of the BTA. However, field enhancement was observed at the corners of the left nanoprism and at the left corner on the right nanoprism. This behavior indicates excitation of resonant plasmonic modes depending on the orientation of the incident k-vector with respect to the nanoprisms. To demonstrate adaptive and deterministic switching, the left nanoprism is discussed in the following and the right nanoprism is shown for comparison only. For the adaptive optimization described in the next section the regions of interest (ROI) are defined as indicated with the red dashed squares. The difference of the photoemission yield of both ROIs that is observed in Fig. 5.2b, i.e., higher yield for ROI-1 than for ROI-2, is due to imperfect fabrication of the BTA. For a perfectly fabricated BTA the photoemission yield of both ROIs should be the same.

The PEEM pattern generated by the s-polarized probe-pulse-induced two-photon photoemission ($2\times3.1\,\mathrm{eV}$) alone revealed a homogeneous emission from the nanoantenna surface (not shown) proving that the whole nanostructure area is uniformly probed. Hence, off-resonant excitation can be assumed for the probe pulse excitation. However, in the control experiments that are presented in the following, the sample was excited with a polarization-shaped pump laser pulse in temporal overlap with the transform-limited probe pulse and the photoemission signals localized at particular spatial regions on the nanoantenna. Under these conditions, the two-photon PEEM pattern reveals the joined excitation probability of pump and probe. Due to the temporal overlap of the pump and probe pulse two possibilities have to be considered: Either the polarization-shaped pump pulse generates—via linear absorption—a distribution of excited electrons that is then homogeneously probed, or the probe pulse generates a homogeneous excitation, which is then locally promoted into the electron continuum. In both cases the observed emission pattern reveals the local one-photon pump interaction. Thus, although a nonlinear method is used, the linear response of the nanoantenna at the pump wavelength is investigated. Additionally, the intermediate state that is needed for the two-photon process is assumed to be a virtual state with a vanishing lifetime (Section 2.6). Hence, only the temporal region of polarization-shaped pump pulse that is in temporal overlap with the probe pulse has a contribution to the two-photon photoemission yield.

5.3 Adaptive Switching of Photoemission

Before demonstrating optimal deterministic nanoplasmonic excitation control in an experiment as described in the next section, adaptive optimizations of the photoemission pattern of the BTAs were performed first. As an optimization goal, the emission ratio from the two corners of the left nanoprism (ROI-1 and ROI-2 in Fig. 5.2b) was defined as

$$f[\varphi_1(\omega),\varphi_2(\omega)] = \frac{F_{\text{ROI-1}}}{F_{\text{ROI-2}}}, \tag{5.1}$$

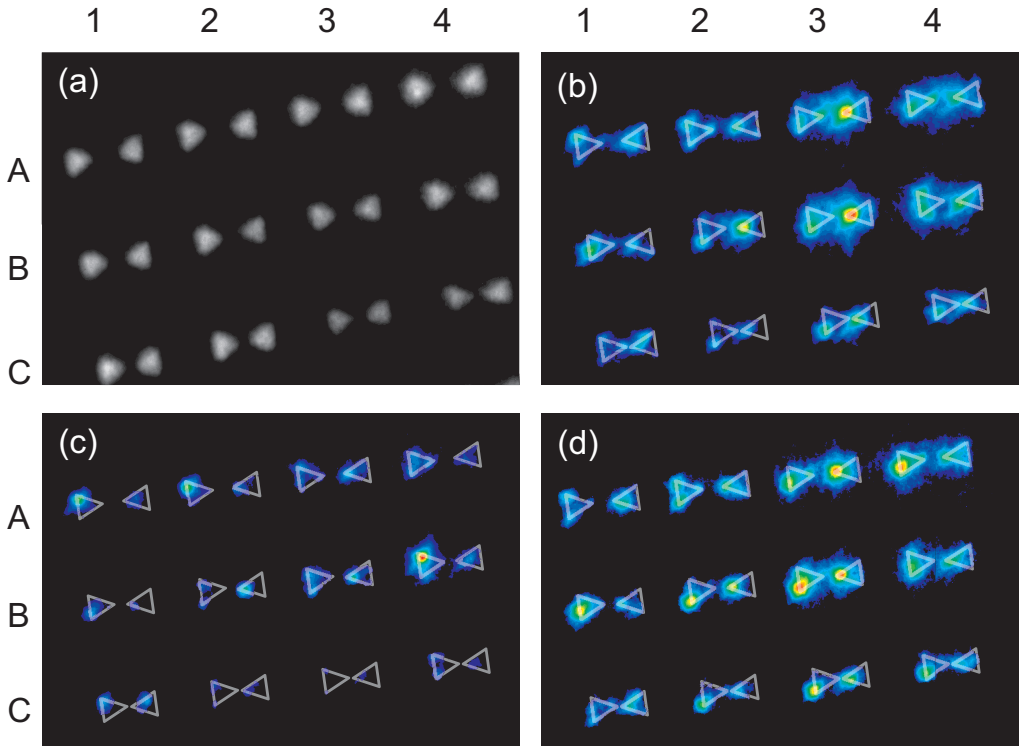

Figure 5.3: Adaptative control demonstrated for an array of BTAs with varying gap size of 100 (C), 200 (B) and 300 nm (A). The four nanostructures of each row are identical to the extend of fabrication. (a) One-photon PEEM image obtained with a Hg lamp UV excitation. (b) Two-photon pump–probe PEEM image obtained with an unshaped p-polarized pump pulse. Two-photon pump–probe PEEM images obtained with an optimally shaped pump laser pulse found by adaptive (c) maximization and (d) minimization of Eq. (5.1). The ROIs are defined on the BTA A2 (cf. Fig. 5.2b) and maximization and minimization corresponds to localization at the upper and lower corners of the left nanoprism. By courtesy of C. Strüber.

where F is the two-photon photoemission yield (i.e., excitation with polarization-shaped pump and transform-limited probe pulse in temporal overlap) averaged over the ROIs and $\varphi_1(\omega)$ and $\varphi_2(\omega)$ are the spectral phases applied to layer 1 and 2 of the pulse shaper, respectively. Maximization and minimization of Eq. (5.1) corresponds to localization of the photoemission at the upper and lower corner of the left nanoprism, respectively.

Figure 5.3 shows PEEM images of the complete array of the twelve investigated BTAs. The photoemission yield of the one-photon UV PEEM image is shown in Fig. 5.3a. A uniform distribution over the nanostructures' surfaces is observed. Rows A, B, and C indicate the three different BTA gap sizes of 300, 200, and 100 nm, respectively. Each row contains four BTAs (1–4) that are identical to the extend of fabrication. Their two-photon PEEM images obtained for excitation with an unshaped pump together with a transform-limited probe pulse are shown in Fig. 5.3b. Similarities as well as observable differences are revealed. For example, the nanoantennas A1 and A3 show stronger hot spots localized in the upper and lower corners of the left triangle, respectively. A2, on the other hand, shows detectable signal yield from both spots. Additionally, no resonant

effect of the coupling of the nanoprisms acting as a BTA is observed. For resonant excitation of the BTAs, the field enhancement should increase with decreasing gap size. However, the opposite trend is observed, BTAs with a gap size of 100 nm, i.e., row C, show small photoemission, whereas the BTAs with larger gap sizes, i.e., rows A and B, show spots with high photoemission. Hence, the excitation frequency of the pump pulse is assumed to be resonant with a single nanoprism but not resonant with the coupled BTA.

To define the feedback for the adaptive optimizations, the nanoantenna A2, also shown as an example in Fig. 5.2, was chosen. The regions of interest were defined as indicated in Fig. 5.2b and the fitness function of Eq. (5.1) was optimized using the evolutionary algorithm.

The two-photon PEEM image that was obtained for excitation with a shaped pump pulse that maximizes the fitness function defined in Eq. (5.1) (i.e., localization of photoemission at the upper corner of A2) together with a transform-limited probe pulse is displayed in Fig. 5.3c. As can be observed, compared to Fig. 5.3b the optimization results in a localization of the photoemission at the upper corner of the left nanoprism of BTA A2 (a zoomed-in image is shown and discussed in the next section). Other BTAs, such as A1, A3, B4 and C1, follow the same trend. However, due to imperfect fabrication, there are also BTAs that do not show localization in the upper corner of the left nanoprism as intended by the optimization. Interestingly, almost all BTAs show higher photoemission at the left nanoprisms than at the right nanoprisms, which is not the case for excitation with an unshaped pump pulse (Fig. 5.3b). The two-photon image obtained for minimizing the fitness function of Eq. (5.1), i.e., localization of photoemission at the lower corner of A2, is shown in Fig. 5.3d. Compared to maximization (cf. Fig. 5.3c), a switching of the photoemission to the lower corner is observed for BTA A2. Although the localization at the lower corner is not as pronounced for BTA A2, the other BTAs show a more pronounced photoemission localization at the desired corner.

Hence, the adaptive closed-loop control, presented here, allows switching of photoemission separated by 400 nm, i.e., on the order of the diffraction limit. The optimal pump-pulse shapes corresponding to maximization and minimization are shown and discussed together with the pulses obtained for deterministic control in Section 5.5.

5.4 Deterministic Switching of Photoemission

In Chapter 4 the knowledge of the control mechanism for spatial near-field control (Section 3.2.1) was used to develop analytic formulas to calculate the optimal phase for guiding the linear flux in nanostructures. Using the fact that the linear flux for phase-only shaping just depends on the phase difference

$$\Phi(\omega) = \varphi_2(\omega) - \varphi_1(\omega), \tag{5.2}$$

of the two polarization components according to the layers 2 and 1 of the pulse shaper, respectively, it was found that the optimal phase differences of two contrary optimizations, e.g., maximization $[\Phi_{\max}(\omega)]$ and minimization $[\Phi_{\min}(\omega)]$ of the fitness function [Eq. (5.1)], is

$$\Delta\Phi(\omega) = \Phi_{\max}(\omega) - \Phi_{\min}(\omega) = \pi. \tag{5.3}$$

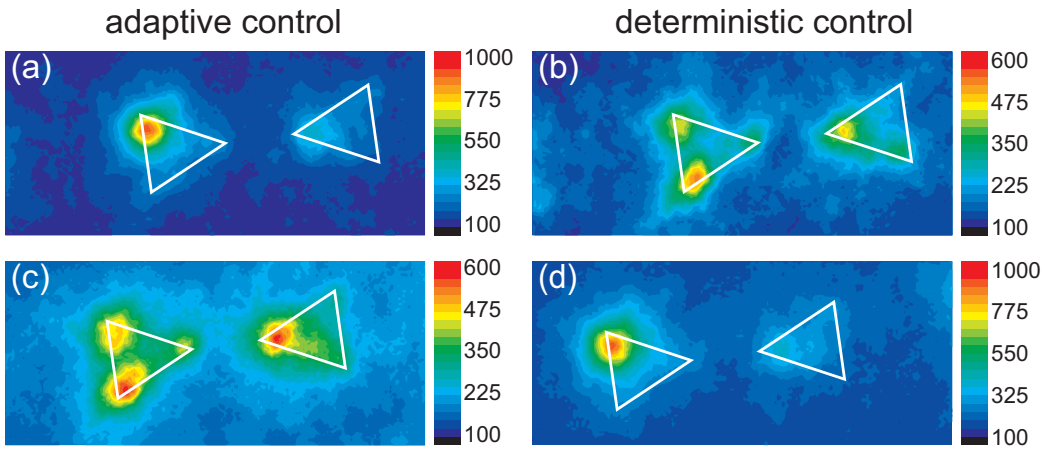

Figure 5.4: Demonstration of deterministic photoemission switching at the two left nanoprism corners of the A2 nanoantenna indicated in Fig. 5.3. The two-photon PEEM images of deterministically (b) minimizing, i.e, localization at the lower corner, and (d) maximizing Eq. (5.1), i.e., localization at the upper corner. The optimal deterministic pulse shapes were calculated from the optimal adaptive pulse shapes inducing the photoemission shown in (a) and (c), respectively, according to the deterministic rule [Eq. (5.3)]. By courtesy of C. Strüber.

Caused by the introduced π spectral phase, the interference of the near-field modes at the corresponding ROIs switches from constructive to destructive interference and vice versa. This results in a switching of the optimization goal, e.g., from maximization to minimization. Hence, by using the adaptively found optimal phase difference of, e.g., maximization of the fitness function, it is possible to calculate the optimal phase difference for the opposite goal, i.e., minimization.

Following this analytic approach, the optimal deterministic pulses were calculated by adding a constant π rad spectral phase to the spectral phase $\varphi_2(\omega)$ of the pulses obtained for the respective opposite adaptive optimizations described in the last section. The resulting two-photon PEEM images of BTA A2 are compared to the images of the adaptive closed-loop optimization in Fig. 5.4. Note that only PEEM images of BTA A2 (cf. Fig. 5.3) are shown and discussed in the following for the sake of clarity. However, as can be inferred from Fig. 5.3, similar results would be obtained by considering a different structure of the array. The two-photon PEEM images of deterministic optimizations for minimizing and maximizing the fitness function of Eq. (5.1) are displayed in Fig. 5.4b and 5.4d, respectively. Comparing them to the two-photon PEEM images obtained for adaptive maximization (Fig. 5.4a) and minimization (Fig. 5.4b), remarkable switching is observed, i.e., from Fig. 5.4a to Fig. 5.4b and from Fig. 5.4c to Fig. 5.4d. Additionally, comparing the two-photon PEEM images of the same optimization goal, i.e., Fig. 5.4a to Fig. 5.4d and Fig. 5.4b to Fig. 5.4c, very similar two-photon PEEM patterns were obtained. This indicates that the two different approaches, i.e., deterministic and adaptive optimization, yield the same excitation pump pulses.

The optimal fitness values for adaptive and deterministic optimizations are summarized in Table 5.1. The values are calculated using the two-photon PEEM patterns

Table 5.1: Averaged photoemission yield over ROI-1 and ROI-2 (first and second column) and the fitness values calculated via Eq. (5.1) (third column) of adaptive (second and fourth row) and deterministic control (third and fifth row). For comparison the values are also given for an unshaped reference pulse (first row). Additionally, the inverse of the fitness values obtained for minimization are given in the last column.

	$F_{\text{ROI-1}}$	$F_{\text{ROI-2}}$	$f[\varphi_1(\omega), \varphi_2(\omega)]$	$f[\varphi_1(\omega), \varphi_2(\omega)]^{-1}$
Reference	788.48	546.08	1.444	-
adaptive maximization	758.80	133.66	5.677	-
deterministic maximization	716.92	201.00	3.567	-
adaptive minimization	305.64	389.04	0.786	1.272
deterministic minimization	294.36	390.16	0.754	1.326

shown in Figs. 5.2b and 5.4. Compared to the reference value (unshaped pump-pulse excitation) all values clearly show the control, i.e., $f[\varphi_1(\omega), \varphi_2(\omega)] > 1.444$ for maximization and $f[\varphi_1(\omega), \varphi_2(\omega)] < 1.444$ minimization. Although the photoemission patterns for maximization (Figs. 5.4a and Figs. 5.4d) are very similar, the maximization was better achieved for the adaptive optimization $\{f[\varphi_1(\omega), \varphi_2(\omega)] = 5.677\}$ than for the deterministic control $\{f[\varphi_1(\omega), \varphi_2(\omega)] = 3.567\}$. Interestingly, the opposite behavior is observed for minimization: The performance of the adaptive minimization is not as good as the deterministic minimization, i.e., the fitness value of the deterministic optimization $f[\varphi_1(\omega), \varphi_2(\omega)] = 0.754$ is smaller than the value for adaptive optimization $f[\varphi_1(\omega), \varphi_2(\omega)] = 0.786$. This characteristic can be understood by recalling the approach that was used for the deterministic optimization: To obtain the optimal phases for the deterministic minimization the optimal phases of the adaptive maximization were used and vice versa. Hence, the adaptive minimization seems to have a poorer performance than the adaptive maximization since the deterministic minimization that is gained from the adaptive maximization has a smaller fitness value than the adaptive minimization. Contrary, the adaptive maximization has a larger fitness value than the deterministic maximization. This observation reveals the advantage of the deterministic approach: If a certain adaptive optimization, e.g., minimization, leads to a poor result, the opposite adaptive optimization, i.e., maximization, might be used to enhance the performance of the original optimization, i.e., minimization.

Comparing the inverse of the fitness values of minimizations, i.e., the last column in Table 5.1, to the fitness values of the maximizations, reflects that it was not possible the achieve the same degree of localization for the two contrary optimizations. This can be explained by two different effects. On the one hand, the imperfection of fabrication already leads to unequal photoemission yield in the two ROIS for the unshaped reference pulse (cf. Fig. 5.2b) and this can also influence the degree of localization for the optimized pulses. On the other hand, due to the limited number of pulse shapes that can be produced with the used pulse shaper, it might not be possible to find a pulse shape that localizes the photoemission yield for minimization as good as for maximization.

The observed results of deterministic control confirm the assumption that two different near-field modes are excited with the two polarization components of the laser pulse. Using the deterministic rule [Eq. (5.3)] the near-field modes are adjusted to either interfere constructively or destructively at the ROIs. The properties of the corresponding optimal pump pulses are shown and discussed in the next section.

5.5 Comparison of Adaptively and Deterministically Obtained Pulse Shapes

In this section three different representations are chosen to compare and discuss the obtained pulse shapes for deterministic and adaptive control.

The quasi-3D representations (Section 2.2.2) of the optimal pulse shapes corresponding to the control targets of Figs. 5.4a–5.4d are shown from −100 fs to 100 fs in Figs. 5.5a–5.5d, respectively. The time limits are chosen to include the frequency-doubled probe pulse (30 fs FWHM), which arrives at 0 fs on this scale, i.e., at the position of the axes. E_1 and E_2 are the temporal profiles of the two polarization components of the electric field corresponding to p and s polarization indicated in Fig. 5.2, respectively. The direction of the layers 1 and 2 of the pulse shaper correspond to $-45°$ and $45°$, respectively. As explained in the last section, the deterministically optimized pulses are derived by adding a spectral phase of π rad to the phase $\varphi_2(\omega)$ of the optimal pulses found by adaptive optimization. Hence, the relative phase of the adaptive pulse shape in Fig. 5.5a was shifted by π and the resulting deterministic pulse shape is shown in Fig. 5.5b. As can be observed the temporal profile of the total intensity is very similar. However, the polarization state is changed from approximately circular polarization in the overlap with the probe pulse to linear polarization oriented along $-45°$ with respect to the E_1 and E_2-axis. The shifted deterministic pulse shape of Fig. 5.5c is shown in Fig. 5.5d. Here, the pulse switches from elliptical polarization to approximately circular polarization. Comparing the optimal pump pulse shapes of deterministic and adaptive maximization, i.e., Figs. 5.5d and 5.5a, respectively, reveal similar circular polarization of both pulses in the overlap with the probe pulse. However, for the pulse shapes of deterministic (Fig. 5.5b) and adaptive minimization (Fig. 5.5c) differences in terms of their polarization state are observed, i.e., elliptical versus linear polarization, respectively.

For a better understanding of the polarization state evolution, the pulses are also plotted on the Poincaré surface (Section 2.2.2) in Fig. 5.6. In this representation the center of the Poincaré surface, i.e., point $(0, 0)$, indicates linear p polarization and the points $(-\pi/4, 0)$ and $(\pi/4, 0)$ correspond to the polarization directions along layer 1 and 2 of the pulse shaper, respectively.

The adaptively and deterministically optimized pulses are depicted as red and blue symbols, respectively. Circles indicate maximization of the fitness function, whereas diamonds indicate minimization. The pulses are shown for a temporal region from −30 to 30 fs, which corresponds to the region of significant overlap with the frequency-doubled probe pulse (30 fs FWHM) that provides the largest contribution to the time-averaged photoemission signals. Incidentally, this also corresponds to the region of high intensity

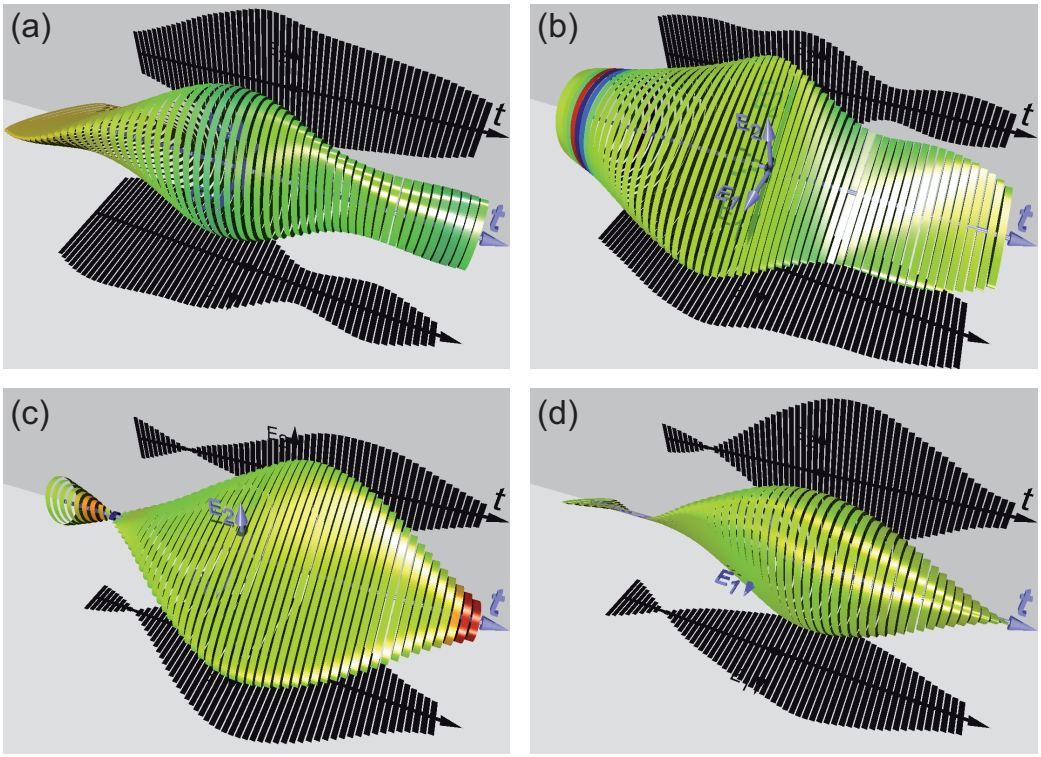

Figure 5.5: Quasi-3D representation of the optimal pump pulses as obtained for optimizations described in Sections 5.3 and 5.4. The optimal pulses displayed in (a)–(d) are used to excite the photoemission patterns of BTA A2 shown in Figs. 5.4a–5.4d, respectively. (a) and (c) Optimal pump pulses obtained for adaptive minimization and maximization, respectively. (b) and (d) Optimal pump pulses obtained for deterministic minimization and maximization, respectively. The time axes are plotted from −100 fs to 100 fs, where 0 fs corresponds to the arrival time of the probe pulse. The temporal separation of two adjacent ellipses is 3.47 fs. Polarizations E_1 and E_2 correspond to p and s polarizations, respectively.

of the shaped pump pulses. This is an indication of the correct scheme of two-photon photoemission and good convergence of the evolutionary algorithm.

The agreement of the optimal pulses for adaptive closed-loop (Fig. 5.5a) and deterministic open-loop maximization (Fig. 5.5d) observed in the quasi-3D representation is confirmed by the overlap of their Poincaré curves (circles) in regions of maximum intensity, i.e., in regions of saturated color. Although the polarization state is expected to be mostly circular from the quasi-3D representations, elliptical light is observed on the Poincaré surface, i.e., $\varepsilon \approx \pi/8$. However, in contrast to the quasi-3D representations of the optimal pulses of adaptive (Fig. 5.5c) and deterministic minimization (Fig 5.5b), showing differences of the polarization state in terms of elliptical and linear polarization, respectively, the Poincaré curves (diamonds) reveal a good agreement at approximately linear polarization. Again, both curves overlap in regions of maximum intensity. It is important to point out that two different approaches of optimization, i.e., deterministic and adaptive control, are compared and therefore the observed agreement is remarkable.

Neglecting effects of the Jones matrix, application of a π phase shift would result in

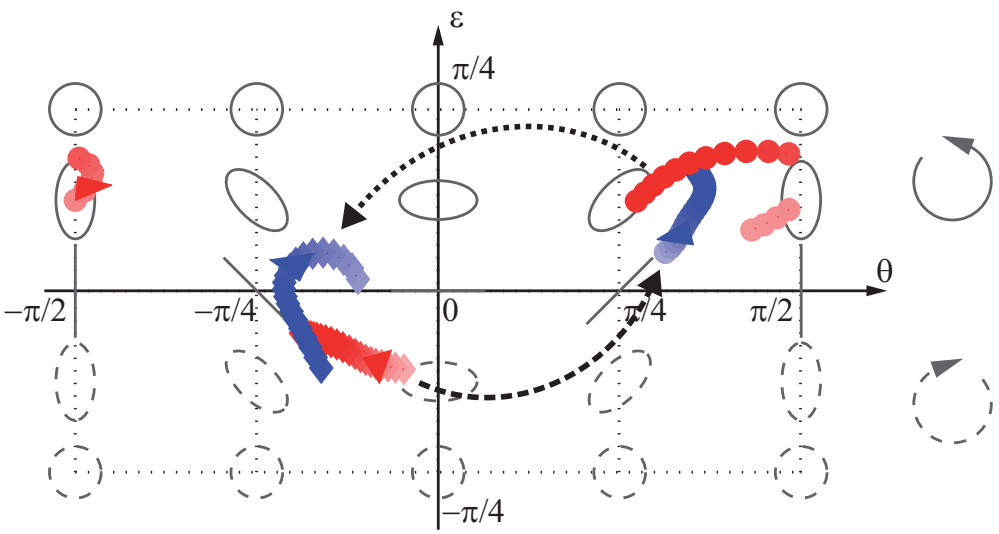

Figure 5.6: Optimal pump pulses derived either by deterministic open-loop (blue symbols) or adaptive closed-loop control (red symbols) represented in the Poincaré plane. Maximizations and minimizations are indicated with circles and diamonds, respectively. As described in Section 5.4 the pulse shapes for deterministic open-loop maximization (blue circles, Fig. 5.5d) and minimization (blue diamonds, Fig. 5.5b) are calculated from the pulse shapes of adaptive closed-loop minimization (red diamonds, Fig. 5.5c) and maximization (red circles, Fig. 5.5a), respectively. The curves cover a time range from -30 to 30 fs, corresponding to the complete temporal overlap with the probe pulse arriving at 0 fs. The temporal separation between adjacent symbols in 3.47 fs and the color saturation reflects the normalized total intensity. The center of the Poincaré surface (0,0) corresponds to p polarization.

an inversion of the pulse with respect to the position of linear polarization along layer 1 of the pulse shaper, i.e., here $(-\pi/4, 0)$, on the Poincaré surface. However, due to the Jones matrix of the used experimental setup (Section 2.4.3) the inversion is not reached. This might also contribute to the better performance of the maximizations with respect to the minimizations. Since the Jones matrix affects the adaptively as well as the deterministically shaped pulses the imperfect inversion does not lesson the obtained results. For further investigation of the phase shift yielding the switching of the photoemission distribution, the polarization state difference ($\Delta\Phi$) of optimal pump pulses controlling the switching between maximization and minimization are shown in Fig. 5.7. The polarization state difference is calculated using the optimal pulse shapes of deterministic switching (blue squares) shown in Figs. 5.5a and Fig. 5.5b and of adaptive switching (red circles) shown in Figs. 5.5a and Fig. 5.5c. As expected from Eq. (5.3), the deterministic switching results in a constant polarization state difference at approximately π. Hence, although the correct polarization state difference was measured the corresponding Poincaré curves do not show an inversion with respect to $(-\pi/4, 0)$. This implies that the imperfect inversion is due to modification of the relative amplitude of the two polarization components introduced by the Jones matrix of the experimental setup. Although the polarization state difference of the adaptive switching does not

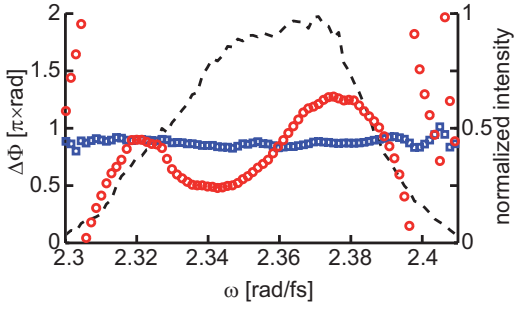

Figure 5.7: Polarization state difference ($\Delta\Phi$) of optimal pump pulses controlling the switching between maximization and minimization. Adaptively optimized switching (red circles) (polarization state difference of the pulses shown in Figs. 5.5a and 5.5c) is compared to deterministically optimized switching (blue squares) (polarization state difference of the pulses shown in Figs. 5.5a and 5.5b). The normalized laser pulse spectrum is indicated with a dashed line.

show a perfect constant spectral π phase, the trend is observed in the spectral region of high intensity. This is another validation of the deterministic rule developed in Chapter 4, predicting a polarization state difference of π.

5.6 Conclusion and Outlook

In this chapter the experimental implementation of the deterministic rule, of obtaining the opposite optimization goal by adding π to the phase difference of the two incident polarizations, introduced in Chapter 4, was shown. This resulted in experimental demonstration of optimal deterministic control of nanooptical excitations.

First, adaptive optimizations of the photoemission pattern of a BTA were performed and the spatial switching of photoemission hot spots between the upper and lower triangle corners was achieved. Following the analytic expectations the switching was then achieved as well by applying the π phase shift to one polarization component. Comparison of the adaptive and deterministic pulse shapes revealed a good agreement, i.e., the pairs of pulses corresponding to the optimizations of the same control targets using two different approaches showed similar states of polarization. It is notable that the optimal pulse for the signal localization in the upper corner tended to be elliptically polarized, while that for the lower part was more linearly polarized. Applying the π phase shift was expected to yield an inversion on the Poincaré surface which was not perfect in the present example. The linear polarization may thus be due to the Jones matrix limitations of the current pulse shaper setup and could be overcome using a full vector field synthesizer (Section 2.3.4) which is capable of shaping all degrees of freedom such as phase, amplitude and polarization state of laser pulses simultaneously. In spite of these imperfections, however, the evolutionary algorithm still found both optimal pulses which provide a good degree of control, and whose polarization states differ approximately by π.

Although the deterministic control was applied here to achieve near-field switching in a gold BTA, the method is general and is not restricted to that particular geometry. If the

optical response function of a plasmonic nanostructure is not known, the deterministic approach may be used together with an adaptive optimization to achieve near-field control and switching. However, as for the deterministic maximization achieved here, the result can only be as good as the adaptive optimization. If the complete spectral response is known, the first adaptive optimization step is not necessary and direct application of the analytically derived formulas of Chapter 4 yield optimal control. In addition, the achieved nanoscale switching demonstrates experimentally the proposed optical near-field control via the local interference of different near-field modes driven by the two independent incident polarization components. These modes can be propagating as well as localized modes.

Near-field control by deterministic pulse shaping is expected to improve the controllability of ultrafast nanooptical light–matter interactions and—fitting to the tenor of the thesis—will enable subdiffraction excitation schemes that might be used in the future for spectroscopic applications. Additionally, it will help to design novel nanoplasmonic devices that can improve the excitation schemes in nanoscopic ultrafast space–time-resolved spectroscopy. Also, it can improve active control of plasmonic nanocircuits and development of single-molecule and nanoplasmonic biosensors. High degree of near-field control in plasmonic nanostructures such as antennas, waveguides, and metamaterials might be achieved. The deterministic scheme may also be useful for other scenarios, such as coherent control of molecules, when suitable response functions are available either through calculation or from (nonlinear) spectroscopic experiments.

6 Coherent Control of Near Fields on a Rough Silver Surface

In this chapter, polarization pulse shaping is used to control the near fields on a corrugated silver surface and thereby investigate the plasmonic properties of the random surface. Adaptive optimizations are performed to control and switch the near field distribution for spatial regions that are separated above and below the diffraction limit (Section 6.3). To gain further insight into underlying control mechanisms a two-parameter scan is carried out (Section 6.4). Interesting and unexpected effects are observed in terms of the temporal profile of the optimal pulse shapes.

The work that is presented in this chapter resulted from the same collaboration that was described in Chapter 5.

6.1 Introduction

Applications of the well-established methods of coherent control [135, 136] to the growing field of ultrafast nanooptics [106] resulted in a number of successful theoretical [11, 47, 114] and experimental [13, 14] achievements. These methods that were originally developed for controlling atoms and molecules can now be applied to plasmonic nanostructures such as resonant optical nanoantennas [84, 134] and nanophotonic circuitry [108, 137], nanoplasmonic waveguides and surfaces, and even artificial plasmonic "atoms" and "molecules" [138]. Near-field enhancement due to light concentration by these nanostructures has been thoroughly investigated offering a large variety of novel applications in nanophotonics, single-molecule applications [133, 139], and manipulation of light-matter interactions simultaneously on the ultrafast temporal and subwavelength spatial scale [11, 14, 47]. An interesting question is how well the currently developed concepts in the field of coherent control can be transferred to nanoplasmonics, and, on the other hand, if any new insights about control itself may be obtained from these investigations. For example, the questions of optimal pulse-shape interpretation and topological structure of the control landscapes are still open areas of active research [140]. Quantum control of complex atomic and molecular systems in condensed phase often yields optimal laser pulse shapes that are too complicated for unambiguous interpretation. On the other hand, as has been shown in Chapters 4 and 5, in nanoplasmonics the interpretation of optimal laser pulse shapes in terms of plasmonic nanostructure responses [48] and their analytic determination can be theoretically described. This analytic approach was then used to simulate the switching of plasmon propagation directions in a branched plasmonic nanoparticle chain waveguide. In this chapter, however, it is not possible to directly apply these concepts and interpret pulse shapes due to the absence of direct

information about the spectral response of the random silver surface investigated here. Alternative approaches, such as predetermined few-parameter scans, have to be used to obtain some insight into the pulse shapes and underlying control mechanisms.

Hot spots on deterministic and randomly structured metal surfaces were found responsible for the increase of the optical signals by many orders of magnitude in the field of ultrasensitive optical spectroscopy. For example, Raman spectroscopic signals from molecules placed on silver surfaces may be enhanced dramatically and single-molecule sensitivity is reached [54, 83, 141, 142]. The highest surface-enhanced Raman signal enhancements have been obtained using randomly structured silver surfaces. However, the drawbacks are the unpredictability of hot spot locations, difficulties in reproducible sample fabrication, and control of the resulting hot spots. One of the mechanisms explaining their high optical signal enhancement is due to the strongly enhanced near fields from the superposition of multiple surface plasmon resonances that can exist in random silver surfaces [54].

The possibility to control the photoemission hot spots in deterministic silver nanostructures by laser pulse shaping was demonstrated [13]. There, it was possible to control the ratio of the two-photon photoemission signals from different spatial locations. Here, these investigations are extended to a more complex structure, a randomly structured corrugated silver surface, and controllability of hot spots separated above and below the diffraction limit is demonstrated. In the case of a small distance separation it may be advantageous to gain control that allows switching hot spots or shaping and focusing the local field enhancement. As already described in Chapters 4 and 5, it might be useful to have two hot spots as close as possible to each other and have a control of their ratio with an ultrafast temporal resolution in order to perform a nanoscopic ultrafast space–time-resolved pump–probe spectroscopy.

Prior to application of local field control several questions have to be addressed. In addition to the controllability the underlying control mechanism, the degrees of freedom in the control and the reproducibility of adaptive control schemes need investigation. Relevant questions that arise are the number of global and local optima in the control landscape, size of available control parameter space, and convergence and reproducibility of sequential identical optimizations. Answering these questions may give insight into the significance of various features of optimal pulses, on limitations of pulse shaping apparatus and controllability of specific nanostructures, and will play a decisive role in developing future applications. These questions are addressed here by using a corrugated silver surface providing a “random” nanostructure.

6.2 Experimental Setup and Sample Characteristics

The investigation of enhancement of optical near fields in a spatially resolved manner was done by employing photoemission electron microscopy (PEEM) where the sample was illuminated with polarization-shaped femtosecond laser pulses. A schematic of the experimental setup is shown in Fig. 6.1. The setup is similar to the setup described in Chapter 5 with the difference that no frequency-doubled probe pulse was used. Light pulses were generated by a Ti:Sapphire oscillator (80 MHz, 795 nm, 30 fs FWHM), beam-

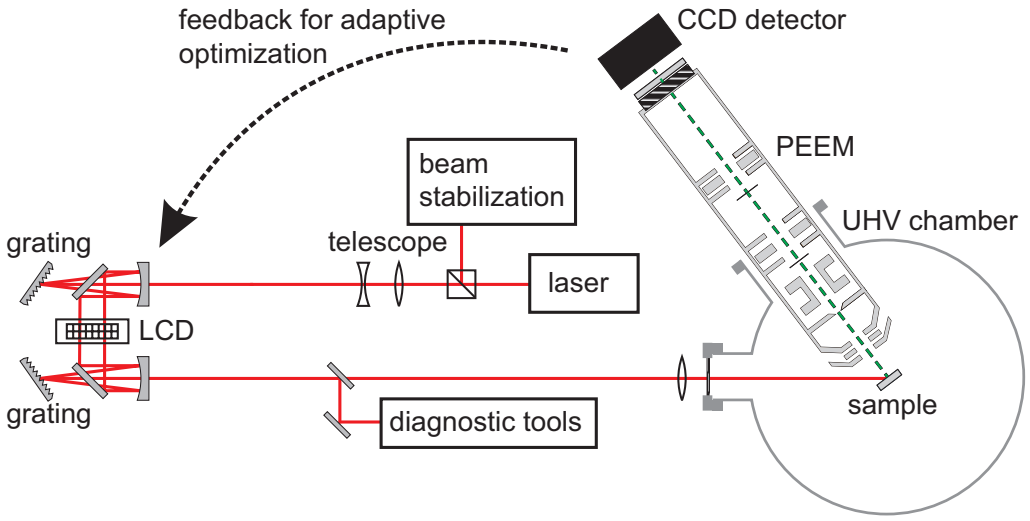

Figure 6.1: Photoemission power dependence of the corrugated silver surface. (a) Contour plot of the photoelectron emission distribution illuminated with an unshaped laser pulse (52.8 mW). (b) The average photoelectron emission yield of the three regions of interest (ROI) indicated with blue circles (ROI-A), green squares (ROI-B) and red triangles (ROI-C) is plotted versus the intensity of the exciting unshaped laser pulse. For comparison a third order power dependence is indicated with a solid black line. Taken from Aeschlimann *et al.* [143]. Copyright (2011) by IEEE.

pointing stabilized, and sent through a polarization pulse shaper (Section 2.3.2). Due to the Jones-matrix of the pulse shaper the transform limited pulse after the pulse shaper had a duration of 50 fs. The polarization-shaped pulses interact with the silver surface at 65° angle of incidence inside the UHV chamber of the PEEM. The adaptive optimized pulses shown in Section 6.3 were characterized using dual-channel spectral interferometry (Section 2.4.2) with reference pulses measured via FROG (Section 2.4.1). As can be observed from Fig. 6.1, the pulses were characterized outside the UHV chamber. Characterization at the position of the sample was not possible since the required characterization tools could not be placed into the chamber. However, since only two additional mirrors were used to guide the beam to the position of characterization, the deviations of the measured pulses are assumed to be small as compared to the pulses impinging on the sample. The optimal pulses of the two-parameter scan shown in Section 6.4 were calculated using the measured Jones-matrix of the experimental setup (Section 2.4.3).

The sample in the presented experiment was a corrugated silver surface prepared by repeated Ar^+ sputtering to eliminate surface contamination. A scanning electron microscope image of an exemplary region of the silver surface is shown in Fig. 6.2, where the brightness of the image reflects the topography of the surface. Structures from several µm down to sizes below 1 µm are observed.

As for the adaptive optimizations described in Chapter 5 an evolutionary algorithm was used here (Section 2.5). Adaptive optimizations were performed using a feedback that is defined via the measured PEEM patterns. Again, independent spectral phase

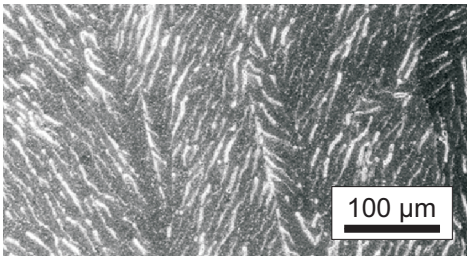

Figure 6.2: Scanning electron microscope image of the corrugated silver surface prepared by repeated Ar^+ sputtering and heating cycles. The brightness of the image indicates the topography of the surface, where locations with white color reflect regions of higher topography and black color indicates lower topography. Taken from Aeschlimann *et al.* [143]. Copyright (2011) by IEEE.

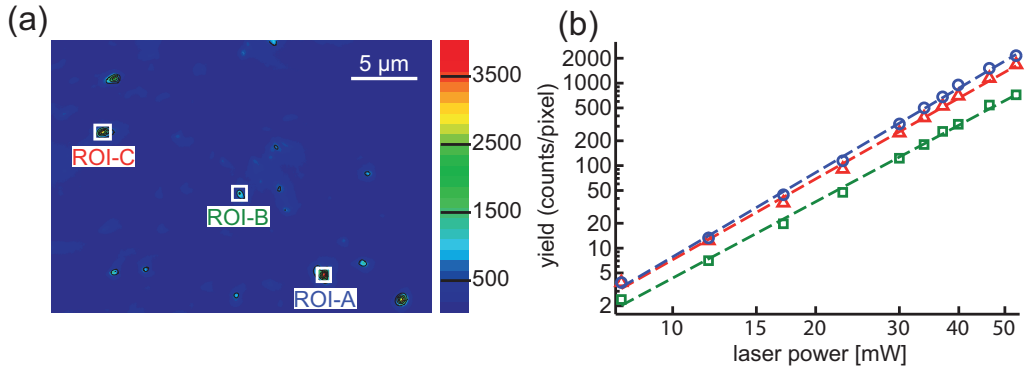

Figure 6.3: Photoemission power dependence of the corrugated silver surface. (a) Contour plot of the photoelectron emission distribution illuminated with an unshaped laser pulse (52.8 mW). Three regions of interest (ROI) are indicated with white rectangles. (b) The average photoelectron emission yield of these ROIs indicated with blue circles (ROI-A), green squares (ROI-B) and red triangles (ROI-C) is plotted versus the power of the exciting unshaped (i.e., transform-limited) laser pulse. Fitting of the data points (dashed lines) results in power dependence orders of 3.39, 3.07 and 3.25 for ROI-A, ROI-B and ROI-C, respectively. Note that both axis are plotted logarithmically.

shaping of each polarization component was performed, i.e., spectral amplitude modulation was only introduced by the Jones matrix of the setup (Section 2.4.3). The spectral phases $\varphi_i(\omega)$ were parameterized independently in the dispersion basis using eleven independent parameter genes. Using forty individuals per generation, convergence was reached after 20–40 generations.

The photoelectron emission distribution of a small region of the sample is depicted in Fig. 6.3a. Here, the silver surface was excited with transform-limited laser pulses with a power of 52.8 mW. Several hot spots, i.e., regions with enhanced photoelectron emission, are observed. This behavior can be explained by strong enhancement of the optical near field in the corresponding regions resulting from resonant structures on the surface (Section 3.1.2). Since the sample was a rough silver surface, a direct assignment of the topology of the surface to the resonant structures is not possible, i.e., it is not possible to assign the hot spots of Fig. 6.3a to regions in the scanning electron microscope

image Fig. 6.2. Although the dimensions of the resonant structure could not be measured directly, due to the effective wavelength scaling in silver nanostructures [113] they are expected to be smaller than half the wavelength of the exciting field.

To investigate the power dependence of the photoelectron emission, i.e., how many photons are needed to emit an electron from the sample (Section 2.6.1), the photoelectron emission of three exemplary hot spots (ROI-A, ROI-B and ROI-C in Fig. 6.3a) was measured as a function of laser power. Figure 6.3b shows the average photoelectron emission yield of the regions, i.e., blue circles, green squares and red triangles corresponding to ROI-A, ROI-B and ROI-C, respectively, plotted versus the power of the excitation laser. Note that both axes are plotted logarithmically. The order of the power dependence is determined by linear fits (dashed lines in Fig. 6.3b) through the logarithmically scaled data points. This results in power dependence orders of 3.39 (ROI-A), 3.07 (ROI-B) and 3.25 (ROI-C). Although the values show small deviations a third-order power dependence can be assumed for all hot spots, i.e., three photons are needed to emit an electron. Due to the nonlinearity of the photoemission serving as the feedback signal for the optimizations, deterministic control as it was utilized in Chapter 5 cannot be conducted here. Contrary, both mechanisms for the near-field control have to be considered (Section 3.2), i.e., spatial control via the relative phase between both incident field polarization components and temporal control via the remaining spectral phase offset of the laser pulse.

6.3 Adaptive Near-Field Control

6.3.1 Near-Field Superenhancement

The PEEM image for a detailed area of the corrugated silver surface is shown in Fig. 6.4a as obtained with unshaped transform-limited femtosecond laser pulse excitation. As in Fig. 6.3a the PEEM images reveal several hot spots, where stronger optical fields initiate larger photoemission signals whose distribution patterns are mapped with a resolution below 50 nm. An area with several hot spots in relative vicinity was chosen here and adaptive pulse shaping was then applied in order to manipulate the ratio of the photoemission intensities from these hot spots. The optimized regions of interest ROI-1 and ROI-2 are shown as red solid and yellow dashed rectangles, respectively, and are separated by about 500 nm.

To demonstrate near-field localization and enhancement of a specific hot spot, the multiphoton photoemission was adaptively optimized in ROI-1 and suppressed in ROI-2 (Fig. 6.4c). As a particular optimization goal the photoemission ratio from ROI-1 and ROI-2 in Fig. 6.4a was selected. The corresponding fitness function was defined as

$$f[\varphi_1(\omega), \varphi_2(\omega)] = \frac{F_{\text{ROI-1}}}{F_{\text{ROI-2}}}, \tag{6.1}$$

where F is the time-integrated average photoemission yield of the respective regions of interest.

Figure 6.4c and 6.4e show the results of adaptive maximization and minimization, respectively, of the fitness function defined in Eq. (6.1). Clear switching of the spatial

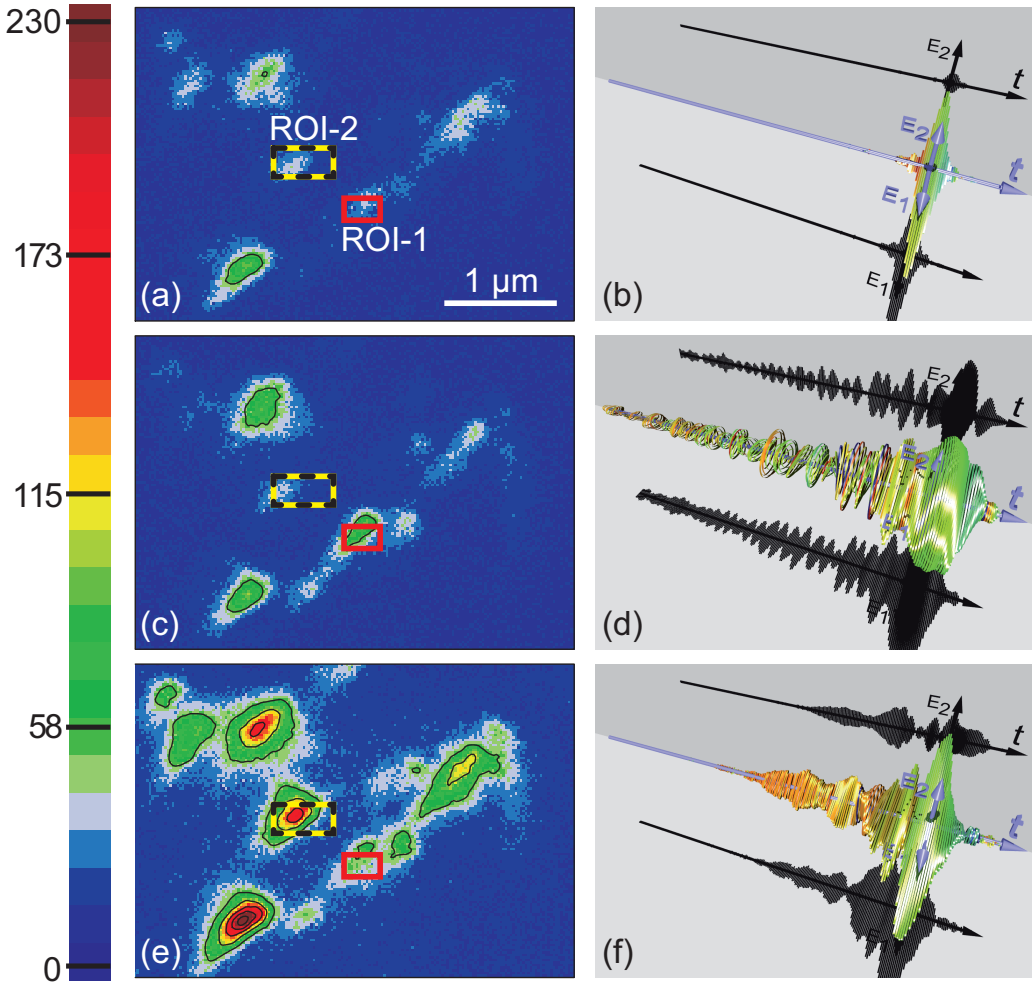

Figure 6.4: Near-field control. (a,c,e) The photoelectron emission distributions are shown as obtained with (a) an unshaped transform-limited pulse and adaptively optimized pulses (c) maximizing and (e) minimizing the ratio of the ROIs [Eq. (6.1)]. The red solid and yellow dashed rectangles represent ROI-1 and ROI-2, respectively. All three images show the same spatial region with the same color map indicated on the left. (b,d,f) Quasi-3D representation (Section 2.2.2) of the laser pulses obtained for optimization of Eq. (6.1) indicated with the time axis ranging from −1800 fs to 300 fs and a temporal separation of the ellipses of 8.7 fs. All pulses are normalized to their individual maximum. (b) Unshaped transform-limited reference pulse is linearly polarized. (d) Optimal polarization-shaped pulse for the maximization and (f) optimal pulse for minimization of Eq. (6.1). Taken from Aeschlimann *et al.* [143]. Copyright (2011) by IEEE.

local field distributions between the selected locations is observed, i.e., in Fig. 6.4c the yield from ROI-1 is higher than from ROI-2 and vice versa in Fig. 6.4e. Surprisingly, in addition to this relative control, the total nonlinear photoemission yield is increased for the target location with respect to the unshaped reference, i.e., ROI-1 has higher yield in Fig. 6.4c than in Fig. 6.4a, and ROI-2 has higher yield in Fig. 6.4e than in Fig. 6.4a. Note that the color scale is identical for all three plots. Even though the pulse shapes are

tailored to optimize the ratio of two hot spots an increased total yield from both spots is obtained. In addition to the optimized regions also the yield of other hot spots in the vicinity was increased. Hence, the optimizations result in a collective enhancement of several hot spots. The enhancement factor of the total yield of up to three is an intriguing phenomenon because often in coherent control the improvement of contrast between two channels, i.e., here the two regions of interest, is obtained at the expense of total efficiency. For example, in the case of purely nonresonant three-photon excitation, the maximum total yield would always be achieved with a bandwidth-limited laser pulse. Here, however, complex-shaped pulses are superior. It has already been shown for control of multiphoton excitation in atoms that intermediate resonances cause transform-limited pulses not to be optimal for excitation, and shaped pulses to increase total yield [144]. In the present case, therefore, it might be possible to obtain insight into these coherences by analyzing the shapes of the optimal pulses.

In accordance with the definition of the term "superradiance" that is related to collective phenomena of the surrounding medium in the process of radiation emission in the following the term "superenhancement" is used for the observed phenomenon. This shall convey the experimental observation of an unexpected strong multiphoton photoemission enhancement, for which the neighboring areas and hot spots of an individual hot spot seem to be crucial.

The polarization-shaped laser pulses of the optimizations discussed above are shown in quasi-3D representations (Section 2.2.2) in Fig. 6.4d and 6.4f. The temporal pulse shapes are given by a sequence of ellipses for different moments in time (separated by 8.7 fs) in a slowly varying envelope approximation. The two perpendicular polarization components E_1 and E_2 correspond to p and s-polarization in the laboratory frame (as indicated in Fig. 2.17), respectively, and are shown as projection shadows. The momentary frequency is indicated by color. The plots share the same time axis from -1800 fs to 300 fs, but are normalized according to their individual peak intensities.

The unshaped reference pulse (Fig. 6.4b) that caused the PEEM signal of Fig. 6.4a has a duration of 50 fs. By contrast, both of the optimal pulses for maximization (Fig. 6.4c) and minimization (Fig. 6.4e) of Eq. (6.1) result in rather complex pulse shapes extending over much longer times. Both optimal pulses in Fig. 6.4d and 6.4f reveal a strong negative third-order dispersion (TOD) leading to a train of prepulses. However, the details are different and they show different complex evolutions of the polarization state. These results are unexpected due to the ultrashort coherence times of localized nanoplasmonic excitations reported in literature [92, 145–148]. Experiments to control nonlinear phenomena in random or disordered metal nanostructures reveal coherences with lifetimes of less than 20 fs [118, 149]. In addition, the stretching of the pulse over several hundred femtoseconds reduces the maximum field intensity and should therefore dramatically decrease the multiphoton photoemission efficiency. On the other hand, if different subpulses of the train are expected to contribute coherently to the optimizations, the coherence has to survive long enough such that the resonant intermediate states can contribute [144]. The pulse durations observed here are on the order of several hundred femtoseconds. According to the knowledge about the short lifetime of localized surface plasmon modes [92, 145–148] these modes can definitely not account for the observed hot spot control and superenhancement.

Although the TOD obviously has the main impact on the strong photoemission the effect of the polarization of the laser pulse cannot be neglected and might also contribute to the photoemission. However, due to the limitations of the closed-loop experiment described here, the two contributions can not be distinguished and further investigation of this phenomenon is performed using two-parameter spectral phase scans in Section 6.4. Other nontrivial contributions to the complex pulse shapes may arise from the randomness of the rough silver surface geometry and dynamics associated with interference of near-field modes that are excited at different spatial positions.

6.3.2 Near-Field Control Below the Diffraction Limit

Next, subwavelength near-field control on the nanoscale was considered. For this purpose, a single hot spot with a photoemission pattern that was spread over a region of $\sim(200\,\mathrm{nm})^2$ was investigated (Fig. 6.5a). Two ROIs within this hot spot, i.e., ROI-3 (red solid rectangle) and ROI-4 (black dashed rectangle), that are separated by $\sim$150 nm were chosen. The optimization goal was to localize the photoemission either in ROI-3 or ROI-4 and the fitness function was defined as the ratio of the time-integrated average photoemission yield of the two ROIs:

$$f[\varphi_1(\omega), \varphi_2(\omega)] = \frac{F_{\text{ROI-3}}}{F_{\text{ROI-4}}}. \tag{6.2}$$

Then the same adaptive optimization strategy as aforementioned to control the ratios of photoemission from ROI-1 and ROI-2 was performed, only now spatially separated on a subwavelength scale. The photoemission patterns for maximization (i.e., localization at ROI-3) and minimization (i.e., localization at ROI-4) are shown in Figs. 6.5b and 6.5c, respectively. As can be observed, the ROIs were adjusted for each optimization goal separately. In case of maximization, ROI-4 was enlarged to the left and in case of minimization, ROI-3 was enlarged to the top. However, in both optimizations the bottom side of ROI-3 and right side of ROI-4 were identical. It is important to point out that the adaption of the ROIs did not change the optimization goal, but it turned out to be useful to ensure convergence of the evolutionary algorithm. As can be inferred from Figs. 6.5a and 6.5b, successful optimizations were achieved. For the maximization of Eq. (6.2) the photoemission pattern is strongly confined and the maximum yield is located within ROI-3. For the minimization the photoemission pattern is spread over a larger region but the maximum is again located in the requested ROI. Since the spatial spread of the photoemission pattern is very different for the two optimizations, the single hot spot seems to contain at least two different resonators that were addressed with different pulse shapes. This is an interesting effect that will be investigated in more detail in Chapter 7.

The overall photoemission yield of the maximization is smaller than that of the unshaped pulse and smaller than that of minimization. The overall photoemission yield for minimization is even higher than that of the unshaped pulse. However, in contrast to the optimizations described in Section 6.3.1, where the yield of both optimizations is enhanced drastically with respect to the yield of the unshaped pulse, the enhancement is small.

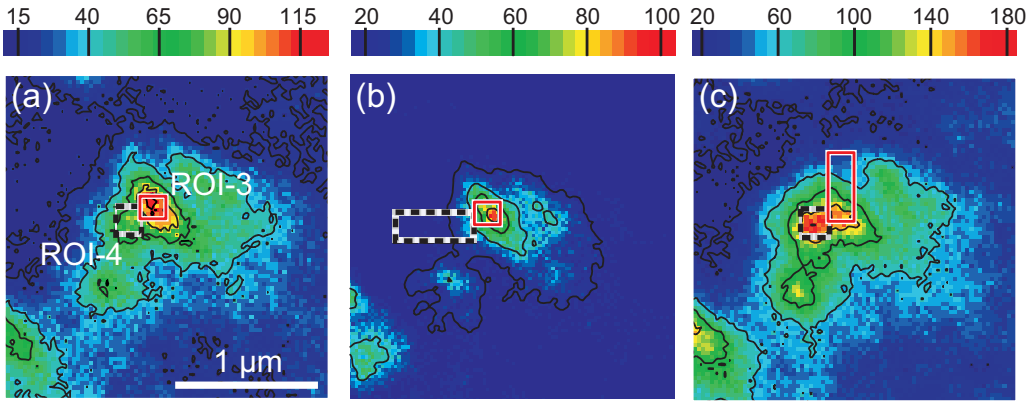

Figure 6.5: Subdiffraction control of the photoemission pattern. (a) The Photoemission yield is shown for an unshaped pulse and ROI-3 and ROI-4 are indicated with red and dashed black rectangles, respectively. The two ROIs are separated by ∼150 nm. (b) Photoemission yield for localization at ROI-3, i.e., maximization of Eq. (6.2), where ROI-4 is enlarged to the left. (c) Photoemission yield for localization at ROI-4, i.e., minimization of Eq. (6.2), the ROI-3 is enlarged to the top. The ROIs are adjusted to ensure convergence of the evolutionary algorithm. All three images show the same spatial region.

6.3.3 Reproducibility of Adaptive Optimizations

The results for maximization obtained in Section 6.3.2 were verified by performing two adaptive optimizations with the identical fitness function and control target. The resulting PEEM images are shown in Fig. 6.6a (same as Fig. 6.5b) and 6.6c. The photoelectron emission distributions are almost identical, and the corresponding optimal laser pulse shapes in Fig. 6.6b and 6.6d are also very similar. Long pulses on the order of hundreds of femtoseconds are again observed as in the case of the optimization of well-separated hot spots shown in Fig. 6.4. Many of the optimal pulse features survive, despite their high complexity. This implies that even weak subpulses potentially provide a significant contribution to the control mechanism. Additionally, the similarity of photoelectron emission as well as the pulse shapes indicate convergence to the same optimum on the control landscape.

For further comparison of the two optimized pulses the evolution of polarization states on the Poincaré surface is depicted in Fig. 6.7. As explained in Section 2.2.2 the Poincaré surface contains all possible polarization states of light as defined by the two parameters orientation θ and ellipticity ε. The temporal evolution of the polarization state is represented by points on the Poincaré surface separated by 8.7 fs and runs from −500 fs to 300 fs where the arrowheads indicate the direction of evolution. The total intensity of the pulse shape is indicated by the color saturation. Adaptively optimized pulses from the two subsequent runs (red circles for Fig. 6.6b and blue circles for Fig. 6.6d) overlap in the same regions of the Poincaré plot and, therefore, confirm a good reproducibility.

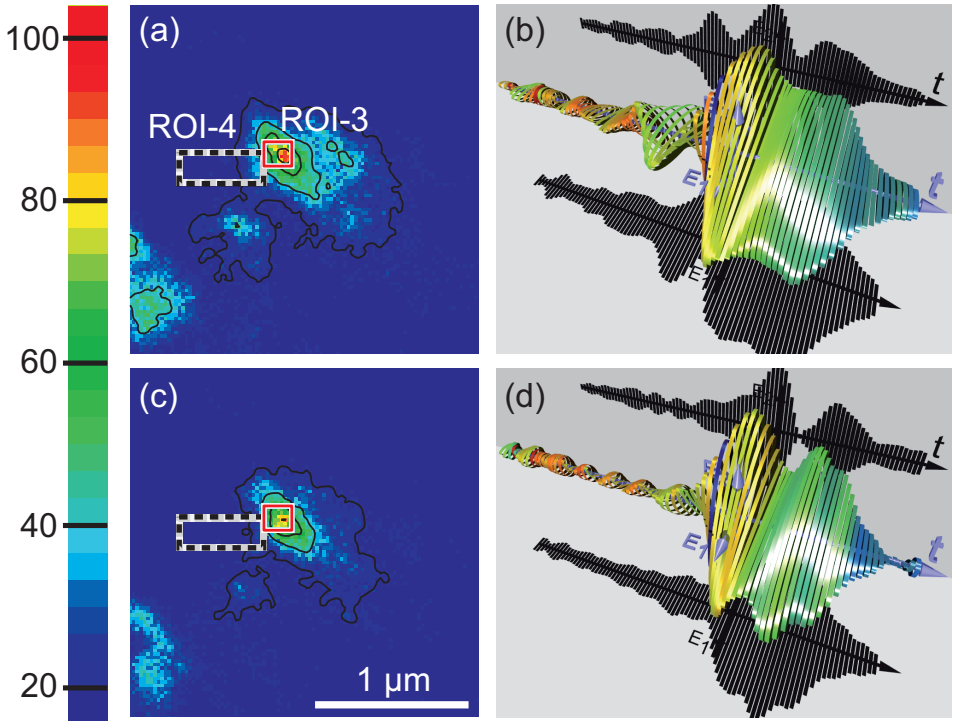

Figure 6.6: Reproducibility of subwavelength near-field coherent control of a hot spot shape. (a) and (c) Adaptively optimized photoemission for two identical repeated optimizations maximizing the fitness function defined in Eq. (6.2). Both images show the same spatial region. (d) and (f) Corresponding optimal laser pulse shapes in a quasi-3D representation are shown for the two subsequent optimizations. Time axes of both pulses run from −500 fs to 300 fs. The temporal separation between two adjacent ellipses is 8.7 fs and the amplitudes of both pulses are normalized to their individual maximum. Taken from Aeschlimann *et al.* [143]. Copyright (2011) by IEEE.

6.4 Two-Parameter Scan

As shown in Section 6.3, adaptive optimizations resulted in complex pulse shapes that are difficult to interpret. The pulse appearance with the prepulse train suggests that third-order dispersion (TOD) might be a dominant control parameter. Therefore, a two-parameter scan was performed to obtain insight into the mechanisms of near-field control on a random surface. One parameter that was scanned is the TOD. This parameter was scanned identically for both polarization layers of the pulse shaper. The other parameter that was scanned is the relative phase $\Phi = \varphi_2 - \varphi_1$ between both pulse shaper layers. The dependences of the multiphoton photoemission for three different ROIs on both parameters are shown in Fig. 6.8.

Again, excitation with an unshaped transform-limited laser pulse leads to field localization and formation of hot spots (Fig. 6.8a). While scanning both parameters of the spectral phase the photoemission yield of all hot spots were recorded simultaneously. The photoemission yields are shown in Figs. 6.8b, 6.8c, and 6.8d for the three hot spots as indicated in Fig. 6.8a by ROI-5, ROI-6, and ROI-7, respectively. Within

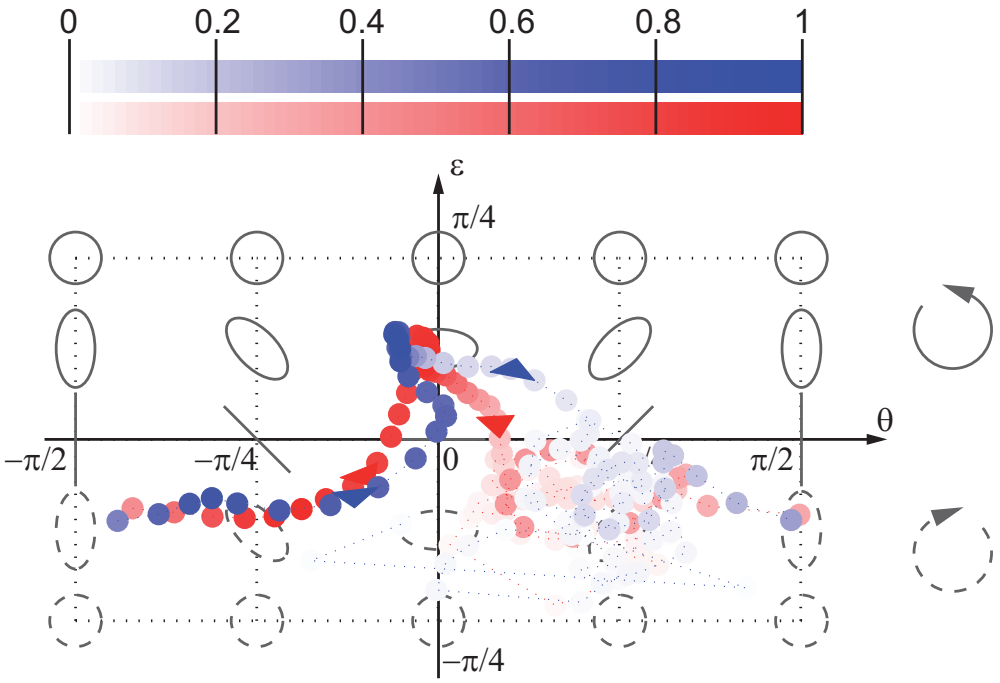

Figure 6.7: Poincaré plot of the pulses of two identical optimizations. The Poincaré curves for the pulses optimizing the fitness function defined in Eq. (6.2) corresponding to the pulses depicted in Figs. 6.6b and 6.6d are plotted as red and blue circles, respectively. As for the quasi-3D representation the Poincaré curves are plotted from −500 fs to 300 fs with the arrowheads indicating the direction of temporal evolution. The temporal separation between adjacent symbols within one curve is 8.7 fs and the color saturation indicates the normalized total intensity of the field at the temporal step. Taken from Aeschlimann *et al.* [143]. Copyright (2011) by IEEE.

these illustrations it is possible to find optimal pulse parameters and compare them for different hot spots. As can be inferred different hot spots show different behavior, i.e., the maximum photoemission yield (blue color in Figs. 6.8b–6.8d) is reached for different parameter values.

The corresponding optimal pulse shapes for each ROI are shown in Figs. 6.9b–6.9d and are compared to an unshaped pulse (Fig. 6.9a). The pulse shapes were calculated using the measured Jones-matrix of the experimental setup (Section 2.4.3) and the temporal separation between two adjacent ellipses is 5.8 fs. While for the hot spot investigated in Fig. 6.8b (ROI-5) maximum emission is reached for an almost bandwidth-limited pulse (Fig. 6.9b), i.e., TOD $= 3.0 \times 10^3\,\mathrm{fs}^3/\mathrm{rad}^2$, the behavior of the photoemission of the hot spots in Fig. 6.8c (ROI-6) and Fig. 6.8d (ROI-7) differs significantly. The optimal pulse shape of the hot spot in ROI-6 (Fig. 6.9c) shows a maximum at a large negative value of TOD $= -14.2 \times 10^3\,\mathrm{fs}^3/\mathrm{rad}^2$ and this leads to a train of prepulses. Contrary, in the case of ROI-7 (Fig. 6.8d), the corresponding optimal pulse shape (Fig. 6.9d) shows a large positive value of TOD $= 17.2 \times 10^3\,\mathrm{fs}^3/\mathrm{rad}^2$ resulting in a train of postpulses. The observation that even the sign of TOD is relevant, reflects the large variability of

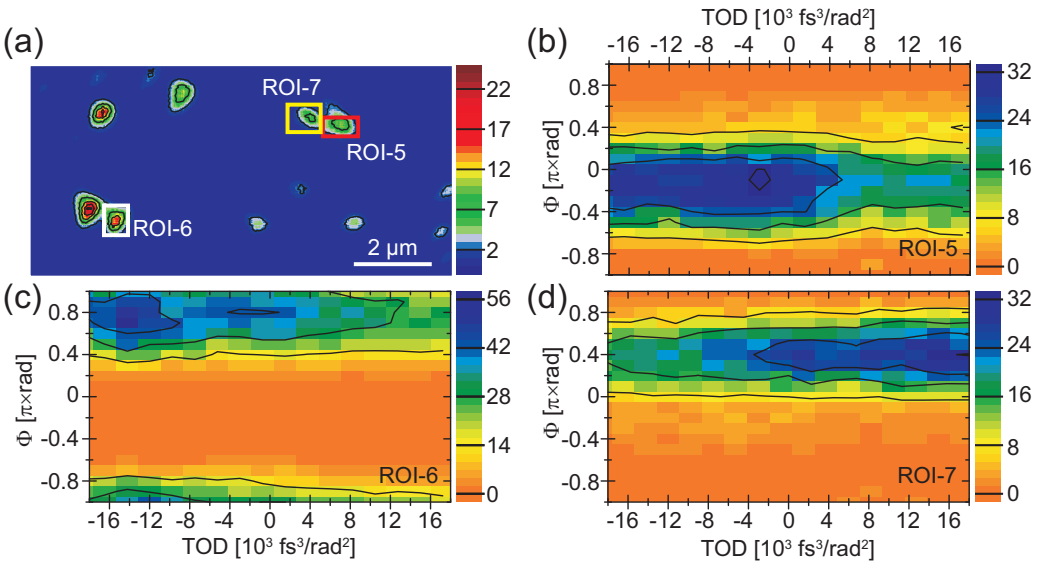

Figure 6.8: Two-parameter scan of third-order dispersion (TOD) and the relative phase Φ of the excitation pulse. (a) The analyzed hot spots are indicated as ROI-5 (red), ROI-6 (white) and ROI-7 (yellow) in the PEEM image observed for excitation with an unshaped pulse. (b)–(d) Average multiphoton photoemission (false colors) of the corresponding ROI plotted against TOD (horizontal axis) and the relative phase Φ (vertical axis). The TOD is scanned from $-18.7\,\mathrm{fs}^3/\mathrm{rad}^2$ to $17.2\,\mathrm{fs}^3/\mathrm{rad}^2$ and the relative phase Φ is scanned from $-\pi$ rad to π rad. Taken from Aeschlimann *et al.* [143]. Copyright (2011) by IEEE.

response functions that are present on the random silver surface.

Furthermore, the optimal value for the phase difference Φ (vertical axis) is different for the three hot spots. As introduced in Section 2.2.2, this parameter mainly determines the polarization state, and its variance for the different ROIs indicates the vectorial dependence of the local response functions of the excited near-field modes. This is typical for a rough metallic surface and can be used in near-field control to achieve switching, for example, between the different hot spots by choosing the appropriate value of Φ. It also generates field enhancement with respect to an unshaped pulse that is p polarized.

However, the two-parameter scans in Fig. 6.8 already indicate clearly that a simple modification of polarization of a transform-limited pulse is not sufficient for optimal field enhancement. If simple polarization variation were enough, the maxima should be found along the TOD = 0 axis or at least at the identical TOD value for the plots shown in Figs. 6.8b–6.8d. Here, rather a specific extended temporal structure was required for the ROI-6 and ROI-7 that lead to increased local fields with respect to unshaped pulses. This indicates that the local optical response on the corrugated silver surface exhibits a coherence memory with respect to the optical excitation on a time scale that is comparable to the stretching of the laser pulses for the optimum TOD values.

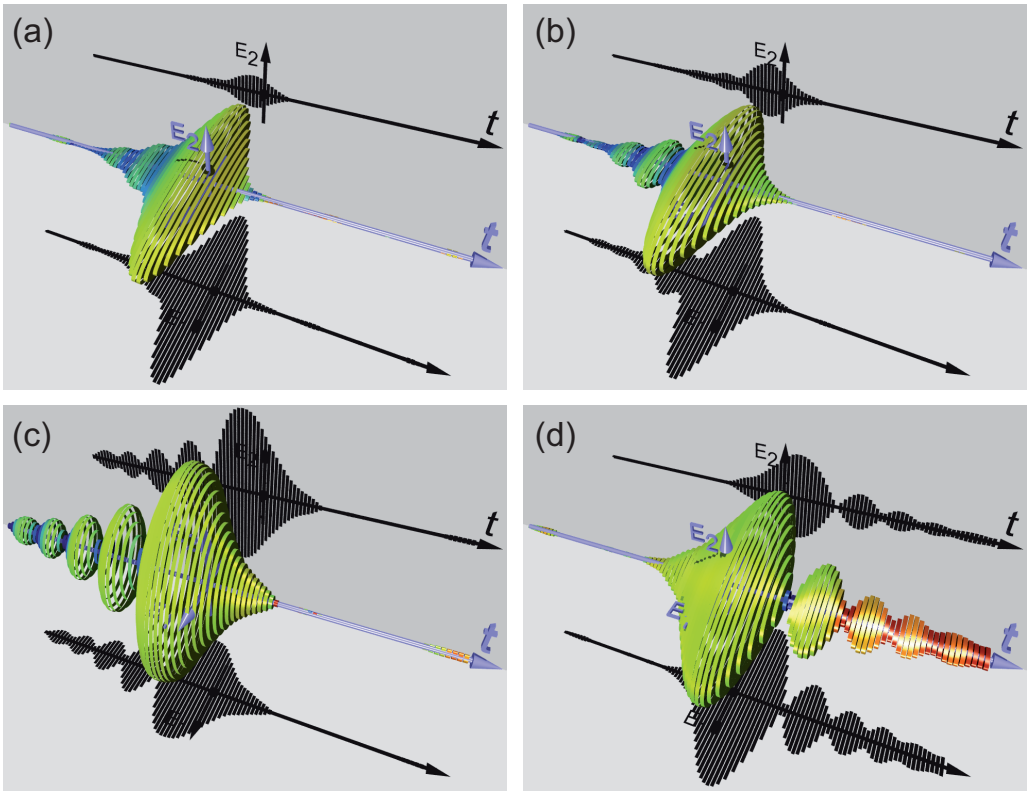

Figure 6.9: Optimal pulses for three different ROIs obtained from the two-parameter scan (Fig. 6.8). The pulses are shown in the quasi 3-D-representation and are plotted from −300 fs to 300 fs where the ellipses have a temporal separation of 5.8 fs. (a) For comparison an unshaped pulse with a pulse duration of 50 fs is plotted. (b) Polarization shaped laser pulse obtained for optimal pulse parameters of the maximum photoemission of ROI-5 (Fig. 6.8b). Optimal parameters: TOD $= 3.0 \times 10^3\,\mathrm{fs}^3/\mathrm{rad}^2$, $\Phi = -0.31\,\mathrm{rad}$. (c) Polarization shaped laser pulse obtained for optimal pulse parameters of the maximum photoemission of ROI-6 (Fig. 6.8c). Optimal parameters: TOD $= -14.2 \times 10^3\,\mathrm{fs}^3/\mathrm{rad}^2$, $\Phi = 2.20\,\mathrm{rad}$. (d) Polarization shaped laser pulse obtained for optimal pulse parameters of the maximum photoemission of ROI-7 (Fig. 6.8d). Optimal parameters: TOD $= 17.2 \times 10^3\,\mathrm{fs}^3/\mathrm{rad}^2$, $\Phi = 1.26\,\mathrm{rad}$.

6.5 Conclusion

In this chapter experimental demonstration of the multiparameter adaptive coherent control of ultrafast nanoscale energy localization on a corrugated silver surface was provided. The achieved control and enhancement was attributed to the presence of resonant electromagnetic modes on the corrugated surface that exhibited long plasmonic dephasing times. These resonant modes were excited by the complex shaped laser pulses and were responsible for the locally enhanced multiphoton photoemission.

Multiparameter adaptive optimizations led to enhancement of multiphoton photoemission signals due to a higher-order spectral-phase modulation of incident laser pulses. The manipulation of photoemission patterns on a corrugated silver surface was shown for regions separated on the order of the diffraction limit (∼500 nm) and for regions within

an individual hot separated below the diffraction limit (∼150 nm). In both cases switching of the photoemission pattern was observed. Surprisingly, the adaptively optimized best pulses exhibited rather long duration indicating that long-lived coherences played an important role for this coherent control of nanoscale energy localization in a random nanostructure. In the case of near-field control on the subdiffraction scale, the hot spot seemed to have a complex behavior involving different plasmonic modes. The switching can then be attributed to the different modes that were addressed depending on the corresponding pulse shape. This is an interesting result for such a small region and suggests near-field control on random silver surfaces to selectively excite molecules on the surface with a spatial resolution below the diffraction limit for spectroscopic applications such as surface enhanced Raman spectroscopy. Unfortunately, a direct identification of the involved plasmonic modes was not possible, since a random structure was used here.

A two-parameter [difference phase Φ and third-order dispersion (TOD)] scan on the same sample demonstrated that the optimal spectral phase leading to maximum local multiphoton photoemission differs significantly for various hot spots. The scan showed maximum photoemission of different ROIs for strong negative, strong positive or zero TOD. Again, this implied long-lived coherences on the surface to play an important role for the coherent control. Since such long-lived coherences can not be explained by localized surface plasmon modes, more complex optical response functions are expected involving delocalized optical modes originating from the close surrounding of the hot spot. Such modes have never been observed on regular planar metal-vacuum interfaces and hence the "randomness" of the surface seems to play an important role. However, the underlying physical mechanism for the observed long-lived coherent modes cannot be unambiguously identified from the available experimental evidence.

The results presented in this chapter are based on the time-averaged photoemission signals and do not yet provide direct information about the dynamics of plasmonic excitations. To obtain more detailed information on the local dynamics, the corrugated silver surface is investigated with 2D nanoscopy in Chapter 7 revealing the complete optical response function of certain hot spots and confirms the existence of delocalized optical modes on the corrugated silver surface.

7 Coherent Two-Dimensional Nanoscopy

In this chapter coherent two-dimensional nanoscopy is presented. The new technique combines two-dimensional spectroscopy with a spatial resolution of a photoelectron emission microscope and hence enables optical spectroscopy below the diffraction limit. It is based on "conventional" two-dimensional spectroscopy (Section 7.2) and similarities as well as differences are described and discussed (Section 7.3). In a first experimental realization, the corrugated silver film that was already investigated in the last chapter is measured with this technique (Section 7.4) and an appropriate model is used (Section 7.5) to assign the response function of the hot spot under investigation.

The work that is presented in this chapter resulted from the same collaboration that was described in Chapter 5.

7.1 Introduction

The phenomenon of coherence lies at the heart of quantum mechanics. Thus coherence-sensitive nonlinear spectroscopies have provided unprecedented insight into the intricacies of complex systems. Recently, long-lasting electronic coherence has been observed in natural light harvesting [150, 151], and hence the reasons for and relevance of such "coherent quantum effects" in biology, chemistry and physics are currently much debated. Extremely powerful in this context is the technique of coherent optical two-dimensional (2D) spectroscopy [7, 8, 152, 153]. Analogous to 2D nuclear magnetic resonance (NMR), the information of congested linear spectra is spread out along a second spectral dimension, and overlapping contributions can be separated. Couplings are revealed as off-diagonal peaks, and analysis of 2D lineshapes furthermore separates the effects of homogeneous versus inhomogeneous broadening. Since the early demonstrations looking at optical nonlinearities [154], vibrational [155] or electronic [156] excitations, a large number of different systems have been studied in the infrared and the visible spectral domains. An exemplary but incomplete list of experiments includes the 2D spectroscopy of atoms [157, 158] single chromophores in a bath [156], coupled vibrational oscillators [159], multichromophore aggregates [150, 151, 160], carotenoids [161], peptides [155, 162], hydrogen-bond networks [163, 164], chemical-exchange systems [165], quantum wells [10, 166], materials [167], and many others. These successes also rely on sophisticated theoretical concepts and modeling [7, 8, 153].

In all implementations of optical spectroscopy the spatial interaction volume has a lower bound as determined by the diffraction limit of light. The laser focus diameter is always larger than roughly half the optical excitation wavelength. This automatically

leads to averaging over a distribution of quantum systems present within the interaction volume. Single-emitter experiments are possible when one quantum system only contributes to the measurement signal, achievable in a combination of tight focusing and low emitter density. This avoids ensemble averaging, and femtosecond experiments have been realized recently [9, 10]. However, the spatial resolution is still diffraction-limited. Subdiffraction imaging resolution can be obtained via reversible fluorophore saturation such that only one emitter is active within the focal spot [168]. This works well for imaging but makes ultrafast spectroscopy challenging because the transitions need to be saturated. As shown in the last chapters, near-field methods provide another way to achieve subdiffraction resolution, and ultrafast experiments have been performed [169]. For this one needs to implement raster-scanning of the sample to obtain spatial-spectral information sequentially for each spot, and near-field 2D spectroscopy has not yet been reported.

In this chapter "Coherent two-dimensional (2D) nanoscopy" is introduced allowing coherent 2D measurements on the nanoscale. "Nanoscopy" is defined in the present context as a technique that measures optical response functions with a spatial resolution below the optical diffraction limit. In contrast to potential near-field implementations, wide-field illumination is used and thus 2D spectral information is captured simultaneously for $\approx 10^6$ different sub-diffraction spatial locations via parallel detection. In conventional 2D spectroscopy, the "input" to a four-wave mixing scheme consists of three incident waves that create a transient coherence (i.e., third-order polarization) which is then radiated off as the "output", converting the coherence to a population. In coherent 2D nanoscopy, by contrast, all four waves will be provided as input fields, and the output corresponds to the remaining electronic population. It has already been shown that (incoherent) fluorescence detection of population can be used for coherent 2D spectroscopy [157, 158]. Also, multidimensional electron spectroscopy has been suggested in the context of X-ray attosecond science [170]. The new key concept in the presented scheme is that upon choosing a non-optical detection signal, spatial resolution is not limited by diffraction of optical waves. Here, locally generated photoelectrons are detected. The theoretical limit of spatial resolution is given by the de-Broglie wavelength of the electron which is 1000 times smaller than the optical wavelength at the same energy of $E = 1\,\mathrm{eV}$. Thus, it becomes possible to carry out 2D spectroscopy on a nanometer length and femtosecond time scale.

The first experimental implementation of coherent 2D nanoscopy is realized for the corrugated silver surface that was investigated in the last chapter, where strong indication for long-lived coherences were found. In contrast to natural light-harvesting systems [150, 151], no surrounding protein could shield off environmental influences thus leading to long coherence times and hence plasmonic collective excitations at metaldielectric interfaces are believed to exhibit longer phase memory. However, for localized surface plasmons investigated in nanostructured Ag samples [92, 146, 147] dephasing times of $T_2 < 10\,\mathrm{fs}$ were reported. It has also been shown in the last chapter that the photoemission within a single hot spot, i.e., on subdiffraction length scale, can be modulated and hence a local response function that strongly depends on the spatial position is suspected. Since 2D nanoscopy is particularly sensitive to phase coherences and additionally enables investigation of these coherences on a nanometer scale it is the perfect

technique to reveal the response function of the corrugated silver surface.

7.2 Principles of Conventional Coherent Two-Dimensional Spectroscopy

Before introducing the main idea of the new coherent two-dimensional (2D) nanoscopy in the next section, an overview of the principles of "conventional" coherent 2D spectroscopy is given. The description is based on the literature of Mukamel [7] and Brixner *et al.* [171].

7.2.1 Density Matrix

In quantum mechanics, a quantum system is described by a pure state $|\psi(t)\rangle$ given by the solution of Schrödinger's equation. However, if the quantum system consists of an ensemble of molecules that might even be coupled to external degrees of freedom, a solution of the Schrödinger equation cannot be found easily and description of the quantum system might not be possible in terms of a pure state. In this case, it is advantageous to describe the quantum system via mixed states. Such mixed states are characterized by the probability p_k to be in a pure state $|\psi_k(t)\rangle$ and are described by the density matrix:

$$\rho(t) = \sum_k p_k |\psi_k(t)\rangle\langle\psi_k(t)|, \tag{7.1}$$

where each element of the density matrix is given by

$$\rho(t)_{nm} = \sum_k p_k \langle n|\psi_k(t)\rangle\langle\psi_k(t)|m\rangle. \tag{7.2}$$

The diagonal elements $\rho_{nn}(t)$, i.e., $n = m$, are positive real-valued quantities that give the probability of the quantum system to occupy the pure state $|n\rangle$ and are called "populations". The other elements, i.e., the off-diagonal elements with $n \neq m$, are generally complex-valued quantities and describe "coherences" of the system. The density matrix is Hermitian

$$\rho^*_{nm}(t) = \rho_{mn}(t) \tag{7.3}$$

and the trace (Tr) is normalized:

$$\mathrm{Tr}\left[\rho(t)\right] = 1. \tag{7.4}$$

This normalization is identical with the statement that the probability of the system to be in any possible state is one, i.e., $\sum_k p_k = 1$.

A measurement of a quantum mechanical quantity, represented by an operator A, is calculated via the expectation value. Using the density matrix the expectation value $\langle A(t)\rangle$ of the operator A is

$$\langle A(t)\rangle = \mathrm{Tr}\left[A\rho(t)\right], \tag{7.5}$$

where Tr denotes the trace of the matrix. Equation (7.5) can then be used to calculate the expectation value of the polarization $P(\vec{r},t)$

$$\langle P(\vec{r},t)\rangle = \mathrm{Tr}\left[P(\vec{r})\rho(t)\right] \tag{7.6}$$

The time evolution of the density matrix can easily be derived by using the Schrödinger equation and results in the Liouville-Von Neumann equation

$$\frac{\partial\rho}{\partial t} = -\frac{\mathrm{i}}{\hbar}\left[H,\rho\right], \tag{7.7}$$

where H is the Hamiltonian of the quantum system and the square brackets define the commutator. The single elements of the density matrix are calculated by

$$\frac{\partial\rho_{nm}}{\partial t} = -\frac{\mathrm{i}}{\hbar}\left[\left(H\rho\right)_{nm} - \left(\rho H\right)_{nm}\right]. \tag{7.8}$$

Choosing a simple example, the Hamiltonian of a coupled two-level system is described by

$$H = \begin{pmatrix} E_1 & V_{12} \\ V_{21} & E_2 \end{pmatrix}, \tag{7.9}$$

where E_1 and E_2 denote the energy levels and V_{12} and V_{21} their coupling. Substituting this Hamiltonian in Eq. (7.8) reveals that a transition, e.g., from ρ_{11} to ρ_{22}, can only occur via the off-diagonal elements ρ_{12} and ρ_{21}. Hence, in an optically excited transition, a coherence is created in a first interaction with the electric field and a second interaction is necessary to transfer the coherence into a population. Further properties of optical transitions in quantum systems are discussed via their Liouville pathways in Section 7.2.3.

7.2.2 Response Function Formalism in Liouville Space

For the following derivations, it is useful to replace the description in Hilbert space—which was used so far—by the description in Liouville space. In Liouville space, the density matrix is represented as a vector and can be treated identical to the description of the wave function in Hilbert space. Consequently, the dynamic of the density function is described analogously to Schrödinger's equation in Hilbert space:

$$\frac{\partial|\rho\rangle\rangle}{\partial t} = -\frac{\mathrm{i}}{\hbar}\mathcal{L}|\rho\rangle\rangle. \tag{7.10}$$

Note that this description is identical with the Liouville-von-Neumann equation defined in Eq. (7.7). According to the Bra-Ket notation in Hilbert space the vectorial character of the density matrix is described as $|\rho\rangle\rangle$. As can be inferred from Eq. (7.7) the Liouville operator $\mathcal{L}$ introduced in Eq. (7.10) is defined as $\mathcal{L}|\rho\rangle\rangle = [H,\rho]$.

In perturbation theory, the Hamiltonian for an interaction of a quantum system with an external electric field is described as

$$H(t) = H_0 - VE(t), \tag{7.11}$$

with H_0 being the unperturbed Hamiltonian. The perturbation is given by the interaction with the electric field via the time independent dipole operator V. Note that vectorial properties are neglected here for the sake of simplicity. The density operator can then be expanded in powers of the electric field

$$|\rho(t)\rangle\rangle = |\rho^{(0)}(t)\rangle\rangle + |\rho^{(1)}(t)\rangle\rangle + |\rho^{(2)}(t)\rangle\rangle + ..., \tag{7.12}$$

where $|\rho^{(n)}\rangle\rangle$ denotes the nth order contribution in the electric field with

$$|\rho^{(n)}(t)\rangle\rangle = \left(-\frac{\mathrm{i}}{\hbar}\right)^n \int_{t_0}^{t} \mathrm{d}\tau_n \int_{t_0}^{\tau_n} \mathrm{d}\tau_{n-1} ... \int_{t_0}^{\tau_2} \mathrm{d}\tau_1 \mathcal{G}(t-\tau_n)\mathcal{L}_{\mathrm{int}}(\tau_n)\mathcal{G}(\tau_n-\tau_{n-1})\mathcal{L}_{\mathrm{int}}(\tau_{n-1})... \\ ...\mathcal{G}(\tau_2-\tau_1)\mathcal{L}_{\mathrm{int}}(\tau_1)\mathcal{G}(\tau_1-t_0)|\rho(t_0)\rangle\rangle. \tag{7.13}$$

The subscript n describes the number of interactions with the electric field. Speaking on a time scale, the equations starts on the right hand side with the density matrix $|\rho(t_0)\rangle$ being in thermal equilibrium. The times τ_n of interaction with the electric field are numbered chronologically such that: $t \geq \tau_n \geq \tau_{n-1} \geq ... \geq \tau_1 \geq t_0$. The interactions with the electric field are denoted by the Liouville operator

$$\mathcal{L}_{\mathrm{int}}(t) = -\mathcal{V}E(t) \tag{7.14}$$

and results from the perturbation term of the Hamiltonian [Eq. (7.11)]. Here, $\mathcal{V}$ is the time independent dipole operator in Liouville space. In the absence of the electric field, the temporal evolution of the quantum system is described by the Liouville space Green function $G(\tau)$. It is defined as

$$\mathcal{G}(\tau) \equiv \Theta(\tau)\,\mathrm{e}^{-\frac{\mathrm{i}}{\hbar}\mathcal{L}\tau}, \tag{7.15}$$

where $\mathcal{L}$ is the Liouville operator of the unperturbed Hamiltonian H_0 and $\Theta(\tau)$ the Heavyside step function.

By changing the time variables

$$t_1 \equiv \tau_2 - \tau_1, \quad t_2 \equiv \tau_3 - \tau_2, \quad ... \quad t_n \equiv t - \tau_n,$$

setting $t_0 \to -\infty$ and using the definitions of Eqs. (7.14) and (7.15), Eq. (7.13) can be rewritten:

$$|\rho^{(n)}(t)\rangle\rangle = \left(\frac{\mathrm{i}}{\hbar}\right)^n \int_{0}^{\infty} \mathrm{d}t_n \int_{0}^{\infty} \mathrm{d}t_{n-1} ... \int_{0}^{\infty} \mathrm{d}t_1 \mathcal{G}(t_n)\mathcal{V}\mathcal{G}(t_{n-1})\mathcal{V}...\mathcal{G}(t_1)\mathcal{V}|\rho(-\infty)\rangle\rangle \\ E(\vec{r}, t-t_n)E(\vec{r}, t-t_n-t_{n-1})...E(\vec{r}, t-t_n-t_{n-1}...-t_1). \tag{7.16}$$

The polarization of the quantum system results from the expectation value of the dipole operator and is given by

$$P(\vec{r}, t) = \mathrm{Tr}\left[V\rho(t)\right] = \langle\langle V|\rho(t)\rangle\rangle, \tag{7.17}$$

where the last definition is in Liouville space [cf. Eq. (7.10)]. Analogously to the description of the density matrix the polarization can also be written as an expansion in powers of the electric field

$$\begin{aligned} P^{(n)}(\vec{r},t) \equiv & \langle\langle V|\rho^{(n)}(t)\rangle\rangle \\ = & \int_0^\infty \mathrm{d}t_n \int_0^\infty \mathrm{d}t_{n-1} ... \int_0^\infty \mathrm{d}t_1 S^{(n)}(t_n, t_{n-1}, ..., t_1) \\ & E(\vec{r}, t-t_n) E(\vec{r}, t-t_n-t_{n-1}) ... E(\vec{r}, t-t_n-t_{n-1} ... -t_1), \end{aligned} \tag{7.18}$$

where the nth order nonlinear response function is defined as

$$S^{(n)}(t_n, t_{n-1}, ..., t_1) \equiv \left(\frac{\mathrm{i}}{\hbar}\right)^n \langle\langle V|\mathcal{G}(t_n)\mathcal{V}\mathcal{G}(t_{n-1})\mathcal{V} ... \mathcal{G}(t_1)\mathcal{V}|\rho(-\infty)\rangle\rangle. \tag{7.19}$$

Note that the polarization described here is identical with the polarization that was introduced in the inhomogeneous wave equation (2.26). Since $P^{(n)}$ is a physical observable it is a real-valued quantity that assumes n interactions at the corresponding points in time $(t_n + t_{n-1} ... + t_1), (t_{n-1} + ... + t_1), ..., t_1$. It carries the complete information that is necessary to calculate optical measurements and is the quantity that is determined in "conventional" 2D spectroscopy.

7.2.3 Liouville Pathways

Two-dimensional spectroscopy as discussed here, is based on the third order polarization. Hence, the corresponding response function is obtained by setting $n = 3$ in Eq. (7.19):

$$S^{(3)}(t_3, t_2, t_1) = \left(\frac{\mathrm{i}}{\hbar}\right)^3 \langle\langle V|\mathcal{G}(t_3)\mathcal{V}\mathcal{G}(t_2)\mathcal{V}\mathcal{G}(t_1)\mathcal{V}|\rho(-\infty)\rangle\rangle. \tag{7.20}$$

In Hilbert space this reads as

$$\begin{aligned} S^{(3)}(t_3, t_2, t_1) = & \left(\frac{\mathrm{i}}{\hbar}\right)^3 \Theta(t_1)\Theta(t_2)\Theta(t_3) \\ & \langle [[[V(t_3+t_2+t_1), V(t_2+t_1)], V(t_1)], V(0)]\, \rho(-\infty)\rangle \\ = & \left(\frac{\mathrm{i}}{\hbar}\right)^3 \Theta(t_1)\Theta(t_2)\Theta(t_3) \sum_{\alpha=1}^{4} \left[R_\alpha(t_3, t_2, t_1) - R_\alpha^*(t_3, t_2, t_1)\right], \end{aligned} \tag{7.21}$$

where the star denotes complex conjugated and the following definitions are assumed:

$$\begin{aligned} R_1(t_3, t_2, t_1) &\equiv \langle V(t_1) V(t_1+t_2) V(t_1+t_2+t_3) V(0) \rho(-\infty)\rangle \\ R_2(t_3, t_2, t_1) &\equiv \langle V(0) V(t_1+t_2) V(t_1+t_2+t_3) V(t_1) \rho(-\infty)\rangle \\ R_3(t_3, t_2, t_1) &\equiv \langle V(0) V(t_1) V(t_1+t_2+t_3) V(t_1+t_2) \rho(-\infty)\rangle \\ R_4(t_3, t_2, t_1) &\equiv \langle V(t_1+t_2+t_3) V(t_1+t_2) V(t_1) V(0) \rho(-\infty)\rangle\,. \end{aligned} \tag{7.22}$$

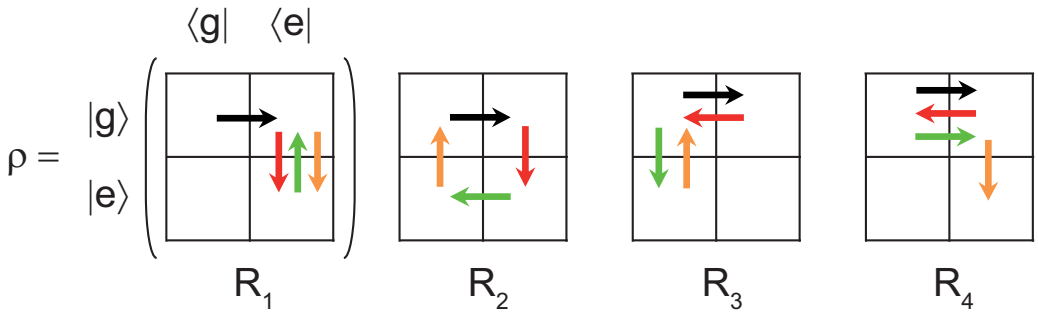

Figure 7.1: Liouville pathways for a coupled two-level system. The 2×2 density matrix is given by the ground state $|g\rangle$ and excited state $|e\rangle$. The diagonal elements $|g\rangle\langle g|$ and $|e\rangle\langle e|$ describe population of the corresponding states, whereas $|g\rangle\langle e|$ and $|e\rangle\langle g|$ describe coherences. Four interactions of the quantum system with the electric field are indicated with four different arrows. The first (black), second (red) and third (green) interaction are interactions with ingoing waves. The remaining fourth interaction that induces an outgoing wave is indicated with a yellow arrow. Four different pathways are considered, where the remaining four pathways can be obtained by an inversion with respect to the diagonal axes.

These terms R_α together with their complex conjugates R_α^* denote eight Liouville pathways. The pathways give a description of the temporal evolution of the density matrix. For each pathway the quantum system interacts four times with electric fields, three of which are ingoing waves and the fourth wave is an outgoing wave due to the induced polarization. Therefore, processes described with the third order polarization are also called four-wave mixing (FWM) processes.

A visualization of the Liouville pathways in a coupled two-level system is given in Fig. 7.1. The two levels are a ground state $|g\rangle$ and an excited state $|e\rangle$. Only four possibilities (R_1–R_4) are exemplified since the remaining complex conjugated pathways (R_1^*–R_4^*) can be easily obtained by an inversion on the diagonal of the density matrix. Hence, starting from the ground state population $\rho(-\infty) = |g\rangle\langle g|$, the first arrow (black)—indicating the first interaction with the electric field—always point to the right. The second, third and fourth interaction are illustrated as red, green and yellow arrows, respectively. Note that the first three arrows (black, red, green) indicate interaction with ingoing electric fields, whereas the yellow arrow indicates an outgoing electric field induced by the polarization. This outgoing electric field carries the complete information of the third order nonlinear response function and is therefore measured in "conventional" 2D spectroscopy.

7.2.4 Experimental Background

Coherent 2D spectroscopy is a nonlinear time-resolved method that enables measurement of the third order response function of a quantum system. The quantity that reveals

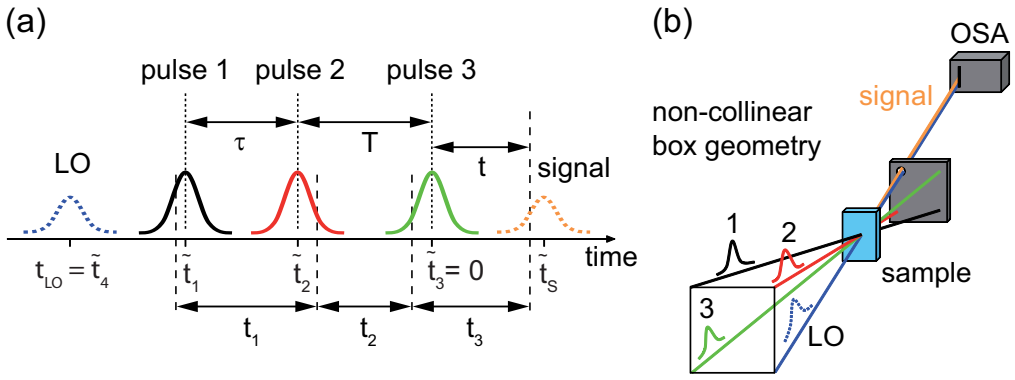

Figure 7.2: Excitation scheme in coherent 2D spectroscopy. (a) A sequence of three femtosecond laser pulses (pulses 1–3 given by $\tilde{t}_1$, $\tilde{t}_2$ and $\tilde{t}_3$, respectively) with variable temporal separations τ, T is used for excitation. Without loss of generality the center of pulse 3 is chosen to be zero. The signal at time t (yellow dashed line) that contains the information of the nonlinear third order response function is induced by interaction of the pulse sequence at times $t-t_1-t_2-t_3$, $t-t_1-t_2$ and $t-t_1$. An additional pulse (LO), which is attenuated to avoid interaction with the sample, is used for characterization of that signal. (b) The sample is excited in a noncollinear box geometry. Therefore, the three pulses propagate in different direction given by $\vec{k}_1$, $\vec{k}_2$ and $\vec{k}_3$. Due to the phase matching condition the signal is emitted in direction $\vec{k}_s = -\vec{k}_1 + \vec{k}_2 + \vec{k}_3$ and is overlapped with the LO for characterization via spectral interferometry.

this third order response function is the third order polarization

$$P^{(3)}(\vec{r},t) = \int_0^\infty \mathrm{d}t_3 \int_0^\infty \mathrm{d}t_2 \int_0^\infty \mathrm{d}t_1 S^{(3)}(t_3,t_2,t_1) E(\vec{r},t-t_3) E(\vec{r},t-t_3-t_2) E(\vec{r},t-t_3-t_2-t_1), \tag{7.23}$$

which is obtained by setting $n=3$ in Eq. (7.18). Herein, $(t-t_3)$, $(t-t_3-t_2)$ and $(t-t_3-t_2-t_1)$ denote the times of interaction with the external excitation. To measure the temporal dependence of $P^{(3)}$ these times have to be varied systematically. Experimentally, this is achieved using three different laser pulses whose temporal separations can be adjusted independently. Mathematically, the electric field $E(t)$ of the excitation pulses is described by

$$E(\vec{r},t) = \hat{A}(t-\tilde{t}_1)\,\mathrm{e}^{\mathrm{i}\left[\omega_0(t-\tilde{t}_1)+\vec{k}_1\vec{r}\right]} + \hat{A}(t-\tilde{t}_2)\,\mathrm{e}^{\mathrm{i}\left[\omega_0(t-\tilde{t}_2)+\vec{k}_2\vec{r}\right]} + \hat{A}(t-\tilde{t}_3)\,\mathrm{e}^{\mathrm{i}\left[\omega_0(t-\tilde{t}_3)+\vec{k}_3\vec{r}\right]} + c.c., \tag{7.24}$$

where each pulse is defined according to Section 2.1 by its complex envelope amplitude $\hat{A}(t)$, carrier frequency ω_0 and propagation direction $\vec{k}$. Since the laser pulses have a finite duration (typically on the order of several tenth of femtoseconds), the interaction times are in general different from the center of the pulses $\tilde{t}_i$ $(i=1,2,3)$. The excitation pulse sequence scheme and the interaction times are illustrated in Fig. 7.2a. The temporal separation between the first (black) and the second pulse (red), i.e., $\tilde{t}_2-\tilde{t}_1$, is called "coherence time" τ and the temporal separation between the second and the third pulse (green), i.e., $\tilde{t}_3-\tilde{t}_2$, is called "population time" T. These descriptions are

chosen according to the corresponding density matrix elements (cf. Fig. 7.1). The first interaction with the external field transfers the quantum state from the ground state into a coherence and the system remains in this coherence during the coherence time τ. Then the second interaction transfers the system from the coherence into a population, where the system remains during the population time T. After the third interaction the quantum system remains in a coherence which is converted into a population by generation of a fourth pulse (yellow). This fourth pulse is the signal that is measured.

By plugging in the mathematical description of excitation pulse sequence [Eq. (7.24)] into Eq. (7.23), six summands are obtained for each electric field. Hence, the third order polarization contains $6 \times 6 \times 6 = 216$ summands and each of them is described by three pulses, e.g., three complex envelope functions and their corresponding exponential functions that contain the frequency and direction of propagation of the corresponding pulses.

Due to the fact that 2D spectroscopy is an optical method, its spatial resolution, i.e., the optical focusing, is limited by diffraction. Consequently, the measured signal results from an ensemble of quantum systems within the focal spot. The signal emitted from the sample is then given by a coherent superposition of emitted signals from the individual quantum systems and obeys the phase matching condition [172]. In 2D spectroscopy this phase matching condition is used to reduce the number of summands in the third order polarization. Therefore, the so-called box geometry (Fig. 7.2b) is employed and only signals are measured that possess the propagation direction along

$$\vec{k}_s = -\vec{k}_1 + \vec{k}_2 + \vec{k}_3, \tag{7.25}$$

where $\vec{k}_i$ with $i = 1, 2, 3$ describe the propagation direction of the corresponding pulses (Fig. 7.2a). Since only six summands have a propagation direction in this direction, i.e., possess the term $\mathrm{e}^{\mathrm{i}\left(-\vec{k}_1+\vec{k}_2+\vec{k}_3\right)\vec{r}}$, the number of summands in Eq. (7.23) is reduced from 216 to six. The third order polarization [Eq. (7.23)] can further be simplified by considering the *rotating wave approximation* (RWA). In this approximation all fast oscillating terms, wich oscillate at optical frequencies are neglected, i.e., only slowly varying terms are selected, in which the optical frequency is cancelled out by the material frequency of opposite sign. Using this simplification, each of the six summands contain the phase factor

$$\mathrm{e}^{-\mathrm{i}\omega_0\left(t-\tilde{t}_1+\tilde{t}_2+\tilde{t}_3\right)} = \mathrm{e}^{-\mathrm{i}\omega_0(t-\tau)} \tag{7.26}$$

and one of the three phase factors

$$\begin{aligned} &\mathrm{e}^{\mathrm{i}\omega_0(t_3-t_1)} \\ &\mathrm{e}^{\mathrm{i}\omega_0(t_3+t_1)} \\ &\mathrm{e}^{\mathrm{i}\omega_0(t_1+2t_2+t_3)}, \end{aligned} \tag{7.27}$$

where always two summands contain the same one. According to the phase factors defined in Eq. (7.27), the third order response function $S^{(3)}$ is classified into $S^{(3)}_{\mathrm{R}}$, $S^{(3)}_{\mathrm{NR}}$ and $S^{(3)}_{\mathrm{DC}}$ representing the sum of the corresponding Liouville pathways. However, they should not be confused with the R_α terms of Eq. (7.22) and their Liouville pathways

(Fig. 7.1). The rephasing (R) term $S_{\mathrm{R}}^{(3)}$ assigned by the phase factor $\mathrm{e}^{\mathrm{i}\omega_0(t_3-t_1)}$ induces a photon echo after the third interaction at $t = \tau$ corresponding to the constant term at $t_3 = t_1$. In density matrix representation: The quantum system evolves in complex conjugate coherences during the coherence time (between first and second interaction) and after the third interaction. Hence, the Liouville pathways R_2 and R_3 in Fig. 7.1 describe rephasing, i.e., the coherence $|g\rangle\langle e|$ is the complex conjugate of $|e\rangle\langle g|$ denoting the density matrix after the first (black arrow) and the third interaction (green arrow), respectively. The terms $S_{\mathrm{NR}}^{(3)}$ and $S_{\mathrm{DC}}^{(3)}$ are assigned by the phase factors $\mathrm{e}^{\mathrm{i}\omega_0(t_3+t_1)}$ and $\mathrm{e}^{\mathrm{i}\omega_0(t_1+2t_2+t_3)}$, respectively. These terms do not induce a photon echo but a free induction decay with the third interaction. Therefore, the subscript NR defines the non-rephasing term. The last term $S_{\mathrm{DC}}^{(3)}$ is only relevant in quantum systems with more than two energy levels. In such systems it describes pathways that do not arrive in a population but in an additional coherence after the second interaction. Therefore, these terms and the corresponding Liouville pathways describe a double coherence (DC). Using these definitions the Liouville pathways R_1 and R_4 in Fig. 7.1 can be assigned as non-rephasing.

So far, the polarization of the investigated sample is considered. However, as already mentioned above, in a 2D spectroscopy experiment it is not the polarization itself that is measured but the electric field E_s (signal, yellow in Fig. 7.2) induced by the polarization. This electric field is measured with a spectrometer (OSA) as a function of the coherence time τ and of the population time T and is related to the polarization via

$$E_s(\tau, T, \omega_t) \propto \frac{\mathrm{i}\omega_t}{n(\omega_t)} P^{(3)}(\tau, T, \omega_t), \tag{7.28}$$

where $n(\omega)$ is the refractive index of the sample. The full characterization, i.e., spectral amplitude and phase, of $E_s(\tau, T, \omega_t)$ is achieved by spectral interferometry (Section 2.4.2). For this purpose, the local oscillator (LO) (blue Fig. 7.2), which is attenuated to avoid interaction with the sample, is overlapped collinearly with the signal.

The measured data is represented as two-dimensional spectra as a function of ω_τ and ω_t. This representation is preferred since it is more intuitive than a representation in time domain, which would yield the same information content. To obtain the 2D spectrum the measured electric field E_s is Fourier transformed, transforming the coherence time τ into frequency ω_τ:

$$\begin{aligned} S_{\mathrm{2D}}(\omega_\tau, T, \omega_t) &= \int_{-\infty}^{\infty} \mathrm{d}\tau \; \mathrm{i}P^{(3)}(\tau, T, \omega_t)\, \mathrm{e}^{\mathrm{i}\omega_\tau} \\ &\propto \int_{-\infty}^{\infty} \mathrm{d}\tau \; \frac{E_s(\tau, T, \omega_t) n(\omega_t)}{\omega_t}\, \mathrm{e}^{\mathrm{i}\omega_\tau \tau}\,. \end{aligned} \tag{7.29}$$

Herein, only τ has to be Fourier transformed because the transformation of t is already employed by measuring the signal E_s as a function of frequency ω_t [Eq. (7.28)]. The spectrum $S_{\mathrm{2D}}(\omega_\tau, T, \omega_t)$ is complex valued and is either displayed as amplitude and phase or as real and imaginary part. The absolute phase has to be determined in a so-called "phasing" procedure by comparison of pump–probe measurements with the 2D spectra in an additional step [152, 171].

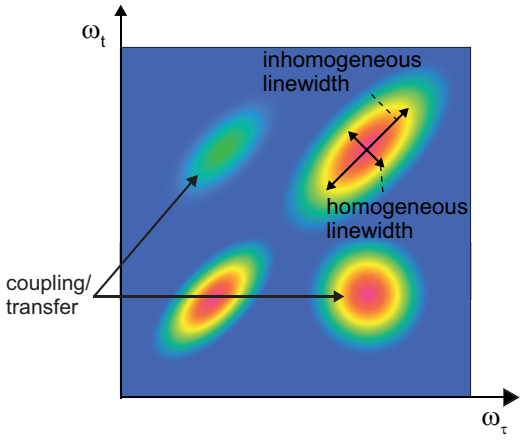

Figure 7.3: Schematic of a 2D spectrum. The spectrum is plotted as a function of ω_τ and ω_t that are related to frequency component of pump and probe excitation, respectively. The two dimensional representation enables separation of contributions that would overlap in a linear spectrum. Coupling and population transfer can be identified as off-diagonal peaks and homogeneous and inhomogeneous linewidth can be determined via the length and width of the diagonal peaks, respectively.

The advantage of 2D spectroscopy is the measurement of the spectral information in two dimensions. Hence, contributions that would overlap in a linear spectrum are separated in a two-dimensional representation and can be assigned. A schematic 2D spectrum is shown in Fig. 7.3. The spectrum can be understood as follows: the quantum system is pumped with a frequency ω_τ indicated on the horizontal axis and is probed with a frequency ω_t indicated on the vertical axis. Hence, the off-diagonal elements reveal coupling and transfer of population. For example, the system that is pumped with a certain frequency ω_τ leads to a signal at a probe frequency at $\omega_t \neq \omega_\tau$ due to a transfer of population from level $E = \hbar\omega_\tau$ to the level $E = \hbar\omega_t$. Additionally, the shape of the diagonal peaks is determined by homogeneous and inhomogeneous linewidth.

7.3 Principles of Two-Dimensional Nanoscopy

As explained in Section 7.2, in "conventional" 2D spectroscopy three ingoing optical waves induce a third order nonlinear polarization that leads to one outgoing wave. This outgoing wave is measured in terms of its amplitude and phase and carries the information of the third order nonlinear response function of the system. Since the spatial resolution of outgoing optical wave that is determined by the wavelength of the optical wave, it is not possible to measure "conventional" 2D spectra with a resolution below the optical diffraction limit. Considering an energy $E = 1\,\mathrm{eV}$ the corresponding wavelength is

$$\lambda_{\mathrm{opt}} = \frac{hc}{E} \approx 1000\,\mathrm{nm}. \tag{7.30}$$

In the newly developed technique 2D nanoscopy that is presented here, the detected signal is measured using PEEM. Four ingoing waves are used in this technique to excite the sample and electrons are detected that are non-optical and therefore do not obey the optical diffraction limit. The theoretical limit for the spatial resolution is then given by the de Broglie wavelength of the emitted electrons. For the same energy $E = 1\,\mathrm{eV}$

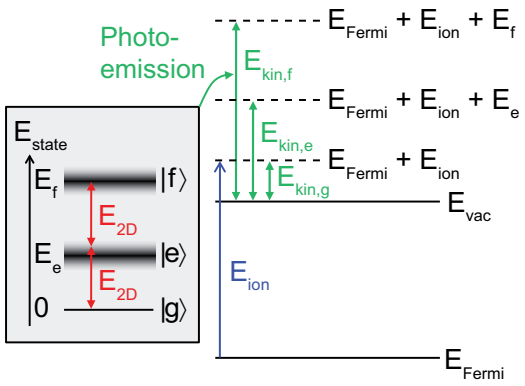

Figure 7.4: Excitation of a quantum 3-level system in 2D nanoscopy. The electric field E_{2D} (red arrows) induces transitions between different energy levels $E_{\text{state}} = \{E_g \equiv 0, E_e, E_f\}$. The remaining quantum state $|g\rangle$, $|e\rangle$ or $|f\rangle$, additionally excited with an ionization laser of energy E_{ion} (blue arrow), leads to emission of photoelectrons with kinetic energies $E_{\text{kin},g}$, $E_{\text{kin},e}$ or $E_{\text{kin},f}$ (green arrows), respectively. Taken from Aeschlimann *et al.* [173]. Copyright (2011) by AAAS.

the wavelength is

$$\lambda_{\text{e}} = \frac{h}{\sqrt{2m_e E}} \approx 1\,\text{nm}. \tag{7.31}$$

This is three orders of magnitude smaller than that of optical waves. This illustrates the power of the new technique since information of the investigated system can be obtained with a spatial resolution that is thousand times smaller than that of "conventional" 2D spectroscopy.

In the following the main idea of 2D nanoscopy is presented and similarities and differences between "conventional" 2D spectroscopy and 2D nanoscopy are discussed in terms of their underlying theory. Additionally the generation of pulse sequences with a pulse shaper as they are needed for the experimental realization is explained.

7.3.1 Main Idea

The principle of the optical excitation in coherent 2D nanoscopy is illustrated in Fig. 7.4. Considered is a quantum three-level system consisting of ground state, $|g\rangle$, first electronically excited state, $|e\rangle$, and second excited state, $|f\rangle$. Transitions between the different levels are induced with an electric field E_{2D} consisting of four femtosecond pulses. As will be discussed in more detail in Section 7.3.4, this four-wave interaction leaves the system in one of the population states $|g\rangle\langle g|$, $|e\rangle\langle e|$, or $|f\rangle\langle f|$ that is probed via photoelectron emission and is measured using PEEM (Section 2.6). In general, $E_{\text{state}} = \{E_g \equiv 0, E_e, E_f\}$, might not exceed the work function, and additional energy can be supplied by an ionization laser of energy E_{ion}. For photoelectrons emitted from an initial state at the Fermi level, E_{Fermi}, the kinetic energy above vacuum level E_{vac} is given by

$$E_{\text{kin}} = E_{\text{Fermi}} + E_{\text{ion}} + E_{\text{state}} - E_{\text{vac}}. \tag{7.32}$$

The horizontal dashed lines therefore correspond to the maximum kinetic energy of the photoelectrons for given E_{ion} and E_{state}. The general excitations can correspond either to states of collective nature, such as, e.g., plasmon polaritons in metallic systems or

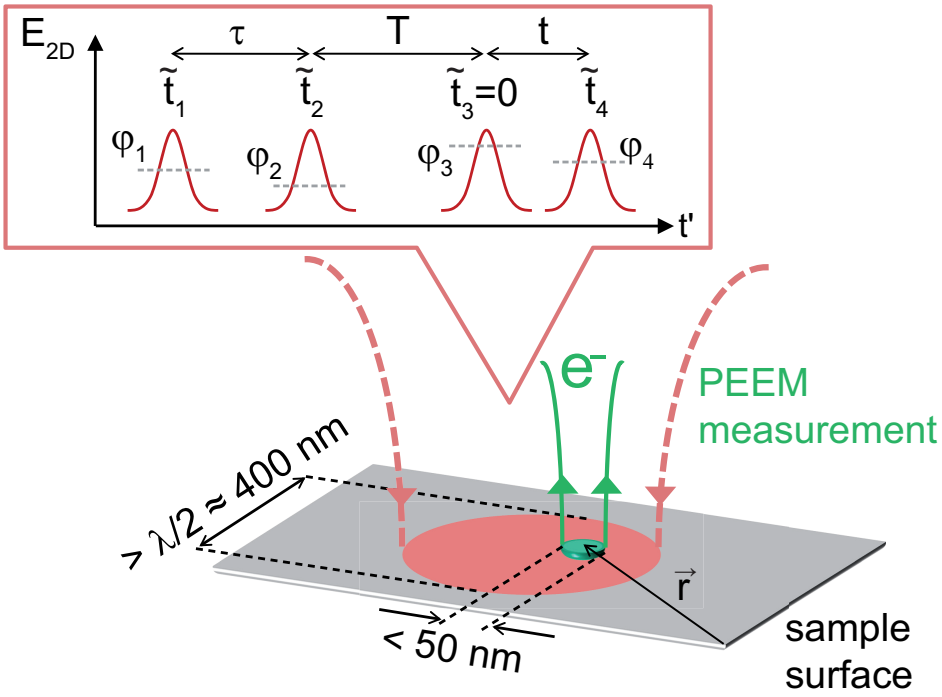

Figure 7.5: Excitation scheme in 2D nanoscopy. A sequence of four femtosecond laser pulses with variable temporal separations τ, T and t and phases φ_i $(i = 1, ..., 4)$ is used for excitation. The optical spot on the sample is larger than $\lambda/2$ (diffraction limit), but the final electronic population is measured via PEEM with a resolution below 50 nm. Taken from Aeschlimann *et al.* [173]. Copyright (2011) by AAAS.

excitons in molecular aggregates, or to single-particle states, such as distinct transitions in the electronic band structure. However, the probe process occurs via a single-particle state, i.e., the photoemission state. Since collective states cannot be represented on a single-particle energy scale, the quantum-state preparation via the interaction with E_{2D} and the probe process are separated in Fig. 7.4.

The excitation scheme of 2D nanoscopy is illustrated in Fig. 7.5. The temporal separations of the four-pulse sequence E_{2D}—inducing the transitions between different levels as explained above—can be varied and are labeled τ, T and t, in analogy with 2D spectroscopy (Fig. 7.2). In addition, the phases of the four subpulses, φ_i $(i = 1, ..., 4)$, can be specified, where the actual variation of these phases is described in Section 7.3.3. As can be seen, the four-pulse sequence E_{2D} excites the sample with a spot size that is diffraction limited, e.g., > 400 nm for 800 nm excitation wavelength. However, since the final electronic population is measured here via PEEM, 2D spectra can be measured with the resolution of the PEEM, i.e., < 50 nm (Section 2.6). Hence, the local nonlinear response function, rather than an averaged quantity, can be measured as a function of position $\vec{r}$. Because no outgoing optical fields are detected, the loss of four-wave-mixing phase matching is irrelevant. The simplest illumination geometry is then fully collinear and allows the required pulse sequences to be created with a femtosecond pulse shaper in amplitude–phase shaping mode. As explained in Section 2.3.3 this insures inher-

ent phase-stable pulse sequences and a separate "phasing" procedure via projection of $S(\omega_\tau, \omega_t)$ onto independently obtained pump-probe data [152, 171], as done in "conventional" 2D spectroscopy, is not required to determine the separation into real and imaginary part [162].

An explicit theoretical description of the obtained signals will be given in Section 7.3.2 and the direct relation between the signal that is measured in "conventional" 2D spectroscopy and the signal that is measured in 2D nanoscopy will be derived. In Section 7.3.4 the Liouville-space pathways of 2D nanoscopy and 2D spectroscopy will be compared and although different linear combinations of them contribute to the final signal, they are found to be completely analogously. Hence, despite the incoherent detection of electrons, electronic coherences are also measured in 2D nanoscopy and can be analyzed with a response-function treatment. The additional feature in 2D nanoscopy is that access to the general spatial-temporal response function [7] is gained.

7.3.2 Theoretical Description

The signal that is measured in 2D nanoscopy using an energy resolved PEEM is the local time-averaged photoemission yield $Y_{\mathrm{PE},m}(\vec{r})$ corresponding to the kinetic energy $E_{\mathrm{kin},m}$ of the emitted photoelectrons (cf. Fig. 7.4). The time-averaged photoemission yield is calculated by temporal integration over the local momentary multiphoton photoemission probability

$$Y_{\mathrm{PE},m} = \int_{-\infty}^{\infty} P_{\mathrm{PE},m}(\vec{r}, t)\mathrm{d}t, \tag{7.33}$$

where the local momentary multiphoton photoemission probability maps the local momentary population of the states of the investigated system. Note that only a mapping of the population of states is considered here, i.e., the photoemission process is assumed to be initiated by the ionization laser that is not included in the following argumentation. Hence, the local momentary multiphoton photoemission probability $P_{\mathrm{PE},m}(\vec{r}, t)$ of electrons with the kinetic energy $E_{\mathrm{kin},m}$ is given by the population of the state $|m\rangle$. Considering n interactions with the electric field, this population is calculated in Liouville space by a scalar product of the corresponding basis vector $|mm\rangle\rangle$ with the n-th order density matrix [Eq. (7.13)]

$$P_{\mathrm{PE},m}(\vec{r}, t) = \langle\langle mm|\rho^{(n)}(\vec{r}, t)\rangle\rangle. \tag{7.34}$$

Since the spatial resolution 2D nanoscopy can not be neglected anymore the density matrix depends explicitly on the spatial coordinate $\vec{r}$. Using the definition of the density matrix given in Eq. (7.19), the local momentary multiphoton photoemission probability is written as

$$\begin{aligned} P_{\mathrm{PE},m}(\vec{r}, t) = \left(\frac{\mathrm{i}}{\hbar}\right)^n \int_0^\infty \mathrm{d}t_n \int_0^\infty \mathrm{d}t_{n-1} ... \int_0^\infty \mathrm{d}t_1 \mathcal{R}_m^{(n)}(\vec{r}, t_n, t_{n-1}, ..., t_1) \\ E(\vec{r}, t - t_n)E(\vec{r}, t - t_n - t_{n-1})...E(\vec{r}, t - t_n - t_{n-1} ... - t_1). \end{aligned} \tag{7.35}$$

Note that the n-th order photoemission response function $\mathcal{R}^{(n)}$ relates the incident electric fields with the population of the final state and hence should not be confused with the n-th order nonlinear response function $S^{(n)}$ that relates the incident electric fields with the polarization [Eq. (7.18)]. The photoemission response function rather describes an analog to the nonlinear response function and is defined by

$$\mathcal{R}_m^{(n)}(\vec{r}, t_n, t_{n-1}, ..., t_1) = \left(\frac{\mathrm{i}}{\hbar}\right)^n \langle\langle mm|\mathcal{G}(\vec{r}, t_n)\mathcal{V}(\vec{r})\mathcal{G}(\vec{r}, t_{n-1})\mathcal{V}(\vec{r})...\mathcal{G}(\vec{r}, t_1)\mathcal{V}(\vec{r})|\rho(-\infty)\rangle\rangle \tag{7.36}$$

Herein, the time-independent dipole coupling $\mathcal{V}$ as well as the Greens function $\mathcal{G}(t)$ [Eq. (7.15)] is assumed to be position dependent.

By introducing the time dependent operator

$$\mathcal{V}(\vec{r}, \tau) \equiv \exp\left(\frac{\mathrm{i}}{\hbar}\mathcal{L}(\vec{r})\tau\right)\mathcal{V}(\vec{r})\exp\left(-\frac{\mathrm{i}}{\hbar}\mathcal{L}(\vec{r})\tau\right) \tag{7.37}$$

defined in the interaction picture, Eq. (7.36) can be rearranged to

$$\begin{aligned}\mathcal{R}_m^{(n)}(\vec{r}, t_n, t_{n-1}, ..., t_1) = \left(\frac{\mathrm{i}}{\hbar}\right)^n &\Theta(t_1)\Theta(t_2)...\Theta(t_n) \\ &\langle\langle mm|\mathcal{G}(\vec{r}, t_n + t_{n-1} + ... + t_1)\mathcal{V}(\vec{r}, t_{n-1} + ... + t_1) \\ &\mathcal{V}(\vec{r}, t_{n-2} + ... + t_1)...\mathcal{V}(\vec{r}, t_1)\mathcal{V}(\vec{r}, 0)|\rho(-\infty)\rangle\rangle.\end{aligned} \tag{7.38}$$

Further, the basis diagonal elements $\{|m\rangle\}$ of the density matrix that describe population are time independent such that

$$\langle\langle mm|\exp\left(-\frac{\mathrm{i}}{\hbar}\mathcal{L}(\vec{r})\tau\right) = \langle\langle mm|. \tag{7.39}$$

Hence, the n-th order photoemission response function is expressed as

$$\begin{aligned}\mathcal{R}_m^{(n)}(\vec{r}, t_n, t_{n-1}, ..., t_1) = \left(\frac{\mathrm{i}}{\hbar}\right)^n &\Theta(t_1)\Theta(t_2)...\Theta(t_n)\langle\langle mm|\mathcal{V}(\vec{r}, t_{n-1} + ... + t_1) \\ &\mathcal{V}(\vec{r}, t_{n-2} + ... + t_1)...\mathcal{V}(\vec{r}, t_1)\mathcal{V}(\vec{r}, 0)|\rho(-\infty)\rangle\rangle.\end{aligned} \tag{7.40}$$

Considering the special case of 2D nanoscopy described in Section 7.3.1, four interactions are assumed, i.e., one interaction for each pulse, and then the corresponding fourth order photoemission response function is described by

$$\begin{aligned}\mathcal{R}_m^{(4)}(\vec{r}, t_4, t_3, t_2, t_1) = \left(\frac{\mathrm{i}}{\hbar}\right)^4 &\Theta(t_1)\Theta(t_2)\Theta(t_3)\Theta(t_4)\langle\langle mm|\mathcal{V}(\vec{r}, t_3 + t_2 + t_1) \\ &\mathcal{V}(\vec{r}, t_2 + t_1)\mathcal{V}(\vec{r}, t_1)\mathcal{V}(\vec{r}, 0)|\rho(-\infty)\rangle\rangle.\end{aligned} \tag{7.41}$$

In Hilbert space this results in

$$\begin{aligned}\mathcal{R}_m^{(4)}(\vec{r}, t_4, t_3, t_2, t_1) = \left(\frac{\mathrm{i}}{\hbar}\right)^4 &\Theta(t_1)\Theta(t_2)\Theta(t_3)\Theta(t_4) \\ &\langle m|[V(\vec{r}, t_3 + t_2 + t_1), [V(\vec{r}, t_2 + t_1), [V(\vec{r}, t_1), [V(\vec{r}, 0), \rho(-\infty)]]]]|m\rangle.\end{aligned} \tag{7.42}$$

Note that opposed to the measurement of "conventional" 2D spectroscopy, different photoemission response functions are measured depending on the measured kinetic energy $E_{\mathrm{kin},m}$. Nevertheless, an expression for the fourth order photoemission response function $\mathcal{R}_m^{(4)}(\vec{r},t_4,t_3,t_2,t_1)$ is found that is described by four dipole couplings $V(\vec{r},\tau)$. This is also reflected in the time dependences. The dependence on the fourth interaction is only due to the Heaviside step function which assures that the fourth pulse arrives after the third pulse, i.e., $t_4 > 0$. In all other cases the response function is zero. Hence, the measured fourth order photoemission response function $\mathcal{R}_m^{(4)}(\vec{r},t_4,t_3,t_2,t_1)$ is very similar to the third order nonlinear response function $S^{(3)}(t_3,t_2,t_1)$ [Eq. (7.20)] measured in "conventional" 2D spectroscopy. This indicates that although a fourth order photoemission response function is considered here, the information content is the same as that of the third order nonlinear response function. Therefore, the incoherent electrons that are detected in 2D nanoscopy reveal electronic coherences as observed in "conventional" 2D spectroscopy. The similarity between the two methods also results in very similar Liouville pathways as will be discussed in Section 7.3.4.

Note that in the theoretical description presented here, relaxation terms due to, e.g, inelastic electron–electron scattering or spontaneous transitions from one state $\langle m|$ to another state $\langle n|$ are neglected. However, incorporation of such terms can be done by adding a corresponding functional in the Liouville-von-Neumann equation [174].

7.3.3 Phase Cycling

To explain phase cycling, first the signal that is measured in 2D nanoscopy is considered. The local photoemission yield is calculated using Eqs. (7.33) and (7.35) and results in

$$Y_{\mathrm{PE},m}(\vec{r}) = \left(\frac{\mathrm{i}}{\hbar}\right)^4 \int_{-\infty}^{\infty} \mathrm{d}t' \int_0^{\infty} \mathrm{d}t_4 \int_0^{\infty} \mathrm{d}t_3 \int_0^{\infty} \mathrm{d}t_2 \int_0^{\infty} \mathrm{d}t_1 \, \tilde{S}_m^{(4)}(\vec{r},t_4,t_3,t_2,t_1) E(\vec{r},t'-t_4) \\ E(\vec{r},t'-t_4-t_3) E(\vec{r},t'-t_4-t_3-t_2) E(\vec{r},t'-t_4-t_3-t_2-t_1). \quad (7.43)$$

The electric field that induces the transitions in 2D nanoscopy is a quadruple-pulse sequence which is described by

$$E(\vec{r},t') = \hat{A}(t'-\tau-T)\,\mathrm{e}^{\mathrm{i}\left(\omega_0 t' - \varphi_\tau - \varphi_T + \vec{k}\vec{r}\right)} + \hat{A}(t'-T)\,\mathrm{e}^{\mathrm{i}\left(\omega_0 t' - \varphi_T + \vec{k}\vec{r}\right)} + \\ \hat{A}(t')\,\mathrm{e}^{\mathrm{i}\left(\omega_0 t' + \vec{k}\vec{r}\right)} + \hat{A}(t'+t)\,\mathrm{e}^{\mathrm{i}\left(\omega_0 t' + \varphi_t + \vec{k}\vec{r}\right)} + c.c. \quad . \quad (7.44)$$

Herein, the relative times are defined according to the illustration in Fig. 7.5 as

$$\tau \equiv \tilde{t}_2 - \tilde{t}_1, \qquad T \equiv \tilde{t}_3 - \tilde{t}_2, \qquad t \equiv \tilde{t}_4 - \tilde{t}_3 \quad (7.45)$$

where $\tilde{t}_3 \equiv 0$ is chosen here as it is customary in "conventional" 2D spectroscopy. The relative phases are introduced according to the relative times

$$\varphi_\tau \equiv \varphi_2 - \varphi_1, \qquad \varphi_T \equiv \varphi_3 - \varphi_2, \qquad \varphi_t \equiv \varphi_4 - \varphi_3, \quad (7.46)$$

where the third pulse is again defined as reference, such that $\varphi_3 \equiv 0$.

The definition of the electric field $E(\vec{r}, t')$ results in $8 \times 8 \times 8 \times 8 = 4096$ summands that contribute to 2D nanoscopy signal in terms of the local photoemission yield [Eq. (7.43)]. However, only contributions are requested that occur from interactions with all four pulses, e.g., contributions that occur from two interactions with the same pulse should be eliminated.

Opposed to "conventional" 2D spectroscopy, the signal measured in 2D nanoscopy is not an optical signal and phase matching is obsolete, which also enables a collinear illumination, i.e., all pulses in the sequence possess the same $\vec{k}$. Hence, a reduction of the terms is not possible in terms of their k vectors. However, each of the summands Eq. (7.43) has a distinct dependence on the relative phases. The number of summands can therefore be reduced by varying the relative phases φ_τ, φ_T, and φ_t, and calculating suitable linear combinations of the signals. This process is called phase cycling and was introduced by Warren *et al.* [157, 175]. In the experiment phase cycling is realized by measuring the signal for different combinations of the relative phases. The simplest possible phase cycling is a two-step phase cycling, where the signal is measured for two different combinations, e.g., for the combinations

$$(\varphi_\tau, \varphi_T, \varphi_t) = \{(0,0,0), (0,0,\pi)\}\,. \tag{7.47}$$

The corresponding phase cycled signal $Y_{\mathrm{PE},m}(\vec{r})$ is then found by the difference of the signal that is measured for the two combinations.

$$Y_{\mathrm{PE},m}(\vec{r}) = Y^{(0,0,0)}_{\mathrm{PE},m}(\vec{r}) - Y^{(0,0,\pi)}_{\mathrm{PE},m}(\vec{r}) \tag{7.48}$$

Since only the phase of the last pulse is modified in this example all contributions that do not depend on the last pulse are eliminated with this phase cycling, whereas all other contributions are doubled. Correspondingly, to eliminate the contributions that do not depend on a different pulse, different two-step phase-cycling combinations have to be applied.

To eliminate signals that are independent of two pulses, e.g., the first and the last pulse, a four-step phase cycling has to be employed with four different combinations of the relative phase, e.g.

$$(\varphi_\tau, \varphi_T, \varphi_t) = \{(0,0,0), (\pi,0,\pi), (0,0,\pi), (\pi,0,0)\}\,. \tag{7.49}$$

The corresponding phase-cycled signal $Y_{\mathrm{PE},m}(\vec{r})$ is the sum over all individual signals $Y^{(\varphi_\tau,\varphi_T,\varphi_t)}_{\mathrm{PE},m}(\vec{r})$ with prefactors according to $\mathrm{e}^{\mathrm{i}(\varphi_\tau+\varphi_T+\varphi_t)}$ such that

$$\begin{aligned} Y_{\mathrm{PE},m}(\vec{r}) =& \mathrm{e}^{\mathrm{i}0}\, Y^{(0,0,0)}_{\mathrm{PE},m}(\vec{r}) + \mathrm{e}^{\mathrm{i}2\pi}\, Y^{(\pi,0,\pi)}_{\mathrm{PE},m}(\vec{r}) + \mathrm{e}^{\mathrm{i}\pi}\, Y^{(0,0,\pi)}_{\mathrm{PE},m}(\vec{r}) + \mathrm{e}^{\mathrm{i}\pi}\, Y^{(\pi,0,0)}_{\mathrm{PE},m}(\vec{r}) \\ =& Y^{(0,0,0)}_{\mathrm{PE},m}(\vec{r}) + Y^{(\pi,0,\pi)}_{\mathrm{PE},m}(\vec{r}) - Y^{(0,0,\pi)}_{\mathrm{PE},m}(\vec{r}) - Y^{(\pi,0,0)}_{\mathrm{PE},m}(\vec{r}) \end{aligned} \tag{7.50}$$

For further eliminations of the contributing summands in Eq. (7.43), higher-step phase-cycling combinations, e.g., 16-step phase-cycling combinations, can be achieved accordingly. In these higher-step phase-cycling combinations imaginary prefactors can appear since relative phases of $\pi/2$ have to be applied. Hence, imaginary phase-cycled signals $Y_{\mathrm{PE},m}(\vec{r})$ can appear. The exact definition of the required combination has to be chosen according to the desired information content of the 2D nanospectra.

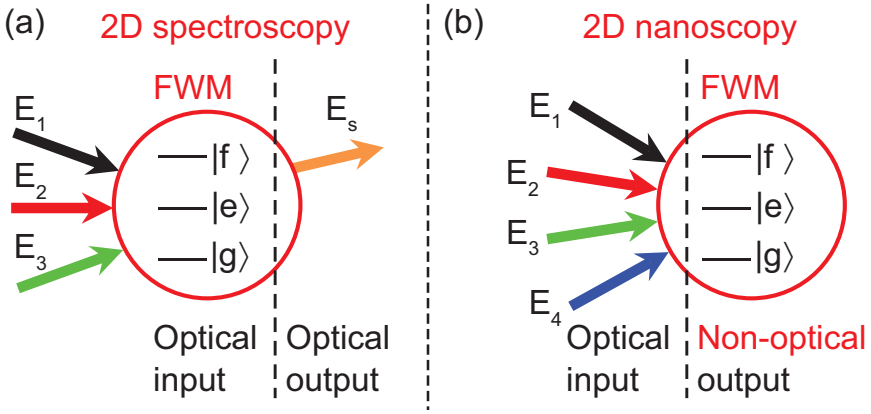

Figure 7.6: Four-wave mixing (FWM) for coherent 2D spectroscopy (left) and 2D nanoscopy (right). (a) In conventional four-wave mixing (FWM), three ingoing optical waves E_1, E_2 and E_3 are converted to one outgoing optical wave E_s via interaction with a three level quantum system. The subscripted numbers indicate time ordering. (b) In 2D nanoscopy, the input consists of four ingoing optical waves E_i $(i = 1, ..., 4)$, and the non-optical output is the resulting electronic population. Taken from Aeschlimann *et al.* [173]. Copyright (2011) by AAAS.

In the example of 2D nanoscopy described in Section 7.4.4 a four-step phase cycling was applied with $\varphi_T = 0$, which was found to be a good compromise between information content and measurement time.

7.3.4 Liouville Pathways

The analogy of 2D spectroscopy and 2D nanoscopy is discussed here by comparing the contributing Liouville-space pathways for a three-level system. For 2D spectroscopy (Fig. 7.6a), electric-field interactions E_1, E_2, and E_3 with the system ("input") create a polarization that is radiated off by the signal field E_s ("output"). This process is also called four-wave mixing (FWM) and is described by considering a linear combination of the response-function contributions (Fig. 7.7a) for a two-level system, R_1, R_2, R_3, R_4 (Fig. 7.1) and additional contributions involving the third level $|f\rangle$, R_{1f}, R_{2f}, R_{3f}, R_{4f} [171] as well as their complex conjugates for which the first interaction arrow would point downward instead of to the right side.

For 2D nanoscopy (Fig. 7.6b), all four interactions E_1, E_2, E_3, and E_4 are on the "input" side, and the final electronic population is the "output". As explained in Section 7.3.3, phase cycling can then be used to assign these interactions to the respective four pulses of E_{2D} from Fig. 7.5. Due to different theoretical descriptions (Section 7.3.2), three cases depending on the kinetic energy of the photoelectrons (Fig.7.4) have to be discriminated. For $E_{\mathrm{kin},g}$, five pathways contribute (Fig. 7.7b). These are analogous to the corresponding ones from 2D spectroscopy (Fig. 7.7a), noting that for 2D nanoscopy the direction of the final interaction arrow (blue) matters, whereas in 2D spectroscopy the final direction (orange) is arbitrary as long as it leads to a population (here displayed vertically always) because the final state of the quantum system is not measured. In

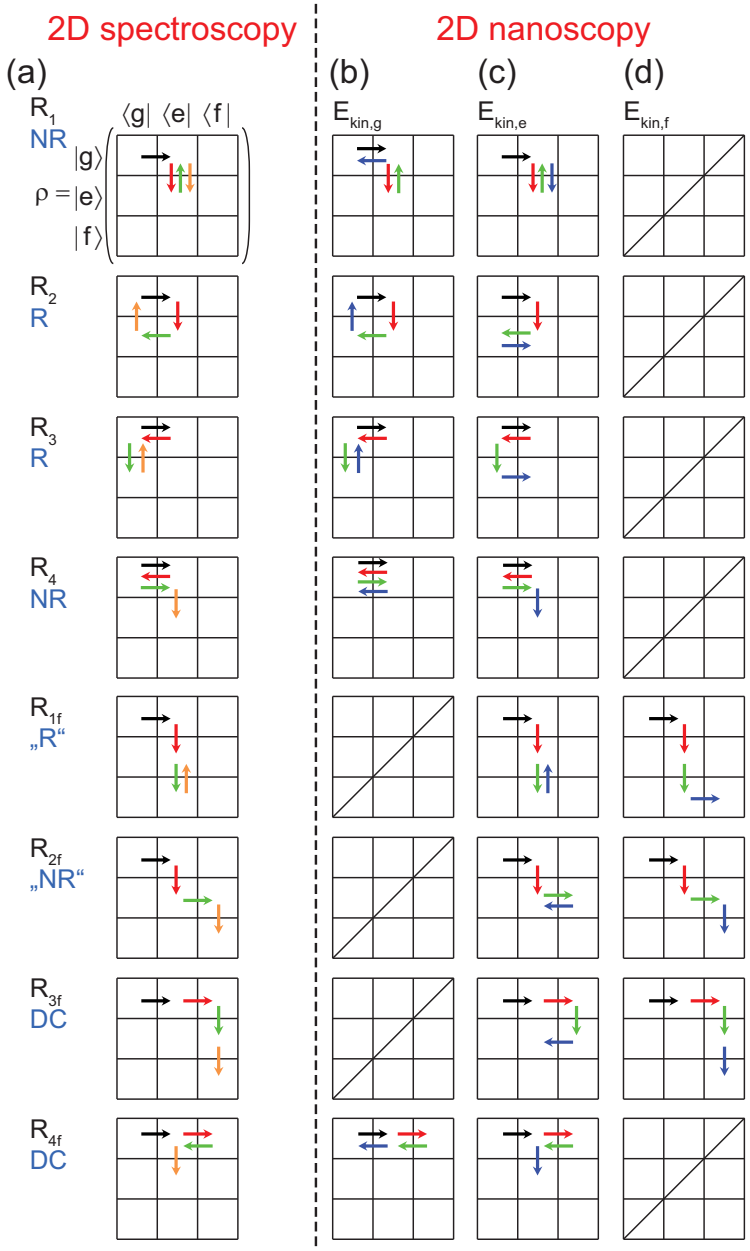

Figure 7.7: Liouville-space pathways for coherent 2D spectroscopy (left) and 2D nanoscopy (right). (a) The pathways contributing in third-order perturbation theory to the detected signal are shown graphically using arrows that connect elements within a reduced density matrix ρ. The colors correspond to the interactions of Fig. 7.6a, the labels R_i and R_{if} ($i = 1, ..., 4$) are taken from the literature [7, 171], and the blue labels indicate rephasing (R), non-rephasing (NR), and double-coherence (DC) contributions. (b)–(d) Contributing pathways in 2D nanoscopy are shown side with their analogous Liouville pathways for different photoelectron kinetic energies (Fig. 7.4): (b) $E_{\mathrm{kin},g}$, (c) $E_{\mathrm{kin},e}$, and (d) $E_{\mathrm{kin},f}$. Taken from Aeschlimann *et al.* [173]. Copyright (2011) by AAAS.

the case of $E_{\mathrm{kin},e}$ all eight Liouville pathways are relevant (Fig. 7.7c), and for $E_{\mathrm{kin},f}$ only three pathways have to be considered (Fig. 7.7d). Thus, in contrast to 2D spectroscopy where all pathways are always relevant, in 2D nanoscopy some of the individual contributions can be disentangled, possibly even by considering different linear combinations of the results for $E_{\mathrm{kin},g}$, $E_{\mathrm{kin},e}$, and $E_{\mathrm{kin},f}$. Note that the pathways depicted in Fig. 7.7 correspond to transitions in a reduced density matrix ρ. In general, the levels labeled $|g\rangle$, $|e\rangle$ and $|f\rangle$ may correspond to collective excitations such as excitonic or plasmonic bands and as such display a substructure. Hence, in the full energy-eigenstate representation, one would have to discriminate between different levels $|e_1\rangle$ and $|e_2\rangle$, say, of the excitonic band $|e\rangle$, that can be reached during the four-pulse electric-field interaction. Indeed, coherence and population transfer processes between such levels (i.e., intraband transitions) are relevant and will show their signature in the resulting 2D nanospectra. In Fig. 7.7, no distinction has been made between processes pertaining to the involvement of different intraband levels.

Nonlinear spectroscopic techniques are often labeled according to the order n of the nonlinear response $S^{(n)}$ that connects incident electric field and resulting polarization. As is shown in Section 7.3.2, 2D nanoscopy cannot be called a $S^{(n)}$ technique, because the final state is a population rather than a polarization/coherence. However, the information content turned out to be analogous to that of a "regular" $S^{(3)}$ spectroscopy (i.e., four-wave mixing) because the Liouville pathways correspond. In this sense, the methods are equivalent though not identical. Different Liouville diagrams enter into the linear combinations that create the signals for either conventional phase-matched 2D spectroscopy or 2D spectroscopy using fluorescence detection or 2D nanoscopy, resulting in slightly different lineshapes for the different methods. As already mentioned in Section 7.3.3, the lineshapes also depend on the extent of phase cycling. With a sufficient amount of phase cycles, the signal corresponding to a phase-matched photon echo can be extracted also in 2D nanoscopy. For reduced phase cycles, one still obtains useful 2D spectroscopic information that however has to fulfill certain symmetry requirements. The main reason for 2D nanoscopy, of course, is not simply to copy the information content of conventional 2D spectroscopy, but to provide genuine subdiffraction spatial resolution.

7.3.5 Generation of a Pulse Sequence with a Pulse Shaper

The method of 2D nansocopy, introduced in Section 7.3.1, uses pulse sequences with variable delays between the pulses and variable offset phases of each pulse to excite the sample. Due to the phase stability that is needed in the experiment, the pulse sequences are generated with a pulse shaper in amplitude and phase-shaping configuration offering inherent phase stability. To calculate the corresponding pulse shaper mask (i.e., the settings of each LCD pixel) the corresponding spectral electric field have to be derived mathematically. Since the adjustable parameters are defined in time domain, the derivation is started with temporal electric fields.

Generating a pulse sequence of N pulses the j-th pulse can be described analogously to Eq. 2.10

$$E_j^+(t) = A(t - t_j)\ \mathrm{e}^{\mathrm{i}\left[\phi(t-t_j)+\phi_j^c\right]}, \tag{7.51}$$

where t_j is the delay of the pulse and ϕ_j^c is the offset phase of the pulse, which both are varied in the experiment. The amplitude $A(t)$ and the phase $\phi(t)$ are the same for each pulse of the sequence and can additionally be defined using the pulse shaper. Assuming the absolute phase to be identical for all pulses, i.e., no shift of the phase is introduced by a temporal shift, the temporal electric field can be written as

$$\begin{aligned} E_j^+(t) =& A(t-t_j)\ \mathrm{e}^{\mathrm{i}\left[\varphi(t-t_j)+\omega_0 t+\phi_j^c\right]} \\ =& \hat{A}(t-t_j)\ \mathrm{e}^{\mathrm{i}\left(\omega_0 t+\phi_j^c\right)} \end{aligned} \tag{7.52}$$

where $\varphi(t-t_j)$ is defined according to Eq. (2.2) and is absorbed into the complex envelope function $\hat{A}(t-t_j)$ in the last step. The complete electric field is then a sequence of N pulses and is described by the sum over all pulses

$$E^+(t) = \frac{1}{N}\sum_{j=1}^{N} E_j^+(t), \tag{7.53}$$

where the pre-factor is the normalization, i.e., the original pulse is recovered by setting $t_j = 0$ and $\phi_j^c = 0$ for all j.

The spectral electric field is obtained by performing a complex-valued Fourier transformation

$$E^+(\omega) = \mathcal{F}\left\{E^+(t)\right\} = \frac{1}{N}\sum_{j=1}^{N} \mathcal{F}\left\{E_j^+(t)\right\}, \tag{7.54}$$

where the linearity of the Fourier transformation was used in the last step. Hence, the spectral electric field of a single pulse j can be written as

$$E_j^+(\omega) = \mathcal{F}\left\{E_j^+(t)\right\} = \frac{1}{\sqrt{2\pi}}\int_{-\infty}^{\infty} A(t-t_j)\ \mathrm{e}^{\mathrm{i}\left[\varphi(t-t_j)+\omega_0 t+\phi_j^c\right]}\,\mathrm{e}^{-\mathrm{i}\omega t}\,\mathrm{d}t. \tag{7.55}$$

The expression can be simplified by setting $t' = t - t_j$ and additional rearrangement of the ω and ω_0 terms yield

$$E_j^+(\omega) = \frac{1}{\sqrt{2\pi}}\int_{-\infty}^{\infty} A(t')\ \mathrm{e}^{\mathrm{i}\left[\varphi(t')-(\omega-\omega_0)t_j+\phi_j^c\right]}\ \mathrm{e}^{-\mathrm{i}(\omega-\omega_0)t'}\ \mathrm{d}t', \tag{7.56}$$

where the lower and upper limit do not change, since it is still integrated over all times and the new variable of integration is $\mathrm{d}t'$. Carrying out the Fourier transformation with the new transform variable $\omega - \omega_0$ results in

$$E_j^+(\omega) = A(\omega-\omega_0)\ \mathrm{e}^{-\mathrm{i}\left[\varphi(\omega-\omega_0)+(\omega-\omega_0)t_j-\phi_j^c\right]}, \tag{7.57}$$

which is the spectral description of a single pulse in the sequence. Combination of the amplitude $A(\omega-\omega_0)$ and the spectral phase $\varphi(\omega-\omega_0)$ reveals the complex-valued

$E_0(\omega-\omega_0)$, which is the full spectral description of $\hat{A}(t)$ [Eq. (7.52)] shifted to be centered around zero frequency. Hence, Eq. (7.57) rewrites as

$$E_j^+(\omega) = E_0(\omega-\omega_0)\ \mathrm{e}^{-\mathrm{i}\left[(\omega-\omega_0)t_j-\phi_j^c\right]}. \tag{7.58}$$

The spectral field of the complete pulse sequence is then obtained by summing up over all N pulses

$$E^{(N)+}(\omega) = \frac{1}{N}\sum_{j=1}^{N} E_j^+(\omega) = \frac{E_0(\omega-\omega_0)}{N}\sum_{j=1}^{N}\mathrm{e}^{-\mathrm{i}\left[(\omega-\omega_0)t_j-\phi_j^c\right]}. \tag{7.59}$$

Herein, $E_0(\omega-\omega_0)$ can be factored out since it is the same for all pulses of the sequence. The calculated spectral electric field contains constructive and destructive interference for the single frequencies, e.g., for a two-pulse sequence a fringe pattern similar to that of spectral interferometry (Section 2.4.2) is observed.

The complex-valued LCD mask transfer function

$$M_{\mathrm{LCD}}^{(N)}(\omega) = \frac{E^{(N)+}(\omega)}{E_0(\omega)} = \frac{1}{N}\sum_{j=1}^{N}\mathrm{e}^{-\mathrm{i}\left[(\omega-\omega_0)t_j-\phi_j^c\right]} \tag{7.60}$$

then describes how the amplitude, $|M_{\mathrm{LCD}}|$, and phase, $\arg\{M_{\mathrm{LCD}}\}$, for each frequency component have to be modified to create the desired pulse sequence from an unshaped input pulse.

To realize the experiment, pulse sequences of two and four pulses are generated. Characterizations of such pulse sequences are shown and discussed in Section 7.4.2.

7.4 Experimental Realization

In this section the experimental realization of 2D nanoscopy in terms of two different implementations is described and the recorded data is discussed qualitatively. A quantitative analyzes of the recorded data is done using appropriate models in Section 7.5.

7.4.1 Experimental Setup and Choice of Sample

The experimental setup that was used to realize 2D nanoscopy is identical with the setup described in Chapter 6 for coherent control on a rough silver surface (Section 6.2). A Ti:Sapphire oscillator provided femtosecond laser pulses (80 MHz, 795 nm, 30 fs FWHM, 9 nJ) that were beam pointing stabilized. Using a pulse shaper, the light pulses were then modulated in amplitude and phase to generate the required pulse sequences. Hence, opposed to the experiments presented in Chapter 6, the pulse shaper was used in amplitude and phase-shaping mode, i.e., the pulse sequences that excited the sample were purely p polarized (cf. Fig. 2.17). The pulses were again characterized outside the UHV chamber since direct characterization at the position of the sample was not possible. To account for dispersion introduced by the window of the UHV chamber a glass plate was inserted into the beam in front of the characterization tool. The pulses

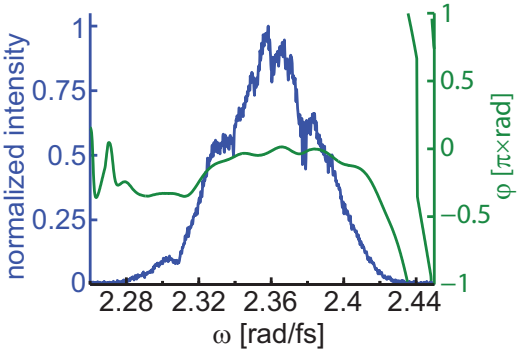

Figure 7.8: The spectral intensity and phase of the transform-limited laser pulse. The pulse was characterized using spectral interferometry (Section 2.4) in the setup shown in Fig. 6.2. This pulse is defined as the unshaped pulse for the experiment described in the following.

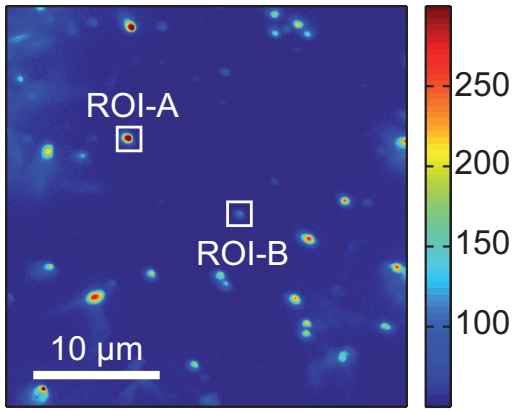

Figure 7.9: Photoemission yield of the sample excited with a pulse shown in Fig. 7.8. The regions that are investigated in more detail are indicated with white rectangles and labeled with ROI-A and ROI-B.

were compressed with the pulse shaper by applying the inverse phase of an unshaped pulse that was measured with FROG. Due to the reduction of the spectral width induced by optical elements within the pulse shaper the transform-limited pulse after the pulse shaper was determined to have a duration of 51 fs. The spectral intensity and phase of the transform-limited pulse is shown in Fig. 7.8 yielding a flat spectral phase and a spectrum that is distorted by the $4f$ setup of the pulse shaper with respect to the gaussian laser spectrum generated with the oscillator. Correspondingly, the center wavelength shifts to about 798 nm. The shown pulse is also used for the quantitative analyzes in Section 7.5. The incidence angle of the excitation pulses were 65° with respect to the sample (Fig. 2.17) and the pulses are focused very weakly on the sample using a lens with a focal length of 30 cm. Accordingly, the spot size on the sample was approximately 70 µm in diameter. The sample that is investigated in this chapter is the same corrugated silver surface that was used for coherent control in the last chapter. The sample was chosen because in the experiments of Chapter 6 unexpected high photoelectron yield was obtained for pulse durations of several hundred femtoseconds. This indicates that long-lived coherences might exist on the random silver surface. Additionally, strong variations on spatial regions that are separated below the diffraction limit were observed and suggests to investigate the temporal dynamics using 2D nanoscopy. A PEEM image of a small region of the investigated sample is shown in Fig. 7.9. Two regions of interest are indicated: the hot spot of ROI-A serves as a reference hot spot and the hot spot of ROI-B is investigated in more detail. Opposed to the order of three determined in

Chapter 6 for the corrugated silver surface, the order of nonlinearity is determined to be four for the presented experiment. This increase of the order of nonlinearity can be explained by the reduction of Cs on the surface resulting in an increase of the vacuum energy.

Although for the most general implementation of 2D nanoscopy introduced in Section 7.3 the usage of a separate ionization laser is suggested, in this first experimental demonstration presented in this Section no extra beam is used, and photoemission is rather induced by the four-pulse sequence itself via four-photon ionization. In conjunction with that, the kinetic energy of the photoelectrons is not measured. However, note that position and energy-resolved (time-of-flight) detectors are available and can be employed for future implementations.

7.4.2 Pulse Sequences

In the experiments described below two different scans were performed. A quadruple pulse sequence scan used for the 2D nanoscopy measurement as described above and a double pulse sequence to obtain further insight into the dynamics as will be shown below. The corresponding LCD masks that were applied to the pulse shaper are obtained by setting $N = 4$ and $N = 2$ in Eq. (7.60). Additionally, the absolute times and offset phases are substituted by relative values, since the absolute values of the pulse sequence used in the experiment is irrelevant. Hence, the times $\tilde{t}_j$ of the pulse centers are substituted by the relative times defined in Eq. (7.45) according to Fig. 7.5 and the corresponding relative phases are defined in Eq. (7.46). As it is customary in "conventional" 2D spectroscopy (Fig. 7.2a), the time of the third pulse is set to zero, i.e., $\tilde{t}_3 = 0$. Using these substitutions [Eqs. (7.45) and (7.46)], Eq. (7.60) can be recast

$$M^{(4)}_{\mathrm{LCD}}(\omega,\tau,T,t,\varphi_\tau,\varphi_t) = \frac{1}{4}\left\{\mathrm{e}^{\mathrm{i}[(\omega-\omega_0)(\tau+T)-\varphi_\tau-\varphi_T]} + \mathrm{e}^{\mathrm{i}[(\omega-\omega_0)T-\varphi_T]} + 1 + \mathrm{e}^{-\mathrm{i}[(\omega-\omega_0)(-t)+\varphi_t]}\right\} \tag{7.61}$$

for the quadruple-pulse sequence. For the double pulse sequence, the separation times and the relative offset phases between the first and the second and between the third and fourth pulse are set to zero, i.e., $\tau = t = 0$ and $\varphi_\tau = \varphi_t = 0$. This results in

$$M^{(2)}_{\mathrm{LCD}}(\omega,T,\varphi_T) = \frac{1}{2}\left\{\mathrm{e}^{\mathrm{i}[(\omega-\omega_0)T-\varphi_T]} + 1\right\}. \tag{7.62}$$

Note that the complex-valued phase masks were applied additionally to the phase that was applied for compression as described in Section 7.4.1. Hence, each pulse of the sequence is compressed, i.e., transform-limited.

To check the pulse sequences generated by the pulse shaper using complex-valued LCD masks derived for double [Eq. (7.62)] and quadrupole-pulse sequences [Eq. (7.61)], several pulse sequences were characterized using dual-channel spectral interferometry (Section 2.4.2) with reference pulses measured via FROG (Section 2.4.1). The temporal evolution of four double-pulse and two quadrupole-pulse sequences, which were also used in the measurements, are shown in Fig. 7.10. The normalized intensities (blue lines) and the phases (red lines) are plotted for each sequence. Above each plot the corresponding pulse separations and relative offset phases are denoted. As can be inferred, the desired

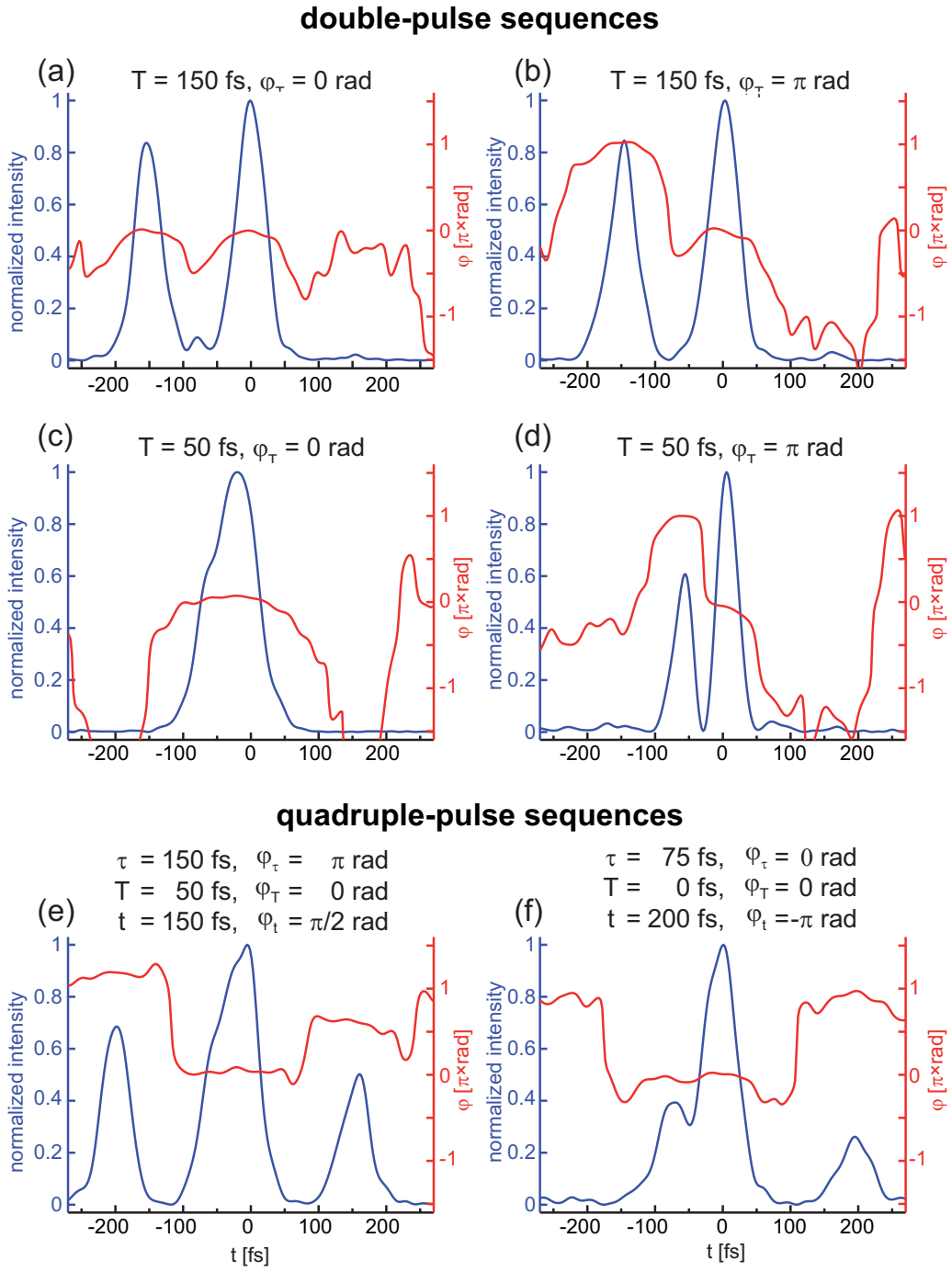

Figure 7.10: 2D nanoscopy pulse sequences. The double (upper panel) and quadruple-pulse sequences (lower panel) are generated with a pulse shaper using the LCD mask transfer function given in Eqs. (7.62) and (7.61), respectively. All pulse sequences are measured using spectral interferometry (Section 2.4.2). Normalized intensities and phases are displayed as blue and red lines, respectively. The corresponding parameters of the relative times and phase offsets between the subpulses are denoted above the plots.

pulse separations as well as the relative phases were achieved in an excellent manner. For example in Fig. 7.10b, the double-pulse sequence with a temporal separation of $T = 150\,\mathrm{fs}$ and a relative phase $\varphi_T = \pi\,\mathrm{rad}$ shows two pulses centered around $-150\,\mathrm{fs}$ and $0\,\mathrm{fs}$ with phases $\pi\,\mathrm{rad}$ and $0\,\mathrm{rad}$, respectively. In case of pulse overlap (e.g., Figs. 7.10c and 7.10d), observed for temporal separations between the pulses in the order of the pulse duration (50 fs FWHM), the pulse amplitudes depend on the relative phase. For zero relative phase (Fig. 7.10c), a broadening due to the interference of the overlapping parts is observed. Differently, destructive interference appears in the region of overlap for a relative phase that is π (Fig. 7.10d). The same accordance of the requested parameters is observed in Figs. 7.10e and 7.10f for the quadruple-pulse sequences. Although the required pulse parameters are in perfect agreement with the observed separations and relative phases, the relative intensities within the pulse sequences show small deviations from the expected ones. For example, the double pulses in Figs. 7.10a and 7.10b should have the same maximum intensity. Similarly, the first and the last pulse of the quadruple-pulse sequence in Fig. 7.10e should have the same maximum intensities. These deviations can have multiple sources. On the one hand, there are intrinsic limitations of the pulse shaper due to the finite pixelation of the LCD. This finite pixelation results in decreasing intensities of the electric fields with increasing separation from $t = 0\,\mathrm{fs}$ (i.e., the center of an unshaped pulse) and allows a maximum available time window of 4.7 ps [30]. However, in the experiments presented in this chapter, the maximum delay introduced between the first and the last pulse in the train is $(\tau + T + t)_{\mathrm{max}} = (280 + 0 + 280)\,\mathrm{fs} = 560\,\mathrm{fs}$ and influences from pulse-shaping artifacts due to the pixellated nature of the LCD are assumed to be small. The intrinsic limitations also contain the small gaps between the pixels that cannot be modulated with the LCD (cf. Fig. 2.8) and, therefore, appear at $t = 0\,\mathrm{fs}$. On the other hand, the deviations can have their origin in a wrong pulse shaper calibration. However, since the required pulse separations as well as their relative phases are found to be correct, the effect of a wrong pulse shaper calibration can be neglected here.

In summary, the obtained pulse shapes seem to fulfill the requirement for 2D nanoscopy and were used for the measurements described in the following.

7.4.3 Spatial Resolution

In this section the spatial resolution of 2D nanoscopy is discussed. The "conventional" imaging resolution of PEEM is usually determined using a continuous-wave ultraviolet lamp because that provides a uniform one-photon linear response excitation and most clearly reflects the spatial resolution. To prove the resolution for the 2D nanoscopy experiment as described in this chapter, such a measurement was carried out on a nanostructured gold sample prepared by focused ion-beam (FIB) milling to obtain a sharp edge. The obtained PEEM image (Fig. 7.11a) was analyzed perpendicular to the edge (Fig. 7.11b) providing an imaging resolution of 57.6 nm using the customary 16–84 criterion.

The spatial resolution in the 2D nanoscopy scheme is expected to be of the same order as in "conventional" PEEM because the photoelectron imaging apparatus is identical. Complications in measuring spatial resolution for nonlinear spectroscopic signals may

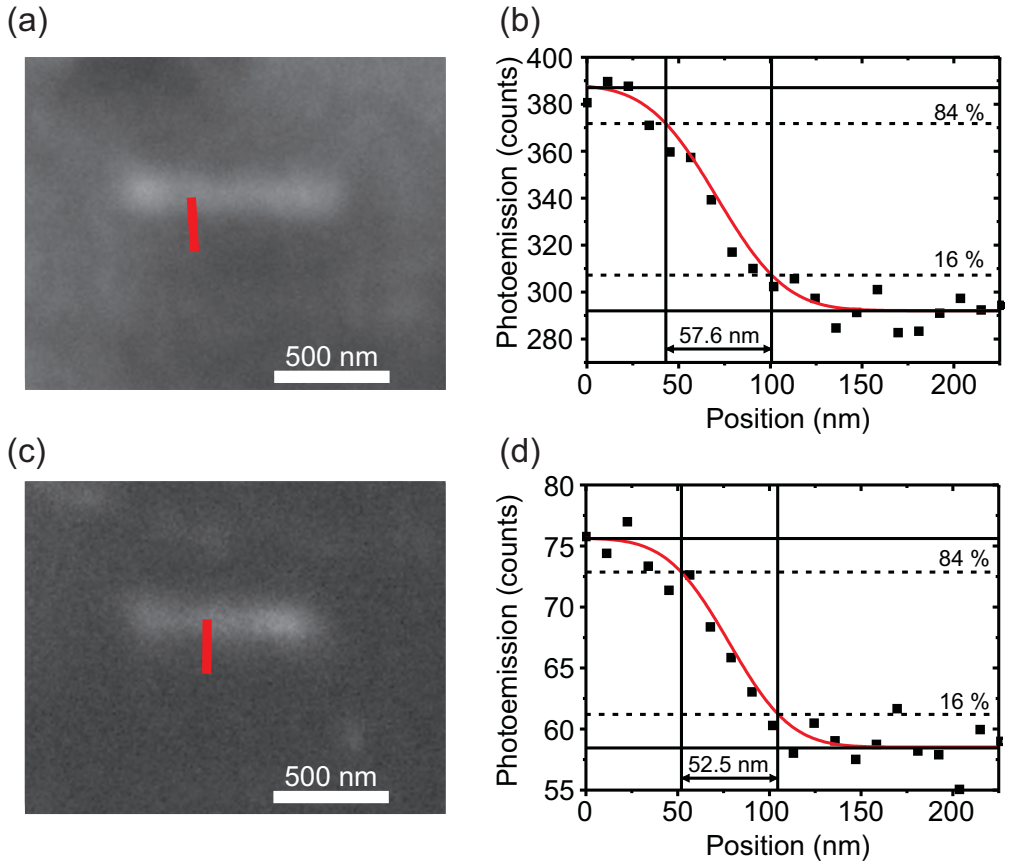

Figure 7.11: Spatial resolution of 2D nanoscopy. The resolution on the edge of a gold nanostructure prepared by focused ion-beam milling is determined. (a) The "conventional" PEEM imaging resolution is obtained with ultraviolet continuous-wave excitation and analyzed with a cut along the red line, providing (b) the data points (squares) and fit (red) that determine spatial resolution with the customary 16–84 criterion. (c) The resolution in 2D nanoscopy is determined with multiphoton photoemission upon femtosecond illumination of the same nanostructure with a single 798 nm pulse, corresponding to $\tau = T = t = 0$ from 2D nanoscopy. The PEEM image is again cut along the red line, providing (d) the data points (squares) and fit (red). The 16–84 criterion provides an upper bound for spatial resolution of 2D nanoscopy that is in agreement with the pure imaging resolution from (b). Taken from Aeschlimann *et al.* [173]. Copyright (2011) by AAAS.

arise, however, when spatially delocalized intermediate states are involved, such as in the case of the corrugated silver surface investigated here. For such samples one measures a convolution of the wavefunctions of the delocalized plasmons and the imaging resolution of the PEEM. Hence, in order to determine the spatial resolution for 2D nanoscopy, the same nanostructured gold sample was used as in the determination of conventional imaging resolution. Gold was used to reduce the effect of resonantly excited delocalized states that would complicate the analysis. Then a multiphoton photoemission image was observed upon illumination with single femtosecond laser pulses at 798 nm (Fig. 7.11c). This corresponds to time settings of $\tau = T = t = 0$ in 2D nanoscopy which were

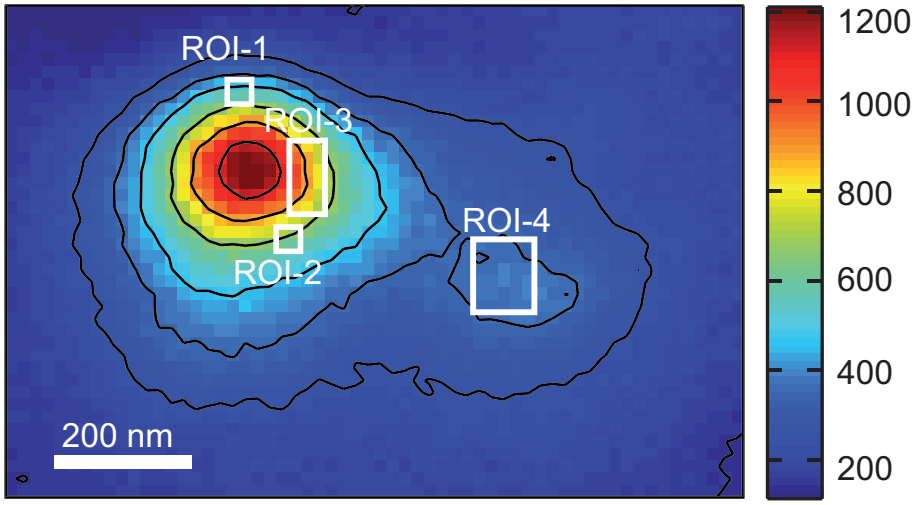

Figure 7.12: A zoomed-in image of hot spot ROI-B indicated in Fig. 7.9. The small ROIs 1–4 that are investigated in more detail are indicated with white rectangles.

chosen because then the signal is maximum and the contrast is best. Evaluation of the cut perpendicular to the edge (Fig. 7.11d) reveals a similar width of ∼50 nm (within the experimental uncertainty) as it was already obtained for "conventional" PEEM imaging.

From the comparison shown in Fig. 7.11 it can clearly be concluded that the well-known and accepted PEEM resolution is also obtained in the 2D nanoscopy scheme within multiphoton processes. Hence 2D nanoscopy indeed provides subdiffraction spatial resolution. In the presented experiments an upper bound of 50 nm was achieved without striving for maximum resolution, but it is possible to obtain ∼25 nm with the same device [69], and 2D nanoscopy has the potential to reach 2 nm resolution with other commercial PEEM devices [67].

The gold sample in Fig. 7.11 was useful for determining the spatial resolution of the method. As indicated above, it was chosen to avoid "hot spot" resonances with complex physics of coupled and partially delocalized oscillators. With the corrugated silver surface used in the main experiment presented here, on the other hand, a sample was chosen for which interesting physics are expected.

7.4.4 2D Nanoscopy Scan

To perform 2D nanoscopy measurements the ROI-B from Fig. 7.9 was investigated in more detail. During the measurements PEEM images were taken of a region with a diameter of ∼18 µm including the hot spot of ROI-B. This corresponds to a pixel size of $(18\,\mathrm{nm})^2$. A zoomed-in PEEM image of the hot spot under investigation (ROI-B) for single pulse illumination (i.e., $\tau = T = t = 0$ and $\varphi_\tau = \varphi_T = \varphi_t = 0$) is depicted in Fig. 7.12. As can be observed, additionally to a hot spot with high photoemission a hot spot with smaller photoemission leads to a combined photoemission pattern that is elongated in the horizontal direction.

The 2D nanospectra were measured with time delays τ and t varying from 0 to 280 fs

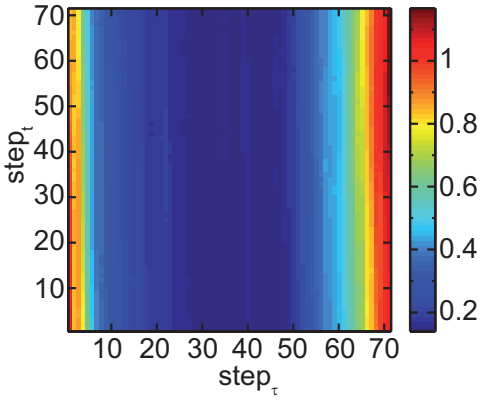

Figure 7.13: Reference signal during the 2D nanoscopy scan. The averaged photoemission yield of ROI-B (Fig. 7.9) that is observed from the reference images taken for the drift correction, i.e., for each step the reference image is taken after taking all images for phase cycling. The scan is performed by first scanning all steps along the t axis and then going one step further on the τ axis. The signal is normalized to the average of the first 25 steps.

in steps of 4 fs for a setting of population time $T = 0$. A fourfold phase cycling was implemented by taking four images for each time step. The images were taken according to Eq. 7.49 for the phase combinations

$$(\varphi_\tau, \varphi_t) = \{(0,0), (\pi,\pi), (0,\pi), (\pi,0)\}, \tag{7.63}$$

where the relative phase φ_T was set to 0 rad. Additionally, a reference image with $\tau = T = t = 0$ and $\varphi_\tau = \varphi_T = \varphi_t = 0$ was taken for drift correction (Section 2.6.3). Hence, five images were taken for each time step and multiplication with $71 \times 71 = 5041$ time step combinations results in 25205 images per scan. Each PEEM image was taken with temporal averaging at 250 ms CCD integration time, chosen to fit the full dynamic range of the camera.

Additionally, to the pure measurement time originating from the integration time of 25205 images taken for a 2D nanoscopy scan (smaller than two hours), the additional reaction time of the pulse shaper and the time that is needed to save the huge amount of data increased the total measurement time to about twelve hours. Hence, fluctuations of the signal during the scanning time had to be considered. The fluctuations of the signal were determined with the reference images. Therefore, the photoemission yield was averaged over the complete hot spot (i.e., approximately the region that is shown in Fig. 7.12) and the noise level (48 counts per pixel) was substracted. Then, the reference was smoothed to avoid higher weighting of short-term fluctuations in regions of small reference. Smoothing was done by averaging over 51 adjacent measurement points, i.e., for step j the reference is averaged from step $j - 25$ to $j + 25$. In addition, the signal was normalized to the average of the first 25 steps. The reference $Y_{\mathrm{PE}}^{\mathrm{ref}}$ as a function of t and τ steps is depicted in Fig. 7.13. While scanning, all t steps were measured first for one τ and then τ was changed to the next value starting from $(\tau, t) = (0, 0)$. As can be inferred, strong variations of the reference signal were measured. The signal decreased to about 20% of the initial signal in the middle of the scan and recovered at the end of the scan to values that even exceeded the initial signal. This variation of the signal can be explained by day–night intervals of the 12 hour scan. The scan was started in the evening at daytime then the signal decreased and stayed roughly constant during the night. The scan ended in the morning during daytime and the signal increased to

about 110% of the initial value meanwhile. Note that the measured modulation in signal strength were independent of the region of investigation and was found to be the same for each position on the sample. To account for the fluctuations, they are considered in the calculation of the 2D spectra as explained below.

For the data evaluation, the photoemission of each pixel $\vec{r}$ of the images of the four phase combinations described in Eq. (7.63) are combined according to the phase cycling process (Section 7.3.3) and divided by the reference signal $Y_{\mathrm{PE}}^{\mathrm{ref}}(\tau, T, t)$ (Fig. 7.13) to reveal the phase cycled time dependent photoemission yield

$$Y_{\mathrm{PE}}(\vec{r}, \tau, T, t) = \frac{Y_{\mathrm{PE}}^{00}(\vec{r}, \tau, T, t) + Y_{\mathrm{PE}}^{\pi\pi}(\vec{r}, \tau, T, t) - Y_{\mathrm{PE}}^{0\pi}(\vec{r}, \tau, T, t) - Y_{\mathrm{PE}}^{\pi 0}(\vec{r}, \tau, T, t)}{Y_{\mathrm{PE}}^{\mathrm{ref}}(\tau, T, t)}. \quad (7.64)$$

A 2D Fourier transformation of the real-valued time domain data then delivers complex-valued 2D spectra:

$$Y_{\mathrm{PE}}(\vec{r}, \omega_\tau, T, \omega_t) = \int_{-\infty}^{\infty} \int_{-\infty}^{\infty} Y_{\mathrm{PE}}(\vec{r}, \tau, T, t)\, \mathrm{e}^{-\mathrm{i}\omega_\tau \tau}\, \mathrm{e}^{-\mathrm{i}\omega_t t}\, \mathrm{d}\tau\, \mathrm{d}t \quad (7.65)$$

Although a continuous Fourier transformation is described here for the sake of simplicity, the 2D spectrum is calculated using a discrete Fourier transformation.

As an example, the 2D nanospectra of ROI-1 and ROI-2 indicated in Fig. 7.12 measured at $T = 0\,\mathrm{fs}$ are shown in Fig. 7.14 in terms of real part (left panels) and imaginary part (right panels). Each ROI contains $2 \times 2 = 4$ pixels yielding a spatial resolution of $(36\,\mathrm{nm})^2$ and the corresponding nanospectra were obtained by averaging over these 4 pixels. Additionally, the spectra were normalized to the absolute value at $(\omega_\tau, \omega_t) = (0, 0)$. The scanned time steps provide a spectral resolution of $0.022\,\mathrm{rad/fs}$ and a maximum detectable frequency shift with respect to the center frequency $\omega_0 = 2.360\,\mathrm{rad/fs}$ of $\pm 0.774\,\mathrm{rad/fs}$. The nanospectra are shown from -0.188 to $0.188\,\mathrm{rad/fs}$ including the complete spectrum of the excitation pulses (cf. Fig. 7.8).

A resonance at $(\omega_\tau, \omega_t) = (\omega_0, \omega_0)$ is observed in the 2D spectra shown in Fig. 7.14. This reflects that the investigated hot spot acts as a nanoantenna for the incident light and has a resonance around center frequency ω_0 of the excitation pulses. This resonant excitation is expected, due to the strong photoemission of the hot spot. However, for the interpretation of the 2D spectra it is important to point out that the response function of the investigated system is weighted with the laser spectrum such that the center of the spectra are more emphasized then the outer parts. In addition, the symmetry argumentation of the 2D spectra that will be discussed below has to be incorporated in the interpretation.

Different 2D lineshapes would be observed if the investigated resonance were sharp enough and located far enough away from the center frequency of the laser pulse. However, for the present sample this is not the case because the excited plasmonic bands are relatively broad as compared to the available laser spectrum, in contrast to, e.g., atomic transitions [157]. Due to the ultrahigh spatial resolution of the presented 2D nanospectra, line shapes that correspond to a single or very few contributing Lorentzian oscillators are observed in Fig. 7.14. Hence, the inhomogeneous distribution of resonances that would be detected in diffraction-limited spectroscopy and that would lead

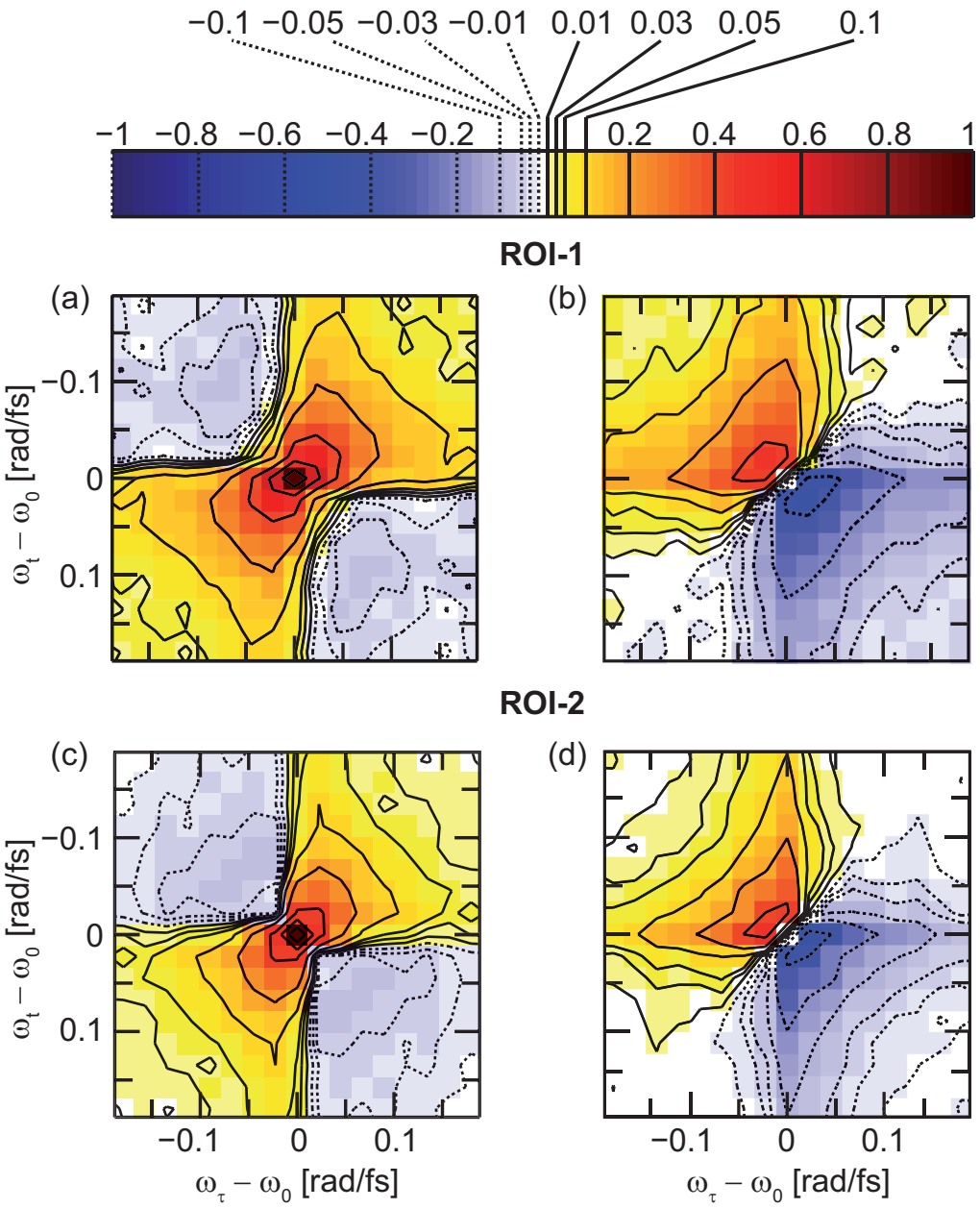

Figure 7.14: 2D nanospectra at $T = 0$ fs. The (a) 2D real and (b) imaginary part is shown for position ROI-1 and ROI-2 (c,d) that is 228 nm away within the same hot spot (Fig. 7.12), as a function of detuning from the center frequency ω_0 of the laser spectrum (Fig. 7.8). The axis ω_τ and ω_t are shown from −0.188 to 0.188 rad/fs and correspond to the frequencies related to the pulse delays τ and t, respectively. (a) and (c) taken from Aeschlimann *et al.* [173]. Copyright (2011) by AAAS.

to elongation of the 2D peak along the diagonal is eliminated to a large extent. Comparing the nanospectra for the two ROIs, i.e., upper versus lower panel, a difference in the linewidth is observed. The linewidth of the nanospectrum of ROI-1 is broader than

that of ROI-2. This is remarkable since the regions are separated by only 228 nm, i.e., below the diffraction limit. Hence, although only a single oscillator would be expected for a single hot spot this indicates contribution of different oscillators. This illustrates the power of the presented 2D nanoscopy since line shape difference for regions that are separated below the diffraction limit can be determined. A quantitive analysis of the 2D spectra in Fig. 7.14 in terms of Lorentz fits is carried out in Section 7.5.1.

As can be inferred from Fig. 7.14, four-step phase cycling creates the result from a real-valued linear combination of real-valued time-domain data. Hence, the 2D traces are point-symmetric in the present demonstration, more precisely they fulfill

$$Y_{\mathrm{PE}}(\omega_\tau, T, -\omega_t) = Y^*_{\mathrm{PE}}(-\omega_\tau, T, \omega_t), \tag{7.66}$$

with the star denoting complex conjugation. For a 2D spectrum of sharp resonance located not at the center frequency of the laser, a copy of the resonance would occur in opposing quadrants of $Y_{\mathrm{PE}}(\omega_\tau, \omega_t)$. Note, however, that this is no principle restriction of the 2D nanoscopy technique. A general possibility to retrieve the unconstrained 2D lineshape is to employ a 16-step phase cycle (Section 7.3.3) because there, in the linear combination constructing the signal, some of the measured (real-valued) contributions enter with a prefactor i and thus the complex nature of the signal is recovered. However, 16-step phase cycling would result in an increase of the measurement time by a factor of four, which was not realized due the issue of signal stability as described above.

7.4.5 Delay–Phase Scan

To support 2D-nanoscopy measurements using four pulses, i.e., three separation times τ, T and t, a two-pulse 2D nanoscopy scheme was conducted. In this scheme the population time T is varied and for each delay step the corresponding interpulse relative phase φ_T is scanned over the complete interval $[-\pi, \pi]$. Qualitatively, phase memory is apparent for those delays T for which the signal varied with φ_T, i.e., the signal depends on the "probe" phase with respect to the phase imprinted on the (quantum) system during excitation with the first pulse.

For the present sample, the delay T was varied in steps of 5 fs and the phase φ_T covers the range $[-\pi, \pi]$ in 41 steps. Figures 7.15a and 7.15b show the results for two closely spaced regions of interest within the hot spot, i.e., ROI-3 and ROI-4 in Fig. 7.12, respectively. The data is normalized to the photoemission measured at $T = 0\,\mathrm{fs}$ and $\varphi_T = 0\,\mathrm{rad}$ and is plotted on a color scale ranging from 0 to 0.1. Both plots show peak structures centered at $T = 0\,\mathrm{fs}$, $\varphi_T = 0\,\mathrm{rad}$ that extend to delays T greater than 200 fs. Without phase memory, the phase-dependent modulation of the photoemission signal would have vanished for a pulse separation greater than the pulse duration (50 fs). A tilt of the extended signal with respect to the vertical axis at $\varphi_T = 0$ indicates that the resonance of the investigated system is shifted with respect to the center frequency of the excitation pulses. In Fig. 7.15 a tilt to the left (right) indicates a shift to smaller (larger) frequencies. Note that the plots are periodic along the phase axis (horizontal axis), i.e., the points $(\varphi_T = -\pi\,\mathrm{rad}, T)$ and $(\varphi_T = \pi\,\mathrm{rad}, T)$ are identical.

The signals for the investigated ROIs exhibit strikingly different phase dependences. Most of the signal from ROI-3 (Fig. 7.15a) shows a tilt to the left that reveals a narrow

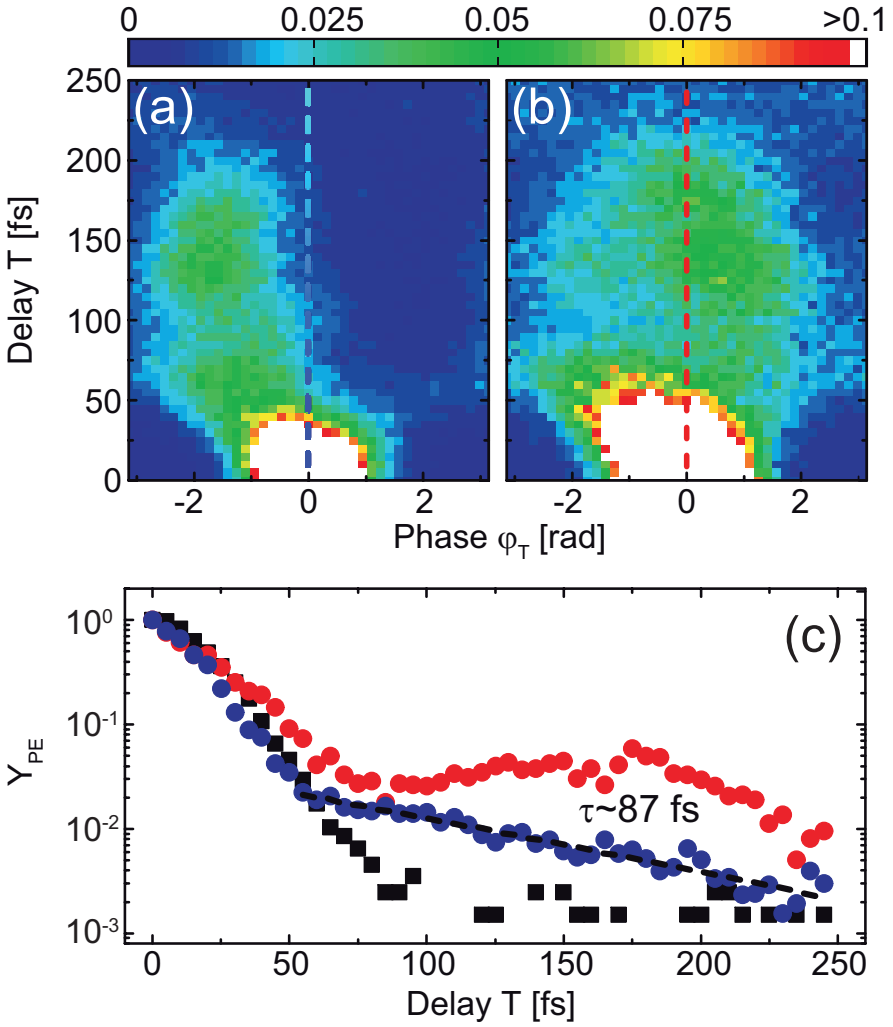

Figure 7.15: Delay–phase scans for ROI-3 (a) and ROI-4 (b) (cf. Fig. 7.12). The shown data is normalized with respect to the emission at $T = 0\,\text{fs}$ and $\varphi_T = 0\,\text{rad}$ and then plotted on a color scale ranging from 0 to 0.1. The vertical dashed lines indicate cuts shown in (c). (c) Comparison of signals for $\varphi_T = 0\,\text{rad}$ from ROI-3 (blue circles) and ROI-4 (red circles) with hot spot of ROI-A (Fig. 7.9) on the surface (black squares). The dashed black line indicates an exponential decay of $\sim$87 fs fitted to the data of ROI-3 (blue circles) for $T > 60\,\text{fs}$. Taken from Aeschlimann *et al.* [173]. Copyright (2011) by AAAS.

spread in the phase direction (horizontal axis). However, a small part is extended to the right and crosses the boundary $\varphi_T = \pi$ at about 75 fs. Destructive interference with the signal part that extended to the left is observed in the region of (1.75 rad, 100 fs). Considering the signal from ROI-4 (Fig. 7.15b), no clear tilt is observed. However, the signal seems to be broadened in the phase direction and again a beating pattern induced by interference of individual signal parts is observed. This can better be seen in cuts along the delay at $\varphi_T = 0\,\text{rad}$ (blue and red dashed lines in Figs. 7.15a and 7.15b, respectively). The signals for ROI-3 and ROI-4 are plotted in Fig. 7.15c as

blue and red circles, respectively, and the signal of the reference hot spot (ROI-B in Fig. 7.9) is plotted as black squares for comparison. Herein, the signal of ROI-3 decreased continuously. The first part between 0 and 50 fs of the signal is dominated by the pulse overlap and a steep slope is observed. However, outside of the pulse-overlap region, the slope is smaller and a dephasing time of $T_2 = 87\,\mathrm{fs}$ can be fitted to an exponential decay (dashed black line). The destructive interference that is observed in Fig. 7.15a is not reflected here since it appears at the vertical cut of $\varphi_T = -2\,\mathrm{rad}$. For ROI-4 (red circles) a nonmonotonic behavior of the signal is observed, reflecting the constructive and destructive interference of different signal parts. The differences between ROI-3 and ROI-4 again demonstrate that spectral features can be resolved that are separated spatially by less than the wavelength (i.e., from within an individual hot spot). The coherent beats, i.e., constructive and destructive interference of different signal parts indicate a local collective response that cannot be modeled by a single resonance and supports the finding of the four-pulse 2D nanoscopy measurements. Therefore, a model of different resonant modes is employed in the next section to quantitatively analyze the delay–phase scans.

7.5 Data Modelling

In this section the modeling procedure used for the simulation and fitting of the 2D nanoscopy data (Sections 7.4.4 and 7.4.5) is described. Since the investigated photoemission of the corrugated silver surface resulting in the observed hot spots was caused by plasmonic modes the model for plasmon-assisted multiphoton photoemission developed by Merschdorf *et al.* [176] is adopted. In this approximation the momentary local multiphoton photoemission probability $P_{\mathrm{PE}}(\vec{r},t)$ is proportional to the n-th power of the local field intensity, i.e., the squared local electric field $E_{\mathrm{loc}}(\vec{r},t)$,

$$P_{\mathrm{PE}}(\vec{r},t) \propto \left[E_{\mathrm{loc}}(\vec{r},t)\right]^{2n}, \tag{7.67}$$

with n being the order of nonlinearity of the multiphoton photoemission process. A description in Liouville space using the density matrix that leads to the same momentary local multiphoton photoemission probability is given in the Appendix A.2. The local electric field $E_{\mathrm{loc}}(\vec{r},t)$ is given by the convolution of the temporal incident field and the temporal local response function caused by the plasmonic mode. In frequency space, this corresponds to a multiplication of the incident electric field $E^{\mathrm{exc}}(\omega)$ with the response function $A(\vec{r},\omega)$ (Section 3.1.2). Hence, the local electric field can be written as

$$E_{\mathrm{loc}}(\vec{r},t) = \mathcal{F}^{-1}\left\{A(\vec{r},\omega)E^{\mathrm{exc}}(\omega)\right\}. \tag{7.68}$$

The local photoemission yield $Y_{\mathrm{PE}}(\vec{r})$ is then proportional to the time integral over the momentary local multiphoton photoemission probability $P_{\mathrm{PE}}(\vec{r},t')$ and is calculated

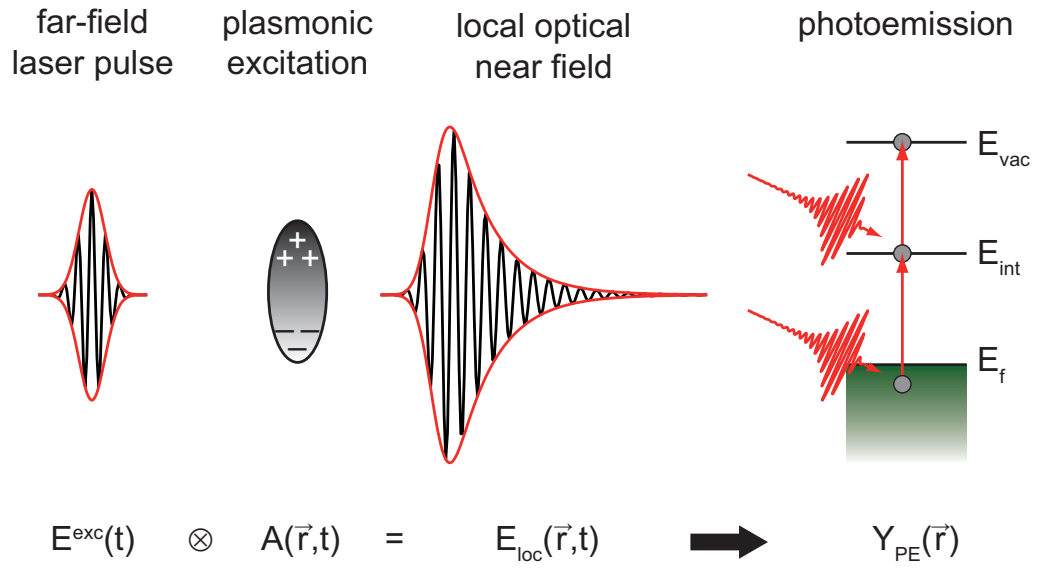

Figure 7.16: Schematic of photoemission induced by local optical near fields. The far-field excitation pulse $E^{\mathrm{exc}}(t)$ excites a metallic nanostructure. The plasmonic excitation leads to field enhancement as well as a modified temporal evolution of the local optical near field. Mathematically, the local optical near field $E_{\mathrm{loc}}(\vec{r},t)$ is described by a convolution of the excitation electric field $E^{\mathrm{exc}}(t)$ with the temporal response function $A(\vec{r},t)$. The two-photon photoemission that is considered here from the metallic nanostructure is then induced by the local optical near field. Since only virtual states with lifetime $\tau = 0\,\mathrm{fs}$ are considered in the photoemission process, the local field that induce the photoemission have to excite the nanostructure at the same time. Adapted from Bayer *et al.* [177].

using Eq. (7.67)

$$\begin{aligned} Y_{\mathrm{PE}}(\vec{r}) &\propto \int_{-\infty}^{\infty} P_{\mathrm{PE}}(\vec{r},t)\mathrm{d}t \\ &\propto \int_{-\infty}^{\infty} \left[\mathcal{F}^{-1}\left\{A(\vec{r},\omega)E^{\mathrm{exc}}(\omega)\right\}\right]^{2n} \mathrm{d}t. \end{aligned} \tag{7.69}$$

Since only one polarization is used for excitation, the vectorial properties of the local response and the electric fields are neglected here for the sake of simplicity. However, it is straightforward to include these by representing incident field and local response as vector and tensor, respectively (Section 3.2).

Apart from the mathematical description the local photoemission yield induced by local near fields is also illustrated in Fig. 7.16. The far-field excitation pulse excites plasmons in a nanostructure. The local near field is modified with respect to the far-field excitation due to the linear response function of the nanostructure [Eq. (7.68)]. The local near field then induces electronic transitions which result in photoemission [Eq. (7.69)]. In Fig. 7.16, two-photon photoemission is indicated assuming a virtual in-

termediate electronic state. This reflects that the considered model [Eqs. (7.67)–(7.69)] neglects any details of the multiphoton photoemission process, such as the anisotropic transition dipoles for photoexcitation in the substrate, the effects of lifetimes of intermediate states in the sequential excitation process, and the finite penetration of the incident light into the substrate. However, since local coherences that are associated with the local collective response are considered to have the main impact on the observed signal, Eq. (7.71) captures the essential physics.

In the following a single Lorentzian response function is considered to simulate and fit the 2D nanoscopy measurements described in Section 7.4.4. In case of the delay–phase scans (Section 7.4.5) a more sophisticated response function is needed to model the observed beating pattern.

7.5.1 2D Nanoscopy Scans

The 2D spectra obtained for the scan described in Section 7.4.4 are simulated by using the excitation field $E_{\mathrm{QS}}^{\mathrm{exc}}$ of the quadruple pulse sequence that can be derived from Eq. (7.61) as

$$E_{\mathrm{QS}}^{\mathrm{exc}}\left(\omega,\tau,T,t,\varphi_\tau,\varphi_t\right)=E_0(\omega)M_{\mathrm{LCD}}^{(4)}\left(\omega,\tau,T,t,\varphi_\tau,\varphi_T=0,\varphi_t\right). \tag{7.70}$$

Herein, $E_0(\omega)$ is the measured complex-valued spectral electric field shown in Fig. 7.8. Using the electric field defined in Eq. (7.70), the local photoemission yield is expressed by

$$Y_{\mathrm{PE}}\left(\vec{r},\tau,T,t,\varphi_\tau,\varphi_t\right)\propto\int_{-\infty}^{\infty}\left[\mathcal{F}^{-1}\left\{A(\vec{r},\omega)E_{\mathrm{QS}}^{\mathrm{exc}}\left(\omega,\tau,T,t,\varphi_\tau,\varphi_t\right)\right\}\right]^{2n}\mathrm{d}t', \tag{7.71}$$

where the inverse Fourier transformation $\mathcal{F}^{-1}$ transforms ω into t'.

Since in the 2D nanospectra obtained in Section 7.4.4 a single resonance is observed that is assumed to be caused by corrugations on the silver surface acting as resonant nanoantennas, a single Lorentzian oscillator is used to simulate the measured 2D spectra. Hence, the local response function is described by

$$A(r,\omega)=\frac{1}{\omega_L^2-\omega^2+\mathrm{i}2\gamma_L(r)\omega}, \tag{7.72}$$

where ω_L represents the resonance frequency, and γ_L the corresponding damping parameter that is related to the dephasing time $T_2=1/\gamma_L$ introduced in Section 3.1.2. To calculate two dimensional spectra the simulated local photoemission yield [Eq. (7.71)] is Fourier transformed with respect to τ and t

$$Y_{\mathrm{PE}}\left(r,\omega_\tau,T,\omega_t\right)=\mathcal{F}\left\{\mathcal{F}\left\{Y_{\mathrm{PE}}(r,\tau,T,t)\right\}\right\}. \tag{7.73}$$

Herein, $Y_{\mathrm{PE}}(r,\tau,T,t)$ represents the four-step phase-cycled time-dependent photoemission yield [Eq. (7.50)].

Analysis of the measured two-dimensional spectra is carried out by minimizing the deviations of the simulated 2D spectra [Eq. (7.73)] with respect to the measured 2D

spectra in terms of a least square fit. Therefore, the resonance frequency ω_L is set to the center frequency $\omega_0 = 2.36\,\mathrm{rad/fs}$ of the exciting laser spectrum. The order of nonlinearity is set $n = 4$. All parameters of the excitation field [Eq. (7.70)] are scanned according to the measured data: the delays τ and t cover the range $[0\,\mathrm{fs}, 280\,\mathrm{fs}]$ in steps of 4 fs, the phases φ_τ and φ_t are modulated according to Eq. 7.63 for the phase cycling process, and the delay T and the corresponding phase φ_T are kept constant at 0 fs and 0 rad, respectively. The position dependent damping parameter $\gamma_L(\vec{r})$ is then fitted for each location separately.

As an example, the 2D spectra of the reference hot spot ROI-A in Fig. 7.9 is fitted. The result is displayed in Fig. 7.17. The 2D nanospectrum for the reference hot spot was measured analogously to the measurement described in Section 7.4.4 and is averaged over the complete hot spot ROI-A. As can be observed from Figs. 7.17a and 7.17b, the measured 2D nanospectrum is much broader than the 2D nanospectra of ROI-B (Fig. 7.14). As can be inferred by comparing the measured and simulated spectrum, a good agreement is achieved. However, small deviations are observed in the antidiagonal width (i.e., from left upper to the right lower corner): the measured data is broader than the simulated data. The fit yields a damping parameter of $\gamma(\text{ROI-A}) = 1.258\,\mathrm{rad/fs}$, which corresponds to a dephasing time $T_2 < 1\,\mathrm{fs}$. However, this short lifetime is only approximate due to the 50 fs laser pulse duration, and is provided mainly for comparison.

Fitting of the 2D nanospectra of ROI-1 and ROI-2 shown in Fig. 7.14 results in damping parameters of $\gamma(\text{ROI-1}) = 0.023 \pm 0.003\,\mathrm{rad/fs}$ and $\gamma(\text{ROI-2}) = 0.012 \pm 0.001\,\mathrm{rad/fs}$, corresponding to coherence lifetimes of 43 fs and 84 fs, respectively. The errors for $\gamma_L(\vec{r})$ are the confidence intervals obtained using the Jacobian of the fit function. Hence, a significant difference of the lifetimes of a factor of two between the two ROIs that are separated by only 228 nm can be determined with the presented technique.

For a further comparison of the measured and fitted data the diagonal and antidiagonal cuts of the measured and simulated real-part 2D spectra are shown in Fig. 7.18a and Fig. 7.18b, respectively. Diagonal cut is the data of the 2D spectrum, e.g., as shown in Fig. 7.17a, along the cut from the lower left to the upper right corner. The red crosses and blue circles indicate the cuts along the data shown in Figs. 7.14a and 7.14c, respectively. The lines show cuts through the associated simulated data. Good agreement is observed, where the antidiagonal cuts show small deviations again. Hence, the model of a single damped oscillator seems to explain the observed 2D spectra. The small deviations that are observed might be due to two different effects. On the one hand, details of the multiphoton photoemission process such as the lifetime of intermediate states are neglected in the applied model. On the other hand, the plasmonic excitation is described here by a single damped oscillator model that excludes coupling to other plasmonic modes. Such a coupling would result in more complex response functions including additional damping parameters.

Apart from these two exemplary locations within the hot spot ROI-B, 2D spectra are calculated and fitted for each simultaneously recorded spatial location separately. For this purpose, always four pixels of the hot spot shown in Fig. 7.12 are binned to reduce the calculation time, yielding a resolution of $(36\,\mathrm{nm})^2$. The resulting spatial map is displayed in Fig. 7.19 and indicates the local dephasing times T_2 for the complete hot-spot region. The contour lines reflect the photoemission yield for a single pulse

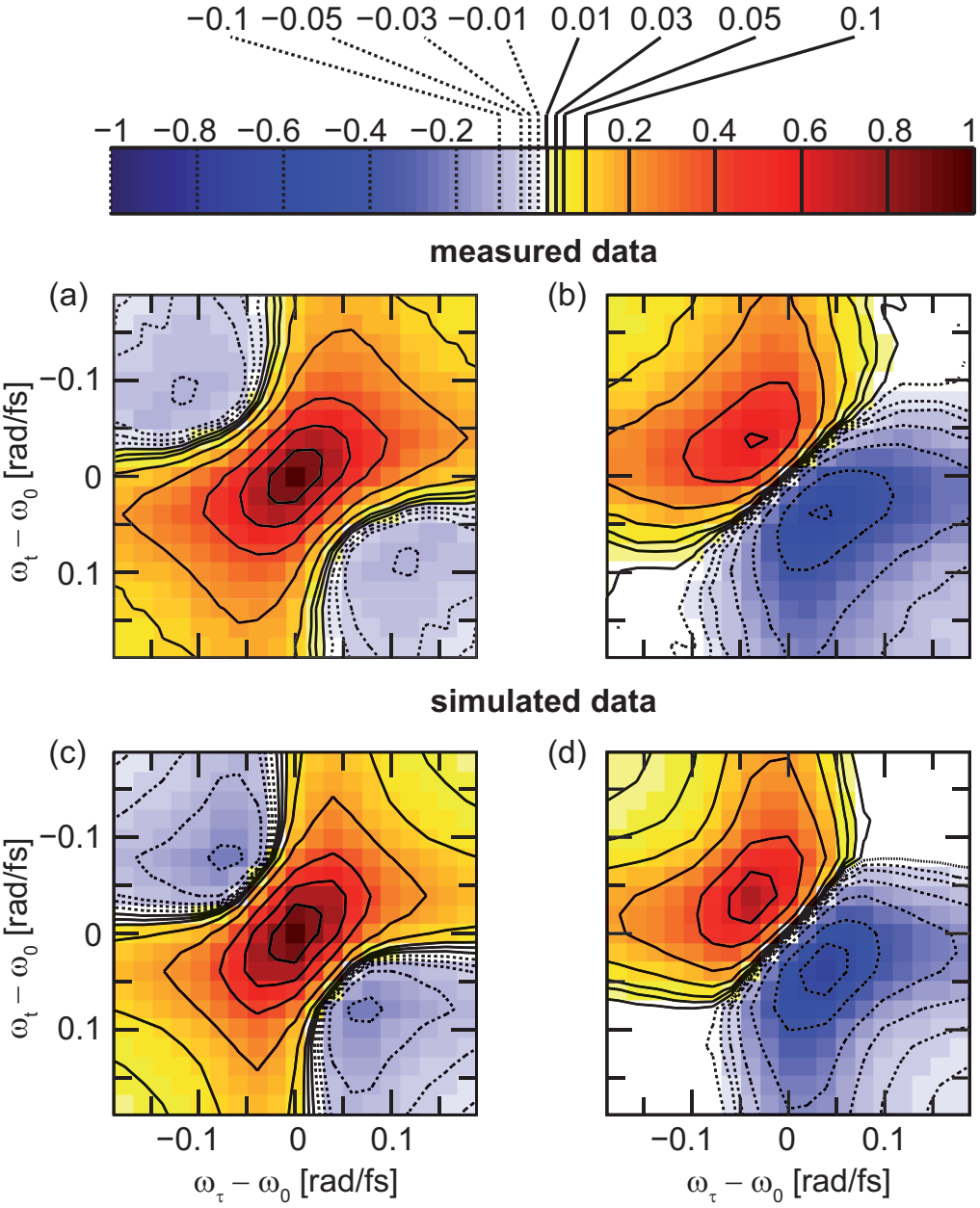

Figure 7.17: Comparison of measured (upper panels) and simulated (lower panels) 2D spectra at $T = 0\,\mathrm{fs}$. According to the illustrations of Fig. 7.14 the spectra are shown as a function of detuning from the center frequency ω_0 of the laser spectrum (Fig. 7.8) and the axis ω_τ and ω_t are plotted from -0.188 to $0.188\,\mathrm{rad/fs}$. Taken from Aeschlimann *et al.* [173]. Copyright (2011) by AAAS.

(Fig. 7.12) and are given for comparison. Note that areas with particularly long local coherence lifetimes do not exactly coincide with the highest photoemission yield, i.e., the contour-plot maximum. A separation of $\sim$100 nm between the point of highest emission and the longest lifetimes in its vicinity was determined. Note that all spatial

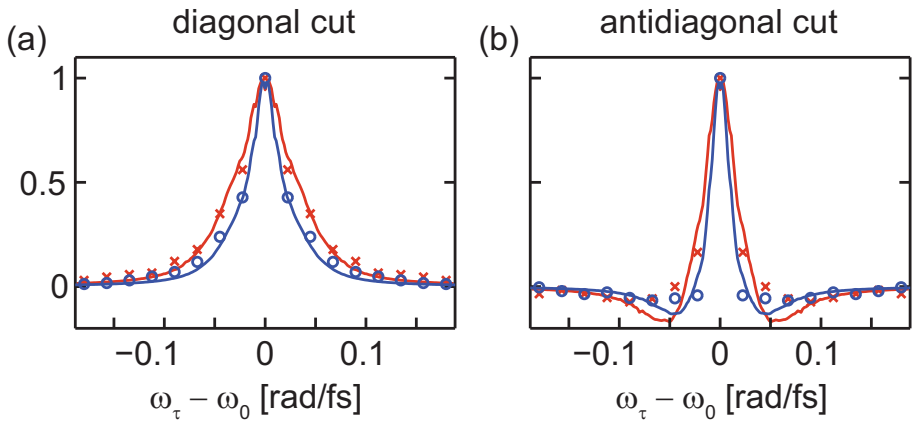

Figure 7.18: Diagonal (a) and antidiagonal cut (b) of the 2D real parts of ROI-1 (red) and ROI-2 (blue) illustrated in Figs. 7.14a and 7.14b, respectively. The measured data (symbols) is compared to the simulated data (lines) calculated with the fitted damping parameters of $\gamma(\text{ROI-1}) = 0.023\,\text{rad/fs}$ and $\gamma(\text{ROI-2}) = 0.012\,\text{rad/fs}$. Taken from Aeschlimann *et al.* [173]. Copyright (2011) by AAAS.

positions were recorded simultaneously under identical experimental conditions, so that line shape comparisons reflect true differences in sample response. The ROIs 1–3 are indicated for comparison. The strong difference between ROI-1 and ROI-2 can again be observed by the blue and red color, respectively. The dephasing time of ROI-3 is found by averaging the dephasing times of the corresponding pixels and results in a dephasing time of $T_2 = 80\,\text{fs}$. This number is in quantitative agreement with the dephasing time of $T_2 = 87\,\text{fs}$ that was fitted to the $\varphi_T = 0\,\text{rad}$ cut of the delay–phase scan shown in Fig. 7.15c.

The 50 nm resolution that was proposed in Section 7.4.3 is confirmed by the variations of 2D-nanoscopy-derived dephasing times, i.e., the dephasing time varies on a length scale of a few tens of nanometers. Hence, the subdiffraction "resolution" is visible qualitatively also for the corrugated silver surface. However, "resolution" in the context of such derived quantities is not and should not be defined quantitatively because the contrast mechanisms are complicated and reflect the physics of the system convoluted with the resolution of the method, rather than the resolution of the method alone.

A line cut along the dashed line in Fig. 7.19 is displayed as a blue line in Fig. 7.20. Strong variations of the dephasing time are observed in the region from 100 nm to 300 nm in this plot. In the other parts, smaller variations are observed showing values from about 50 fs to 90 fs. For comparison the dephasing time that is determined for the hot spot of ROI-A (green line) and the dephasing times for resonant localized plasmons from the literature [92, 146, 147] (red shaded) are indicated. Hence, the detected dephasing times are up to 10 times the dephasing times expected for resonant localized plasmonic modes. To explain these long dephasing times a model of coupled oscillators is used below to simulate the beating pattern observed for the delay–phase scan (Section 7.4.5).

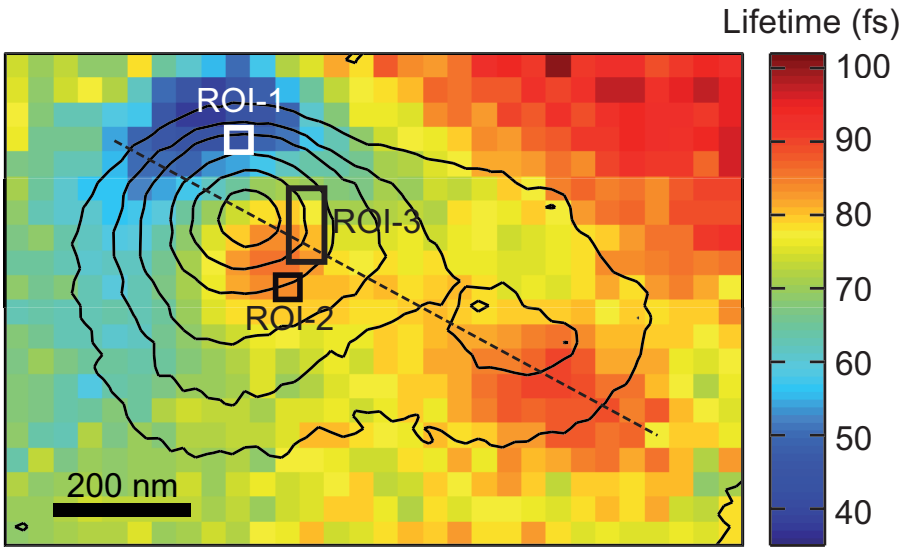

Figure 7.19: Dephasing-time map of the hot spot shown in Fig. 7.12. The map indicates the dephasing times $T_2(\vec{r}) = 1/\gamma(\vec{r})$ (false colors) for the complete hot spot (photoemission yield in black contour lines). Each pixel that is shown in the dephasing-time map contains a spatial region of $(36\,\mathrm{nm})^2$, i.e., always four of the pixels shown in Fig. 7.12 are binned. The white and black rectangles mark the locations of ROIs 1–3 and the dashed line indicates the cut shown in Fig. 7.20. Taken from Aeschlimann *et al.* [173]. Copyright (2011) by AAAS.

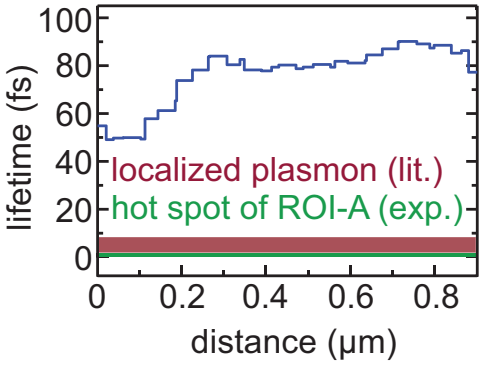

Figure 7.20: Cut through the dephasing-time map shown in Fig. 7.19 as a dashed black line. The dephasing time is shown as a function of position (blue line) along with the measured dephasing time of ROI-A (green) and the expected lifetime [92, 146, 147] for a localized plasmon mode (red shaded). Taken from Aeschlimann *et al.* [173]. Copyright (2011) by AAAS.

7.5.2 Delay–Phase Scans

The modeling procedure used for the two-pulse 2D nanoscopy scans shown in Section 7.4.5 is described here. For this purpose, the delay times τ and t as well as the phases φ_τ and φ_t of the general scheme are set to zero. Thus only two pulses with variable delay T and phase difference φ_T interact with the surface. The resulting double-pulse excitation field $E_{\mathrm{DS}}^{\mathrm{exc}}$ is derived from Eq. (7.60) as

$$E_{\mathrm{DS}}^{\mathrm{exc}}(\omega, T, \varphi_T) = |E_0(\omega)| \frac{1}{2} \left\{1 + \mathrm{e}^{\mathrm{i}[(\omega-\omega_0)T-\varphi_T]}\right\}, \tag{7.74}$$

where $E_0(\omega)$ is the spectral amplitude of the used laser pulse (Fig. 7.8). To model the delay–phase scans the delay T and the phase φ_T are varied according to the experiments described in Section 7.4.5, i.e., T is varied in steps of 5 fs and φ_T covers the range $[-\pi, \pi]$ in 41 steps. The local photoemission yield is then calculated analogously to Section 7.5.1

$$Y_{\mathrm{PE}}(\vec{r}, T, \varphi_T) \propto \int_{-\infty}^{\infty} \left[\mathcal{F}^{-1}\left\{A(\vec{r}, \omega) E_{\mathrm{DS}}^{\mathrm{exc}}(\omega, T, \varphi_T)\right\}\right]^{2n} \mathrm{d}t', \tag{7.75}$$

where the inverse Fourier transform $\mathcal{F}^{-1}$ again transforms ω into t'.

To account for the long dephasing times determined in the modelling of the 2D nanospectra (Section 7.5.1) and observed in the delay–phase scan (Section 7.4.5) a coupling of strongly damped localized plasmonic modes to dark modes is assumed in the following. The strongly damped plasmonic modes arise from corrugations on the silver surface acting as resonant nanoantennas. These modes couple strongly to the incident light, i.e., they act as a bright mode, and exhibit a large spatial overlap with the bulk material. Both effects lead to a strong damping and result in typical dephasing times on the order of ∼10 fs [92, 146, 147]. Hence, these modes alone cannot account for the long coherence lifetime and its spatial variation (Figs. 7.19 and 7.15). In contrast to short-lived localized plasmon modes, the surface plasmon polariton mode on a planar silver surface exhibits a coherence lifetime of ∼200 fs for an 800 nm excitation wavelength, as estimated from the dielectric function of silver [178] and the surface plasmon polariton resonance condition [77]. Surface plasmon polaritons neither couple directly to the far field nor have large overlap with bulk electronic states (Section 3.1.1), hence they have a rather long dephasing time. However, because of the vanishing interaction with transverse radiation fields (i.e., incident light), it is denoted as a dark mode and thus, on its own, cannot explain the observations of Figs. 7.19 and 7.15.

The properties of the fitting model are illustrated as a schematic in Fig. 7.21. The exciting electric field E^{exc} (orange) couples strongly to two bright modes (blue and red) that exhibit a large spatial overlap with the silver surface (gray). In the fitting process these two bright modes will be associated with ROI-3 and ROI-4. The bright modes are strongly localized and do not couple to each other. However, each bright mode couples to the dark mode (green) due to their spatial overlap. The dark mode has a large spatial spread, i.e., is delocalized, and has a small overlap with the silver surface. Hence, both bright modes couple to the same dark mode. Since the strength of the photoemission (green dashed arrows) is mainly determined by the spatial overlap of the electric field with the metal, the photoemission is dominated by the two bright modes. However, hybridization causes the response function of the bright mode to adopt characteristics of the dark mode—it strongly interacts with the incident radiation, and electronic excitations in the metal will exhibit spectral features that correspond to a much longer coherence lifetime, as would be expected for an uncoupled bright mode. Hence, by fitting the photoemission the characteristics of bright and dark mode are determined.

The local response function $A(\vec{r}, \omega)$ is then obtained from a model of two coupled oscillators. As motivated above, one of the oscillators interacts strongly with the incident radiation and is in the following denoted as a bright mode (BM), whereas the other

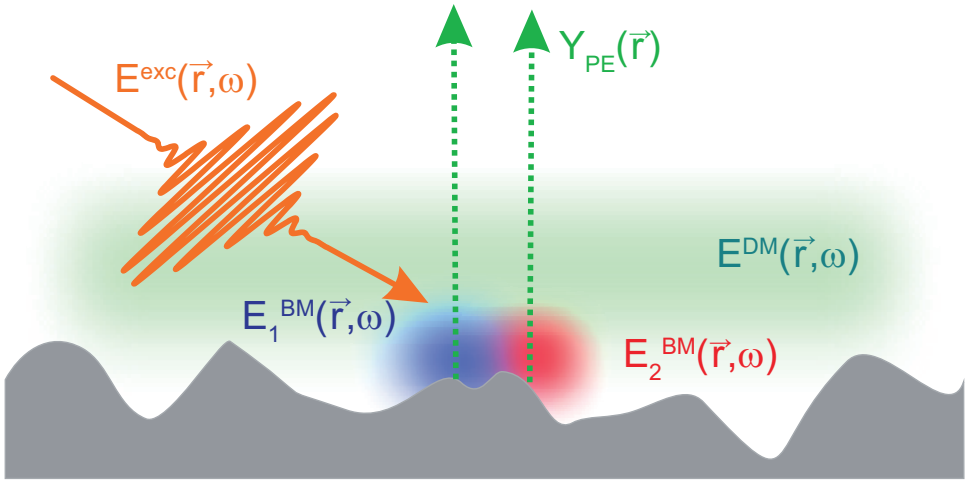

Figure 7.21: Excitation scheme of the corrugated silver surface. The incident wave $\vec{E}^{\mathrm{exc}}(\vec{r},t)$ (orange) excites localized surface plasmon modes $\vec{E}_1^{\mathrm{BM}}(\vec{r},\omega)$ (blue) and $\vec{E}_2^{\mathrm{BM}}(\vec{r},\omega)$ (red) that are coupled to a weakly damped delocalized dark mode $\vec{E}^{\mathrm{DM}}(\vec{r},\omega)$ (green). Due to the larger overlap of the bright modes and the metallic surface with respect to the overlap of the dark mode and the metal, the local photoemission yield $Y_{\mathrm{PE}}(\vec{r})$ is dominated by the bright modes. Taken from Aeschlimann *et al.* [173]. Copyright (2011) by AAAS.

oscillator couples only weakly to the far-field radiation and is therefore denoted as a dark mode (DM). A mathematical expression for the local response function is derived following the procedure outlined by Zhang *et al.* [179]. The dynamics of the coupled oscillators is described by the differential equations

$$\begin{aligned}
&\frac{\partial^2 E^{\mathrm{BM}}(\vec{r},t)}{\partial t^2} + 2\gamma^{\mathrm{BM}}\frac{\partial E^{\mathrm{BM}}(\vec{r},t)}{\partial t} + \omega_{0,\mathrm{BM}}^2 E^{\mathrm{BM}}(\vec{r},t) - \kappa\left[E^{\mathrm{BM}}(\vec{r},t) - E^{\mathrm{DM}}(\vec{r},t)\right] = gE_0(t)\\
&\frac{\partial^2 E^{\mathrm{DM}}(\vec{r},t)}{\partial t^2} + 2\gamma^{\mathrm{DM}}\frac{\partial E^{\mathrm{DM}}(\vec{r},t)}{\partial t} + \omega_{0,\mathrm{DM}}^2 E^{\mathrm{DM}}(\vec{r},t) - \kappa\left[E^{\mathrm{DM}}(\vec{r},t) - E^{\mathrm{BM}}(\vec{r},t)\right] = 0,
\end{aligned} \tag{7.76}$$

where $\omega_{0,i}^2$ ($i = \mathrm{BM}, \mathrm{DM}$, for dark and bright mode, respectively) represents the local restoring force and γ^i the corresponding damping parameter that is related to the dephasing time $T_2 = 1/\gamma$. The parameter κ determines the effective coupling strength of the two modes and g is the coupling constant of the incoming light with the bright mode. Thus, the fields of the localized surface plasmon mode $E^{\mathrm{BM}}(\vec{r},t)$ and the delocalized dark mode $E^{\mathrm{DM}}(\vec{r},t)$ are coupled linearly via κ. The present qualitative model neglects effects arising from different "masses" of the two oscillators, i.e., the model assumes that the "forces" exerted by one mode on the other mode leads in both coupling directions to the same field "displacements". Hence, on the present level of modeling the coupling of two bright modes via the dark mode is neglected. As is derived in Appendix A.3, the

local response functions for dark and bright modes are given by

$$A^{\mathrm{BM}}(\vec{r},\omega) = \frac{-\omega^2 + \mathrm{i}2\omega\gamma^{\mathrm{DM}} + \omega_{0,\mathrm{DM}}^2 - \kappa}{\left(\omega_{0,\mathrm{BM}}^2 - \omega^2 + \mathrm{i}2\omega\gamma^{\mathrm{BM}} - \kappa\right)\left(\omega_{0,\mathrm{DM}}^2 - \omega^2 + \mathrm{i}2\omega\gamma^{\mathrm{DM}} - \kappa\right) - \kappa^2} \tag{7.77}$$

$$A^{\mathrm{DM}}(\vec{r},\omega) = \frac{-\kappa}{\left(\omega_{0,\mathrm{BM}}^2 - \omega^2 + \mathrm{i}2\omega\gamma^{\mathrm{BM}} - \kappa\right)\left(\omega_{0,\mathrm{DM}}^2 - \omega^2 + \mathrm{i}2\omega\gamma^{\mathrm{DM}} - \kappa\right) - \kappa^2} \tag{7.78}$$

Note that these response functions are already hybridized modes that describe the coupled system, i.e., each response function contains parameters of bright and dark mode. As can be inferred, the properties of the response functions are mainly affected by the center frequencies ω_0 of the two modes, as well as the damping factors γ and the coupling constant κ. The coupling strength g between the light and localized plasmons effectively changes the oscillator strength but does not influence the shape of the spectral intensity or the phase and hence is not considered in the fitting process. For the calculation of local photoemission yield, the response function of the hybridized bright mode $A^{\mathrm{BM}}(\vec{r},\omega)$ is then inserted into Eq. (7.75).

The fit parameters for the delay–phase scans are obtained by simultaneously fitting the signals from both ROIs in an iterative scheme. Since the interesting effects of the delay–phase scans, i.e., long-lived coherences, were observed for times $T \geq 60\,\mathrm{fs}$ the fits are performed in a least-square sense including only photoemission signals for $T \geq 60\,\mathrm{fs}$. The bright modes $E^{\mathrm{BM}}(\text{ROI-3},t)$ and $E^{\mathrm{BM}}(\text{ROI-4},t)$ are fitted to the photoemission patterns observed for ROI-3 (Fig. 7.15a) and ROI-4 (Fig. 7.15b), respectively. Although the bright modes are independent from each other, i.e., they do not couple to each other, both bright modes couple to the same dark mode $E^{\mathrm{DM}}(\vec{r},t)$. Hence, first the response function of the bright mode $A^{\mathrm{BM}}(\text{ROI-3},\omega)$ is fitted to the delay–phase scan observed for ROI-3 (Fig. 7.15a). This response function also contains the parameter of the dark mode. In the next step the response function of the bright mode $A^{\mathrm{BM}}(\text{ROI-4},\omega)$ is fitted to ROI-4 starting with the dark mode parameters determined via $A^{\mathrm{BM}}(\text{ROI-3},\omega)$ in the first step. Then again, $A^{\mathrm{BM}}(\text{ROI-3},\omega)$ is fitted, starting with the newly determined dark mode parameters that were obtained via $E_2^{\mathrm{BM}}(\text{ROI-4},t)$. This iterative fitting process is performed until convergence. A good convergence of the fit procedure is obtained for dark modes characterized by $\omega_{0,\mathrm{DM}} = 2.38\,\mathrm{rad/fs}$, $\gamma^{\mathrm{DM}} = 0.0043\,\mathrm{rad/fs}$. The corresponding bright-mode parameters for ROI-3 and ROI-4 are $\omega_{0,\mathrm{BM1}} = 2.28\,\mathrm{rad/fs}$, $\gamma_{\mathrm{BM1}} = 0.02\,\mathrm{rad/fs}$ and $\omega_{0,\mathrm{BM2}} = 2.41\,\mathrm{rad/fs}$, $\gamma_{\mathrm{BM2}} = 0.01\,\mathrm{rad/fs}$, respectively. The coupling parameter κ for the two modes dominating the emission from ROI-3 and ROI-4 is $0.11\,\mathrm{rad/fs}$ and $0.06\,\mathrm{rad/fs}$, respectively. The resulting simulated delay–phase scans are shown in Figs. 7.22a and 7.22b. Good agreement between measured (Figs. 7.15a and 7.15b) and simulated data (Figs. 7.22a and 7.22b) is achieved. The tail with strong photoemission tilted to the left that is observed in Fig. 7.15a is nicely reproduced in the simulated data shown in Fig. 7.22a. Also, a small part of the signal evolves to the right. However, no beating pattern in terms of constructive and destructive is obtained here. The simulated data for ROI-4 (Fig. 7.22b) shows a strong beating that is also present in the measured data, but not as pronounced. The corresponding hybridized response functions $A^{\mathrm{BM}}(\text{ROI-3},\omega)$ (blue) and $A^{\mathrm{BM}}(\text{ROI-4},\omega)$ (red) are displayed in Fig. 7.22c. Hence, the hot spot (Fig. 7.12) actually consisted of two bright modes E_1^{BM} and E_2^{BM} that were

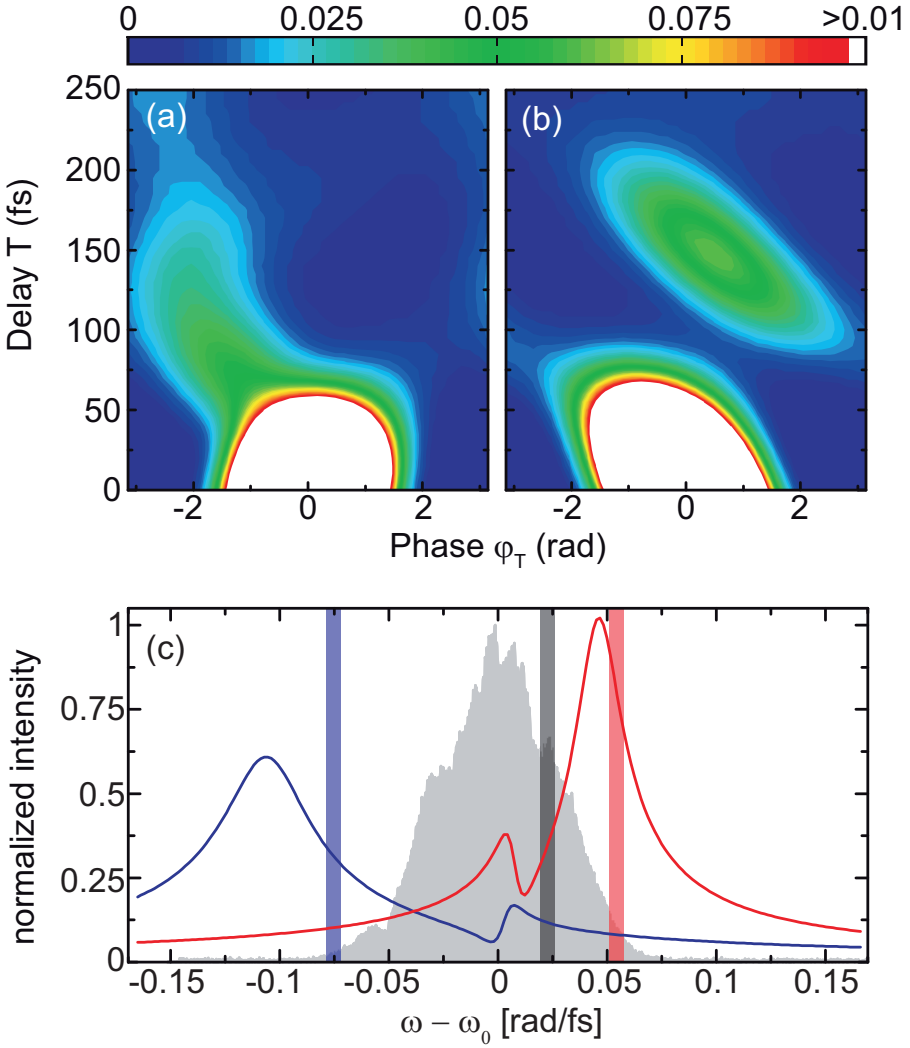

Figure 7.22: Simulated photoemission yield (a) fitted to the measured data shown in Figs. 7.15a and (b) 7.15b. The data is simulated using the bright-mode response function defined in Eq. 7.77. (c) The derived response functions of the two hybridized modes $\vec{E}_1^{\mathrm{BM}}(\vec{r},\omega)$ (blue) and $\vec{E}_2^{\mathrm{BM}}(\vec{r},\omega)$ (red) are shown together with vertical shaded bars indicating the spectral positions of the uncoupled oscillators and the dark mode (gray bar). The excitation laser spectrum is indicated as shaded area. Taken from Aeschlimann *et al.* [173]. Copyright (2011) by AAAS.

slightly detuned from the dark mode E^{DM} to higher and lower frequencies, respectively. The qualitative trend for the linewidth contrast between dark and bright mode is well reflected in the optimized model parameters. The somewhat smaller contrast in comparison to the contrast expected for localized surface plasmon modes interacting with a surface plasmon polariton is attributed to the fact that the actual resonance position of the bright modes is in the wings of the driving laser spectrum and thus their spectral position and linewidth can only be determined with large uncertainties.

It is important to point out that similar good agreement between measurements and

simulated spectra is achieved either for two independent dark modes coupling to the different bright modes or one individual dark mode interacting with both bright modes simultaneously. However, the latter model reduces the number of free parameters and thus represents a better test for the applied model.

These results indicate that the observed long-lived coherence in hot-spot multiphoton photoemission can indeed be attributed to the coupling between bright localized plasmon modes and a dark surface plasmon polariton mode. Interestingly, the coupling between bright and dark modes led to Fano-like resonances in the vicinity of the resonance of the dark mode. The mirror-like behavior of this spectral feature for one versus the other bright mode was responsible for the striking differences in the signals shown in Figs. 7.15a and 7.15b, and the variations in Fig. 7.19. Subtleties of the overlap of these spectral features with the excitation spectrum, such as the exact spectral position and the "sharpness" of the Fano-like resonance, determined the observed beating behavior. This sensitivity of the model parameters for the two ROIs showed that the local response significantly varies on a 100 nm length scale, as is also seen for the dephasing time measured by 2D nanoscopy.

7.6 Conclusion and Outlook

In this chapter, coherent two-dimensional (2D) nanoscopy was developed as a combination of 2D spectroscopy and photoelectron emission microscopy. This technique carries the principle of nonlinear techniques from an ensemble measurement to the nanometer length scale and spatially localized few emitters. Thus one can map out nonlinear response functions in time/frequency as well as real space. 2D nanoscopy can also be considered a generalization of time-resolved two-photon photoemission and it may be of similar beneficial value for the field of photoemission research as it has proven to be for optical spectroscopy and NMR. Measurement of local decoherence is relevant for applications and devices for which keeping phase coherence is essential, and the method can be used to study the suitability of potential materials. Applications are also envisaged for nonlinear spectroscopy of nanostructures or "artificial molecules" on surfaces, nanophotonic circuits, photovoltaic devices, coupled quantum wells, and others. Sample preparation requirements (ultra-high vacuum) are analogous to those of conventional photoemission suggesting broad applicability. It should hence also be possible, for example, to study coherences with spatial resolution in self-organized molecular aggregates on surfaces. In general any spatially inhomogeneous or nanostructured system offers an interesting playground to observe processes of spatialtemporal correlations of electronic coherences and populations. It should thus become possible in the future to study a broad range of fascinating quantum phenomena not accessible otherwise, such as nanoscopic coherences, transport and entanglement with direct space-time resolution, nonlocal phase correlations, and others.

First experimental realization of the developed technique was provided with a corrugated silver surface. In Chapter 6 the same sample was investigated in terms of near-field control using polarization shaped pulses. Due to the long duration of the optimal pulses, long-lived coherence were expected to be present on the silver surface. In this chapter,

these long-lived coherences could be attributed to coupled plasmonic modes. Short-lived local resonant modes that strongly overlap with the metal and hence are responsible for photoemission were found to be coupled to dark propagating plasmon polariton modes with dephasing times on the order of several hundreds of femtoseconds. The coupling between bright and dark modes led to sharp Fano-like resonances. Due to the high spatial resolution of the presented technique, different bright modes within the same hot spot could be distinguished.

2D nanoscopy may be generalized in different ways. Using polarization pulse shaping (Section 2.3), one could map out the tensor character of the nonlinear response by selecting the appropriate polarization directions of the excitation subpulses. Indeed, the pulse shapes themselves could be varied, allowing combination of 2D nanoscopy with coherent control techniques. Higher-order processes and $N>3$-level systems could be investigated with pulse trains consisting of more than four pulses. Extension to short wavelengths [170, 180] should be possible. 2D nanoscopy as presented here is still limited by diffraction in its excitation. Hence, a combination of the technique with ultrashort nanoscopic excitation schemes using near-field control as described in Chapters 4 and 5, might enable coherent control on the nanoscale in complex quantum systems and provide insight in energy transfer in, e.g., light-harvesting systems.

8 Summary and Outlook

Time-resolved optical spectroscopy has become an important tool to investigate the dynamics of quantum mechanical processes in matter. In typical applications, a first "pump" pulse excites the system under investigation from the thermal equilibrium to an excited state, and a second variable time-delayed "probe" pulse then maps the dynamics of the excited system. The characteristic dynamics of excited systems, e.g., nuclear motion in molecules or relaxation of charge carriers in solids, occur on the order of femtoseconds. Experiments that investigate such processes require laser pulses with durations on this timescale, which have become commonly accessible in the last decades. Although advanced nonlinear techniques have been developed to investigate, e.g., coherent quantum effects, all of these techniques are limited in their spatial resolution. The laser focus diameter has a lower bound given by Abbe's diffraction limit, which is roughly half the optical excitation wavelength—corresponding to about 400 nm in the presented experiments. In the time-resolved experiments that have been suggested so far, averaging over the sample volume within this focus cannot be avoided. Even though single molecule experiments have been realized by combination of tight focusing and low molecule density, the spatial resolution in these experiments is still diffraction limited.

In this thesis, two approaches were developed to overcome the diffraction limit in optical spectroscopy and to enable the investigation of coherent processes on the nanoscale. In the first approach, analytic solutions were found to calculate optimal polarization-shaped laser pulses that provide optical near-field pump–probe pulse sequences in the vicinity of a nanostructure. These near-field pulse sequences were designed to allow excitation of a quantum system at one specific position at a certain time and probing at a different position at a later time. In the second approach, the concept of coherent two-dimensional (2D) spectroscopy, which has had great impact on the investigation of coherent quantum effects in recent years, was combined with photoemission electron microscopy, which yields a spatial resolution well below the optical diffraction limit.

Using the analytic solutions, optical near fields were investigated in terms of spectroscopic applications. Near fields that are excited with polarization-shaped femtosecond laser pulses in the vicinity of appropriate nanostructures feature two properties that are especially interesting in the view of spectroscopic applications: On the one hand, control of the spatial distribution of the optical fields is achieved on the order of nanometers. On the other hand, the temporal evolution of these fields can be adjusted on the order of femtoseconds. In this thesis, solutions were found to calculate the optimal polarization-shaped laser pulses that control the near field in a general manner. The main idea to achieve this deterministic control was to disentangle the spatial and temporal near-field control. First, the spatial distribution of the optical near field was controlled by assigning the correct state of polarization for each frequency within the polarization-shaped laser pulse independently. The control mechanism for the spatial near-field distribution is the

constructive or destructive interference of two near-field modes that are excited with the two independent far-field polarization components. Therefore, the relative phases between the polarization components found for two optimizations with opposite goals, e.g., maximization and minimization of the near field intensity at a certain position, differed by π. The remaining total phase—not employed for spatial control—was then used for temporal near-field compression, which, in experimental applications, would lead to an enhancement of the nonlinear signal at the respective location.

In a collaboration with Javier García de Abajo and Walter Pfeiffer the analytic solutions were used in simulations to guide electromagnetic energy in a branching T-chain of nanospheres. Switching of the propagating near fields was achieved by either maximizing or minimizing the difference between the linear signals at the ends of the two arms. The temporal compression at the desired positions was then gained by compensating the dispersion of the T-chain. The obtained optimal polarization-shaped laser pulses were compared to adaptive optimizations and the agreement of the analytic solutions with the ones found adaptively was impressive, since two different observables were compared: The analytic results were obtained by first guiding the linear flux to a desired position and then compressing the temporal evolution of the near-field at that position using the remaining degree of freedom. The adaptive results were found by directly optimizing the difference of the nonlinear signals. Possible applications of the analytic results in the branching T-chain are the control in logic elements used in plasmonic circuits. On top of that, the derived rules enable optimal design of nanostructures for spectroscopic or plasmonic applications.

The importance of the analytic solutions in terms of spectroscopic applications was then illustrated by generating near-field pump–probe pulse sequences that enable space–time resolved excitation on nanometer and femtosecond scale, respectively. The advantage with respect to pulse sequences found by adaptive optimizations is that the analytically derived formulas provide a direct handle to pulse sequence parameters, such as delays or relative phases, which are scanned in spectroscopic applications. Contrarily, without using the analytic solutions, the pulse shapes would have to be found for each parameter step in a separate time-consuming adaptive optimization. Hence, the derived solutions simplify and expedite the realization of future spectroscopic applications using optical near fields.

Experimental implementation of the analytic rules for the spatial control of near fields was achieved in a collaboration with the groups of Martin Aeschlimann and Walter Pfeiffer. The near-field distribution in gold nanoprisms was investigated with a photoemission electron microscope. Near-field control was first achieved adaptively by localization of the near-field at one corner of a nanosprism with respect to another corner. Then, the analytic rule for switching was employed by adding a π phase to one polarization component of the adaptively optimized laser pulse. This resulted in a change of the excitation polarization and deterministic near-field switching from one corner to the other was achieved. As in the simulations, the deterministic optimal pulses were compared to adaptively optimized pulses and good agreement was found. The results confirm the theoretically derived optimal solutions and verify the interference of different near-field modes as the control mechanism in gold nanoprisms.

In contrast to the use of optical near fields, where pump–probe sequences themselves

are localized below the diffraction limit and the detection does not have to provide the spatial resolution, a different approach was suggested in this thesis to gain spectroscopic information on the nanoscale. The new method was termed "Coherent two-dimensional (2D) nanoscopy" and transfers the concept of "conventional" coherent 2D spectroscopy to photoemission electron microscopy. The pulse sequences used for the investigation of quantum systems in this method are still limited by diffraction. However, the new key concept is to detect locally generated photoelectrons instead of optical signals. This yields a spatial resolution that is well below the optical diffraction limit. In "conventional" 2D spectroscopy a triple-pulse sequence initiates a four wave mixing process that creates a coherence. In a quantum mechanical process, this coherence is converted into a population by emission of an electric field, which is measured in the experiment. Contrarily, in the developed 2D nanoscopy, four-wave mixing is initiated by a quadruple-pulse sequence, which leaves the quantum system in an electronic population. This electronic population carries coherent information about the investigated quantum system and can be mapped with a spatial resolution down to a few nanometers given by the spatial resolution of the photoemission electron microscope. Hence, 2D nanoscopy can be considered a generalization of time-resolved photoemission experiments. In the future, it may be of similar beneficial value for the field of photoemission research as "conventional" 2D spectroscopy has proven to be for optical spectroscopy and nuclear magnetic resonance experiments.

First experimental implementation of coherent 2D nanoscopy was realized in a collaboration with the groups of Martin Aeschlimann and Walter Pfeiffer. In these experiments, coherent processes on a corrugated silver surface were measured. In a preceding coherent control experiment, which was also presented in this thesis, the application of near-field control to surface-enhanced Raman spectroscopy was investigated. For that purpose, the electron yield from several photoemission hot spots, i.e., locations with enhanced photoemission, were adaptively optimized and durations of several hundreds of femtoseconds were found for the optimal laser pulses. These pulse durations strongly indicated unexpected long-lived coherences on the surface. Using 2D nanoscopy, these observations were further analyzed and 2D nanospectra were recorded with a spatial resolution of about 50 nm. The 2D nanospectra were then modelled by using single Lorentzian oscillators and dephasing times between 40 fs and 100 fs were fitted for a region of about $1\,\mu m^2$. Interestingly, dephasing times were observed that differed by a factor of two for spatial regions separated by only 230 nm. By performing a special case of 2D nanoscopy, where the temporal separation as well as the relative phase between two pulses was scanned, the unexpected long-lived coherences could be attributed to two different localized plasmonic modes that were coupled to the same propagating plasmon polariton mode. In the example presented here, the coherent effects observed on the corrugated silver surface were discussed in terms of a classical model. However, 2D nanoscopy should also enable the investigation of a broad range of fascinating quantum phenomena not accessible otherwise. In the future, the technique might be generalized by employing pulse sequences featuring different polarizations to map out tensor characteristics of the investigated sample.

The presented approaches transfer the principle of time-resolved spectroscopic techniques from an ensemble measurement to the nanometer length scale and spatially local-

ized few emitters. In the future, these advances can enable a wide range of space–time resolved spectroscopy. Applications might be nonlinear spectroscopy of arbitrary nanostructured samples, such as nanophotonic circuits, photovoltaic devices, coupled quantum wells or molecular aggregates. In such experiments, direct mapping of spatial coupling and transfer would be possible. New insights of the energy transfer in light harvesting complexes might be obtained that can improve the efficiency of solar cells. Even though the two approaches discussed in this thesis are very powerful in themselves, a combination of near-field excitation with coherent 2D nanoscopy can facilitate not only investigation of coherent quantum processes but also control of such processes on the nanoscale.

Zusammenfassung und Ausblick

Zur Untersuchung von Dynamiken quantenmechanischer Prozesse in Materie hat sich die zeitaufgelöste optische Spektroskopie zu einem zentralen Werkzeug entwickelt. Eine Standardmethode ist hierbei die Anrege-Abfrage-Spektroskopie. Bei solch einem Experiment wird das zu untersuchende System zunächst mit einem Anregepuls aus dem thermischen Gleichgewicht in einen höheren Zustand angeregt. Anschließend untersucht man mit einem zweiten zeitverzögerten Abfragepuls die Dynamik des angeregten Systems. Bei der Untersuchung von z.B. Kernbewegungen in Molekülen oder Relaxation von Ladungsträgern in Festkörpern ereignen sich solche Dynamiken auf der Femtosekunden Zeitskala. Die Untersuchung solcher Prozesse erfordert dementsprechend auch Laserpulsdauern auf dieser Zeitskala, welche in den letzten Jahrzehnten allgemein zugänglich geworden sind. Obwohl fortgeschrittene experimentelle Methoden entwickelt wurden um kohärente Quanteneffekte zu untersuchen, sind all diese Experimente nach wie vor in ihrer räumlichen Auflösung begrenzt. Aufgrund von Beugung ist der Fokus eines Laserstrahls limitiert. Diese untere Grenze ist durch Abbe's Auflösungsgrenze gegeben und entspricht etwa der Hälfte der optischen Anregungswellenlänge, d.h. etwa 400 nm in den hier vorgestellten Experimenten. Daher kann eine Mittelung über das Probenvolumen, gegeben durch die Fokusgröße, in den bisher vorgestellten Experimenten nicht vermieden werden. Obwohl Untersuchungen von Einzelmolekülen durch Kombination von harter Fokussierung und geringer Moleküldichte realisiert werden konnten, ist die räumliche Auflösung in diesen Experimenten immer noch beugungsbegrenzt.

In dieser Arbeit wurden zwei Ansätze verfolgt, um die Beugungsgrenze in der optischen Spektroskopie zu überwinden und die Untersuchung von kohärenten Prozessen auf der Nanometerskala zu ermöglichen. Im ersten Ansatz wurden analytische Lösungen gefunden, um optimal polarisationsgeformte Laserpulse zu berechnen, die optische Anrege-Abfrage-Nahfeld-Pulsfolgen in der Nähe einer Nanostruktur ermöglichen. Diese Nahfeld-Pulsfolgen wurden entwickelt, um ein quantenmechanisches System an einer bestimmten Position zu einem bestimmten Zeitpunkt anzuregen und an einer anderen Position zu einem späteren Zeitpunkt abzufragen. Im zweiten Ansatz wurde das Konzept der kohärenten zweidimensionalen (2D) Spektroskopie, die in den letzten Jahren großen Einfluss auf die Untersuchung von kohärenten Quanteneffekten gehabt hat, mit Photoelektronenmikroskopie kombiniert. Letztere ermöglicht eine räumliche Auflösung deutlich unter der optischen Auflösungsgrenze.

Mit Hilfe der analytischen Lösungen wurden optische Nahfelder in Bezug auf spektroskopische Anwendungen untersucht. Nahfelder, die mit polarisationsgeformten Femtosekunden-Laserpulsen in der Nähe von entsprechenden Nanostrukturen angeregt werden, verfügen über zwei Eigenschaften, die besonders interessant für spektroskopische Anwendungen sind: Zum einen kann die räumliche Verteilung der optischen Felder auf der Größenordnung von Nanometern kontrolliert werden. Zum anderen kann die zeit-

liche Entwicklung dieser Felder in der Größenordnung von Femtosekunden manipuliert werden. In dieser Arbeit wurden Lösungen gefunden, um optimale polarisationsgeformte Laserpulse zu berechnen, die diese Nahfeld-Steuerung in einer allgemeinen Art und Weise erlauben. Die Hauptidee, um diese deterministische Steuerung zu erreichen, war die räumliche und zeitliche Nahfeld-Kontrolle zu entkoppeln. Zuerst wurde dafür die räumliche Verteilung der optischen Nahfelder durch die Zuordnung des korrekten Polarisationszustandes für jede Frequenz, innerhalb des polarisationsgeformten Laserpulses, unabhängig gesteuert. Der Kontrollmechanismus für die räumliche Nahfeld-Verteilung ist die konstruktive bzw. destruktive Interferenz von zwei Nahfeldmoden, die mit den zwei unabhängigen Fernfeld-Polarisationskomponenten angeregt werden. Daher wurde herausgefunden, dass sich die relativen Phasen zwischen den beiden Polarisationskomponenten für zwei Optimierungen mit gegenteiligen Zielen, z.B. Maximierung und Minimierung der Nahfeld-Intensität an einer bestimmten Position, um π unterscheiden. Die verbleibende totale Phase, die nicht für die räumliche Kontrolle benötigt wird, wurde dann verwendet um den nichtlinearen Fluss an den gewünschten Positionen durch zeitliche Nahfeldkomprimierung zu erhöhen.

In Zusammenarbeit mit Javier García de Abajo und Walter Pfeiffer wurden die analytischen Lösungen in Simulationen verwendet, um die Ausbreitung von Nahfeldern in einer verzweigten T-Kette bestehend aus Nanokugeln zu steuern. Durch entweder Maximierung oder Minimierung der Differenz der linearen Signale an den Enden der beiden Arme wurde Schalten der sich ausbreitenden Nahfelder erzielt. Die zeitliche Komprimierung an den gewünschten Positionen wurde dann durch die Kompensation der Dispersion der T-Kette erzielt. Die so gefundenen polarisationsgeformten Laserpulse wurden dann mit adaptiven Optimierungen verglichen. Die Übereinstimmung der analytischen Lösungen mit den adaptiv gefundenen war bemerkenswert, da zwei unterschiedliche Messgrößen optimiert wurden. Die analytischen Ergebnisse wurden erhalten, indem zuerst der lineare Fluss zu der gewünschten Position geführt und dann mit dem verbleibenden Freiheitsgrad das Feld an dieser Stelle zeitlich komprimiert wurde. Die adaptiven Ergebnisse wurden durch die direkte Optimierung der Differenz der nichtlinearen Signale gefunden. Eine mögliche Anwendung der analytischen Ergebnisse, der verzweigten T-Kette, ist die Verwendung zur Kontrolle von logischen Elementen in plasmonischen Schaltkreisen. Darüber hinaus ermöglichen die hergeleiteten Regeln ein optimales Design von Nanostrukturen für sowohl spektroskopische als auch plasmonische Anwendungen.

Die Bedeutung der analytischen Lösungen für spektroskopische Anwendungen wurde dann durch die Erzeugung von Anrege-Abfrage-Nahfeld-Pulsfolgen verdeutlicht. Diese Pulsfolgen ermöglichen eine gleichzeitige raum- und zeitaufgelöste Anregung auf einer Nanometer- und Femtosekundenskala. Der Vorteil gegenüber Pulsfolgen, die durch adaptive Optimierungen erzeugt werden, ist, dass die analytischen Lösungen eine direkte Modulation der Parameter ermöglichen, die in spektroskopischen Anwendungen variiert werden. Diese Parameter sind z.B. die Verzögerung oder die relative Phase zwischen den Pulsen. Ohne analytische Lösungen müsste für jeden Parameterschritt der entsprechende polarisationsgeformte Laserpuls durch eine langwierige adaptive Optimierung gefunden werden. Dementsprechend vereinfachen die hergeleiteten analytischen Lösungen experimentelle Realisierungen und eine zukünftige Anrege-Abfrage-Spektroskopie mit Nahfeldern.

Diese analytischen Regeln für die räumliche Steuerung der Nahfelder wurden in Zusammenarbeit mit den Arbeitsgruppen von Martin Aeschlimann und Walter Pfeiffer experimentell angewendet. Dabei wurde die Nahfeldverteilung in goldenen Nanoprismen mit einem Photoemissionselektronenmikroskop untersucht. Zunächst wurde adaptiv das Intensitätsverhältnis der Nahfelder zweier Prismenecken optimiert und somit Lokalisierung der Nahfelder erreicht. Aufgrund der analytischen Regel zum Schalten wurde dann eine π-Phase zu einer der Polarisationskomponenten des adaptiv optimierten Laserpulses addiert. Dies führte zu einer Änderung des Anregepolarisationszustands und zu deterministischem Schalten der Intensität von der einen zu der anderen Ecke. Wie bei den Simulationen wurde dabei festgestellt, dass die deterministisch gefundenen Pulse mit den adaptiv optimierten Pulsen gut übereinstimmen. Somit bestätigen die experimentellen Ergebnisse die theoretisch hergeleiteten Lösungen und zeigen, dass die Interferenz von unterschiedlichen Nahfeldmoden der Kontrollmechanismus in goldenen Nanoprismen ist.

Im Gegensatz zur Verwendung von optischen Nahfeldern, in der die Anrege-Abfrage-Nahfeld-Pulsfolgen selbst unter dem Beugungslimit lokalisiert sind und die Detektion nicht räumlich aufgelöst sein muss, wurde in dieser Arbeit noch ein anderer Ansatz vorgeschlagen, um spektroskopische Informationen auf der Nanometerskala zu erhalten. Die neue Methode wurde als „kohärente zweidimensionale (2D) Nanoskopie“ beschrieben und überträgt das Konzept der „herkömmlichen“ kohärenten 2D Spektroskopie auf die Photoemissionselektronenmikroskopie. In dieser neuen Methode ist die räumliche Auflösung der zur Untersuchung des quantenmechanischen Sytems erforderlichen Pulssequenzen zwar durch Beugung begrenzt. Die wesentliche Neuerung ist allerdings, lokal erzeugte Photoelektronen anstelle von optischen Signalen zu messen. Daraus ergibt sich eine räumliche Auflösung, die weit unterhalb der optischen Beugungsgrenze liegt. In der „herkömmlichen“ kohärenten 2D Spektroskopie initiiert eine Dreifach-Pulsfolge einen Vier-Wellen-Mischprozess, der eine Kohärenz erzeugt. Diese Kohärenz wird in einem quantenmechanischen Prozess in eine Population überführt und dabei kommt es zur Abstrahlung eines elektromagnetischen Feldes, dass im Experiment gemessen wird. Im Gegensatz dazu wird in der in dieser Arbeit entwickelten 2D Nanoskopie die Vier-Wellen-Mischung durch eine Vierfach-Pulsfolge erzeugt, die das quatenmechanische System direkt in eine elektronische Population überführt. Diese elektronische Population trägt dann kohärente Information über das untersuchte System und kann mit einer räumlichen Auflösung von wenigen Nanometern abgebildet werden. Die Auflösung ist dabei durch das verwendete Photoemissionsmikroskop vorgegeben. Demzufolge kann 2D Nanoskopie als eine Verallgemeinerung der zeitaufgelösten Photoemissionsexperimente gesehen werden. Sie könnte von gleichem Nutzen für das Feld der Photoemissionsexperimente sein, wie es die „herkömmliche“ 2D Spektroskopie für sowohl optische als auch Kernspinresonanz Experimente ist.

Eine erste experimentelle Umsetzung der kohärenten 2D Nanoskopie wurde in Zusammenarbeit mit den Arbeitsgruppen von Martin Aeschlimann und Walter Pfeiffer realisiert. In diesen Experimenten wurden kohärente Prozesse auf einer rauhen Silberoberfläche gemessen. In einem vorangegangenen kohärenten Kontrollexperiment, dass auch in dieser Arbeit präsentiert wurde, wurde die Anwendung der Nahfeldsteuerung für die oberflächenverstärkte Raman-Streuung untersucht. Zu diesem Zweck wurde die Elektronenausbeute aus mehreren „Hot-Spots“, d.h. Positionen mit erhöhter Photoemission, ad-

aptiv optimiert und Dauern von mehreren hundert Femtosekunden für die optimalen Laserpulse gefunden. Diese Pulsdauern wiesen stark auf unerwartet langlebige Kohärenzen auf der rauhen Silberoberfläche hin. Mit der 2D Nanoskopie wurden diese Beobachtungen weiter untersucht und 2D Nanospektren mit einer räumlichen Auflösung von etwa 50 nm aufgenommen. Die 2D Nanospektren wurden dann mit einzelnen Lorentz-Oszillatoren modelliert und Dephasierungszeiten zwischen 40 fs und 100 fs für eine Region von etwa 1 μm^2 bestimmt. Interessanterweise wurden Dephasierungszeiten ermittelt, die sich, für Regionen die nur 230 nm voneinander entfernt waren, um einen Faktor von zwei unterschieden. Diese langlebigen Kohärenzen wurden mit einer speziellen Art der 2D Nanoskopie untersucht. In diesem Experiment wurde sowohl der zeitliche Abstand als auch die relative Phase zwischen zwei Pulsen variiert. Es wurde festgestellt, dass sich die lange Lebenszeit durch zwei verschiedene lokalisierte Plasmonenmoden ergibt, die an die gleiche sich ausbreitende Oberflächenplasmonenmode gekoppelt sind. In dem hier vorgestellten Beispiel konnten die kohärenten Effekte, die auf der rauhen Silberoberfläche beobachtet wurden, mit Hilfe eines klassischen Modells beschrieben werden. Dennoch sollte es mit Hilfe der 2D Nanoskopie auch möglich sein, ein breites Spektrum an faszinierenden Quantenphänomenen zu beobachten, die sonst nicht zugänglich wären. In Zukunft könnte die Technik durch den Einsatz von Pulsfolgen mit unterschiedlichen Polarisationen verallgemeinert werden, um Tensoreigenschaften der untersuchten Probe aufzuzeichnen.

Die vorgestellten Ansätze übertragen das Prinzip der zeitaufgelösten spektroskopischen Techniken von einer Ensemblemessung auf die Nanometerlängenskala und wenige räumlich lokalisierte Emitter. In Zukunft können diese Fortschritte eine breite Palette von raumzeitaufgelöster Spektroskopiemethoden ermöglichen. Anwendungen könnten die nichtlineare Spektroskopie willkürlich nanostrukturierter Proben sein, wie z.B. nanophotonische Schaltungen, photovoltaische Elemente, gekoppelte Quantentöpfe oder molekulare Aggregate. In solchen Experimenten wäre eine direkte Zuordnung der räumlichen Kopplungen und Übertragungen möglich. In einer direkten Anwendung auf Lichtsammelkomplexe könnten neue Erkentnisse des Energietransfers zur Verbesserung der Effizienz von Solarzellen beitragen. Auch wenn die beiden in dieser Arbeit diskutierten Ansätze schon in sich selbst sehr vielseitig sind, könnte eine Kombination von Nahfeldanregung mit 2D Nanoskopie nicht nur die Untersuchung von kohärenten Quantenprozessen erleichtern, sondern auch Kontrolle über diese Prozesse auf der Nanometerskala ermöglichen.

A Mathematical Supplements

A.1 Spatial Analytic Control for a Region

Based on the analytic solutions for near-field control in nanostructures for single points $\vec{r}_1$ and $\vec{r}_2$ found in Section 4.3, here the solutions are extend to describe the near-field control with feedback functions defined for volumes V. The local spectrum of volume V is then defined as the sum over all local spectra within the volume V:

$$\begin{aligned} S(V,\omega) &= \sum_{\vec{r}} w(\vec{r}) S(\vec{r},\omega) \\ &= I_1(\omega) \sum_{\alpha=x,y,z} b_\alpha \left[\sum_{\vec{r}} w(\vec{r}) |A_\alpha^{(1)}(\vec{r},\omega)|^2 \right] + I_2(\omega) \sum_{\alpha=x,y,z} b_\alpha \left[\sum_{\vec{r}} w(\vec{r}) |A_\alpha^{(2)}(\vec{r},\omega)|^2 \right] \\ &\quad + 2\sqrt{I_1(\omega) I_2(\omega)}\, \mathrm{Re} \left\{ \left[\sum_{\vec{r}} w(\vec{r}) A_{\mathrm{mix}}(\vec{r},\omega) \right] \mathrm{e}^{\mathrm{i}\Phi(\omega)} \right\}, \end{aligned} \tag{A.1}$$

where $w(\vec{r})$ is a real-valued weighting function that reflects a spatial dependent contribution of the local spectrum $S(\vec{r},\omega)$ of a certain position $\vec{r}$ to the local spectrum $S(V,\omega)$ of the volume V [e.g., if $w(\vec{r}) = 1$ all local spectra $S(\vec{r},\omega)$ contribute equally to $S(V,\omega)$].

By defining:

$$B_\alpha^{(i)}(V,\omega) = \sum_{\vec{r}} w(\vec{r}) |A_\alpha^{(i)}(\vec{r},\omega)|^2, \quad i = 1,2, \tag{A.2}$$

and

$$B_{\mathrm{mix}}(V,\omega) = \sum_{\vec{r}} w(\vec{r}) A_{\mathrm{mix}}(\vec{r},\omega) = |B_{\mathrm{mix}}(V,\omega)|\, \mathrm{e}^{\mathrm{i}\chi_{\mathrm{mix}}(V,\omega)}, \tag{A.3}$$

Eq. (A.1) can be rewritten to have the same form as Eq. (4.5):

$$\begin{aligned} S(V,\omega) = I_1(\omega) \sum_{\alpha=x,y,z} b_\alpha B_\alpha^{(1)}(V,\omega) + I_2(\omega) \sum_{\vec{r}} \sum_{\alpha=x,y,z} b_\alpha B_\alpha^{(2)}(V,\omega) \\ + 2\sqrt{I_1(\omega) I_2(\omega)}\, \mathrm{Re} \left\{ B_{\mathrm{mix}}(V,\omega)\, \mathrm{e}^{\mathrm{i}\Phi(\omega)} \right\}. \end{aligned} \tag{A.4}$$

Consequently, the linear flux of volume V reads as

$$F_{\mathrm{lin}}(V) = \frac{\delta\omega}{2\pi} \sum_{\omega=\omega_{\min}}^{\omega_{\max}} S(V,\omega) \tag{A.5}$$

and the optimal phase differences for the optimization of the linear flux at one position is found analogously to Eq. (4.8)

$$\Phi_{\max}(\omega) = -\chi_{\mathrm{mix}}(V,\omega) \qquad \text{and} \tag{A.6}$$

$$\Phi_{\min}(\omega) = -\chi_{\mathrm{mix}}(V,\omega) - \pi. \tag{A.7}$$

Using the definition of the linear flux the difference of linear flux at two spatial regions V_1 and V_2 is given by

$$f_{\mathrm{lin}}\left[\varphi_1(\omega),\varphi_2(\omega),I_1(\omega),I_2(\omega)\right] = F_{\mathrm{lin}}(V_1) - F_{\mathrm{lin}}(V_2). \tag{A.8}$$

By plugging in the corresponding definitions of the linear flux the difference recasts to

$$\begin{aligned} f_{\mathrm{lin}} &= \sum_{\omega=\omega_{\min}}^{\omega_{\max}} S(V_1,\omega) - \sum_{\omega=\omega_{\min}}^{\omega_{\max}} S(V_2,\omega) \\ &= \sum_{\omega=\omega_{\min}}^{\omega_{\max}} \Big(I_1(\omega)D_1(V_1,V_2,\omega) + I_2(\omega)D_2(V_1,V_2,\omega) + \\ &\qquad 2\sqrt{I_1(\omega)I_2(\omega)}\big\{ |B_{\mathrm{mix}}(V_1,\omega)|\cos[\chi_{\mathrm{mix}}(V_1,\omega)+\Phi(\omega)] - \\ &\qquad |B_{\mathrm{mix}}(V_2,\omega)|\cos[\chi_{\mathrm{mix}}(V_2,\omega)+\Phi(\omega)]\big\}\Big), \end{aligned} \tag{A.9}$$

where

$$D_i(\omega) = \sum_{\alpha=x,y,z} b_\alpha \left[B_\alpha^{(i)}(V_1,\omega) - B_\alpha^{(i)}(V_2,\omega)\right], \quad i=1,2. \tag{A.10}$$

The optimal phase difference that maximizes or minimizes Eq. (A.9) is obtained according to Section 4.3.2

$$\Phi(\omega) = \arctan\left\{ \frac{|B_{\mathrm{mix}}(V_2,\omega)|\sin[\chi_{\mathrm{mix}}(V_2,\omega)] - |B_{\mathrm{mix}}(V_1,\omega)|\sin[\chi_{\mathrm{mix}}(V_1,\omega)]}{|B_{\mathrm{mix}}(V_1,\omega)|\cos[\chi_{\mathrm{mix}}(V_1,\omega)] - |B_{\mathrm{mix}}(V_2,\omega)|\cos[\chi_{\mathrm{mix}}(V_2,\omega)]} \right\} + k\pi, \tag{A.11}$$

After calculation of the optimal phase difference the optimal amplitudes can be calculated by rewriting Eq. (A.9) such that

$$f_{\mathrm{lin}}\left[\gamma_1(\omega),\gamma_2(\omega)\right] = I_G(\omega)\left[D_1(\omega)\gamma_1^2(\omega) + D_2(\omega)\gamma_2^2(\omega) + 2D_{\mathrm{mix}}(\omega)\gamma_1(\omega)\gamma_2(\omega)\right], \tag{A.12}$$

with

$$D_{\mathrm{mix}}(\omega) = |B_{\mathrm{mix}}(V_1,\omega)|\cos\left[\chi_{\mathrm{mix}}(V_1,\omega)+\Phi(\omega)\right] - |B_{\mathrm{mix}}(V_2,\omega)|\cos\left[\chi_{\mathrm{mix}}(V_2,\omega)+\Phi(\omega)\right]. \tag{A.13}$$

Hence, the optimal amplitudes can be found analogously to Eq. (4.20) by two-variable extremum analysis of the function in Eq. (A.12) under the constraints $0 \le \gamma_1(\omega) \le 1$ and $0 \le \gamma_2(\omega) \le 1$ such that

$$\left[\gamma_1(\omega),\gamma_2(\omega)\right] \in \left\{[0,0],[1,-D_{\mathrm{mix}}(\omega)/D_2(\omega)],[-D_{\mathrm{mix}}(\omega)/D_1(\omega),1],[1,1]\right\}. \tag{A.14}$$

It has been shown that the analytic solutions to spatial control defined by regions are found completely analogously to the solutions described in Section 4.3.

A.2 Momentary Local Multiphoton Photoemission Probability

The momentary local multiphoton photoemission probability defined in Section 7.5 can be calculated using the expression of Eq. 7.16 for the density matrix in Liouville space:

$$|\rho^{(2n)}(t)\rangle\rangle = \left(\frac{\mathrm{i}}{\hbar}\right)^{2n} \int_0^\infty \mathrm{d}t_{2n} \int_0^\infty \mathrm{d}t_{2n-1} ... \int_0^\infty \mathrm{d}t_1 \mathcal{G}(t_{2n})\mathcal{V}\mathcal{G}(t_{2n-1})\mathcal{V}...\mathcal{G}(t_1)|\rho(t_0)\rangle\rangle$$
$$E(\vec{r}, t-t_{2n})E(\vec{r}, t-t_{2n}-t_{2n-1})...E(\vec{r}, t-t_{2n}-t_{2n-1}...-t_1). \quad \text{(A.15)}$$

Herein, a power dependence of n is assumed for the photoemission, i.e., n photons are needed to emit an electron. This corresponds to $2n$ interactions with the electric field.

To model the data that was obtained in the 2D nanoscopy measurements described in Sections 7.4.4 and 7.4.5, the photoemission is assumed to occur via virtual states (Section 2.6.1). This results in vanishing lifetime of the corresponding states and the Liouville Greens function for the material system in the absence of electric field [Eq. (7.15)] is described by a Dirac delta function:

$$\mathcal{G}(\tau) \equiv \delta(\tau). \quad \text{(A.16)}$$

Plugging in the Dirac delta function in Eq. (A.15) yields

$$|\rho^{(2n)}(t)\rangle\rangle = \left(\frac{\mathrm{i}}{\hbar}\right)^{2n} \int_0^\infty \mathrm{d}t_{2n} \int_0^\infty \mathrm{d}t_{2n-1} ... \int_0^\infty \mathrm{d}t_1 \delta(t_{2n})\mathcal{V}\delta(t_{2n-1})\mathcal{V}...\delta(t_1)|\rho(-\infty)\rangle\rangle$$
$$E(\vec{r}, t-t_{2n})E(\vec{r}, t-t_{2n}-t_{2n-1})...E(\vec{r}, t-t_{2n}-t_{2n-1}...-t_1), \quad \text{(A.17)}$$

where $t_n \geq 0$ represent the time intervals between successive interactions. By carrying out the integrals, this expression simplifies to

$$|\rho^{(2n)}(t)\rangle\rangle = \left(\frac{\mathrm{i}}{\hbar}\right)^{2n} \mathcal{V}^{2n}|\rho(-\infty)\rangle\rangle \left[E(\vec{r}, t)\right]^{2n}, \quad \text{(A.18)}$$

where the products of $\mathcal{V}$ with the density matrix are described by commutators in Hilbert space.

As described in Section 7.3.2, the momentary local multiphoton photoemission probability is then proportional to the population of the corresponding electronically excited state. Since a power dependence of n is assumed above, an electron is emitted if the n-th excited state $|n\rangle$ is populated. Hence, the momentary local multiphoton photoemission probability is determined by calculating the momentary population of the n-excited state

$$\begin{aligned} P_{\mathrm{PE}}(\vec{r}, t) &= \langle\langle nn|\rho^{(2n)}(t)\rangle\rangle \\ &= \left(\frac{\mathrm{i}}{\hbar}\right)^{2n} \langle\langle nn|\mathcal{V}^{2n}|\rho(-\infty)\rangle\rangle \left[E(\vec{r}, t)\right]^{2n}. \end{aligned} \quad \text{(A.19)}$$

Since the effect of anisotropic transition dipoles and the finite penetration depth is neglected here, the dipole-coupling operator $\mathcal{V}$ can assumed to be independent of the

spatial position $\vec{r}$. Hence, the first part of Eq. A.19 is constant in time and spatial position and the momentary local multiphoton photoemission probability is proportional to the $2n$-th power of the local electric field

$$P_{\mathrm{PE}}(\vec{r},t) \propto \left[E_{\mathrm{loc}}(\vec{r},t)\right]^{2n}. \tag{A.20}$$

A.3 Derivation of the Response Function of Two Coupled Modes

The response function for two coupled electric field modes is derived by first considering the corresponding differential equations [Eq. (7.76)].

$$\begin{aligned}
&\frac{\partial^2 E^{\mathrm{BM}}(\vec{r},t)}{\partial t^2} + 2\gamma^{\mathrm{BM}}\frac{\partial E^{\mathrm{BM}}(\vec{r},t)}{\partial t} + \omega_{0,\mathrm{BM}}^2 E^{\mathrm{BM}}(\vec{r},t) - \kappa\left[E^{\mathrm{BM}}(\vec{r},t) - E^{\mathrm{DM}}(\vec{r},t)\right] = gE_0(t)\\
&\frac{\partial^2 E^{\mathrm{DM}}(\vec{r},t)}{\partial t^2} + 2\gamma^{\mathrm{DM}}\frac{\partial E^{\mathrm{DM}}(\vec{r},t)}{\partial t} + \omega_{0,\mathrm{DM}}^2 E^{\mathrm{DM}}(\vec{r},t) - \kappa\left[E^{\mathrm{DM}}(\vec{r},t) - E^{\mathrm{BM}}(\vec{r},t)\right] = 0,
\end{aligned} \tag{A.21}$$

These equations describe the dynamics of a bright mode (BM) and a dark mode (DM) that are coupled via the effective coupling strength κ. Additionally, the bright mode is driven by an external electric field $E_0(t)$. Using the Fourier relation of Eq. (2.6) the electric field can be decomposed into monochromatic waves such that

$$E(\vec{r},t) = \frac{1}{\sqrt{2\pi}}\int_{-\infty}^{\infty} E(\vec{r},\omega)\,\mathrm{e}^{\mathrm{i}\omega t}\,\mathrm{d}\omega. \tag{A.22}$$

and the differential equations (A.21) can be written in frequency space as

$$\begin{aligned}
-\omega^2 E^{\mathrm{BM}}(\vec{r},\omega) + \mathrm{i}2\omega\gamma^{\mathrm{BM}}E^{\mathrm{BM}}(\vec{r},\omega) + \omega_{0,\mathrm{BM}}^2 E^{\mathrm{BM}}(\vec{r},\omega)&\\
- \kappa\left[E^{\mathrm{BM}}(\vec{r},\omega) - E^{\mathrm{DM}}(\vec{r},\omega)\right] &= gE_0(\omega)\\
-\omega^2 E^{\mathrm{DM}}(\vec{r},\omega) + \mathrm{i}2\omega\gamma^{\mathrm{DM}}E^{\mathrm{DM}}(\vec{r},\omega) + \omega_{0,\mathrm{DM}}^2 E^{\mathrm{DM}}(\vec{r},\omega)&\\
- \kappa\left[E^{\mathrm{DM}}(\vec{r},\omega) - E^{\mathrm{BM}}(\vec{r},\omega)\right] &= 0,
\end{aligned} \tag{A.23}$$

In vector notation this recasts to

$$\underbrace{\begin{pmatrix} -\omega^2 + \mathrm{i}2\omega\gamma^{\mathrm{BM}} + \omega_{0,\mathrm{BM}}^2 - \kappa & \kappa \\ \kappa & -\omega^2 + \mathrm{i}2\omega\gamma^{\mathrm{DM}} + \omega_{0,\mathrm{DM}}^2 - \kappa \end{pmatrix}}_{\hat{A}^{-1}} \begin{pmatrix} E^{\mathrm{BM}}(\vec{r},\omega) \\ E^{\mathrm{DM}}(\vec{r},\omega) \end{pmatrix} = \begin{pmatrix} gE_0(\omega) \\ 0 \end{pmatrix}. \tag{A.24}$$

To solve the set of differential equations the inverse of the matrix $\hat{A}^{-1}$ on the left hand side have to be multiplied from the left such that

$$\begin{pmatrix} E^{\mathrm{BM}}(\vec{r},\omega) \\ E^{\mathrm{DM}}(\vec{r},\omega) \end{pmatrix} = \hat{A}\begin{pmatrix} gE_0(\omega) \\ 0 \end{pmatrix}, \tag{A.25}$$

with

$$\hat{A} = C \begin{pmatrix} -\omega^2 + \mathrm{i}2\omega\gamma^{\mathrm{DM}} + \omega_{0,\mathrm{DM}}^2 - \kappa & -\kappa \\ -\kappa & -\omega^2 + \mathrm{i}2\omega\gamma^{\mathrm{BM}} + \omega_{0,\mathrm{BM}}^2 - \kappa \end{pmatrix} \tag{A.26}$$

and

$$C = \frac{1}{\left(-\omega^2 + \mathrm{i}2\omega\gamma^{\mathrm{BM}} + \omega_{0,\mathrm{BM}}^2 - \kappa\right)\left(-\omega^2 + \mathrm{i}2\omega\gamma^{\mathrm{DM}} + \omega_{0,\mathrm{DM}} - \kappa\right) - \kappa^2}. \tag{A.27}$$

The electric field of bright and dark mode is then described in frequency space by

$$\begin{pmatrix} E^{\mathrm{BM}}(\vec{r},\omega) \\ E^{\mathrm{DM}}(\vec{r},\omega) \end{pmatrix} = \begin{pmatrix} A^{\mathrm{BM}}(\vec{r},\omega) \\ A^{\mathrm{DM}}(\vec{r},\omega) \end{pmatrix} g E_0(\omega) \tag{A.28}$$

and according to the definition of the optical response function (Section 3.1.2), the response functions of bright and dark mode are given by

$$\begin{aligned} A^{\mathrm{BM}}(\vec{r},\omega) &= \frac{-\omega^2 + \mathrm{i}2\omega\gamma^{\mathrm{DM}} + \omega_{0,\mathrm{DM}}^2 - \kappa}{\left(\omega_{0,\mathrm{BM}}^2 - \omega^2 + \mathrm{i}2\omega\gamma^{\mathrm{BM}} - \kappa\right)\left(\omega_{0,\mathrm{DM}}^2 - \omega^2 + \mathrm{i}2\omega\gamma^{\mathrm{DM}} - \kappa\right) - \kappa^2} \\ A^{\mathrm{DM}}(\vec{r},\omega) &= \frac{-\kappa}{\left(\omega_{0,\mathrm{BM}}^2 - \omega^2 + \mathrm{i}2\omega\gamma^{\mathrm{BM}} - \kappa\right)\left(\omega_{0,\mathrm{DM}}^2 - \omega^2 + \mathrm{i}2\omega\gamma^{\mathrm{DM}} - \kappa\right) - \kappa^2}, \end{aligned} \tag{A.29}$$

where the coupling of the driving field g is neglected here since it just results in a scaling of both response functions.

Bibliography

[1] C. Dobell.
Antony van Leeuwenhoek and his "Little animals".
Harcourt, Brace Aand Company (1932).

[2] E. Abbe.
Beiträge zur Theorie des Mikroskops und der mikroskopischen Wahrnehmung.
Archiv für Mikroskopische Anatomie **9**, 413–418 (December 1873).

[3] D. W. Pohl, W. Denk, and M. Lanz.
Optical stethoscopy: Image recording with resolution $\lambda/20$.
Applied Physics Letters **44**, 651–653 (April 1984).

[4] A. H. Zewail.
Femtochemistry: Atomic-Scale Dynamics of the Chemical Bond.
The Journal of Physical Chemistry A **104**, 5660–5694 (June 2000).

[5] A. Assion, T. Baumert, M. Bergt, T. Brixner, B. Kiefer, V. Seyfried, M. Strehle, and G. Gerber.
Control of Chemical Reactions by Feedback-Optimized Phase-Shaped Femtosecond Laser Pulses.
Science **282**, 919–922 (October 1998).

[6] J. R. Lakowicz.
Principles of Fluorescence Spectroscopy.
Fourth edition. Springer US (May 2010).

[7] S. Mukamel.
Principles of Nonlinear Optical Spectroscopy.
Oxford University Press, New York (April 1999).

[8] S. Mukamel.
Multidimensional femtosecond correlation spectroscopies of electronic and vibrational excitations.
Annual Review of Physical Chemistry **51**, 691–729 (October 2000).

[9] D. Brinks, F. D. Stefani, F. Kulzer, R. Hildner, T. H. Taminiau, Y. Avlasevich, K. Mullen, and N. F. van Hulst.
Visualizing and controlling vibrational wave packets of single molecules.
Nature **465**, 905–908 (June 2010).

[10] J. Kasprzak, B. Patton, V. Savona, and W. Langbein.
Coherent coupling between distant excitons revealed by two-dimensional nonlinear hyperspectral imaging.
Nature Photonics **5**, 123 (February 2011).

[11] T. Brixner, F. J. García de Abajo, J. Schneider, and W. Pfeiffer.
Nanoscopic Ultrafast Space-Time-Resolved Spectroscopy.
Physical Review Letters **95**, 093901–4 (May 2005).

[12] T. Brixner, F. J. García de Abajo, J. Schneider, C. Spindler, and W. Pfeiffer.
Ultrafast adaptive optical near-field control.
Physical Review B **73**, 125437–11 (March 2006).

[13] M. Aeschlimann, M. Bauer, D. Bayer, T. Brixner, F. J. García de Abajo, W. Pfeiffer, M. Rohmer, C. Spindler, and F. Steeb.
Adaptive subwavelength control of nano-optical fields.
Nature **446**, 301–304 (March 2007).

[14] M. Aeschlimann, M. Bauer, D. Bayer, T. Brixner, S. Cunovic, F. Dimler, A. Fischer, W. Pfeiffer, M. Rohmer, C. Schneider, F. Steeb, C. Strüber, and D. V. Voronine.
Spatiotemporal control of nanooptical excitations.
Proceedings of the National Academy of Sciences of the United States of America **107**, 5329–5333 (March 2010).

[15] O. Schmidt, M. Bauer, C. Wiemann, R. Porath, M. Scharte, O. Andreyev, G. Schönhense, and M. Aeschlimann.
Time-resolved two photon photoemission electron microscopy.
Applied Physics B: Lasers and Optics **74**, 223–227 (March 2002).

[16] J. Diels and W. Rudolph.
Ultrashort Laser Pulse Phenomena: Fundamentals, Techniques, and Applications on a Femtosecond Time Scale.
Second edition. Academic Press Inc (May 1996).

[17] T. Brixner.
Adaptive Femtosecond Quantum Control.
Dissertation, Universität Würzburg (October 2001).

[18] M. Wollenhaupt, A. Assion, and T. Baumert.
Femtosecond Laser Pulses: Linear Properties, Manipulation, Generation and Measurement.
In *Springer Handbook of Lasers and Optics*, pp. 937–983 (2007).

[19] I. N. Bronstein, K. A. Semendyayev, G. Musiol, and H. Muehlig.
Handbook of Mathematics.
Fourth edition. Springer-Verlag GmbH (August 2002).

[20] J. D. Jackson.
Classical Electrodynamics.
Third edition. Wiley & Sons (January 1999).

[21] T. Brixner, G. Krampert, P. Niklaus, and G. Gerber.
Generation and characterization of polarization-shaped femtosecond laser pulses.
Applied Physics B: Lasers and Optics **74**, 133–144 (June 2002).

[22] T. Brixner.
Poincaré representation of polarization-shaped femtosecond laser pulses.
Applied Physics B: Lasers and Optics **76**, 531–540 (May 2003).

[23] A. Gerrard and J. M. Burch.
Introduction to Matrix Methods in Optics.
Dover Publications (June 1994).

[24] R. C. Jones.
A New Calculus for the Treatment of Optical Systems.
Journal of the Optical Society of America **31**, 488–493 (July 1941).

[25] J. P. Heritage, A. M. Weiner, and R. N. Thurston.
Picosecond pulse shaping by spectral phase and amplitude manipulation.
Optics Letters **10**, 609–611 (December 1985).

[26] A. M. Weiner, J. P. Heritage, and E. M. Kirschner.
High-resolution femtosecond pulse shaping.
Journal of the Optical Society of America B **5**, 1563–1572 (1988).

[27] A. M. Weiner.
Femtosecond pulse shaping using spatial light modulators.
Review of Scientific Instruments **71**, 1929 (2000).

[28] S. Fechner.
Quantenkontrolle im Zeit-Frequenz-Phasenraum.
Dissertation, Universität Würzburg (August 2008).

[29] P. J. Collings.
Liquid Crystals: Nature's Delicate Phase of Matter.
Second edition. Princeton University Press (December 2001).

[30] S. Rützel.
Adaptive Synthese von Femtosekunden-Laserpulsen im Zeit-Frequenz-Phasenraum.
Master thesis, Universität Würzburg (May 2009).

[31] M. Ninck, A. Galler, T. Feurer, and T. Brixner.
Programmable common-path vector field synthesizer for femtosecond pulses.
Optics Letters **32**, 3379–3381 (December 2007).

[32] D. Kane and R. Trebino.
Characterization of arbitrary femtosecond pulses using frequency-resolved optical gating.
Quantum Electronics, IEEE Journal of **29**, 571–579 (February 1993).

[33] R. Trebino and D. J. Kane.
Using phase retrieval to measure the intensity and phase of ultrashort pulses: frequency-resolved optical gating.
Journal of the Optical Society of America A **10**, 1101–1111 (May 1993).

[34] R. Trebino, K. W. DeLong, D. N. Fittinghoff, J. N. Sweetser, M. A. Krumbügel, B. A. Richman, and D. J. Kane.
Measuring ultrashort laser pulses in the time-frequency domain using frequency-resolved optical gating.
Review of Scientific Instruments **68**, 3277–3295 (May 1997).

[35] K. W. DeLong, R. Trebino, and D. J. Kane.
Comparison of ultrashort-pulse frequency-resolved-optical-gating traces for three common beam geometries.
Journal of the Optical Society of America B **11**, 1595–1608 (1994).

[36] J. Paye, M. Ramaswamy, J. G. Fujimoto, and E. P. Ippen.
Measurement of the amplitude and phase of ultrashort light pulses from spectrally resolved autocorrelation.
Optics Letters **18**, 1946–1948 (November 1993).

[37] K. W. DeLong, R. Trebino, J. Hunter, and W. E. White.
Frequency-resolved optical gating with the use of second-harmonic generation.
Journal of the Optical Society of America B **11**, 2206–2215 (November 1994).

[38] K. W. DeLong, D. N. Fittinghoff, R. Trebino, B. Kohler, and K. Wilson.
Pulse retrieval in frequency-resolved optical gating based on the method of generalized projections.
Optics Letters **19**, 2152–2154 (December 1994).

[39] K. W. DeLong and R. Trebino.
Improved ultrashort pulse-retrieval algorithm for frequency-resolved optical gating.
Journal of the Optical Society of America A **11**, 2429–2437 (September 1994).

[40] P. Schlup, O. Masihzadeh, L. Xu, R. Trebino, and R. A. Bartels.
Tomographic retrieval of the polarization state of an ultrafast laser pulse.
Optics Letters **33**, 267–269 (February 2008).

[41] D. Keusters, H. Tan, P. O'Shea, E. Zeek, R. Trebino, and W. S. Warren.
Relative-phase ambiguities in measurements of ultrashort pulses with well-separated multiple frequency components.
Journal of the Optical Society of America B **20**, 2226–2237 (October 2003).

[42] L. Lepetit, G. Chériaux, and M. Joffre.
Linear techniques of phase measurement by femtosecond spectral interferometry for applications in spectroscopy.
Journal of the Optical Society of America B **12**, 2467–2474 (December 1995).

[43] W. J. Walecki, D. N. Fittinghoff, A. L. Smirl, and R. Trebino.
Characterization of the polarization state of weak ultrashort coherent signals by dual-channel spectral interferometry.
Optics Letters **22**, 81–83 (January 1997).

[44] C. Dorrer.
Influence of the calibration of the detector on spectral interferometry.
Journal of the Optical Society of America B **16**, 1160–1168 (July 1999).

[45] C. Dorrer, N. Belabas, J. Likforman, and M. Joffre.
Spectral resolution and sampling issues in Fourier-transform spectral interferometry.
Journal of the Optical Society of America B **17**, 1795–1802 (October 2000).

[46] C. Dorrer, N. Belabas, J. Likforman, and M. Joffre.
Experimental implementation of Fourier-transform spectral interferometry and its application to the study of spectrometers.
Applied Physics B: Lasers and Optics **70**, 99–107 (May 2000).

[47] M. I. Stockman, S. V. Faleev, and D. J. Bergman.
Coherent Control of Femtosecond Energy Localization in Nanosystems.
Physical Review Letters **88**, 067402 (January 2002).

[48] X. Li and M. I. Stockman.
Highly efficient spatiotemporal coherent control in nanoplasmonics on a nanometer-femtosecond scale by time reversal.
Physical Review B **77**, 195109 (May 2008).

[49] P. Tuchscherer, C. Rewitz, D. V. Voronine, F. J. García de Abajo, W. Pfeiffer, and T. Brixner.
Analytic coherent control of plasmon propagation in nanostructures.
Optics Express **17**, 14235–14259 (2009).

[50] G. Volpe, G. Molina-Terriza, and R. Quidant.
Deterministic Subwavelength Control of Light Confinement in Nanostructures.
Physical Review Letters **105**, 216802 (November 2010).

[51] D. E. Goldberg.
Genetic Algorithms in Search, Optimization, and Machine Learning.
First edition. Addison-Wesley Professional (January 1989).

[52] H. Schwefel.
Evolution and Optimum Seeking.
Wiley-Interscience (January 1995).

[53] M. Nowak.
Evolutionary Dynamics: Exploring the Equations of Life.
Harvard University Press (September 2006).

[54] L. Novotny and B. Hecht.
Principles of Nano-Optics.
Cambridge University Press, Cambridge (June 2006).

[55] S. A. Maier.
Plasmonics: Fundamentals and Applications.
First edition. Springer, Berlin (August 2007).

[56] M. Minsky.
Memoir on Inventing the Confocal Scanning Microscope.
Scanning **10**, 128–138 (1988).

[57] R. H. Webb.
Confocal optical microscopy.
Reports on Progress in Physics **59**, 427–471 (March 1996).

[58] H. P. Bonzel and C. Kleint.
On the history of photoemission.
Progress in Surface Science **49**, 107–153 (June 1995).

[59] H. Hertz.
Ueber einen Einfluss des ultravioletten Lichtes auf die electrische Entladung.
Annalen der Physik **267**, 983–1000 (1887).

[60] W. Hallwachs.
Ueber den Einfluss des Lichtes auf electrostatisch geladene Körper.
Annalen der Physik **269**, 301–312 (1888).

[61] A. Einstein.
Über einen die Erzeugung und Verwandlung des Lichtes betreffenden heuristischen Gesichtspunkt.
Annalen der Physik **322**, 132–148 (1905).

[62] C. Kramer.
Kohärente zweidimensionale Nanoskopie.
Diploma thesis, Universität Würzburg (March 2011).

[63] P. M. Echenique, J. M. Pitarke, E. V. Chulkov, and A. Rubio.
Theory of inelastic lifetimes of low-energy electrons in metals.
Chemical Physics **251**, 1–35 (January 2000).

[64] C. A. Schmuttenmaer, M. Aeschlimann, H. E. Elsayed-Ali, R. J. D. Miller, D. A. Mantell, J. Cao, and Y. Gao.
Time-resolved two-photon photoemission from Cu(100): Energy dependence of electron relaxation.
Physical Review B **50**, 8957 (September 1994).

[65] H. Petek and S. Ogawa.
Femtosecond time-resolved two-photon photoemission studies of electron dynamics in metals.
Progress in Surface Science **56**, 239–310 (December 1997).

[66] S. Günther, B. Kaulich, L. Gregoratti, and M. Kiskinova.
Photoelectron microscopy and applications in surface and materials science.
Progress in Surface Science **70**, 187–260 (July 2002).

[67] R. Tromp, J. Hannon, A. Ellis, W. Wan, A. Berghaus, and O. Schaff.
A new aberration-corrected, energy-filtered LEEM/PEEM instrument. I. Principles and design.
Ultramicroscopy **110**, 852–861 (June 2010).

[68] P. Melchior.
Nahfelduntersuchungen an nanooptischen Bowtie-Antennen.
Diploma thesis, Universität Kaiserslautern (July 2009).

[69] J. Lin, N. Weber, A. Wirth, S. H. Chew, M. Escher, M. Merkel, M. F. Kling, M. I. Stockman, F. Krausz, and U. Kleineberg.
Time of flight-photoemission electron microscope for ultrahigh spatiotemporal probing of nanoplasmonic optical fields.
Journal of Physics: Condensed Matter **21**, 314005 (August 2009).

[70] C. Schneider.
Zeit- und energieaufgelöste Time-of-Flight-PEEM-Messungen an strukturierten Oberflächen.
Diploma thesis, Universität Kaiserslautern (May 2008).

[71] M. Cinchetti, A. Gloskovskii, S. A. Nepjiko, G. Schönhense, H. Rochholz, and M. Kreiter.
Photoemission Electron Microscopy as a Tool for the Investigation of Optical Near Fields.
Physical Review Letters **95**, 047601 (July 2005).

[72] C. Strüber.
Subwavelength Spatial and Femtosecond Temporal Control of Optical Near-Fields with Polarization Shaped Laser Pulses.
Master thesis, Universität Bielefeld (November 2008).

[73] C. Rewitz.
Analytische und adaptive kohärente Kontrolle optischer Nahfelder durch Formung ultrakurzer Laserpulse.
Diploma thesis, Universität Würzburg (April 2009).

[74] W. L. Barnes, A. Dereux, and T. W. Ebbesen.
Surface plasmon subwavelength optics.
Nature **424**, 824–830 (August 2003).

[75] A. Otto.
Excitation of nonradiative surface plasma waves in silver by the method of frustrated total reflection.
Zeitschrift für Physik **216**, 398–410 (July 1968).

[76] E. Kretschmann.
Die Bestimmung optischer Konstanten von Metallen durch Anregung von Oberflächenplasmaschwingungen.
Zeitschrift für Physik **241**, 313–324 (August 1971).

[77] H. Raether.
Surface Plasmons on Smooth and Rough Surfaces and on Gratings, volume 111 of *Springer Tracts in Modern Physics.*
Springer, Berlin (December 1988).

[78] E. D. Palik.
Handbook of Optical Constants of Solids.
Academic Press, New York (October 1997).

[79] E. Ozbay.
Plasmonics: Merging Photonics and Electronics at Nanoscale Dimensions.
Science **311**, 189–193 (January 2006).

[80] S. Kim, J. Jin, Y. Kim, I. Park, Y. Kim, and S. Kim.
High-harmonic generation by resonant plasmon field enhancement.
Nature **453**, 757–760 (June 2008).

[81] N. Liu, M. L. Tang, M. Hentschel, H. Giessen, and A. P. Alivisatos.
Nanoantenna-enhanced gas sensing in a single tailored nanofocus.
Nature Materials **10**, 631–636 (May 2011).

[82] S. Lal, S. Link, and N. J. Halas.
Nano-optics from sensing to waveguiding.
Nature Photonics **1**, 641–648 (November 2007).

[83] S. Schlücker and W. Kiefer.
Surface Enhanced Raman Spectroscopy: Analytical, Biophysical and Life Science Applications.
First edition. Wiley-VCH (December 2010).

[84] P. Mühlschlegel, H. Eisler, O. J. F. Martin, B. Hecht, and D. W. Pohl.
Resonant Optical Antennas.
Science **308**, 1607–1609 (June 2005).

[85] P. Biagioni, J. Huang, and B. Hecht.
Nanoantennas for visible and infrared radiation.
1103.1568 (March 2011).

[86] H. Kuwata, H. Tamaru, K. Esumi, and K. Miyano.
Resonant light scattering from metal nanoparticles: Practical analysis beyond Rayleigh approximation.
Applied Physics Letters **83**, 4625 (December 2003).

[87] G. Mie.
Beiträge zur Optik trüber Medien, speziell kolloidaler Metallösungen.
Annalen der Physik **330**, 377–445 (January 1908).

[88] T. Kokkinakis and K. Alexopoulos.
Observation of Radiative Decay of Surface Plasmons in Small Silver Particles.
Physical Review Letters **28**, 1632 (June 1972).

[89] S. Link and El-Sayed.
Shape and size dependence of radiative, non-radiative and photothermal properties of gold nanocrystals.
International Reviews in Physical Chemistry **19**, 409–453 (2000).

[90] G. T. Boyd, Z. H. Yu, and Y. R. Shen.
Photoinduced luminescence from the noble metals and its enhancement on roughened surfaces.
Physical Review B **33**, 7923 (June 1986).

[91] M. R. Beversluis, A. Bouhelier, and L. Novotny.
Continuum generation from single gold nanostructures through near-field mediated intraband transitions.
Physical Review B **68**, 115433 (September 2003).

[92] C. Sönnichsen, T. Franzl, T. Wilk, G. von Plessen, and J. Feldmann.
Plasmon resonances in large noble-metal clusters.
New Journal of Physics **4**, 93–93 (November 2002).

[93] J. R. Krenn, M. Salerno, N. Felidj, B. Lamprecht, G. Schider, A. Leitner, F. R. Aussenegg, J. C. Weeber, A. Dereux, and J. P. Goudonnet.
Light field propagation by metal micro- and nanostructures.
Journal of Microscopy **202**, 122–128 (April 2001).

[94] S. A. Maier, M. L. Brongersma, P. G. Kik, and H. A. Atwater.
Observation of near-field coupling in metal nanoparticle chains using far-field polarization spectroscopy.
Physical Review B **65**, 193408 (May 2002).

[95] S. A. Maier, P. G. Kik, and H. A. Atwater.
Observation of coupled plasmon-polariton modes in Au nanoparticle chain waveguides of different lengths: Estimation of waveguide loss.
Applied Physics Letters **81**, 1714–1716 (2002).

[96] S. A. Maier, P. G. Kik, and H. A. Atwater.
Optical pulse propagation in metal nanoparticle chain waveguides.
Physical Review B **67**, 205402 (May 2003).

[97] S. Maier, P. Kik, H. Atwater, S. Meltzer, E. Harel, B. Koel, and A. Requicha.
Local detection of electromagnetic energy transport below the diffraction limit in metal nanoparticle plasmon waveguides.
Nature Materials **2**, 229–232 (March 2003).

[98] D. Yelin, D. Meshulach, and Y. Silberberg.
Adaptive femtosecond pulse compression.
Optics Letters **22**, 1793–1795 (December 1997).

[99] T. Baumert, T. Brixner, V. Seyfried, M. Strehle, and G. Gerber.
Femtosecond pulse shaping by an evolutionary algorithm with feedback.
Applied Physics B: Lasers and Optics **65**, 779–782 (December 1997).

[100] J.-S. Huang, D. V. Voronine, P. Tuchscherer, T. Brixner, and B. Hecht.
Deterministic spatiotemporal control of optical fields in nanoantennas and plasmonic circuits.
Physical Review B **79**, 195441–5 (May 2009).

[101] F. J. García de Abajo.
Interaction of Radiation and Fast Electrons with Clusters of Dielectrics: A Multiple Scattering Approach.
Physical Review Letters **82**, 2776 (March 1999).

[102] F. J. García de Abajo.
Multiple scattering of radiation in clusters of dielectrics.
Physical Review B **60**, 6086 (August 1999).

[103] J. J. Rehr and R. C. Albers.
Scattering-matrix formulation of curved-wave multiple-scattering theory: Application to x-ray-absorption fine structure.
Physical Review B **41**, 8139 (April 1990).

[104] V. Fritzsche.
A new spherical-wave approximation for photoelectron diffraction, EXAFS and MEED.
Journal of Physics: Condensed Matter **2**, 1413–1424 (February 1990).

[105] C. Tutsch.
Adaptive femtosecond near-fiel control.
Diploma thesis, Universität Würzburg (December 2005).

[106] P. Vasa, C. Ropers, R. Pomraenke, and C. Lienau.
Ultra-fast nano-optics.
Laser & Photonics Review **3**, 483 (February 2009).

[107] S. I. Bozhevolnyi, V. S. Volkov, E. Devaux, J. Laluet, and T. W. Ebbesen.
Channel plasmon subwavelength waveguide components including interferometers and ring resonators.
Nature **440**, 508–511 (March 2006).

[108] J.-S. Huang, T. Feichtner, P. Biagioni, and B. Hecht.
Impedance Matching and Emission Properties of Nanoantennas in an Optical Nanocircuit.
Nano Letters **9**, 1897–1902 (May 2009).

[109] S. A. Maier, M. L. Brongersma, P. G. Kik, S. Meltzer, A. A. G. Requicha, and H. A. Atwater.
Plasmonics - A Route to Nanoscale Optical Devices.
Advanced Materials **13**, 1501–1505 (September 2001).

[110] P. Andrew and W. L. Barnes.
Energy Transfer Across a Metal Film Mediated by Surface Plasmon Polaritons.
Science **306**, 1002–1005 (November 2004).

[111] B. Lamprecht, J. R. Krenn, G. Schider, H. Ditlbacher, M. Salerno, N. Felidj, A. Leitner, F. R. Aussenegg, and J. C. Weeber.
Surface plasmon propagation in microscale metal stripes.
Applied Physics Letters **79**, 51–53 (July 2001).

[112] A. Kuzyk, M. Pettersson, J. J. Toppari, T. K. Hakala, H. Tikkanen, H. Kunttu, and P. Törmä.
Molecular coupling of light with plasmonic waveguides.
Optics Express **15**, 9908–9917 (July 2007).

[113] L. Novotny.
Effective Wavelength Scaling for Optical Antennas.
Physical Review Letters **98**, 266802–4 (June 2007).

[114] M. Sukharev and T. Seideman.
Phase and Polarization Control as a Route to Plasmonic Nanodevices.
Nano Letters **6**, 715–719 (April 2006).

[115] J. R. Krenn and J. Weeber.
Surface plasmon polaritons in metal stripes and wires.
Philosophical Transactions of the Royal Society A: Mathematical, Physical and Engineering Sciences **362**, 739–756 (April 2004).

[116] T. Brixner, F. García de Abajo, C. Spindler, and W. Pfeiffer.
Adaptive ultrafast nano-optics in a tight focus.
Applied Physics B: Lasers and Optics **84**, 89–95 (July 2006).

[117] M. Durach, A. Rusina, M. I. Stockman, and K. Nelson.
Toward Full Spatiotemporal Control on the Nanoscale.
Nano Letters **7**, 3145–3149 (October 2007).

[118] A. Kubo, K. Onda, H. Petek, Z. Sun, Y. S. Jung, and H. K. Kim.
Femtosecond Imaging of Surface Plasmon Dynamics in a Nanostructured Silver Film.
Nano Letters **5**, 1123–1127 (June 2005).

[119] S. Choi, D. Park, C. Lienau, M. S. Jeong, C. C. Byeon, D. Ko, and D. S. Kim.
Femtosecond phase control of spatial localization of the optical near-field in a metal nanoslit array.
Optics Express **16**, 12075–12083 (July 2008).

[120] M. Sukharev and T. Seideman.
Coherent control of light propagation via nanoparticle arrays.
Journal of Physics B: Atomic, Molecular and Optical Physics **40**, 283–298 (May 2007).

[121] K. S. Yee.
Numerical Solution of Initial Boundary Value Problems Involving Maxwell's Equations in Isotropic Media.
IEEE Transactions on Antennas and Propagation **14**, 302–307 (May 1966).

[122] M. Sandtke, R. J. P. Engelen, H. Schoenmaker, I. Attema, H. Dekker, I. Cerjak, J. P. Korterik, B. Segerink, and L. Kuipers.
Novel instrument for surface plasmon polariton tracking in space and time.
Review of Scientific Instruments **79**, 013704 (January 2008).

[123] M. Schnell, A. Garcia-Etxarri, A. J. Huber, K. B. Crozier, A. Borisov, J. Aizpurua, and R. Hillenbrand.
Amplitude- and Phase-Resolved Near-Field Mapping of Infrared Antenna Modes by Transmission-Mode Scattering-Type Near-Field Microscopy.
Journal of Physical Chemistry C **114**, 7341–7345 (January 2010).

[124] C. Rewitz, T. Keitzl, P. Tuchscherer, J. Huang, P. Geisler, G. Razinskas, B. Hecht, and T. Brixner.
Ultrafast Plasmon Propagation in Nanowires Characterized by Far-Field Spectral Interferometry.
Nano Letters **12**, 45–49 (January 2012).

[125] M. Shapiro and P. Brumer.
Laser control of product quantum state populations in unimolecular reactions.
The Journal of Chemical Physics **84**, 4103 (April 1986).

[126] D. J. Tannor and S. A. Rice.
Control of selectivity of chemical reaction via control of wave packet evolution.
The Journal of Chemical Physics **83**, 5013–5018 (November 1985).

[127] R. S. Judson and H. Rabitz.
Teaching lasers to control molecules.
Physical Review Letters **68**, 1500–1503 (March 1992).

[128] K. L. Shuford, M. A. Ratner, and G. C. Schatz.
Multipolar excitation in triangular nanoprisms.
The Journal of Chemical Physics **123**, 114713 (June 2005).

[129] M. Rang, A. C. Jones, F. Zhou, Z. Li, B. J. Wiley, Y. Xia, and M. B. Raschke.
Optical Near-Field Mapping of Plasmonic Nanoprisms.
Nano Letters **8**, 3357–3363 (September 2008).

[130] J. Nelayah, M. Kociak, O. Stéphan, N. Geuquet, L. Henrard, F. J. García de Abajo, I. Pastoriza-Santos, L. M. Liz-Marzán, and C. Colliex.
Two-Dimensional Quasistatic Stationary Short Range Surface Plasmons in Flat Nanoprisms.
Nano Letters **10**, 902–907 (February 2010).

[131] R. Zia, J. A. Schuller, A. Chandran, and M. L. Brongersma.
Plasmonics: the next chip-scale technology.
Materials Today **9**, 20–27 (January 2006).

[132] T. H. Taminiau, F. D. Stefani, F. B. Segerink, and N. F. van Hulst.
Optical antennas direct single-molecule emission.
Nature Photonics **2**, 234–237 (April 2008).

[133] A. Kinkhabwala, Z. Yu, S. Fan, Y. Avlasevich, K. Müllen, and W. E. Moerner.
Large single-molecule fluorescence enhancements produced by a bowtie nanoantenna.
Nature Photonics **3**, 654–657 (November 2009).

[134] P. Bharadwaj, B. Deutsch, and L. Novotny.
Optical Antennas.
Advances in Optics and Photonics **1**, 438–483 (November 2009).

[135] S. A. Rice and M. Zhao.
Optical Control of Molecular Dynamics.
Wiley-Interscience, New York (February 2000).

[136] P. W. Brumer and M. Shapiro.
Principles of the Quantum Control of Molecular Processes.
Wiley-Interscience, New York (2003).

[137] N. Engheta.
Circuits with Light at Nanoscales: Optical Nanocircuits Inspired by Metamaterials.
Science **317**, 1698 –1702 (September 2007).

[138] H. Wang, D. W. Brandl, P. Nordlander, and N. J. Halas.
Plasmonic Nanostructures: Artificial Molecules.
Accounts of Chemical Research **40**, 53–62 (January 2007).

[139] S. Kühn, U. Hakanson, L. Rogobete, and V. Sandoghdar.
Enhancement of Single-Molecule Fluorescence Using a Gold Nanoparticle as an Optical Nanoantenna.
Physical Review Letters **97**, 017402–4 (July 2006).

[140] R. Chakrabarti and H. Rabitz.
Quantum control landscapes.
International Reviews in Physical Chemistry **26**, 671 (October 2007).

[141] K. Kneipp, Y. Wang, H. Kneipp, L. T. Perelman, I. Itzkan, R. R. Dasari, and M. S. Feld.
Single Molecule Detection Using Surface-Enhanced Raman Scattering (SERS).
Physical Review Letters **78**, 1667–1670 (March 1997).

[142] J. R. Lombardi and R. L. Birke.
A Unified View of Surface-Enhanced Raman Scattering.
Accounts of Chemical Research **42**, 734–742 (June 2009).

[143] M. Aeschlimann, T. Brixner, S. Cunovic, A. Fischer, P. Melchior, W. Pfeiffer, M. Rohmer, C. Schneider, C. Strüber, P. Tuchscherer, and D. V. Voronine.
Nano-optical Control of Hot-Spot Field Superenhancement on a Corrugated Silver Surface.
IEEE Journal of Selected Topics in Quantum Electronics **PP**, 1–8 (April 2011).

[144] N. Dudovich, B. Dayan, S. M. Gallagher Faeder, and Y. Silberberg.
Transform-Limited Pulses Are Not Optimal for Resonant Multiphoton Transitions.
Physical Review Letters **86**, 47 (January 2001).

[145] B. Lamprecht, J. R. Krenn, A. Leitner, and F. R. Aussenegg.
Resonant and Off-Resonant Light-Driven Plasmons in Metal Nanoparticles Studied by Femtosecond-Resolution Third-Harmonic Generation.
Physical Review Letters **83**, 4421 (November 1999).

[146] N. Nilius, N. Ernst, and H. Freund.
Photon Emission Spectroscopy of Individual Oxide-Supported Silver Clusters in a Scanning Tunneling Microscope.
Physical Review Letters **84**, 3994 (April 2000).

[147] T. Hanke, G. Krauss, D. Träutlein, B. Wild, R. Bratschitsch, and A. Leitenstorfer.
Efficient Nonlinear Light Emission of Single Gold Optical Antennas Driven by Few-Cycle Near-Infrared Pulses.
Physical Review Letters **103**, 257404 (December 2009).

[148] A. Anderson, K. Deryckx, X. Xu, G. Steinmeyer, and M. Raschke.
Few-Femtosecond Plasmon Dephasing of a Single Metallic Nanostructure from Optical Response Function Reconstruction by Interferometric Frequency Resolved Optical Gating.
Nano Letters **10**, 2519–2524 (July 2010).

[149] J. M. Gunn, S. H. High, V. V. Lozovoy, and M. Dantus.
Measurement and Control of Ultrashort Optical Pulse Propagation in Metal Nanoparticle-Covered Dielectric Surfaces.
The Journal of Physical Chemistry C **114**, 12375–12381 (July 2010).

[150] G. S. Engel, T. R. Calhoun, E. L. Read, T. Ahn, T. Mancal, Y. Cheng, R. E. Blankenship, and G. R. Fleming.
Evidence for wavelike energy transfer through quantum coherence in photosynthetic systems.
Nature **446**, 782–786 (April 2007).

[151] E. Collini, C. Y. Wong, K. E. Wilk, P. M. G. Curmi, P. Brumer, and G. D. Scholes.
Coherently wired light-harvesting in photosynthetic marine algae at ambient temperature.
Nature **463**, 644–647 (February 2010).

[152] D. M. Jonas.
Two-dimensional femtosecond spectroscopy.
Annual Review of Physical Chemistry **54**, 425–463 (October 2003).

[153] M. Cho.
Coherent two-dimensional optical spectroscopy.
Chemical Reviews **108**, 1331–1418 (April 2008).

[154] L. Lepetit and M. Joffre.
Two-dimensional nonlinear optics using Fourier-transform spectral interferometry.
Optics Letters **21**, 564–566 (April 1996).

[155] P. Hamm, M. Lim, and R. M. Hochstrasser.
Structure of the amide i band of peptides measured by femtosecond nonlinear-infrared spectroscopy.
The Journal of Physical Chemistry B **102**, 6123–6138 (July 1998).

[156] J. D. Hybl, A. W. Albrecht, S. M. Gallagher Faeder, and D. M. Jonas.
Two-dimensional electronic spectroscopy.
Chemical Physics Letters **297**, 307–313 (November 1998).

[157] P. Tian, D. Keusters, Y. Suzaki, and W. S. Warren.
Femtosecond phase-coherent two-dimensional spectroscopy.
Science **300**, 1553–1555 (June 2003).

[158] P. F. Tekavec, G. A. Lott, and A. H. Marcus.
Fluorescence-detected two-dimensional electronic coherence spectroscopy by acousto-optic phase modulation.
The Journal of Chemical Physics **127**, 214307–21 (December 2007).

[159] O. Golonzka, M. Khalil, N. Demirdöven, and A. Tokmakoff.
Vibrational anharmonicities revealed by coherent two-dimensional infrared spectroscopy.
Physical Review Letters **86**, 2154–2157 (March 2001).

[160] T. Brixner, J. Stenger, H. M. Vaswani, M. Cho, R. E. Blankenship, and G. R. Fleming.
Two-dimensional spectroscopy of electronic couplings in photosynthesis.
Nature **434**, 625–628 (March 2005).

[161] N. Christensson, F. Milota, A. Nemeth, J. Sperling, H. F. Kauffmann, T. Pullerits, and J. Hauer.
Two-Dimensional Electronic Spectroscopy of β-Carotene.
The Journal of Physical Chemistry B **113**, 16409–16419 (December 2009).

[162] S. Shim, D. B. Strasfeld, Y. L. Ling, and M. T. Zanni.
Automated 2D IR spectroscopy using a mid-IR pulse shaper and application of this technology to the human islet amyloid polypeptide.
Proceedings of the National Academy of Sciences **104**, 14197–14202 (September 2007).

[163] M. L. Cowan, B. D. Bruner, N. Huse, J. R. Dwyer, B. Chugh, E. T. J. Nibbering, T. Elsaesser, and R. J. D. Miller.
Ultrafast memory loss and energy redistribution in the hydrogen bond network of liquid H_2O.
Nature **434**, 199–202 (March 2005).

[164] C. Kolano, J. Helbing, M. Kozinski, W. Sander, and P. Hamm.
Watching hydrogen-bond dynamics in a beta-turn by transient two-dimensional infrared spectroscopy.
Nature **444**, 469–472 (November 2006).

[165] J. Zheng, K. Kwak, J. Asbury, X. Chen, I. R. Piletic, and M. D. Fayer.
Ultrafast Dynamics of Solute-Solvent Complexation Observed at Thermal Equilibrium in Real Time.
Science **309**, 1338–1343 (August 2005).

[166] K. Stone, K. Gundogdu, D. Turner, X. Li, S. Cundiff, and K. Nelson.
Two-Quantum 2D FT Electronic Spectroscopy of Biexcitons in GaAs Quantum Wells.
Science **324**, 1169–1173 (May 2009).

[167] A. V. Pakoulev, S. B. Block, L. A. Yurs, N. A. Mathew, K. M. Kornau, and J. C. Wright.
Multiply Resonant Coherent Multidimensional Spectroscopy: Implications for Materials Science.
The Journal of Physical Chemistry Letters **1**, 822–828 (March 2010).

[168] S. W. Hell.
Far-Field Optical Nanoscopy.
Science **316**, 1153 –1158 (May 2007).

[169] T. Guenther, C. Lienau, T. Elsaesser, M. Glanemann, V. Axt, T. Kuhn, S. Eshlaghi, and A. Wieck.
Coherent nonlinear optical response of single quantum dots studied by ultrafast near-field spectroscopy.
Physical Review Letters **89**, 057401 (July 2002).

[170] S. Rahav and S. Mukamel.
Multidimensional attosecond photoelectron spectroscopy with shaped pulses and quantum optical fields.
Physical Review A **81**, 063810 (June 2010).

[171] T. Brixner, T. Mancal, I. V. Stiopkin, and G. R. Fleming.
Phase-stabilized two-dimensional electronic spectroscopy.
The Journal of Chemical Physics **121**, 4221–4236 (June 2004).

[172] R. W. Boyd.
Nonlinear Optics.
Third edition. Academic Press (April 2008).

[173] M. Aeschlimann, T. Brixner, A. Fischer, C. Kramer, P. Melchior, W. Pfeiffer, C. Schneider, C. Strüber, P. Tuchscherer, and D. V. Voronine.
Coherent Two-Dimensional Nanoscopy.
Science **333**, 1723 –1726 (September 2011).

[174] C. Timm and K. H. Bennemann.
Response theory for time-resolved second-harmonic generation and two-photon photoemission.
Journal of Physics: Condensed Matter **16**, 661–694 (February 2004).

[175] D. Keusters, H. Tan, and W. S. Warren.
Role of Pulse Phase and Direction in Two-Dimensional Optical Spectroscopy.
The Journal of Physical Chemistry A **103**, 10369–10380 (December 1999).

[176] M. Merschdorf, C. Kennerknecht, and W. Pfeiffer.
Collective and single-particle dynamics in time-resolved two-photon photoemission.
Physical Review B **70**, 193401 (November 2004).

[177] D. Bayer, C. Wiemann, O. Gaier, M. Bauer, and M. Aeschlimann.
Time-Resolved 2PPE and Time-Resolved PEEM as a Probe of LSP's in Silver Nanoparticles.
Journal of Nanomaterials **2008**, 1–11 (2008).

[178] P. B. Johnson and R. W. Christy.
Optical Constants of the Noble Metals.
Physical Review B **6**, 4370 (December 1972).

[179] S. Zhang, D. A. Genov, Y. Wang, M. Liu, and X. Zhang.
Plasmon-induced transparency in metamaterials.
Physical Review Letters **101**, 047401 (July 2008).

[180] M. I. Stockman, M. F. Kling, U. Kleineberg, and F. Krausz.
Attosecond nanoplasmonic-field microscope.
Nature Photonics **1**, 539–544 (2007).

Acknowledgements

At this point, I want to state that this dissertation would not have been possible without joint innovative efforts and excellent team work. I am thankful to all the people I have had the pleasure to work with. The pleasant and cooperative atmosphere that I experienced in the "Physikalische Chemie 1" as well as in all collaborations deserves a special mention and I am grateful that I could be a part of them. Apart from that, many people have contributed in one way or another, and regrettably, I cannot acknowledge everyone of them by name. However, I want to thank explicitly:

- Prof. Dr. Tobias Brixner for giving me the opportunity to work under excellent working conditions in this exciting research field, for the valuable advices that he provided in many fruitful discussions, for his encouraging personality and for the funding to visit several conferences, skiseminars and graduate schools,
- Prof. Dr. Walter Pfeiffer for his patience and willing during all the beneficial discussions that have been substantial for the presented results,
- Prof. Dr. Martin Aeschlimann for providing the research facilities in his lab, for his advices concerning PEEM, and for his humorous personality,
- Christian Rewitz for being such a great teammate and friend in all matters, and for carefully proof-reading this thesis,
- Dr. Dmitri V. Voronine for introducing me into the field of nano optics, for the assistance in all the projects that were presented in this thesis, and for his encouraging and cheerful personality,
- Dr. Jer-Shing Huang for his open-minded personality, for providing his expertise in nanocircuitry, and for enabling a unique trip to Taiwan,
- Christian Strüber, Dmitri Voronine, Alexander Fischer, Pascal Melchior, Christian Schneider, Christian Kramer, Martin Rohmer, Daniela Bayer and Stefan Cunovic for the enjoyable, cooperative and very productive atmosphere during the measurement sessions,
- Christian Strüber and Christian Kramer for their valuable help with the analysis of the obtained data and for continuing the 2D nanoscopy project in the future,
- Prof. Dr. Bert Hecht for sharing his profound knowledge about nano optics,
- Prof. Dr. Javier García de Abajo for providing the MESME code and for useful advices during the near-field simulations in the T-chain nanostructure,

- Alexander Fischer for the excellent cakes and meals,
- the Ultrafast Surface Science Group for the friendly atmosphere during the measurement sessions in their lab,
- Ulrike Selig, Philipp Terberger and Michael Förster for teaching me a lot about 2D spectroscopy,
- Dr. Patrick Nuernberger for his ability to welcome any question,
- the technical assistants, the workshops managed by Wolfgang Liebler and Jürgen Zimmerman and our secretary Andrea Hoffelner for their help in several occasions,
- Philipp Rudolf for always putting me in a good mood while stopping by at my office, and for proof-reading parts of this thesis,
- Christoph Schwarz for all the coffee-breaks, and for his drive for perfection while proof-reading parts of this thesis,
- the "Stammtisch" guys for the relaxing and mostly nonscientific lunch breaks, and for simply being good friends,
- my parents and family for supporting me in every sense and for equipping me with everything I needed to reach this point,
- my girlfriend Eva for being such a wonderful person, for her faith in me, and for her incredible support and unlimited love.